CRANFIELD UNIVERSITY

Samer Aldhaher

Design and Optimization of Switched-Mode Circuits for Inductive Links

School of Engineering
Energy & Power Engineering Division

PhD Thesis
Academic Year: 2010 - 2014

Supervisor: Prof. Patrick Chi-Kwong Luk
January 2014

CRANFIELD UNIVERSITY

School of Engineering
Energy & Power Engineering Division

PhD THESIS

Academic Year 2010 - 2014

Samer Aldhaher

DESIGN AND OPTIMIZATION OF SWITCHED-MODE CIRCUITS FOR INDUCTIVE LINKS

Supervisor: Prof. Patrick Chi-Kwong Luk

January 2014

This thesis is submitted in partial fulfilment of the requirements for the degree of Doctor of Philosophy

to my parents

Abstract

Wireless power transfer (WPT) via magnetic induction is an emerging technology that is a result of the significant advancements in power electronics. Mobiles phones can now be charged wirelessly by placing them on a charging surface. Electric vehicles can charge their batteries while being parked over a certain charging spot. The possible applications of this technology are vast and the potential it has to revolutionise and change the way that we use today's application is huge.

Wireless power transfer via magnetic induction, also referred to as inductive power transfer (IPT), does not necessarily aim to replace the cable. It is intended to coexist and operate in conjunction with the cable. Although significant progress has been achieved, it is still far from reaching this aim since many obstacles and design challenges still need to be addressed. Low power efficiencies and limited transfer range are the two main issues for IPT. A tradeoff is usually associated with these two issues. Higher efficiencies are only achieved at very short transmission distances, whereas transferring large amounts of power at large distances is possible but at reduced efficiencies.

This thesis addressed the limitations and design challenges in IPT systems such as low efficiency and short transmission range, in addition to poor power regulation and coil displacement and misalignment sensitivity. Novel circuit topologies and design solutions have developed for DC/AC inverters and DC/AC rectifiers that will allow for increased performance, higher efficiencies and reduced sensitivity to coil misalignments and displacements.

This thesis contributes in four key areas towards IPT. Firstly, a detailed mathematical analysis has been performed on the electric circuit model of inductively coupled coils. This allows for better understanding on how power is distributed amongst the circuit's elements. Equivalent circuit representations were presented to simplify the design process of IPT systems. Secondly, a review of the different classes and configurations of DC/AC inverters that can be used as primary coil drivers in IPT systems were presented. Class E DC/AC inverters were mathematically analysed in great detail and their performance as primary coil drivers in IPT systems was investigated. Thirdly, novel electronic tuning methods were presented to allow Class E primary coil drivers to operate at optimum switching conditions regardless of the distance between the coils of an IPT system and the value of the load. The saturable reactor was used as the electronic tunable element. Lastly, Class D and Class E AC/DC rectifiers have been used for the first time in IPT systems. Detailed mathematical analysis and extensive experimental results show their superior performance over the conventional half-wave and full-wave AC/DC rectifiers.

Acknowledgements

I would like to thank my supervisor Professor Patrick Luk for his supervision and experienced guidance. His continuous support and encouragements gave me more confidence in my work and abilities and led me to complete my project successfully. I would also like to thank my second supervisor Dr. James Whidborne for his valuable discussions, cooperation and support.

This journey would not have been pleasant without my friends and fellow PhD students at Cranfield University, especially Milena Traczyk, Francis Salama, Quentain McEnteggert, Robert Christie, Kirsty Wallis, Sue Richardson, Atma Parkash and Solange Baena. I am very grateful to Glenda Metcalf for her continuous support, love and friendship since day one.

I owe every part of this work, my education and every step forward in my life to my parents. I would like to thank them for their love, support and encouragement.

x

CONTENTS

LIST OF FIGURES

LIST OF TABLES

NOMENCLATURE

Roman letters

C	Capacitance
C_P	Parallel resonant capacitor
c_p	Power-output capability
C_S	Series resonant capacitor
D	Duty cycle
f	Switching frequency in Hertz
f_o	Resonant frequency in Hertz
G	Transfer function
I	Current
i	Current (time varying)
I_i	Input current
i_m	Magnitude of a current sinusoidal signal
I_o	Output current
j	Imaginary number
k	Coupling Coefficient
L	Inductance
L_f	DC-feed inductance
L_P	Primary coil inductance
L_S	Secondary coil inductance
M	Mutual inductance
N	Number of turns
P	Power
P_i	Input power
P_o	Output power
Q	Quality factor

Q_L	Load quality factor
R	Resistance
r	Equivalent series resistance
r_{OFF}	MOSFET OFF resistance
r_{ON}	MOSFET ON resistance
R_{Ref}	Real part of the reflected impedance
r_C	ESR of a capacitor
R_L	Load resistance
r_P	ESR of the primary coil
r_Q	MOSFET drain channel resistance
r_S	ESR of the secondary coil
R_T	Total resistance
R_{Opt}	Optimum resistance
t	Time in seconds
V	Voltage
v	Voltage (time varying)
V_i	Input voltage
v_m	Magnitude of a voltage sinusoidal signal
V_o	Output voltage
X	Reactance
X_{Ref}	Imaginary part of the reflected impedance
X_b	Residual reactance
Z	Impedance
Z_{Ref}	Reflected impedance of the secondary coil circuitry
Z_L	Load impedance
z_m	Magnitude of an impedance
Z_o	Characteristic impedance

Greek letters

η	Efficiency
μ	Permeability
ω	Switching frequency in radians per second
ω_o	Resonant frequency in radians per second

ϕ	Phase or magnetic flux
τ	Time constant

Units

Ω	Ohm
^{o}C	Degree of Celsius
A	Ampere
F	Farad
H	Henry
Hz	Hertz
m	Metre
t	Second
V	Voltage
W	Watt
rad	Radian

Acronyms

A4WP	Alliance for wireless power
AC	Alternating current
ADC	Analog to digital converter
DAC	Digital to analog converter
DC	Direct current
DS	Drain to source
EMF	Electromotive force
ESR	Equivalent series resistance
GS	Gate to source
IPT	Inductive power transfer
KCL	Kirchhoff's current law
KVL	Kirchhoff's voltage law
LED	Light emitting diode
Mag-Amp	Magnetic amplifier
MAX	Maximum
MIN	Minimum
MOSFET	Metal-oxide-semiconductor field-effect transistor

norm	Normalised
Opt	Optimum
PF	Power factor
PSPICE	Personal simulation program with Integrated circuit emphasis
PWM	Pulse width modulation
Qi	Wireless power consortium symbol
Ref	Reflected
RFC	Radio frequency choke
RFID	Radio frequency identification
RLC	Resistor inductor capacitor
RMS	Root mean square
Sat	Saturable reactor
THD	Total harmonic distortion
UAV	Unmanned aerial vehicle
V2V	Vehicle to vehicle
WPC	Wireless power consortium
WPT	Wireless power transfer
ZCDS	Zero-current derivative switching
ZCS	Zero-current switching
ZVDS	Zero-voltage derivative switching
ZVS	Zero-voltage switching

1

INTRODUCTION

1.1 OVERVIEW OF AN INDUCTIVE POWER TRANSFER SYSTEM

Ampere's circuital law and Faraday's law of induction are the two key principles behind the operation of every magentic induction wireless power transfer (WPT), or inductive power transfer (IPT), system. Ampere's circuital law states that a magnetic field is produced around a conductor carrying electric current with a strength proportional to the current. On the other hand, Faraday's law of induction states that an alternating magnetic field can induce an electromotive force (EMF) in a conductor that is proportional to the magnetic field's strength and its rate of change. Fig. 1.1 illustrates how these two laws can be applied together to transfer power wirelessly. An alternating current is passed into a coil, referred to as the primary or transmitting coil, producing an alternating magnetic field. If a second coil, referred to as the secondary or receiving coil, is placed in close proximity with the transmitter, then the alternating magnetic field will induce an electromotive force in the receiver's coil and current will flow if a load is connected to the coil. Thus, power is being transferred from the transmitter's coil to the receiver's coil.

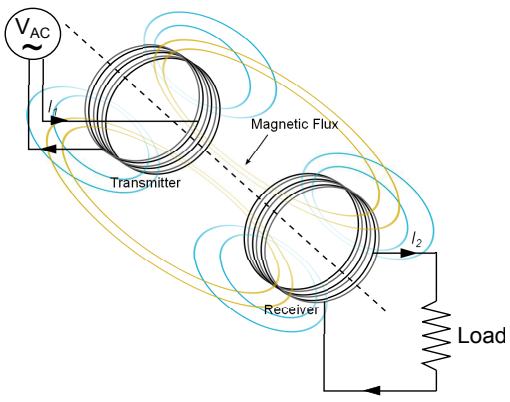

Fig. 1.1: Principle of operation of a IPT system

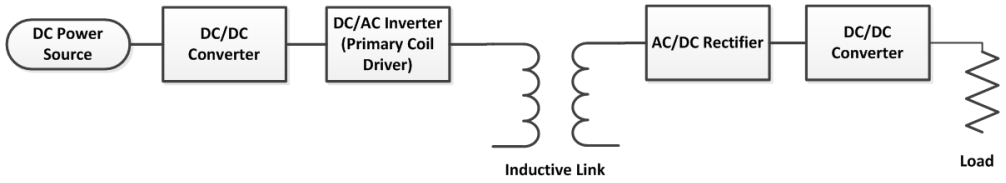

Fig. 1.2: Block diagram of a basic modern IPT system

The block diagram of a basic modern IPT system is shown in Fig. 1.2. The major sections of the system that implement Ampere's and Faraday's laws are the transmitting and receiving coupled coils pair, and the DC/AC inverter. The transmitting and receiving coupled coils are referred to as the 'inductive link' section of the IPT system. The coupled coils do not necessary have to be identical; they could have different dimensions and shapes. The coupled coils could be located at any distance and orientation with respect to each other. The DC/AC inverter, also referred to as the 'primary coil driver', generates a high frequency alternating current (AC) output from a constant direct current (DC) voltage supply. The high frequency AC current flows in the primary coil of the inductive link which transforms it into a high frequency alternating magnetic field. The high frequency alternating magnetic field is picked up by the secondary coil of the inductive link which then transforms it into a high frequency AC voltage. The AC voltage is then used to power a certain load such as an incandescent light bulb . An AC/DC rectifier may be required to transform the high frequency AC voltage into a DC voltage if the load to be powered is a DC load such as, a light emitting diode (LED) or any electronic device. Additional DC/DC converters may be required to provide a regulated input DC voltage to the DC/AC inverter and a regulated output voltage from the AC/DC rectifier.

Inductive links can be considered as an AC transformer with a high leakage inductance. Such a transformer is referred to as 'loosely coupled transformer'. In a loosely coupled transformer, a small amount of the magnetic flux produced by the first coil enters the second coil. As a result, the amount of energy that can be transferred by a loosely coupled system is generally low. This issue limits the use of the WPT based on inductive coupling. Recently, the use of finite element modelling in analysing and designing coils has allowed designers to achieve higher coupling factors compared to what used to be achieved a few decades ago, however they still remain at a very low level.

IPT systems are more suitable for transmission of power over short distances that are up to twice as large as the coils' dimensions, since the magnetic field's strength produced by the transmitter's coil becomes very weak at further distances. Unlike other WPT methods, the efficiency of an IPT system can reach up to 95 % at short distances. However, it degrades rapidly as the distance increases.

1.2 MOTIVATION

IPT technology has certainly matured to a level where applications and products can now be developed and commercialised. Infact, it is one of the fastest growing technologies that evolved from a concept, to technology demonstration, and finally to product development. The number publications in IPT system are increasing exponentially, with a large number of international conferences and exhibitions entirely dedicated for wireless power transfer.

In spite of its maturity, IPT technology is still yet to unleash its full potential. The applications and products that are being developed still do not demonstrate what IPT technology can achieve. Although the research and development in IPT technology is at its peak since it was first conceptualised in the '90s, today's application are only confined to stationary charging of mobile devices and electric vehicles. It is about time to take IPT technology into the next level by introducing applications and concepts that can never be realised without it. Concepts such as dynamic vehicle-to-vehicle charging, in-flight charging for electric airborne vehicles and wireless power for remote-controlled planetary exploration robots are all examples of what IPT technology can potentially achieve.

1.3 AIMS AND OBJECTIVES

This research project aims to contribute in developing new switched-mode circuit topologies, optimization and tuning methods that can lead to the next generation of IPT applications. The objectives of this research project can be summarised as follows:

- To undertake a critical review of the current state of IPT technology and identify the areas and gaps for further research and investigation.

- To design, analyse and implement novel switched-mode circuits for DC/AC inverters and AC/DC rectifiers, such as Class E inverters and Class E rectifiers, that can result in better performance and higher operating efficiencies for IPT systems.

- To develop novel tuning and control methods for DC/AC inverters, specifically Class E inverters, to allow for optimised operation regardless of coil displacement and load variation.

- To develop a controller for DC/DC converters that are used in IPT systems to allow for voltage regulation and control.

1.4 METHODOLOGY

The research in IPT technology has been focusing on improving the power transfer efficiency of the inductive link section only. New coil shapes, materials and design methods have been developed that can certainly lead to better performance, increased power transfer range and efficiency. However, the remaining sections of an IPT system haven't received the same level of attention. It cannot be assumed that only the performance and efficiency of an IPT system depends solely on its inductive link section, its remaining parts also play a key role in determining its overall performance especially when it come to its ability to operate efficiently when variations in coils' distance and the load occur. Therefore, this thesis mainly focus on the sections of an IPT system other than the inductive link section.

Referring to the block diagram of a IPT system in Fig. 1.2, each section of the IPT system will be studied as an independent subsystem. DC/AC inverters that are commonly used as primary coil drivers will be identified. An investigation is performed to identify any potential areas of improvement and research. Similarly, AC/DC rectifiers that are commonly used are identified. Since the AC/DC rectifier can be the final stage of the IPT system, it can have an significant impact on the performance of the entire IPT system. Therefore, new topologies of AC/DC rectifiers will be investigated.

Mathematical modelling and analysis was used extensively for every circuit. An analytical approach provided an initial insight on how a circuit will perform under ideal assumptions. Then, a more advanced state-space representation approach was used to be completely characterize the behaviour the circuit while considering non-idealities in its components. Each developed circuit was implemented and experimental measurements were used to validate the design process and the analysis. Fig. 1.3 shows a block diagram that describes the methodology.

1.5 THESIS STRUCTURE

Chapter 2 begins by giving a brief history of WPT technology which spans over a century. Methods of transferring power wirelessly other than magnetic induction will be presented. Several commercial products and applications that rely magnetic induction are shown. A review of the current state of IPT technology is given and the trend-

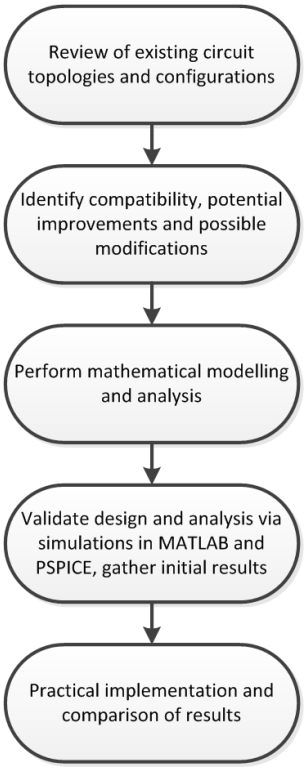

Fig. 1.3: Methodology overview

ing research topics are noted. The Chapter ends with several suggested concepts and applications that can be potentially implemented with IPT technology.

Chapter 3 describes the principle of operation of inductive links from circuit point of view. The important quantities and parameters that are associated with inductive links will be defined. The technique of using magnetic resonance to improve the performance of the inductive link is described. A more accurate circuit model will be introduced to provide a better understanding on how the losses are distributed amongst the elements of the inductive link.

Chapter 4 provides a review on Class D and Class E DC/AC inverters that can be used as primary coil drivers. Class E DC/AC inverters will be analysed in further details. The loading conditions that will cause them to operate at optimum or sub-optimum conditions will be shown. The chapter ends with a summary and comparison on the presented configurations and topologies

Chapter 5 investigates the performance of Class E DC/AC inverters when used as the primary coil driver for an inductive link. Based on the investigation, novel tuning methods will be presented to allow the Class E DC/AC inverters to operate at optimum switching conditions regardless of any variations that may occur in the distance of the inductive link and the load. Experimental results are presented for each tuning method.

Chapter 6 reviews the AC/DC rectifiers that are currently being used in IPT systems. It will be shown how the traditional half-wave and full-wave rectifiers are not suitable with resonant inductive links and resonant primary coil drivers. The chapter provides an overview of Class D rectifiers and discusses their principle of operation. A mathematical analysis is performed to investigate their compatibility with resonant inductive links. Class E rectifiers are then introduced. It will be shown that they can be integrated seamlessly with resonant inductive links and resonant primary coil drivers. Detailed analysis of Class D and Class E rectifiers is performed and is validated by experimental results.

Chapter 7 introduces the Class E^2 converter which is a combination of a Class E inverter and a Class E rectifier separated by an inductive link. Detailed mathematical analysis is performed. A design case is given detailing the design procedure and the implementation process. Experimental results are given to verify the performed analysis.

Chapter 8 discusses the control of the DC/DC converters that are used to provide a regulated input voltage of the primary coil driver, and a regulated output from the AC/DC rectifier. A novel controller is introduced that would allow the DC/DC converter to provide a regulated output voltage regardless of the dynamics of primary coil driver and the load.

Chapter 9 reviews the outcomes of the work presented in this research project and concludes the thesis. Recommendations for future work are also presented.

1.6 CONTRIBUTIONS

The work in this research has resulted in the following contributions:

- A more accurate model of inductive links has been introduced. The improved model can determine how the power received at the secondary coil circuitry is distributed amongst its elements.

- A novel method to analyse Class E DC/AC inverters that are used as primary coil drivers using a piece-wise linear state-space representation has been presented. The analysis method allows for determining the values of the Class E inverter's elements at any quality factor of its load network.

- Novel tuning methods have been presented that would allow Class E DC/AC inverters that are used as primary coil drivers to operate at optimum switching conditions regardless of any variations in the distance of the inductive link and the load that may occur during operation.

- Introduced a novel technique to electronically tune Class E inverters using saturable reactors to allow for optimum operation over wide load and distance ranges.

- Class D rectifiers have been used for the very first time in inductive links to improve the overall performance and efficiency of a IPT system.

- Class E rectifiers have been used for the very first time in inductive links to improve the overall performance and efficiency of a IPT system.

- Class E^2 converters have been used for the very first time in inductive links.

- A novel digital controller for DC/DC converters has been developed featuring simplicity, low component count and a very good performance compared to other complex digital control methods.

1.7 PUBLICATIONS

This research project has resulted in the following publications:

- S. Aldhaher, P. C. K. Luk and J. F. Whidborne, *'Tuning Class E Inverters Applied In Inductive Links Using Saturable Reactors,'* IEEE Transactions on Power Electronics, vol.29, no.6, pp.2969-2978, June 2014.

- S. Aldhaher, J. F. Whidborne, *'A One-Comparator Counter-Based Controller for Synchronous DC/DC Converters,'* IET Power Electronics. (accepted for publication)

- S. Aldhaher, P. C. K. Luk and J. F. Whidborne, *'Electronic Tuning of Misaligned Coils In Wireless Power Transfer Systems,'* IEEE Transactions on Power Electronics. (accepted for publication)

- S. Aldhaher, P. C. K. Luk and J. F. Whidborne, *'High Input Voltage High Frequency Class E Rectifiers for Resonant Inductive Links,'* IEEE Transactions on Power Electronics. (accepted for publication)

- S. Aldhaher, P. C. K. Luk and A. Bati, *'Wireless power transfer using Class E inverter with saturable DC-feed inductor,'* IEEE Transactions on Industry Applications (accepted for publication)

- S. Aldhaher, P. C. K. Luk and J. F. Whidborne, *'State-Space Modelling of a Class E^2 Converter for Inductive Links ,'* IEEE Transactions on Power Electronics. (under review)

- S. Aldhaher and P. C. K. Luk, *'Modelling and Analysis of a Half-wave Class D rectifier for Inductive Links ,'* 40th Annual Conference of the IEEE Industrial Electronics Society, IECON 2014 (under review)

- S. Aldhaher and P. C. K. Luk, *'Bidirectional Class E converter for inductive links,'* IEEE Energy Conversion Congress & Expo, Pittsburgh, PA, USA, 2014 (under review)

- S. Aldhaher, P. C. K. Luk and J. F. Whidborne, *'Electronic Tuning of a High Frequency DC/AC Inverter for Inductive Links,'* IEEE International Conference on Power Electronics Systems and Applications , Hong Kong, 2013

- S. Aldhaher, P. C. K. Luk and J. F. Whidborne, *'Wireless power transfer using Class E inverter with saturable DC-feed inductor,'* IEEE Energy Conversion Congress & Expo, Denver, Colorado, USA, 2013

- S. Aldhaher, P. C. K. Luk and J. F. Whidborne, *'Wireless Power Transfer Using Class E Inverter with Non-Linear Finite DC Feed Inductance,'* 9th International Symposium on Linear Drives and Industry Applications LDIA, Jul. 2013, Hangzhou, China.

- J. Leonard, S. Aldhaher, A. Savvaris and A. Tsourdos, *'Automated Recharging Station For Swarm of Unmanned Aerial Vehicles,'* Proceedings of the ASME 2012 International Mechanical Engineering Congress & Exposition IMECE, Nov. 2012, Texas, USA.

2

WIRELESS POWER TRANSFER TECHNOLOGY

2.1 INTRODUCTION

Electrical energy has always been transferred by utilising the free electrons in conductive materials. Electric current can flow in a conductor if an electric potential difference is applied across the conductor, consequently electric power can be transferred from a source such as a generator or a battery to a load. For instance, connecting a wire from the positive terminal of a battery to the load and another from the load back to the negative terminal of the battery will form a closed circuit. This will cause the free electrons in the wires and the load to circulate due to the voltage potential of the battery. Since the battery is forcing the flow of electrons through the load, energy is being transferred from the battery and consumed in the load.

The usage of cables and wires is the preferred choice to connect a source to a load. It is a simple and efficient method to transfer electrical energy and it is suitable for most of today's applications since the loads, whether in industry or in our homes, are stationary and motionless. However, as technology advances, products are becoming smaller and portable. Relying on a cable connected to a power outlet to obtain energy may not be a practical solution any more. New applications are being developed and introduced that are mobile and require a continuous or semi-continuous power supply. Therefore, having a direct cable connection may limit their freedom of movement and in some cases may not be a safe option. For example, the research and development in hybrid and electrical vehicles is on the rise due to the increase in oil prices and to environmental concerns. These vehicles have an on board battery that can provide power partially or entirely for the entire trip duration. Although a direct cable connection to a power outlet is suitable to a certain degree to provide power and recharge the batteries, more options will be available if that power was supplied wirelessly without cables and contacts. The vehicle, for example, could be powered 'on the go' while it is moving. The risk of electric shock and sparks is highly reduced since no contacts

are used, maintenance requirements are also reduced since there is no wear and tear involved in the powering and charging process.

In wireless transfer of electrical energy, instead of using conductive cables and wires, electrical energy is converted to another form that can be transferred through a certain media without the need for conductive wires. A simple example of transferring energy wirelessly is the use of radio waves to transfer information such as sound, video and data. A voltage signal representing the information to be transferred is generated in a radio station. It is then transformed into an electromagnetic energy signal and beamed into the air, spreading in all directions. The electromagnetic energy signal is picked up by an antenna at a reduced energy level and then transformed back into an electrical voltage signal and the information is extracted afterwards.

Wireless transfer of energy or wireless power transfer may seem as an alternative method to power today's and the future's applications. However, many design challenges and technological obstacles need to be addressed and overcome. The following literature review aims to:

- Present the different wireless methods of energy transmission.
- Discuss current applications based on IPT.
- Review the current research state in IPT.
- Identify the gaps and topics in IPT that require further investigation and research.

2.2 HISTORICAL ACHIEVEMENTS AND SCIENTIFIC BREAKTHROUGHS

Perhaps the first person to introduce the concept of wireless power transfer was Nikola Tesla. In 1893 at the World's Columbian Exposition in Chicago, Tesla was able to demonstrate the illumination of phosphorescent lamps (gas discharge tubes) without any electrical connections [1]. He achieved this by using a high frequency electrostatic field produced from a system that generates lightning sparks. He conducted further experiments in the Wardenclyffe Tower (Fig. 2.1) until it was demolished in 1917. He concluded that electrical energy could be transferred through the upper atmosphere and the Earth to any point on the globe [2]. His work also resulted in major contributions for long distance radio telecommunication. Many researchers and inventors confirmed his findings and discoveries later on.

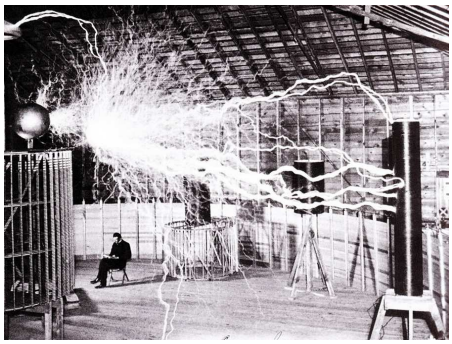

(a) Lightning discharges demonstrated at Tesla's Laboratory

(b) Wardenclyffe Tower

Fig. 2.1: Tesla's work in his Laboratory(images: www.teslascience.org)

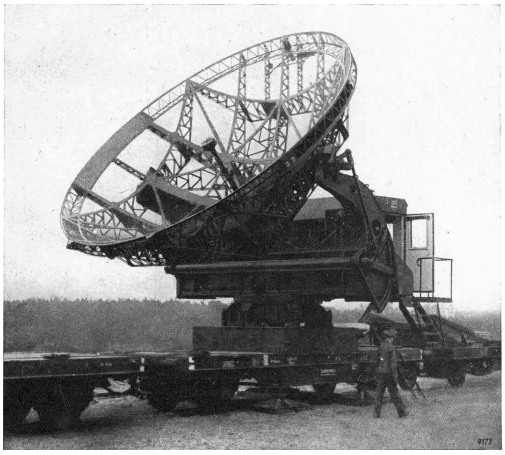

Fig. 2.2: The Würzburg radar used in Germany during WWII (image: www.radarworld.org)

The research continued in WPT especially for telecommunications during the first few decades of the twentieth century. Radio stations and long distance communications links were developed during the first world war. TV broadcasts and radar stations (Fig. 2.2) were deployed across Europe during the second world war.

The next major advancement in WPT was the use of microwaves to supply power to distant objects. Brown [3] was able to fly a small unmanned helicopter 60 feet away relying entirely on microwave power as a part of a joint project between the Department of Defence and NASA. It was also the first time that semiconductors were used in WPT applications. The interest in transferring power wirelessly increased during the energy crisis of the '70s. A new concept for obtaining renewable solar energy was proposed by NASA and the Department of Energy (Fig. 2.3). The concept aimed to deploy giant space satellites to collect solar energy and beam it to the Earth by using microwaves [4]. Ground based experiments conducted by NASA proved the possibility of such a system and the ability to transfer high power levels over several kilometres. The 1975 'ASA JPL Goldstone Demonstration of Wireless Power Transfer' showed the transmission of 34 kW of power over a distance of 1.5 km at an efficiency of 82 %. However,

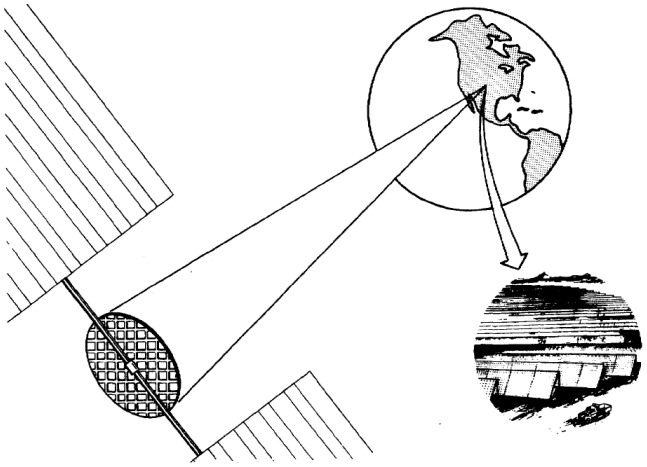

Fig. 2.3: Concept image of a space power station. The sun's radiation is collected by satellites, converted to microwaves and beamed to earth where they are reconverted into useful power [5]

(a) The unmanned plane, the circular dish captures the micrwave power beam and converts it to DC current to power the motors

(b) Microwave transmitting station

Fig. 2.4: The SHARP program [4]

due to the high implementation and energy costs the concept of deploying these energy collecting satellites was never realised. Another project conducted by Canada's Communication Centre in 1987 successfully created a small airplane capable of being powered remotely by focusing a 2.45 GHz microwave beam to an on board microwave antenna. The project which was referred to by the name SHARP (Stationary High Altitude Relay Platform) and aimed to design an airborne communications relay that would fly in circles of two kilometres in diameter at an altitude of about 21 km.

The use of lasers for wireless powering has also been researched since their discovery (or invention) in the '50s. Similar to microwaves, a high power laser beam focused on a photovoltaic cell will generate an electric current. However, due to the low efficiencies of a photovoltaic cell, the use of lasers to transfer energy wirelessly was not

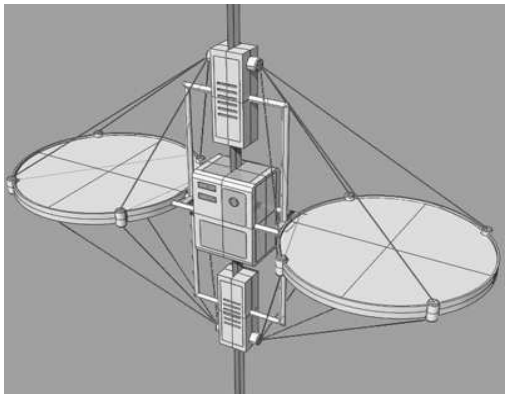

Fig. 2.5: Concept image of the space elevator, the elevator is powered using a high power laser beam emitted from a ground station (Image: LiftPort Group)

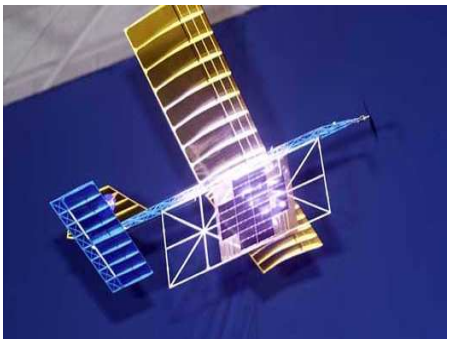

(a) The model weighing only 300g generates power from a laser beam focused onto its solar panel

(b) Ground based infrared laser emitter

Fig. 2.6: NASA's laser powered aircraft model (Images: NASA)

preferred. As a result, microwaves were the only option for transferring power wirelessly over several kilometres during the second half of the twentieth century.

The concept of using lasers for long distance power transfer resurfaced again in the late twentieth century. The Japanese Space Agency (JAXA) had been conducting extensive research programmes in space power stations with the aim to transfer up to 1 GW of power via lasers from large mirrors placed in the Earth's orbit [6]. Using lasers to power ground rovers for lunar and planetary exploration missions has also been investigated [7]. Recent concepts have emerged for using lasers in powering tethered climbers, such as the space elevator project (Fig. 2.5). In 2003, a NASA research team claimed to design and build a laser powered aircraft [8]. The full structure of the model plane is covered with solar panels that generated power from a ground-based infrared laser (Fig. 2.6).

Till this date no major scientific breakthroughs have been reported in WPT technology. However, it has become more energy efficient and more applicable to today's applications due to the advancements in electronics and computers. It can be observed

that there is an increased interest in magnetic induction based power transmission technology. Numerous applications for consumers and for industry have emerged. Research, development and investing in systems for charging hybrid and electrical vehicles by major manufacturers is increasing. It can be assumed that using magnetic induction for the transmission of power for short distances will be the preferred method for many years to come.

2.3 WIRELESS POWER TRANSFER METHODS

Several methods exists for transferring energy wirelessly between a source and a load. This section presents the different possible coupling methods for WPT other than magnetic induction. Every WPT system consists of two separate parts; a transmitter and a receiver. The transmitter is located where energy from a power source is to be transferred. The receiver and is located where the load that needs to be powered is.

2.3.1 *Capacitive Coupling*

In capacitive coupling, power is transferred by means of an electric field. A capacitive coupled system can be thought of as a pair of capacitors each consisting of two parallel plates separated by a certain distance. The transmitter is connected to the first plates of each capacitor and the receiver is connected to the second plates. If an alternating voltage is applied to the first plates, then a varying electric field will be generated across the two plates of both capacitors. According to Maxwell's equations, a time-varying electric field will produce a displacement current proportional to the rate of change of the electric field. The displacement current allows energy to be transferred across the medium between the plates of the capacitors. If a load is connected between the second plates of the capacitors, then the time-varying displacement current will cause electric charges to be continuously moved back and forth between the plates. Consequently an electric current is formed in the receiver. Fig. 2.7 illustrates the process.

Capacitive coupling was one of the first methods used to transfer energy wirelessly as demonstrated by Nikola Tesla. However, it wasn't considered as a suitable method to transfer power due to the requirement of high voltages that can reach up to several kilo volts and the need for large plates for long distances. Capacitive coupled system are generally used in applications that require an intense electric field such as cathode ray tubes.

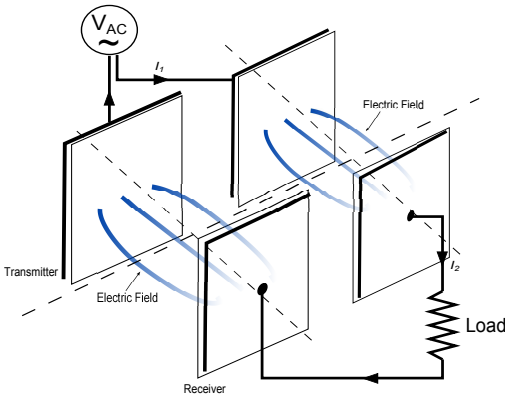

Fig. 2.7: Coupled coils

2.3.2 *Laser Coupling*

The operation of a laser coupled WPT system is based on the photovoltaic effect. This is achieved by focusing an intense laser beam with a specific wavelength on a photovoltaic cell resulting in an electrical current. Although the photovoltaic effect was discovered in the nineteenth century, it wasn't until lasers had become available in the late '50s that the idea of using a beam of light to transfer power over long distances was possible. Many different types of high power lasers exist today, but they all share the same principle of operation. A laser beam is a phase-coherent light that consists of photons emitted from excited atoms of a specific crystal. The atoms are excited via an external source such as a DC current source. Thus, a laser converts electric current into a beam of photons and the process can be referred to as DC-to-laser conversion [9].

The photovoltaic effect is the ejection of electrons from a material's surface if exposed to a photon with a specific wavelength. Photodiodes (or solar cells) make use of this effect; an electron is generated when a photon with a specific wavelength falls on the p-n junction of the photodiode. Photodiodes can be assembled into large arrays to capture more light by connecting them in either a series combination,which leads to an increase in generated voltage, or in parallel which results in an increase in generated current. The major setback in using photodiodes for any power application is in its poor conversion efficiencies. The typical conversion efficiency from light to current is between 40-50 % for a single wavelength and 20-30 % for the entire light spectrum.

The concept of a space power station to collect solar energy and beam it to earth using lasers was first proposed by Peter Glaser, a NASA scientist, in 1968. Solar-pumped lasers which use the sun's energy to excite an Nd:YAG crystal to release photons would be used to convert solar energy directly into a high power laser beam [10]. This eliminates the need to install solar cells in space and improves the overall efficiency

of the system, since the solar-to-light energy conversion process is 10 % more efficient than that of a solar cell [11]. Solar cells will then be used to convert the laser beam to electricity on Earth. The concept was studied extensively by NASA and the Department of Energy in the '70s and '80s [12]. However, due to the low efficiencies of solar cells and the high attenuation of laser beams due to weather conditions, the concept was never realised.

2.3.3 *Microwave Coupling*

Microwaves are radio waves that have a spectrum range of 1-30 GHz. They are used extensively in many of today's applications especially in communications. Unlike other radio waves, microwaves can be transmitted in narrow beams allowing the transmitter to focus its energy towards the receiver. In low power applications, such as mobile cell phones, microwaves are generated or radiated from an antenna that is fed with a high frequency current. The microwaves can then be picked up by another antenna and converted back to an electric current. Another method for generating microwaves is the use of a magnetron. The magnetron, first developed in Great Britain during the second world war, is a vacuum tube device that consists of several cavities. The cavities are designed to allow electrons to resonate at high frequencies which leads them to radiate microwaves. The magnetron allowed high power microwaves to be generated and was used in radar systems after WWII. The further developments and improvements in magnetrons in the '60s allowed the process of generating and radiating microwaves more efficient and less expensive. High power microwaves up to several hundred kilowatts could be generated and focused on a point several kilometres away. The main obstacle that had to be overcome in order transfer high levels of power using microwaves, was the conversion of microwaves back to electricity. When a microwave signal is picked by an antenna, an alternating current is generated that has the same frequency of the microwave signal and is proportional to the microwave's signal power. Since all applications and devices either operate at an AC voltage at 50 Hz or 60 Hz or from a constant DC Voltage, the high frequency current generated by the microwave antenna therefore has to be converted to a suitable voltage form. In 1963, William C. Brown invented the 'rectenna' (Fig. 2.8a) or 'rectifying antenna' that rectifies the high frequency current generated by the microwave antenna into a DC voltage by using a bridge rectifier [13]. The rectennas developed had a rectification efficiency (i.e. from microwave-to-DC) of 40 %.

With the invention of the rectenna, the idea of using microwaves to transfer power over long distances was now possible. Brown proved the possibility of a microwave-based WPT system in 1964 with the conduction of a microwave-powered helicopter experiment. Brown attached a helicopter's rotor to a rectenna array that picked up

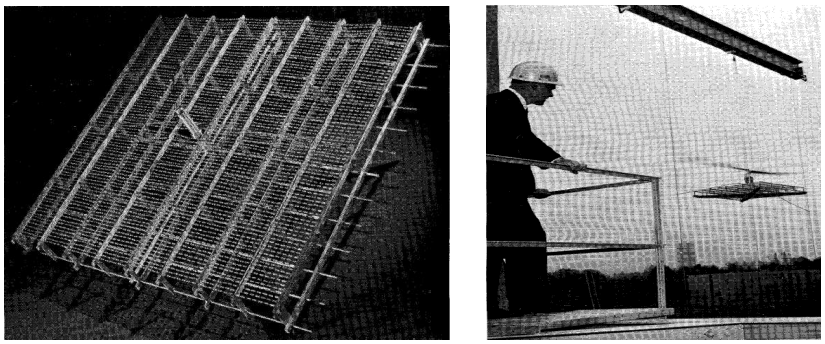

(a) Rectenna array (b) Microwave-powered helicopter

Fig. 2.8: The microwave-powered helicopter experiment conducted in 1964 [13]

microwaves beamed from a ground-based transmitter. The array weighed 1.3 kg, it contained 4480 diodes, the rotor required up to 270 W of power and the complete assembly was able to fly for ten continuous hours (Fig. 2.8b).

Further developments in semiconductors during the '70s and the availability of Schottky-barrier diodes led to further improvements in the rectenna design achieving higher efficiencies, high power capabilities and reduced sizes. Another major experiment demonstrated in 1975 by NASA at the Jet Propulsion Laboratory (JPL) Goldstone facility showed the transmission of over 30 kW of power via a microwave beam over a distance of 1.54 km [14]. In the experiment (Fig. 2.9), the transmitter consisted of a klystron (a magnetron variant device) capable of generating up to 450 kW of microwave power at 2.388 GHz and a 26 m diameter parabolic reflector antenna that focused the microwave energy towards the receiver. The receiver was located 1.54 km away from the transmitter and consisted of 17 rectenna subarrays each containing 270 Schottky-barrier diodes. The loads used to dissipate the received energy from the rectenna were resistive loads and lamps. Due to the size mismatch between the receiver and the transmitter antennae, only 11.3 % of the transmitted power was received. The measured output DC power was 30.4 kW and the conversion efficiency, i.e. ratio of the DC output power to the incident microwave power was 82 %, thus the overall efficiency of the output power to the transmitted power could be found to be 9.3 %.

The Goldstone experiment was part of a research interest by NASA to develop a solar-power satellite (SPS), a concept which was introduced by Dr. Peter Glaser of the Arthur D. Little Company in 1968. The sun's energy is captured by a satellite placed in geosynchronous orbit, converted to microwaves and beamed to Earth to be converted to useful electricity. The success of the Goldstone experiment proved to NASA that the concept of an SPS is possible. As a result, the concept was extensively studied in the '70s and was part of a development and evaluation program that lasted for three years

Fig. 2.9: NASA's JPL Goldstone WPT demonstration (Image: NASA)

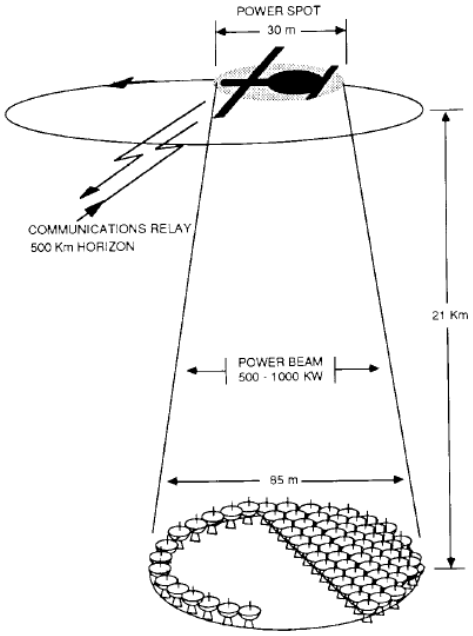

Fig. 2.10: The SHARP system [16]

and concluded that there was no 'show stoppers' for the SPS application. However, the concept was not developed and funding to the SPS program was terminated due to the immaturity of available technologies [15].

Other experiments and projects demonstrated the use of microwaves to power distant objects were conducted in the '80s. As mentioned earlier, the first unmanned plane to fly entirely on microwaves was the SHARP program (Fig. 2.10). The program aimed to develop an unmanned airplane to circle at an altitude of about 21 km for several months to be used as a communications relay link. Large antenna arrays on the ground would beam 500 km of microwave power at 2.45 GHz to the platform. Rectennas on the bottom surface of the plane would then provide 35 kW of power to be used by the motor and other systems onboard [16]. Thus, the efficiency of the output received power to the transmitted power can be found to be 7 %. A 1/8 scale prototype flew in 1987 and the flight duration lasted for 20 minutes.

During the '80s and '90s, the research for using microwave-based WPT shifted to Japan. Scientists and researchers studied and analysed the losses and effects of microwave transmission in the ionosphere. The first attempt to transfer microwave power on space was achieved by the Microwave Ionosphere Nonlinear Interaction Experiment (MINIX). The results of the experiment proved that microwave power transfer in space is possible and that the transmission losses are less than 1 % [15]. New control methods to track a moving vehicle to focus the transmitted power beam on to it were also developed. The Microwave Lifted Airplane Experiment (MILAX), which was conducted in 1992, verified new microwave power beam controlling methods on to an airplane. Phase-array antennas were used at the transmitter which allowed the microwave power beam to be steered and directed electronically [15].

2.3.4 *Pressure Waves*

WPT using pressure or sound waves was never discussed before. It was demonstrated for the first time by two graduate students from the University of Pennsylvania in April 2011. The prototype presented consisted of multiple ultrasound sensors that transmitted high frequency sound waves above 20 kHz, microphones at the receiver located less than one metre away were used to pick-up these sound waves and convert them to electrical current (Fig. 2.11).

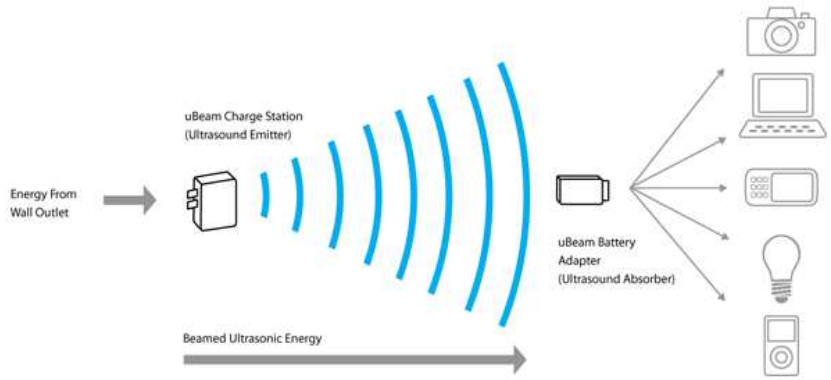

Fig. 2.11: WPT using ultrasound (Image: uBeam)

(a) The Palm Pre. charger referred to as the "Touchstone"

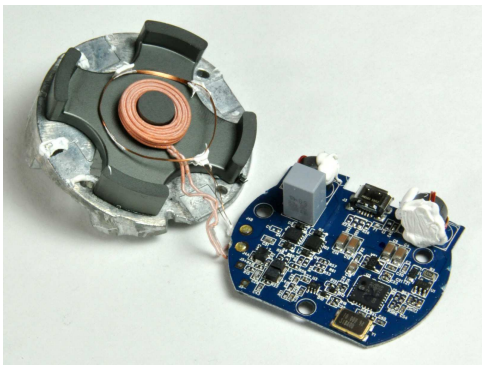

(b) A teardown view of the charger

Fig. 2.12: The Palm Pre. charger based on inductive coupling (image: www.ifixit.com)

2.4 RELATED WORK FROM THE LITERATURE IN WPT VIA MAGNETIC INDUCTION (IPT)

This section presents the recent development and research in IPT that can be found in the literature which includes including journal papers, scientific magazines, technical papers, patents and products. This section will only focus on applications that operate at power levels above a few watts and up to a few kilowatts.

2.4.1 *Current Applications and Technologies*

A. Inductive Charging

A lot of research has been devoted to charging low power portable devices such as cell phones via inductive coupling [17–21]. Palm Inc. (which is now acquired by HP) was the first company to introduce inductive charging for cell phones. The user would place the phone on a wireless charging pad and the phone would charge as if it was charged via a cable. Fig. 2.12a shows the transmitter (charger) and Fig. 2.12b shows a teardown picture of it. Fig. 2.13 shows the receiver that is located in the back cover of the cell phone. It can be noticed that magnets are used to align the receiver with the transmitter in order to ensure that a high coupling coefficient is achieved. No information is available on the topology of the internal circuitry used. One can assume that the charger is capable of delivering up to 5 W since the phone can be charged also from a USB connection which has a maximum power capability of 5 W.

As more manufactures were introducing more inductive chargers for portable devices, an association was established in 2008 between several electronics manufacturers

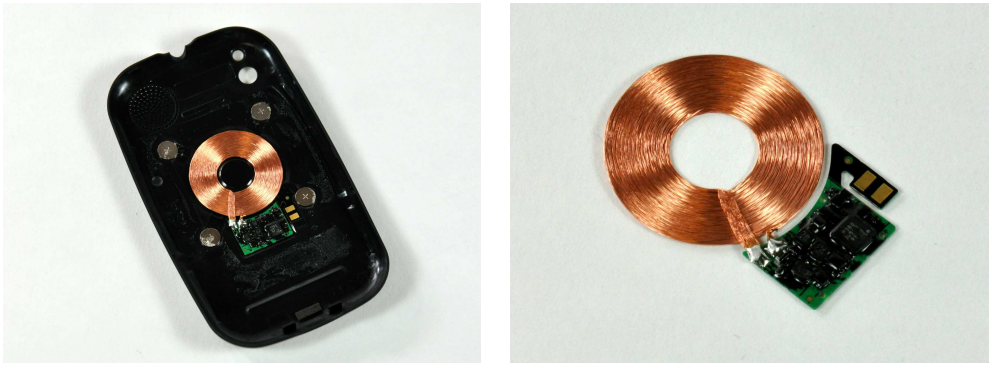

(a) The receiver located in the back cover of the cell phone

(b) An expanded view of the reciever's components

Fig. 2.13: The receiver used in the Palm Pre cell phone (image: www.ifixit.com)

Fig. 2.14: The logo of the WPC standard referred to as 'Qi (chee)' [22]

that aimed to create a universal wireless power charging standard that would allow devices to be charged by chargers built by different manufactures. The association is referred to as the 'Wireless Power Consortium' [22]. The WPC standard is referred to as 'Qi' (pronounced 'chee') and has the logo shown in Fig. 2.14. The specification document for this standard shows that a Qi system will consist of the blocks shown in Fig. 2.15 [22]. Additional control methods and techniques are implemented to detect when the receiver inside the mobile device is in close proximity with the transmitter. Based on a feedback message from the receiver, the transmitter will initiate the charging process if the distance between the transmitter and the receiver is less than 0.5 cm The feedback message is sent from the receiver to the transmitter by modulating the reflected impedance. A signal processor in the transmitter detects the changes in the reflected impedance by monitoring the current in the primary coil. Systems that follow the Qi standard operate at a frequency range between 110 kHz and 205 kHz and can deliver up to 5 W power to a load.

Another standard that has been developed recently is the Alliance for Wireless Power (A4WP) which aims to improve the power range and spatial freedom when charging mobile devices [23].

The DC/AC inverter in the transmitter and the AC/DC rectifier in the receiver for a Qi systems could be of any topology. For example, a system following the Qi standard built by Texas Instruments uses a Class D Inverter for the transmitter (Fig. 2.16a) and a

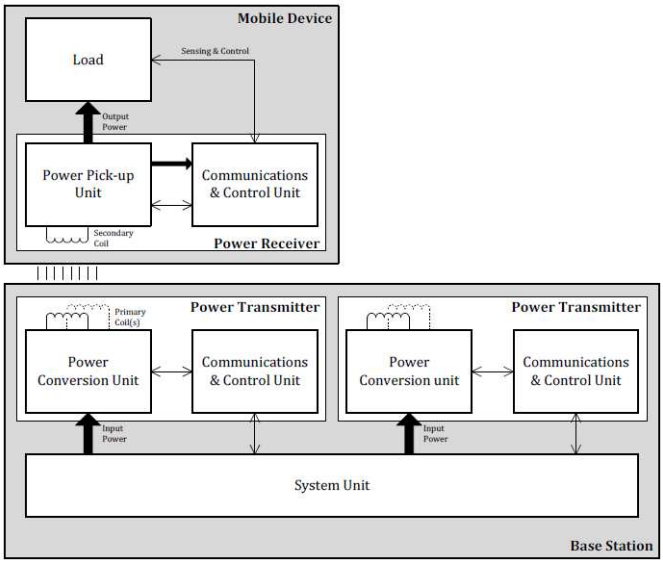

Fig. 2.15: The internal building blocks of any system implementing the Qi standard [22]

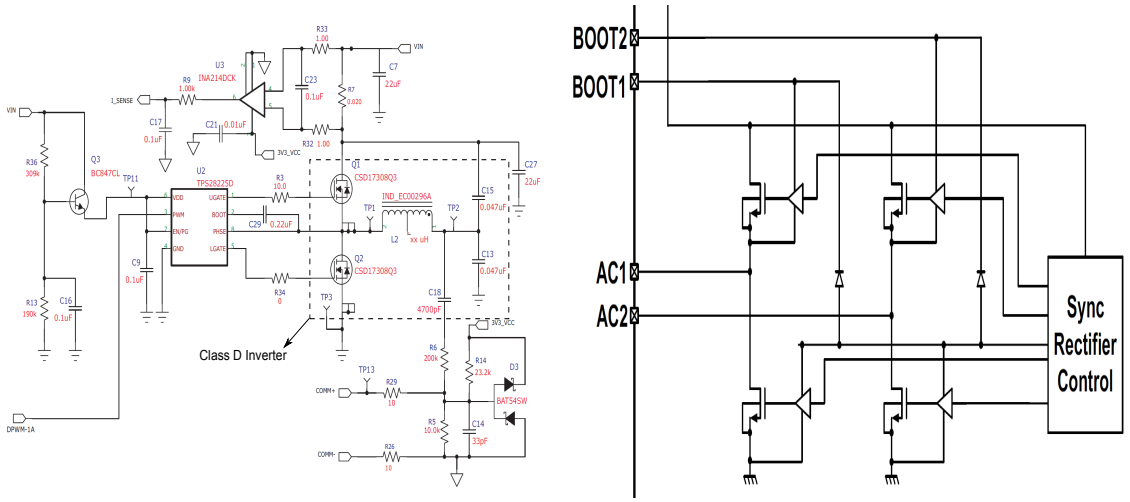

(a) A Class D Inverter used in the transimtter [24]

(b) The full-wave synchronous rectifier part of the BQ51011 integrated circuit [25]

Fig. 2.16: The circuits of the AC/DC inverter and the DC/AC rectifier of the Qi induction-based charging system implemented by Texas Instruments

synchronous full-wave bridge rectifier in the receiver (Fig. 2.16b)[24, 25]. The efficiency curve which is the ratio of the output power to the input power is shown in Fig. 2.17. The efficiency of system increases as the load increases and is at a maximum of 72 % at 5 W.

Another example of a low power induction based charger that has been in the market since the early '90s is the electric toothbrush. The electric toothbrush contains a battery that needs to be charged regularly. Induction-based charging is used as a safety precaution since having exposed electric contacts might result in a short circuit fault or can cause an electric shock. Fig. 2.18 shows an electric toothbrush along with its

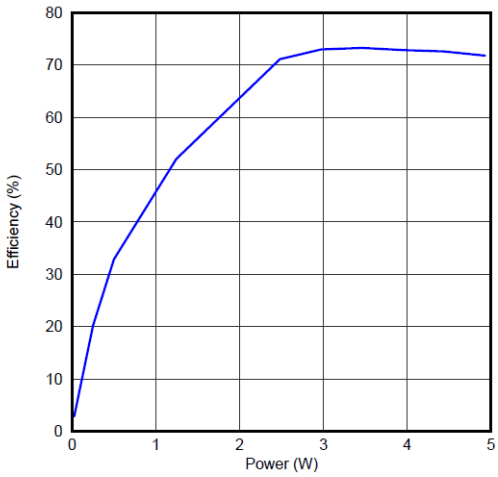

Fig. 2.17: The efficiency curve of the Qi induction-based charging system implemented by Texas Instruments [24]

Fig. 2.18: The induction based rechargeable electric toothbrush developed by Braun Oral-B (image: www.oralb.co.uk)

charger developed by Braun Oral-B. The development of an inductive-based charger for electric toothbrushes has begun in the '60s. A patent filed by Emanuel [26] in 1965 shows how an electric toothbrush can be charged (Fig. 2.19). The coils are more like a tightly coupled transformer rather than a loosely coupled pair of coils. Therefore the complete system can be considered as a contactless power system rather than a wireless power system. The mains voltage is applied to the primary coil and the secondary voltage is simply rectified using a full-wave rectifier. Another patent filed by Inakagata [27] in 1992 shows how the design of the charger or transmitter has progressed. Instead of applying the mains voltage directly to the primary coil, it is rectified into a DC voltage and inverted into a high frequency AC voltage via a Colpitts oscillator as shown in Fig. 2.20. Efficency is not of major interest since the batteries charge at low power levels over a long period of time.

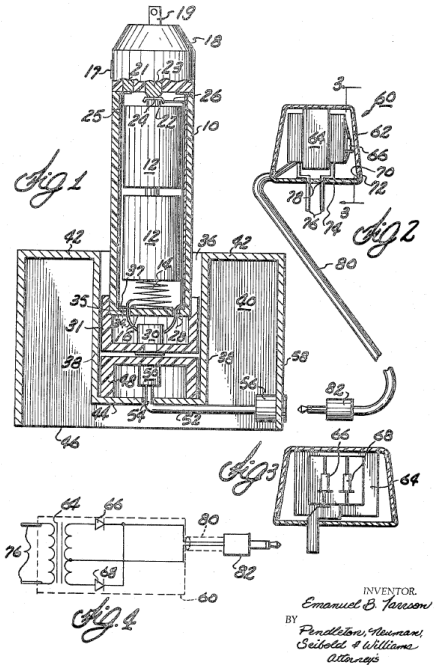

Fig. 2.19: An early rechargeable electric toothbrush [26]

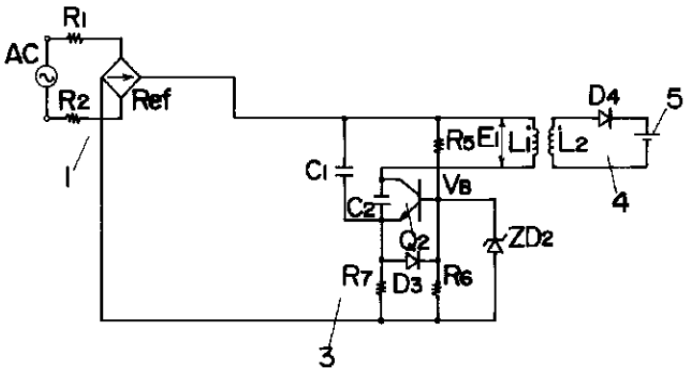

Fig. 2.20: The internal circuitry of the electric toothbrush including the transmitter and the receiver [27]

With the rapid development of hybrid and battery powered vehicles, new methods and techniques are being researched on how to charge the batteries on board the vehicle. A simple method would be to directly connect the battery to a mains socket via an AC/DC rectifier. Another method would be to use inductive coupling for a more safer operation in harsh weather conditions such as rain or snow. The Magne Charge™ (Fig. 2.21) was the first commercially available system to charge the batteries of electric vehicles by using magnetic induction. The system was developed by Delco Electronics to be used on battery powered vehicles developed by General Motors.

According to the operator's manual [28], the Magne Charge™system is capable of delivering up to 6.6 kW of output power (6.6 kW available at the primary coil) and has an efficiency of 86 %. The overall efficiency including the inductively coupled coils

(a) The charger (b) The coupler

Fig. 2.21: The Magne Charge™system used to charge electric vehicles [28]

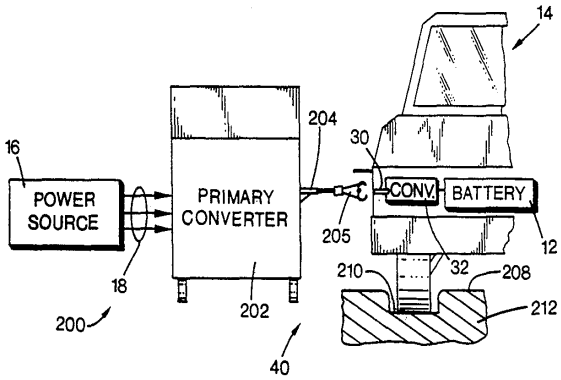

Fig. 2.22: An illustration of how the Magne Charge™system is implemented [29]

and the rectifier is likely to be much lower than 86 %. The operation of the Magne Charge™ system is described in a patent filed in 1992 by Klontz [29]. An illustration of how the system was implemented is shown in Fig. 2.22 and the system diagram is shown in Fig. 2.23. The system rectifies the main supply voltage into a DC voltage, which is then converted into an AC voltage at a frequency of 77 kHz and then applied to the primary coil. The voltage induced in the secondary coil is rectified via a AC/DC rectifier and is used to charge the batteries. The coils are tightly coupled and form a U-shaped core transformer. The Magne Charge™ system is now obsolete and has been replaced by a conductive charging system.

The technologies and applications presented so far all rely on a transmitter that is always stationary. The transmitter could be placed on a moving vehicle that is equipped with an inductive charger and portable electronic devices and systems could be powered or charged while the vehicle is moving. A patent filed in 2004 illustrates this concept (Fig. 2.24) [30].

The use of hybrid electric and all-electric vehicles has opened a new door for IPT. New ideas and concepts on how to power these vehicles are being introduced. As mentioned in Sec. 2.2, the idea of charging the batteries on board a vehicle while it is parked or if in motion has been studied recently [31–35]. Inductive charging systems

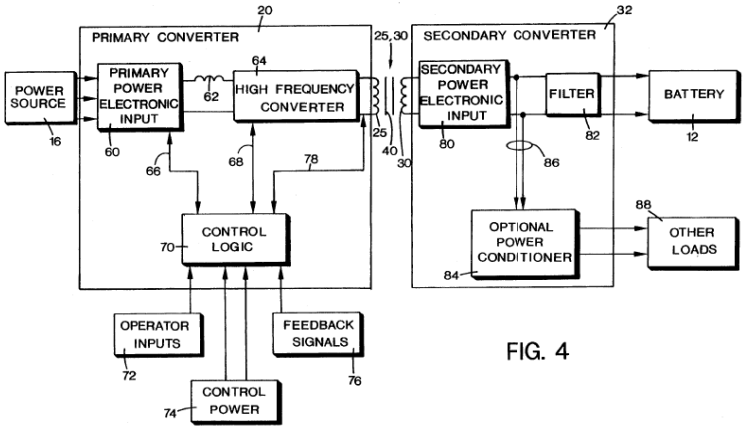

Fig. 2.23: The system diagram of the Magne Charge™ system [29]

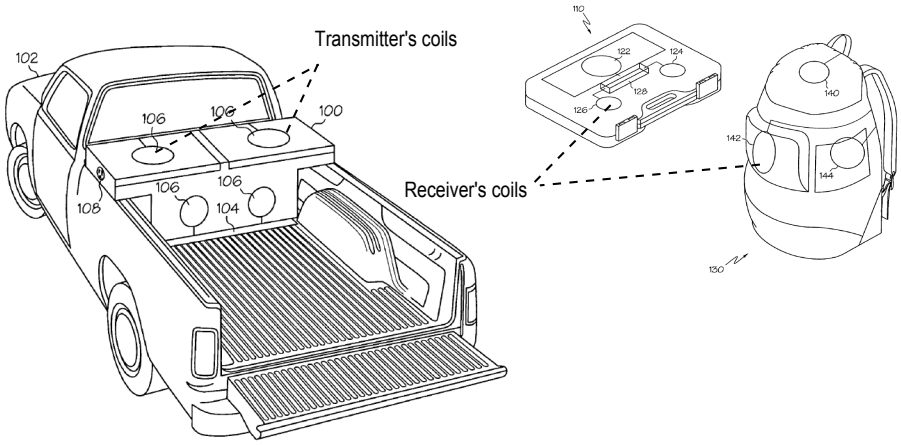

Fig. 2.24: A portable inductive power station mounted on a truck to power and charge portable tools [30]

eliminate the need for contacts thus improving the reliability of charging systems since there is no tear and wear. Safety risks due to electric shocks and fire hazards are greatly reduced since no contacts are available. Inducting charging systems are also weather proof and can be used in high humidity environments. Fig. 2.25 shows an inductive charging system developed by Delphi Automotive in cooperation with WiTricity Corp. that can supply up to 3.3 kW to a load over a distance of 20 cm.

The use of inductive charging for underwater applications has also been studied. Mcginnis [36] used inductive coupling to charge a lithium-ion battery for an underwater mooring profiler. Power transfer occurs at a depth of 100 m from a powered float to the profiler. Induction coupling was chosen as electrical contacts cannot be used since the system is submerged. Other forms of water proof contacts can be used but require a relatively high mating force.

Numerous other patents for contactless powering and charging are available. A patent filled in 1994 [37] shows how inductive coupling can be used to provide power

Fig. 2.25: Components of an inductive charging system developed by WiTricity Corp. (Image: WiTricity Corp.)

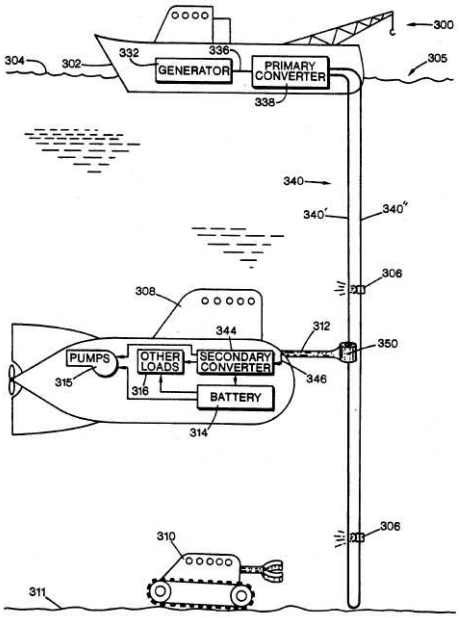

Fig. 2.26: Inductive coupling used to provide power to submersible loads as presented in [37]

in underwater applications. Fig. 2.26 shows a concept image of how submersible systems and vehicles can be powered. Instead of using a coil, a long conductive wire that is submerged carries the high frequency current generated by the DC/AC inverter. A clamp attached to the conductive wire receives power via induction and transfers it to the load or device.

B. Induction Heating

Induction heating is another form of transferring energy wirelessly via induction. The main aim is to heat an object that is located in the vicinity of the transmitter. The object is heated by inducing eddy currents in it. Only one coil is used in an induction heating system which is inside the transmitter and is only used to direct the magnetic

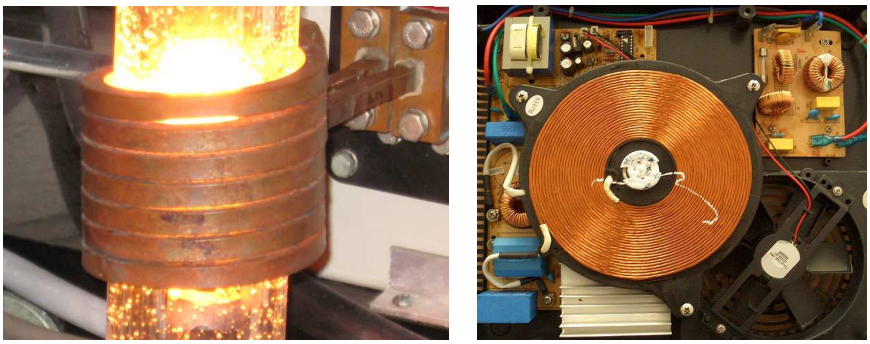

(a) A solenoid coil used in induction furnaces (Image: University of Waterloo)

(b) A planar coil used in induction cookers (Image: Wikipedia Commons)

Fig. 2.27: Coils used in inductive heating

field towards the object. Since only heating is required, induction heating systems can be considered as 100 % efficient.

Induction heating systems can be found in furnaces where metals are heated up to their melting point. The transmitter consists of a solenoid and the metal to be melted is inserted inside the solenoid. A high power high frequency AC current (up to several kilohertz) flows in the solenoid which produces an intense magnetic field. The magnetic field induces eddy currents in the metal that lead to an increase in its temperature due to the ohmic losses. Another use for induction heating is for cooking and is referred to as 'induction cooking'. Induction cookers operate using the same principle, however the coil used in the transmitter is a planar coil which produces a magnetic field in parallel to its axis. A pot is then placed on top of the coil and once current flows in the coil, the pot's temperature increases and heat is transferred to the contents inside it. Fig. 2.27 shows two coils used in induction furnaces and cooking.

C. Passive Radio Frequency Identification

Radio frequency identification (RFID) is a technology that allows data stored in a device to be transferred wirelessly using electromagnetic waves. More specifically a magnetic field is used for short distances and radio waves are used for longer distances. As discussed in [38], an RFID system consists of a 'reader' which represents the transmitter and is also referred to as the 'interrogator', and a 'tag' which represents the receiver that holds certain data that the reader needs to obtain. Three types of tags are available; passive, semi-passive and active tags. Passive tags don't have an internal power source and are powered from the transmitter's radiated field. Data is transferred between the reader and the tag by means of load modulation techniques

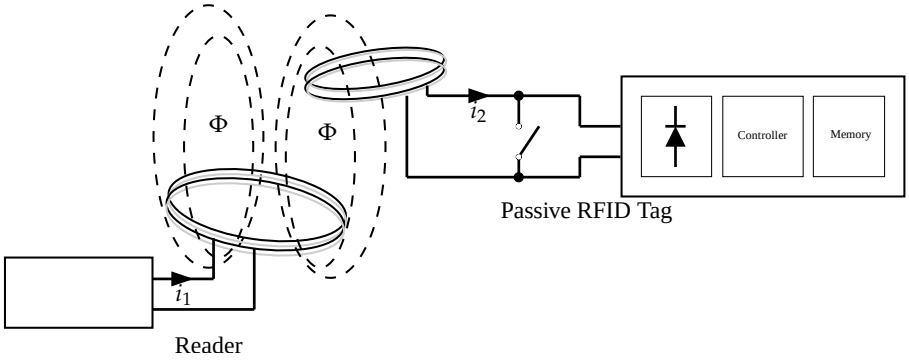

Fig. 2.28: RFID principle of operation

where the reflected impedance of the tag seen by the reader is modulated by the tag to represent data. In semi-passive tags, power is obtained from a separate power supply in the tag, but the transmission of data is done in a similar manner to that of passive tags. Active tags have their own power supply and transmitter to transfer data.

Passive RFID tags make use of inductive coupling for power and data. The operating principle of a passive RFID system using magnetic induction is shown in Fig. 2.28. An AC current at a certain frequency flows in the coil of the reader producing an alternating magnetic field. If a passive tag is placed in close proximity to the reader, the reader's magnetic field will induce a voltage in the tag. The induced voltage is rectified and is used to power the digital logic circuitry in the tag. When data is to be transmitted from the tag to the reader, the tag will change its reflected impedance seen by the reader. The variations in the reflected impedance are sensed by the reader by measuring the current flowing in the reader's coil. More details about reflected impedances can be found in Sec. 3.2.3.

RFID tags can be embedded in numerous objects due to their small size and low manufacturing cost (Fig. 2.29). RFID tags are currently being attached to identity cards, travel documents and passports for personal identification purposes. They are also attached to persons, animals and objects for tracking. Fig. 2.29 shows several passive RFID tags that are currently in use [39]. Efficiency is typically low for an RFID system, however it is not of major interest since the system operates at low power levels.

D. Medical Implants and Endoscopes

Inductive links are also used in biomedical implants such as pacemakers, cochlear implants and muscle and nerve stimulation devices [40–42]. As these implants are becoming more and more smaller, having a battery on board limits their miniaturization and increases their mass. By using magnetic induction, the battery is replaced with a coil and the implant receives power and data from a transmitter located outside the

(a) A micro RFID tag used in implants (Image: Texa's Intruments)

(b) RFID tags used in travel cards and objects (Image: Wikipedia Commons)

Fig. 2.29: Passive RFID tags used in various applications

body as describe in [41]. Another possible application for inductive links in medicine is in diagnosis and endoscopy systems. Research is being conducted in developing micro robots in the form of small capsules. These capsules are injected in the body and are powered externally via inductive coupling [43, 44]. Since no batteries are used, they can be made in very small sizes and more space is available to include more functions in them such as high resolution image sensors, LEDs for illuminations and more actuators to improve their movement inside the body. In [43], a complete system was developed that would deliver up to 300 mW of power to a robotic capsule (Fig. 2.30). The overall efficiency is less than 5 % which us considerably low due to the size mismatch of the coils in the robotic capsule and the transmitter. However it is not of major interest due to the low power operation of the capsule.

2.4.2 *Research Trends*

Extensive research has been conducted on inductive links for contactless power and for wireless power transfer. The areas that are being researched can be narrowed into the following topics [45–47] :

- Increasing the distance between two coupled coils while still transferring a reasonable amount of energy.

- Achieving high power transfer efficiencies.

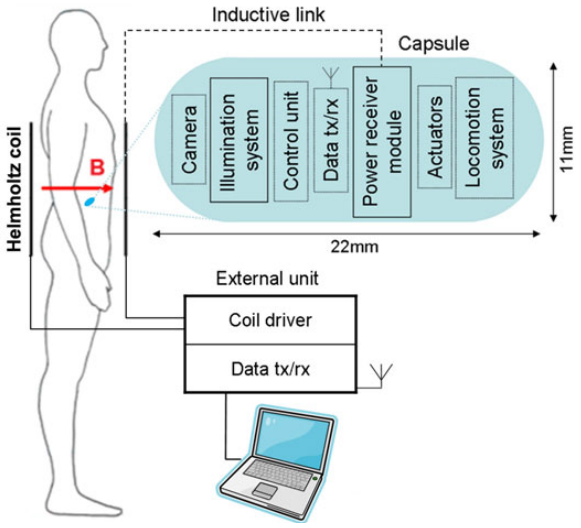

Fig. 2.30: An endoscopy system using an inductive link to power a micro robot inside the body [43]

- Reducing the losses due to the ESR of the coils and other passive components that are involved in the transfer of power.

- Using the latest developments in power electronics to create efficient primary drivers and rectifiers.

- Control methods to regulate the power transferred.

- Transferring data and information between the transmitter and the receiver over the power link.

It is difficult to cover all of the research topics found in literature, a brief summary about the current research trends for WPT based resonant inductive coupling will be mentioned in the remainder of this chapter.

Although the technique of using magnetic resonance to improve the transfer power and efficiency has been reported in numerous IPT applications and in publications over the years, the term 'magnetic resonance for WPT' was first introduced by a team led by Dr. Marin Soljačić from Massachusetts Institute of Technology in 2007 [48]. The team was able to transfer up to 60 W over a distance in excess of two meters; eight times the radius of the coils used. The team claims that they were able to achieve a transmission efficiency (i.e. from the primary coil to the secondary coil) of approximately 40 %. To fully understand the magnetic resonance 'phenomena', the team used coupled-mode theory to analyse a system consisting of two helical coils which rep-

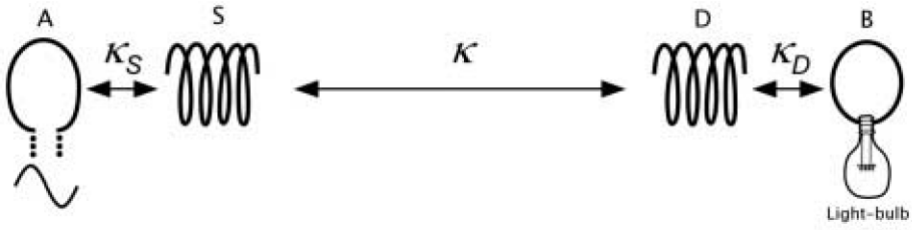

Fig. 2.31: Schematic of the experimental setup to illustrate the magnetic resonance 'phenomena' [48]

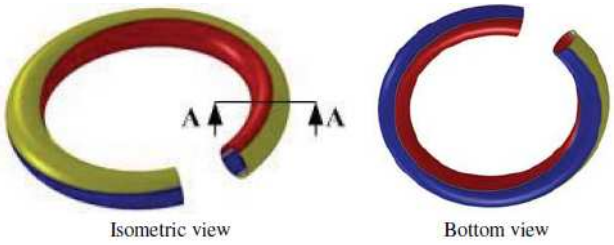

Fig. 2.32: The developed spiral coil with reduced ESR [49, 50]

resent the primary and secondary of a pair of inductively coupled coils (Fig. 2.31). The primary and secondary helical coils themselves are inductively coupled to a high frequency generator at 9.9 MHz and to a resistive load in the form of a light bulb respectively. The calculated coupling coefficient and the transmission efficiency were within 5% agreement with the theory. The team also states that the overall efficiency, from the mains to load is 15% due to the losses in the high frequency generator.

The equivalent series resistance (ESR) of the coils and other passive components contribute significantly to the overall losses of any inductio- based system. Minimising these losses can lead to higher efficiencies and can allow more power to be transmitted over larger distances. Lee and Lorenz were able to develop a model for transmitting up to 220 W over a 30 cm air gap at an efficiency of 95 % [49]. The efficiency here is ratio of the power transmitted by the first coil to the total power received at the secondary coil. The coils each had a radius of 17 cm and were operated at a frequency of 3.7 MHz. By means of finite element analysis (FEA), a new surface spiral coil (Fig. 2.32) was developed that a had a reduced ESR compared to other similar coils. Fig. 5.11 shows the experimental setup and the instruments used. It can be concluded that the overall system efficiency will be far less than 95 % due to the losses in the HF transceiver, the antenna tuner and the linear amplifier. Further FEA simulations published afterwards show that the system is capable of delivering up to several kilowatts of power at an efficiency of 95 % [50].

Improving the efficiency and reducing the losses in the DC/AC inverter is important in systems were a limited amount of energy is available. Achieving an DC/AC inversion efficiency of a 100 % is now theoretically possible by using power electron-

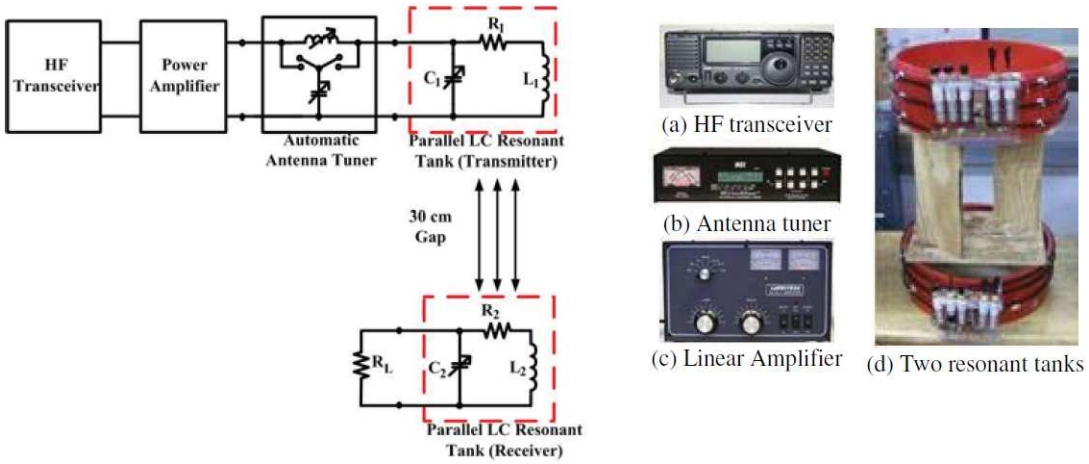

Fig. 2.33: The experimental setup used to validate the model of the developed coils [49]

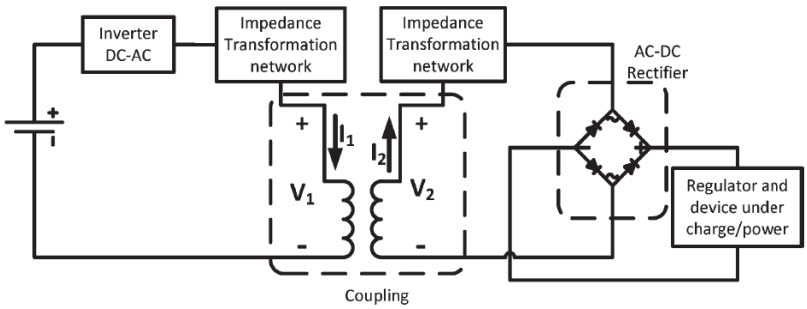

Fig. 2.34: The block diagram of a contactless power system using a Class E Inverter as presented in [51]

ics. However, the non-idealities in today's electronic components limit the maximum achievable inversion efficiency. Zhen has developed a few induction based contactless systems (for small air gaps) by using a Class E Inverter for inverting a DC voltage into a high frequency AC voltage [51–53]. Since Class E Inverters operate efficiently for a certain load range, Zhen used multiple Class E inverters to allow for wider load range. Fig. 2.34 shows the block diagram used in all of the systems he developed. Zhen was able to transmit up to 295 W of power with overall efficiencies reaching up to 76 %. It can be noticed that the a full-wave bridge rectifier has been used in the secondary coil using ordinary diodes. The overall efficiency could be further improved if Schottky diodes or other more efficient rectifier topologies were used.

The development in simulation tools and electromagnetic analysis software packages allowed engineers and developers to create IPT systems that can deliver higher power levels at higher efficiencies. An article published by ANSYS® shows the modelling and simulation of a complete IPT system starting from a DC source to the DC/AC inverter, along with an electromagnetic model of the coils [54].

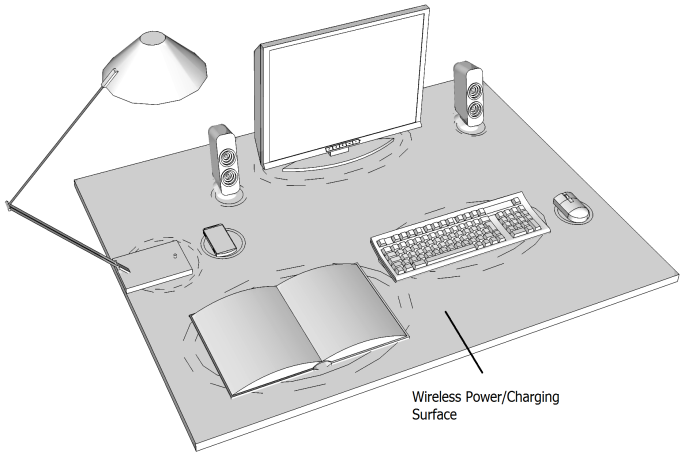

Fig. 2.35: A surface that and power and charge miscellaneous devices placed on top of it

2.5 SUGGESTED APPLICATIONS BASED ON IPT

This section will present several application examples and concepts that are only possible to be implemented using IPT.

A. Rollable and Foldable Displays

The next generation of electronic displays is expected to bring foldable and rollable displays. These displays could be as thin as a sheet paper and would require a small amount of power to operate. The idea of reading a book or a newspaper that could display animated text and images will soon be become a reality. Using inductive coupling to provide power to these displays might be the perfect solution. RFID coils which are mass produced at very low costs and are a few millimetres thick could be installed in these displays and power can be transferred wirelessly to them from a power transmitter placed in close proximity.

B. Wireless Power and Charging Surface

The workspace for most people in a typical office desk includes miscellaneous systems and devices such as computers, monitors, mobile devices etc... A possible application could be embedding an inductive power transfer system beneath a surface such as a desk. The system will be able to provide power to any device placed on top of the surface. This will eliminate cluttering of electrical cables and connectors, it would also allow the freedom of placing and moving any device on top of the surface. Figure 2.35 shows a concept image of a wireless power surface.

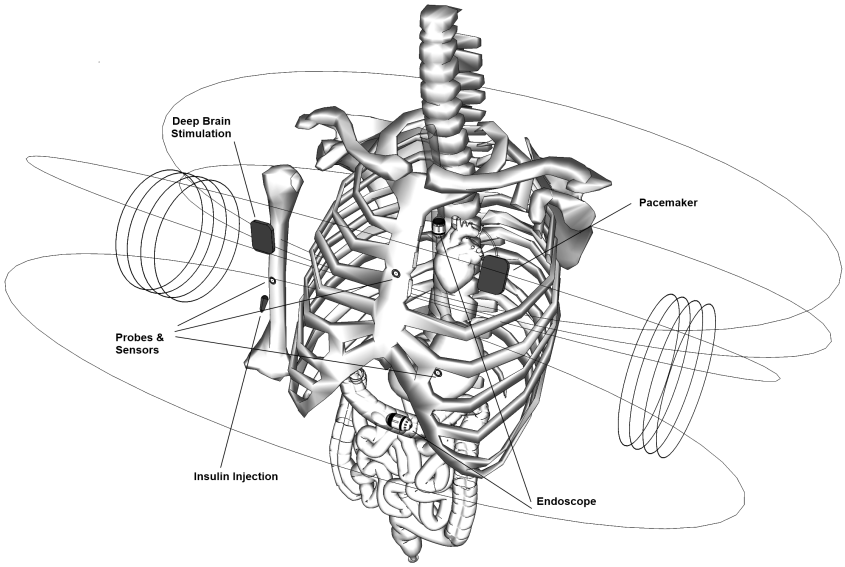

Fig. 2.36: Wireless power transfer for medical implants

C. Biomedical Implants and Body Sensors

As miniaturising technologies continue to evolve, more applications are being developed to implant numerous types of micro medical devices inside the human body to perform various functions such as monitoring different body functions, levels of certain compounds, enhancing the operation of organs and as a replacement to a particular failed organ. While a miniaturization levels in the range of nanometres can be achieved, the main obstacle that limits the use of these medical devices is the batteries that power them. The battery could be several times larger than the device itself if the device is to operate for a long period of time (up to several years) which consequently narrows the range of areas where the device can operate in. If a smaller battery is used then the medical device will have to be removed from the body on a frequent basis to replace or recharge the battery. Therefore the ability to power these biomedical devices wirelessly can address these issues by allowing smaller batteries to be used and eliminating the need to replace the devices by directly providing power to them via inducting coupling. Figure 2.36 shows how an inductive link can provide power to numerous biomedical devices and sensors implanted throughout the human body.

D. Wireless Power for Drones and UAVs

By relying only on wireless power, a rotor drone could be powered and charged whilst hovering above a wireless power transfer platform. This might be useful in cases where landing is not possible or difficult, a situation that is encountered when a helicopter

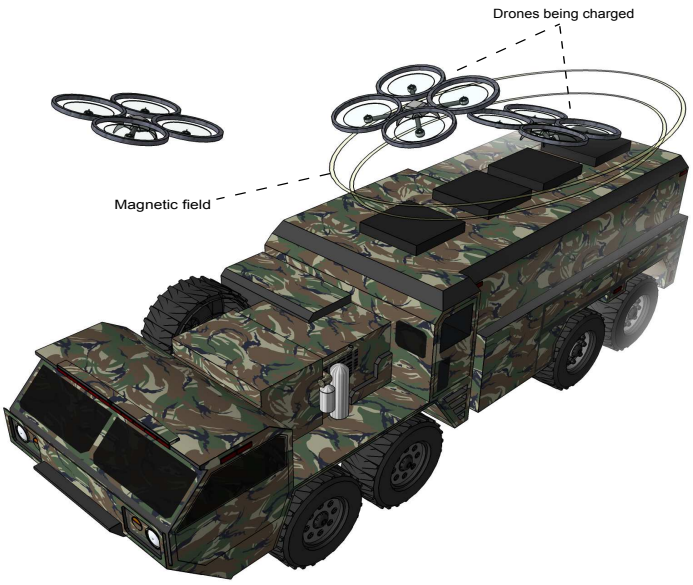

(a)

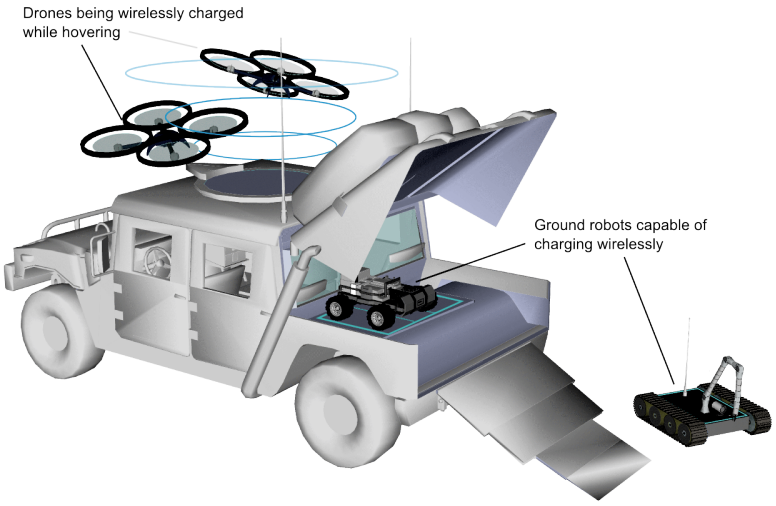

(b)

Fig. 2.37: Concept image showing the application of wireless charging IPT onboard a vehicle

attempts to dock on a landing pad or land on an aircraft carrier in heavy seas. Fig. 2.37 illustrates a possible application where an armoured truck could carry surveillance drones and deploy them while the truck is moving. The drones could perform their tasks and return to the truck to recharge. Another novel application that could be implemented is "In-flight refuling" for battery powered airborne vehicles or in other words transferring electric power from one drone to another as shown in the concept image in Fig. 2.38

The system can also be used in providing power for autonomous underwater vehicles or unmanned surface vehicles where electrical contacts cannot be used.

Fig. 2.38: Wireless power transfer from one UAV to another

E. Planetary Exploration

An IPT can be deployed in remote, dangerous and inhabitable environments to provide power to a swarm of autonomous ground and air vehicles that perform miscellaneous tasks. Fig. 2.39 shows how such a system can be deployed in planetary exploration missions. For instance the system can be used on Mars to provide power to a swarm of rotor drones or robots that are performing scientific tasks. Power supplies could be sent regularly to the planet at reduced costs. Since the entire system including the rotor drones and the robots can be autonomous, minimum or no human interaction should be involved, therefore reducing the maintenance requirements is essential in this case. A major issue that leads to an increase in maintenance requirements is the use of electrical contacts. The tear and wear due to the forces and pressures that result from docking operations as well as erosion and oxidation can increase the contacts' resistances and can significantly affect the amount of current that they can carry. Therefore, replacing contacts with a contactless or a wireless power transfer system can eliminate these maintenance requirements and can significantly increase the service life of the system.

F. Wireless Sensor Networks

The deployment of sensors to monitor and record physical and environmental conditions in spacious areas might cause difficulties in providing power to them. In many cases having long power cables or batteries that need replacement is not feasible. A remote controlled vehicle could be sent to those sensors recharging their batteries wire-

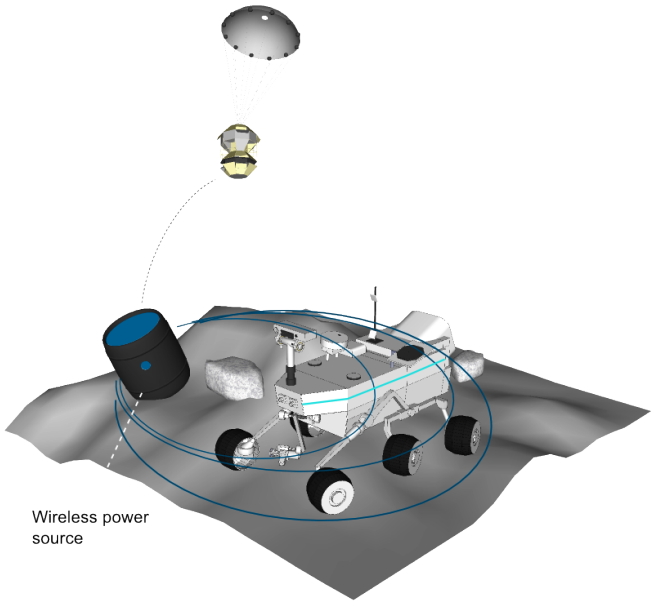

Fig. 2.39: Concept image showing how IPT can be used in planetary exploration missions

Fig. 2.40: IPT in wireless sensor networks

lessly. Fig. 2.40 shows a concept image of a drone could be sent to a remote location to recharge the batteries of underground and overground sensors.

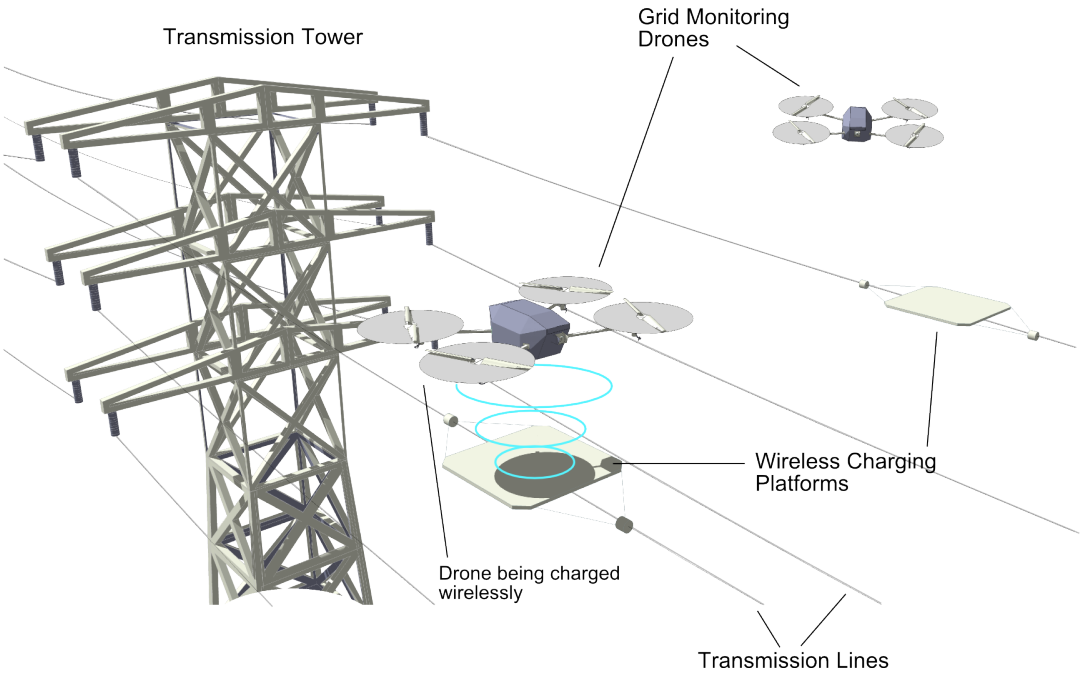

Fig. 2.41: IPT in grid monitoring

G. *Grid Monitoring*

Remote controlled drones provide a low cost, effective and safe method for routine health monitoring of overhead power transmission lines and towers. An onboard camera records and streams video which is then assessed by engineers and technicians to report for faults and maintenance requirements. The capacity of the battery packs installed on such drones limit their flying and operating time to 15-20 minutes. This requires the drones to return and recharge or replace their battery packs. Consequently, the range of operation, monitoring and surveillance capability of theses drones are reduced.

By using IPT, wireless charging platforms could be hooked on the overhead power transmission lines at regular distances. The drone will then hover over the platforms and recharge their battery packs wirelessly. This will enable the drones to operate at extended flight times and allow them to continue their monitoring and surveillance mission without interruption. Fig. 2.41 illustrates this concept.

2.6 CONCLUSIONS

Wireless power transfer is not a new concept, it was first demonstrated by Nikola Tesla in 1893. Several methods were investigated throughout the twentieth century to transfer power wirelessly between two distant locations. The research in microwave-based

WPT was of high interest during the '70s and '80s. Several proof of concept experiments were conducted and concluded that microwave-based WPT has the potential to transfer large amounts of energy over several kilometres. However, the cost of building such a system can be significant.

Induction-based WPT or IPT has gained a lot momentum recently due to the increasing reliance on battery-powered applications ranging from electric vehicles to mobile devices and medical implants. Several standards, such as the Qi and A4WP standards, have been developed to allow for a better integration between various charging devices.

Various applications and research areas for IPT have been presented in this chapter. By reviewing several products and their related patents, it can be noticed that the two important aspects for a IPT system, which are its overall efficiency and the distance between the transmitter and the receiver, are generally ignored and are not mentioned. Whereas in research papers, only the power transmitting efficiency; from the primary coil to the secondary coil, is mentioned.

It was noticed that the main aim in recent publications was to increase the efficiency of an IPT system by minimising any losses and increasing the amount of power that is available to the load. Using magnetic resonance has allowed more power to be delivered to the load due to the cancellation of the coils' reactances. The research has now shifted towards creating novel electric circuits and methods to increase the ability of an IPT system to transfer higher energy levels, as well as to reduce the losses due to the electronic switches involved in the inversion and rectification processes and the ohmic losses in the passive components.

It was also noticed while conducting the literature review that although research has been conducted in developing efficient DC/AC inverters, the DC/AC rectifier on the other hand is still implemented using classical DC/AC rectifier topologies based on ordinary PN silicon diodes. Therefore, introducing more efficient AC/DC rectifiers will be a significant advantage and a topic worth investigating.

3

INDUCTIVE LINKS

3.1 INTRODUCTION

The chapter will discuss the principle of operation of inductive links from a circuit point of view. An electric circuit representation is used to analyse the inductive link and to calculated the induced voltages and currents across the transmitting and receiving coils. The use of magnetic resonance in inductive links and how it can improve the inductive link's efficiency will be discussed. A novel circuit model will be introduced that will allow the inductive link to be represented by an equivalent reflected impedance to simplify its analysis and to determine how power is distributed amongst its elements.

3.2 MODELLING OF INDUCTIVE LINKS

3.2.1 *Quantities and Parameters*

Two independent circuits are said to be magnetically coupled if they both affect each other through a magnetic field generated by either one of them. In other words, two circuits are magnetically coupled if a magnetic flux produced by the coil of one circuit enters the coil of the other circuit. Thus, in addition to the self inductances of each coil, a third inductance exists between the two coils which is referred to as the 'mutual inductance M'.

According to Faraday's law of induction, a voltage v is induced in a single coil that is proportional to its number of turns N and the time rate of change of the magnetic flux Φ crossing the coil (Fig. 3.1), i.e.,

$$v = N\frac{d\Phi}{dt}. \tag{3.1}$$

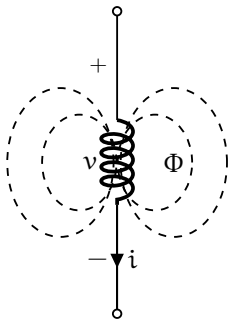

Fig. 3.1: Magnetic flux produced by a current flowing in a coil

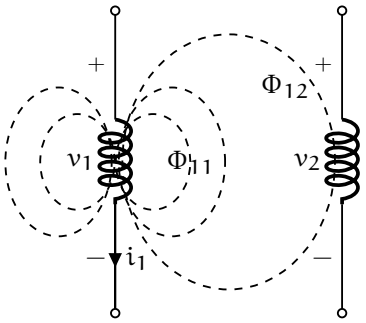

Fig. 3.2: The total magnetic flux produced due to i_1 crossing both coils

From Ampere's law, the magnetic flux Φ is produced by a current i flowing in the coil. The magnetic flux is given by

$$\phi = \frac{\mu_o N i A}{w} \tag{3.2}$$

where μ_o is the permeability of free space, A is the area of the coil and w is the width of the coil. Thus, Eq. 3.1 can be written as

$$v = \frac{\mu_o N^2 A}{w}\frac{di}{ft} = L\frac{di}{dt} \tag{3.3}$$

where L is referred to as the 'self-inductance' of the coil and is equal to

$$L = \frac{\mu_o N^2 A}{w}. \tag{3.4}$$

If another coil is in close proximity with the first coil, then the flux produced due to the current in the first coil will have two components; flux Φ_{11} which crosses the first coil and flux Φ_{12} which crosses the second coil (Fig. 3.2). The total produced flux due to the current in the first coil is given by

$$\Phi_1 = \Phi_{11} + \Phi_{12}. \tag{3.5}$$

The voltage induced in the first coil consisting of N_1 turns is

$$v_1 = N_1\frac{d\Phi_{11}}{dt} \tag{3.6}$$

and the voltage induced in the second coil consisting of N_2 turns is

$$v_2 = N_2\frac{d\Phi_{12}}{dt}. \tag{3.7}$$

The total flux Φ_1 is produced due to current i_1 flowing in the first coil. Eq. 3.6 and 3.7 can be written as

$$v_1 = N_1 \frac{d\Phi_1}{di_1}\frac{di_1}{dt} = L_1 \frac{di_1}{dt} \tag{3.8}$$

$$v_2 = N_2 \frac{d\Phi_{12}}{di_1}\frac{di_1}{dt} = M_{21} \frac{di_1}{dt} \tag{3.9}$$

where L_1 is the self-inductance of the first coil and M_{21} is referred to as the mutual inductance of the second coil with respect to the first coil. The mutual inductance M_{21} is equal to

$$M_{21} = N_2 \frac{d\Phi_{12}}{di_1}. \tag{3.10}$$

Similarly, it can be shown that if a current i_2 flows in the second coil then the total flux produced by the second coil is

$$\Phi_2 = \Phi_{22} + \Phi_{21} \tag{3.11}$$

and the voltages induced in the first and second coils are

$$v_1 = N_1 \frac{d\Phi_{21}}{di_2}\frac{di_2}{dt} = M_{12} \frac{di_2}{dt} \tag{3.12}$$

$$v_2 = N_2 \frac{d\Phi_2}{di_2}\frac{di_2}{dt} = L_2 \frac{di_2}{dt} \tag{3.13}$$

where L_2 is the self-inductance of the second coil and the M_{12} is referred to as the mutual inductance of the first coil with respect to the second coil. The mutual inductance M_{12} is equal to

$$M_{12} = N_1 \frac{d\Phi_{21}}{di_2}. \tag{3.14}$$

It can be proved that both mutual inductances M_{12} and M_{21} are equal by calculating the amount of energy stored in the circuit due to a change in either currents flowing into the coils as shown in [55]. Thus,

$$M_{12} = M_{21} = M \tag{3.15}$$

M is defined as the mutual inductance between two coils whether they are identical or not, i.e. they could have different geometries and number of turns. The mutual inductance specifies the strength of coupling between two coils by comparing the mutual inductance to their self inductances. A coupling coefficient k can be defined as the ratio between the mutual inductance and the self inductances of the coil [55]

$$k \equiv \frac{M}{\sqrt{L_1 L_2}} \tag{3.16}$$

The coupling coefficient is zero if there is no coupling between the two coils, i.e. the magnetic flux produced by either coil does not enter the other. The coupling coefficient is unity when there is a perfect coupling between the two coils, i.e all of the

magnetic flux produced by either coil enters the other. For k<0.5, the two coils are said to be 'loosely coupled', and for k>0.5, the two coils are said to be 'tightly coupled' [55]. The coupling coefficient is a function of the coils' dimensions, their orientation with respect to each other, their number of turns, the distance between them and the magnetic core that they are wound on (if any) [55]. As an example, the AC transformer can be considered to be tightly coupled if it is wound on a magnetic core. A magnetic core aids in guiding the magnetic flux from one coil to other. AC transformer with cores are used in numerous power applications. The coupling coefficient is governed by the core's magnetic properties and is generally assumed to be higher than 0.9. The AC transformer could be considered as loosley coupled if it has an air core. Air core or coreless AC transformers are used in radio circuits for signal conditioning purposes. Their coupling coefficient is governed by the windings' dimensions and their orientation. Consequently, IPT applications can be considered as a loosely coupled system since they behave much like a coreless AC transformer.

The mutual inductance M is always a positive quantity, however the voltage induced due to the mutual inductance maybe either be positive or negative. The polarity of the induced voltage is determined by examining the orientation and the windings of the coils and applying Lenz's law. Consider the two coils in Fig. 3.3. In Fig. 3.3a, if current i_1 enters coil 1 and is increased linearly with time, then it will generate an increasing magnetic flux. According to Lenz's law, a current i_2 will be induced in coil 2 which will then produce a magnetic flux that opposes that of coil 1. If a voltmeter is placed across coil 2, its voltage reading will be positive since current i_2 exits the upper terminal of coil 2 and enters it lower terminal. Now if coil 2 is flipped up side down as shown in Fig. 3.3b, then reapplying the same increasing current i_1 in coil 1 will produce the same increasing magnetic flux and according to Len's law, the same current i_2 will be induced in coil 2 which will then produce an opposing magnetic flux to that of coil 1. Measuring the voltage across coil 2 again will result in a negative reading since now current i_2 enters the upper terminal of coil 2 and leaves its lower terminal.

In a circuit representation, the polarity of the induced voltage is determined by the 'dot convention'. In this convention, a dot is placed besides one terminal of each inductor to indicate the direction of the applied or induced current. For example, if a current enters the dotted terminal of one coil, then the induced current will leave the dotted terminal of the other coil. If a current enters the undotted terminal of one coil, then an induced current will enter the dotted terminal of the other coil. Fig. 3.4 shows examples on how this convention is used to determine the direction of the induced current and the polarity of the generated voltage.

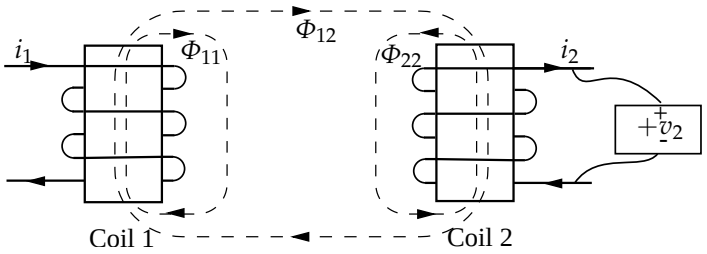

(a) Positive induced voltage

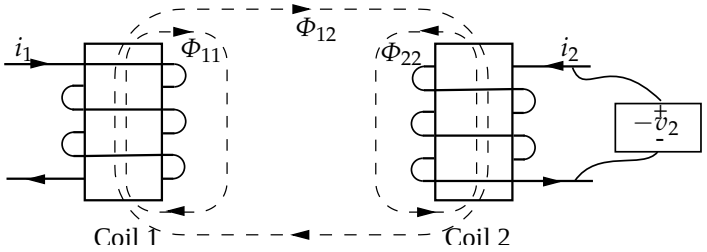

(b) Negative induced voltage

Fig. 3.3: Induced voltage's polarity depending on the orientation and winding of the coil

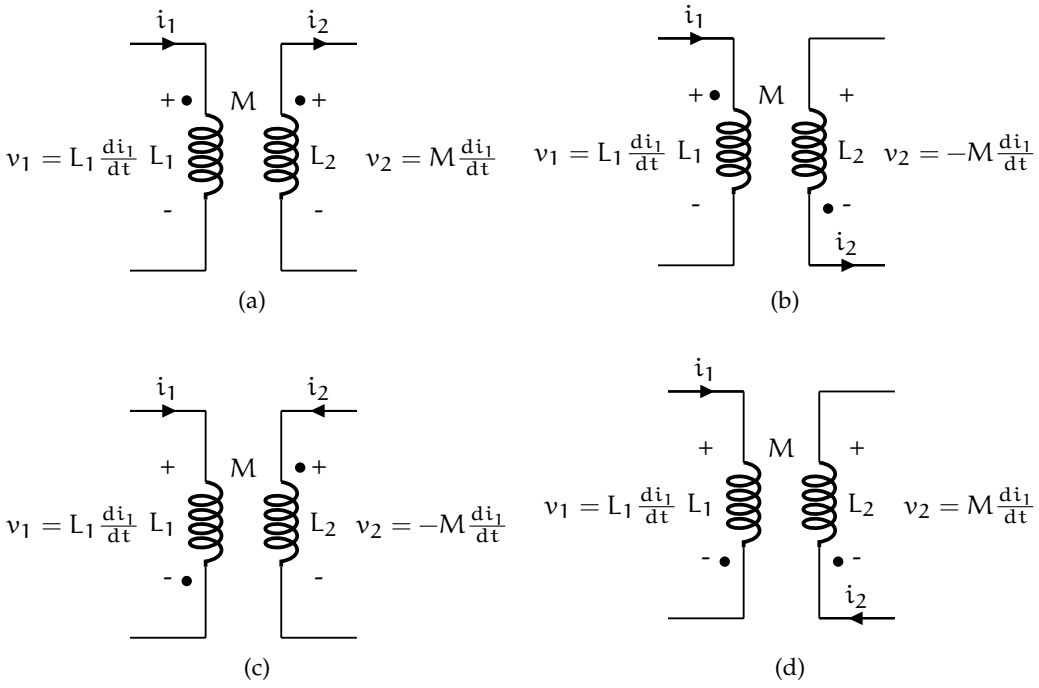

Fig. 3.4: Dot convention

3.2.2 *Equivalent Series Resistance and Quality Factor*

Inductors and coils are wound using copper wires. These wires have a certain resistance that depends on their length and their cross sectional area. It is desirable to have a coil with a negligible resistance to reduce losses and minimise heat. If used in AC applications, a wire's resistance tends to increase as the frequency of its current

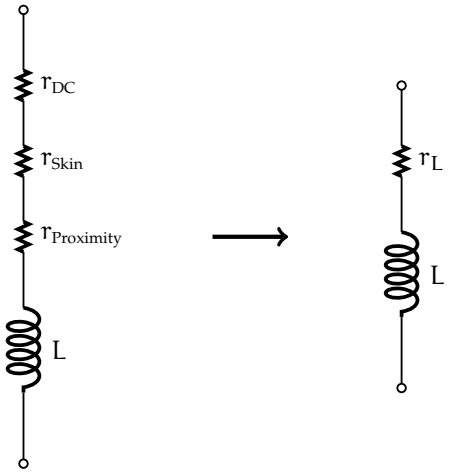

Fig. 3.5: The ESR of a coil

increases due to the 'skin effect' and the 'proximity effect' [56]. The skin effect causes the current flowing in a wire to be more dense near its surface rather than being evenly distributed along its entire cross section area. This reduces the effective cross sectional area of the wire and thus its resistance is increased. The proximity effect results when two adjacent wires are carrying an alternating current. The magnetic field produced by each wire causes a repelling force to act on them resulting in the current to be constrained in smaller regions. As a result, the effective cross sectional area of the wire is further decreased which leads to an increase in its resistance. The skin and proximity effects become more significant as the frequency of the current increases. Therefore these two effects can influence the power transferred between two coils in IPT applications especially at higher frequencies. Hence, the total resistance r_L of a coil operating at a certain frequency can be represented as

$$r_L = r_{DC} + r_{Skin} + r_{Proximity} \tag{3.17}$$

where r_{DC} is the total DC resistance of the coil's wires , r_{Skin} is the resistance of the wires due to the skin effect and $r_{Proximity}$ is the resistance of the wires due to the proximity effect. The total resistance is often referred to as the Equivalent Series Resistance (ESR) (Fig. 3.5). The term 'Quality Factor Q' is used to indicate the ratio between the reactance of the coil X_L to its resistance at a specific frequency. Q is defined as

$$Q \equiv \frac{\omega L}{r_L} = \frac{X_L}{r_L}. \tag{3.18}$$

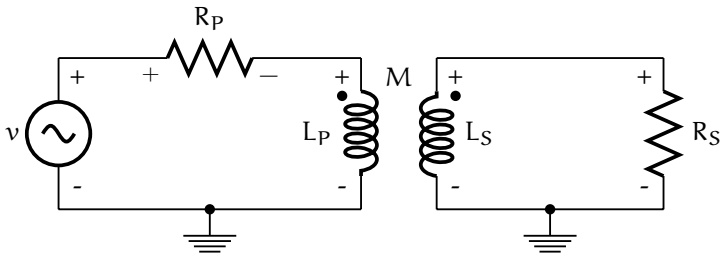

Fig. 3.6: An example of a circuit with coupled inductors

3.2.3 *Circuit Representation*

Having defined all the parameters and quantities for two magnetically coupled coils, they can now be used along with circuit analysis theory to calculate the voltages and currents in any electrical system that contains a pair of coupled coils. Analysing magnetically coupled coils in circuits can be either done directly by calculating the induced voltages and currents or by replacing the coupled coils with an equivalent circuit to simplify the calculations. Deciding on which approach to follow depends on the required quantity to be calculated and the complexity of the system.

The example circuit in Fig. 3.6 will be analysed to demonstrate the application of the two aforementioned approaches. All of the circuit elements in primary coil side will be designated by the subscript 'P' and all of the circuit elements in the secondary coil side will be designated by the subscript 'S'. The example circuit is to be solved by calculating the current flowing in the primary coil i_P, the voltage across the primary coil v_{L_P}, the induced voltage v_{L_S}, current i_S in the secondary coil, the power delivered by the voltage source P_v and the power dissipated in the load P_{R_S} connected to the secondary coil. The circuit is first solved by directly calculating the induced voltage and current in the secondary coil, and then solving for the current in the primary coil. By using the mesh analysis method [55], two current meshes can be formed as shown in Fig. 3.7. By applying KVL to each mesh, the following two equations are obtained

$$v = i_P R_P + j i_P X_{L_P} - j i_S X_M \tag{3.19}$$

$$j i_P X_M = j i_S X_{L_S} + i_S R_S \tag{3.20}$$

where X_{L_P}, X_{L_S} and X_M are the reactances of inductances L_P, L_S and M respectively. The polarity of the voltages induced in L_P and L_S due to the mutual inductance is determined by applying the dot convention. In Eq. 3.19, the induced voltage in L_P is negative at its top terminal with reference to ground since the current i_S enters the undotted terminal of L_S. Whereas in Eq. 3.20, the induced voltage in L_S is positive at

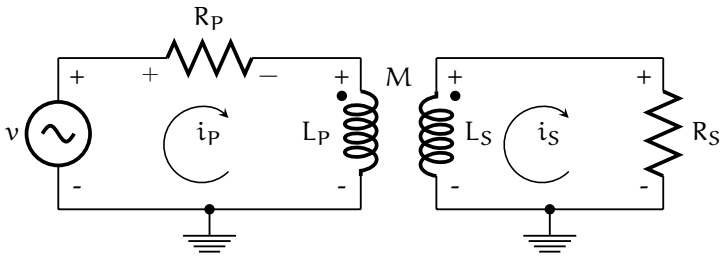

Fig. 3.7: Using Mesh analysis method to solve a circuit

its top terminal with reference to ground since the current i_P enters the dotted terminal of L_P. Rewriting Eq. 3.20 with respect to i_S and substituting in Eq. 3.19,

$$v = i_P(R_P + jX_{L_P} + \frac{{X_M}^2}{R_S + jX_{L_S}}). \tag{3.21}$$

The circuit can now be solved for the other required quantities and are found to be equal to

$$i_P = \frac{v}{R_P + jX_{L_P} + \frac{{X_M}^2}{R_S + jX_{L_S}}} \tag{3.22}$$

$$i_S = i_P \frac{jX_M}{R_S + jX_{L_S}} \tag{3.23}$$

$$v_{L_P} = ji_P X_{L_P} - ji_S X_M \tag{3.24}$$

$$v_{L_S} = ji_P X_M - ji_S X_{L_S} \tag{3.25}$$

$$P_v = P_{R_S} = \frac{1}{2}{i_S}^2 R_S. \tag{3.26}$$

A different method to solve the previous circuit is to transform the coupled coils into another circuit representation which does not include any magnetically coupled coils. Two equivalent circuits can be used [55]; the T circuit representation and the π circuit representation. Fig. 3.8 illustrates the two equivalent circuits. For the equivalent T circuit, inductances L_P, L_S and M are replaced with inductances L_a, L_b and L_c and are given as [55]

$$L_a = L_P - M, \qquad L_b = L_S - M, \qquad L_c = M. \tag{3.27}$$

For the Π circuit, inductances L_P, L_S and M are replaced with inductances L_A, L_B and L_C and are given as [55]

$$L_A = \frac{L_P L_S - M^2}{L_S - M} \qquad L_B = \frac{L_P L_S - M^2}{L_P - M} \qquad L_C = \frac{L_P L_S - M^2}{M}. \tag{3.28}$$

By using the T circuit, the circuit in Fig. 3.6 can be solved as shown in Fig. 3.9. By using the nodal analysis method [55] and applying KCL, the following equation is obtained

$$\frac{V_x - v}{R_P + jX_{L_a}} + \frac{V_x}{jX_{L_c}} + \frac{V_x}{R_S + jX_{L_b}} = 0. \tag{3.29}$$

Solving Eq. 3.29 for V_x gives

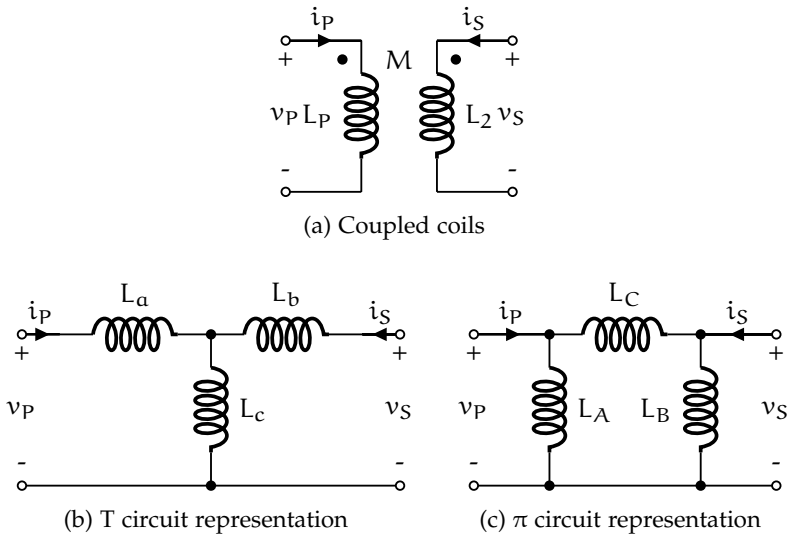

(a) Coupled coils

(b) T circuit representation

(c) π circuit representation

Fig. 3.8: The equivalent T and π circuits representing magnetically coupled coils

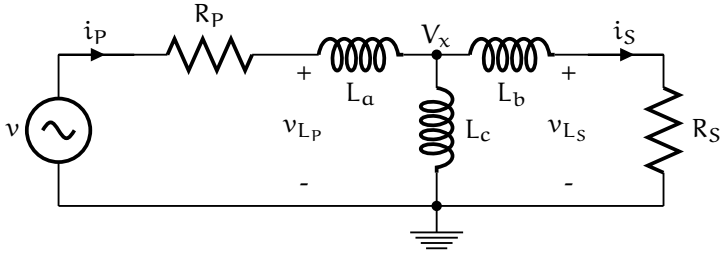

Fig. 3.9: Using Nodal analysis to solve a circuit

$$V_x = \left(\frac{v}{R_P + jX_{L_a}}\right)\left(\frac{1}{R_P + jX_{L_P}} + \frac{1}{jX_{L_c}} + \frac{1}{R_S + jX_{L_b}}\right)^{-1}. \tag{3.30}$$

The circuit can now be solved for the other required quantities are found to be equal to

$$i_P = \frac{V_x - v}{R_P + jX_{L_a}} \tag{3.31}$$

$$i_S = \frac{V_x}{R_S + jX_{L_b}} \tag{3.32}$$

$$v_P = ji_P X_{L_a} + V_x \tag{3.33}$$

$$v_S = -ji_S X_{L_b} + V_x \tag{3.34}$$

$$P_v = P_{R_S} = \frac{1}{2} {i_S}^2 R_S. \tag{3.35}$$

The circuit in Fig. 3.6 has now been solved using two different approaches. A parameter that can be obtained from Eq. 3.21 is the input impedance Z_{in} as seen from the source v and is given by

$$Z_{in} = \frac{v}{i_P} = R_P + jX_{L_P} + \frac{{X_M}^2}{R_S + jX_{L_S}} \tag{3.36}$$

In Eq. 3.36, the input impedance contains two terms. The first term $(R_P + jX_{L_P})$ is the impedance of the primary coil, where R_P could be represent the ESR of the primary

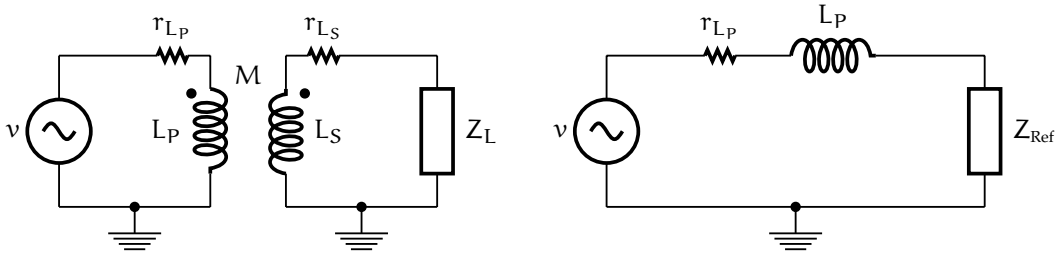

(a) Coupled coils circuit including r_{ESR} (b) Equivalent circuit

Fig. 3.10: Representing a coupled coil circuit with a reflected impedance

coil, i.e. $R_P = r_{L1}$. The second term results from the coupling between the two coils and is referred to as the 'reflected impedance Z_{Ref}' and is given by

$$Z_{Ref} = \frac{{X_M}^2}{R_S + jX_{L_S}}. \tag{3.37}$$

The reflected impedance term in Eq. 3.37 consists of the impedance of the secondary coil. Similar to R_P, R_S could represent the ESR of the secondary coil, i.e. $R_S = r_{L_S}$. If load impedance Z_L is added in series with the secondary coil as shown in Fig. 3.10a, then Z_{Ref} is equal to

$$Z_{Ref} = \frac{{X_M}^2}{r_{L_S} + jX_{L_S} + Z_L}. \tag{3.38}$$

Fig. 3.10a can now be transformed to a simpler circuit representation as shown in Fig. 3.10b.

The reflected impedance is a measure of how much of the actual load is seen by the source. It is a function of the mutual inductance between the coils which in turn is affected by the distance between the coils (assuming the two coils are identical). The closer the coils are to each other, the higher the mutual inductance and the higher the reflected impedance. And the further apart the coils are from each other, the lower the mutual inductance and the lower the reflected impedance.

3.3 RESONANT COUPLING

Referring to Eq. 3.38, the reflected impedance consists of the load and the impedance of the secondary coil. Assuming an ideal coil ($r_{L_S} = 0$) and a resistive load ($Z_L = R_L$), the absolute value of the reflected impedance is equal to

$$|Z_{Ref}| = \frac{{X_M}^2}{\sqrt{{R_L}^2 + {X_{L_S}}^2}}. \tag{3.39}$$

Thus, the reflected impedance is inversely proportional to the load resistance and magnitude of the secondary coil's impedance. Ideally, a higher reflected impedance

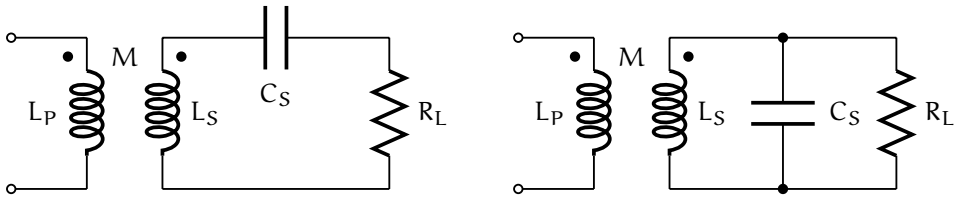

(a) Series resonance (b) Parallel resonance

Fig. 3.11: Including a capacitor with the secondary coil can create resonance and eliminate the secondary coil's reactance

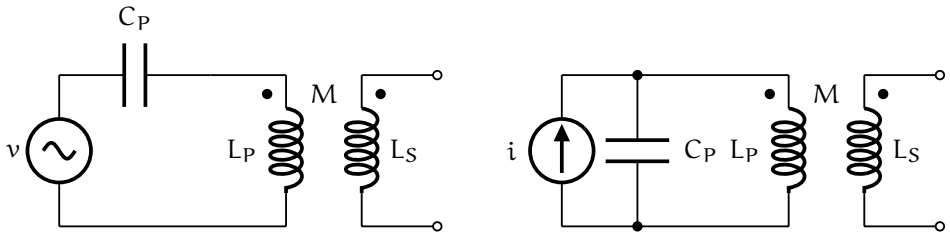

(a) Series resonance (b) Parallel resonance

Fig. 3.12: Including a capacitor with the primary coil can create resonance and eliminate the primary coil's reactance

is preferred since more power can be delivered at higher efficiencies as the required voltage to be induced in the receiver's secondary coil will be low. Eliminating the secondary coil's reactance term X_{L_S} in Eq. 3.39 will reduce the secondary's impedance which will increase the reflected impedance. This can be done at a certain frequency by connecting an external capacitor. The value of the capacitor is chosen such that its reactance will be equal to the reactance of the secondary coil's inductance, therefore creating resonance. The external capacitor can be connected in series or parallel as shown in Fig. 3.11. The reflected impedance is now equal to

$$Z_{Ref} = \frac{{X_M}^2}{R_L}. \tag{3.40}$$

The decision on whether to use a series or parallel capacitor depends on the value of the load. A series capacitor is used if $R_L \ll X_{L_S}$ causing the secondary coil's circuit to behave as if it was a current source. Whereas a parallel capacitor is used if $R_L \gg X_{L_S}$ causing the secondary's coil circuit to behave as if it was a voltage source [57].

Resonating the primary coil can also help in delivering more power to the load by eliminating the reactance of the primary coil X_{L_P} in Eq. 3.37. In a similar manner, adding an external capacitor in series or parallel with the primary coil creates resonance and eliminates its reactance. Depending on the power source, a series capacitor is used if the power source was represented as a voltage source. Whereas a parallel capacitor is used if the power source was represented as a current source. Fig. 3.12 shows the two possible resonant circuits. Both primary and secondary resonance allows the load to receive maximum power from the source. For example, using series resonance

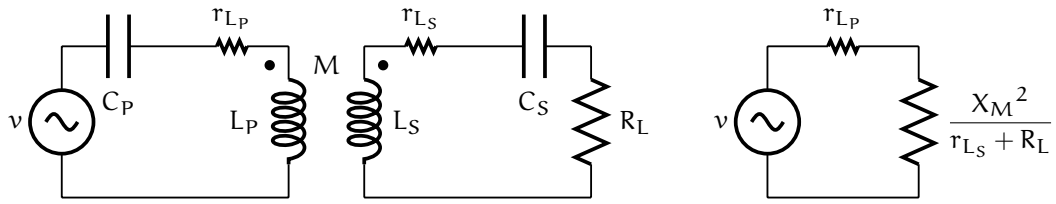

(a) Series resonance used in primary and secondary coils (b) Equivalent circuit

Fig. 3.13: Resonant coupled circuit by adding tuned capacitors to the primary and secondary coils

in the primary and secondary coils and assuming non ideal coils ($r_{L_P} \neq 0, r_{L_S} \neq 0$) as shown in Fig. 3.13a, the total input impedance Z_{in} seen by a voltage source is equal to

$$Z_{in} = r_{L_P} + jX_{L_P} - jX_{C_P} + \frac{X_M{}^2}{r_{L_S} + R_L + jX_{L_S} - jX_{C_S}} = r_{L_P} + \frac{X_M{}^2}{r_{L_S} + R_L} \tag{3.41}$$

where X_{C_P} and X_{C_S} are the reactances of the series capacitors connected to the primary and secondary coils respectively. Fig. 3.13b shows the equivalent circuit.

It can be noticed from Eq. 3.41 that using resonance or resonant coupling increases the reflected impedance and decreases the primary coil's impedance, this allows for more power to be delivered to the load compared to non-resonant coupling.

3.4 ANALYSIS OF A PARALLEL RESONANT SECONDARY COIL

As mentioned in Sec. 3.3, using resonance increases the reflected impedance seen by the source which allows it to deliver more power to the load. When using resonance, the reflected impedance only consists of the ESR of the secondary coil, its resonant capacitor and the load resistance. That means that the power delivered by the source will be dissipated in the ESRs and the load only. Ideally we would want all of that power delivered by the source to be dissipated only in the load. Practically, energy lost in the ESR cannot be avoided and in the following sections it will be shown that the ESR is the main obstacle that limits the use of IPT systems over large distances.

The amount of power lost in the ESRs can be minimised if the current flowing in them is reduced. Since $P = I^2R$, if the current flowing into a resistance is halved, then the power lost is quartered. Therefore in order to transfer power efficiently, especially at large distances, using parallel resonance will minimise the power lost in the ESRs since high voltages are generated at low current levels in a parallel tuned LC circuit.

3.4.1 *Near Resonance Operation*

Consider the secondary resonant circuit with a parallel capacitor shown in Fig. 3.11b. The total reflected impedance Z_{Ref} seen by a power source connected to the primary coil is given by

$$Z_{Ref} = \frac{X_M^2}{jX_{L_S} + \dfrac{-jX_{C_S}R_L}{R_L - jX_{C_S}}} = \frac{X_M^2(R_L^2 + X_{C_S}^2)}{jX_{L_S}R_L^2 + jX_{L_S}X_{C_S}^2 - jX_{C_S}R_L^2 + X_{C_S}^2R_L}. \tag{3.42}$$

For resonance, the imaginary terms in the denominator of Eq 3.42 should be zero, hence the following equation is obtained

$$X_{C_S}^2X_{L_S} - X_{C_S}R_L^2 + X_{L_S}R_L^2 = 0 \tag{3.43}$$

giving the capacitor's reactance

$$X_{C_S} = \frac{R_L^2 - \sqrt{R_L^4 - 4X_{L_S}^2R_L^2}}{2X_{L_S}} \tag{3.44}$$

and the resonant capacitance is

$$C_S = \frac{2X_{L_S}}{\omega R_L^2\left(1 - \sqrt{1 - \dfrac{4X_{L_S}^2}{R_L^2}}\right)} = \frac{1 + \sqrt{1 - \dfrac{16\pi^2f^2L_S^2}{R_L^2}}}{8\pi^2f^2L_S}. \tag{3.45}$$

Note that the resonant capacitance depends on the load resistance. From Eq. 3.45, the resonant frequency for a certain inductor and a parallel capacitor and resistor is equal to

$$f = \frac{1}{2\pi}\sqrt{\frac{1}{L_SC_S} - \frac{1}{C_S^2R_L^2}}. \tag{3.46}$$

From a practical point of view, it is not feasible to change the parallel capacitor as the load changes. Therefore, the secondary coil will have to operate at a frequency close or near to its resonant frequency. Fortunately, due to inverse squared term of the load resistance in Eq. 3.46, it is safe to assume that the secondary coil will be operating in resonance with the primary coil for high load resistance values only.

3.4.2 *Reflected Load Formulae*

The load's share of the total power received at the secondary coil can be found by analysing the total reflected impedance of the secondary coil's circuitry. The total reflected impedance can be broken down into several components each representing

the reflected impedance of a particular element of the secondary coil's circuitry. The amount of power delivered to each element can then be calculated. The following cases will demonstrate this in further details.

A. Ideal Case

The first case that will be considered is the ideal case where all of the circuit elements are lossless. This case can be applied on the circuit in Fig. 3.11b. The total reflected impedance was given in Eq. 3.42. If the circuit is to be operated at its resonant frequency, then $X_{C_S} = X_{L_S}$, and therefore the total reflected impedance is

$$Z_{Ref} = \frac{X_M^2 (R_L - jX_{C_S})}{X_{C_S}^2}. \tag{3.47}$$

Taking the real part of the total reflected impedance,

$$R_{Ref} = \text{real}\{Z_{Ref}\} = \frac{X_M^2 R_L}{X_{C_S}^2} = \omega^4 M^2 {C_S}^2 R_L. \tag{3.48}$$

Resistance R_{Ref} can be referred to as the reflected resistance of the load. Taking the imaginary part of the total reflected impedance,

$$X_{Ref} = \text{imag}\{Z_{Ref}\} = -\frac{jX_M^2}{X_{C_S}} = -j\omega^3 M^2 C_S. \tag{3.49}$$

Reactance X_{Ref} can be referred to as the reflected reactance of the mutual inductance and the parallel capacitor C_S. Consequently, the total reflected impedance can be represented as shown in Fig. 3.14. Since the real part of the total reflected impedance corresponds to the load, all of the power received at the secondary coil will be dissipated in the load. Therefore the efficiency in the ideal case is 100 %. It can be noted that although the secondary coil might be operating at resonance, its total reflected impedance contains a reactive part. Therefore, in order to operate the complete system at resonance, an external reactive element should be included at the primary coil circuitry to compensate for the reactive part of the total reflected impedance and the reactance of the primary coil.

B. Non-ideal coil with parasitic capacitance

A second case can be considered to represent a practical non-ideal coil. The coil in this case is modelled as an inductor and its ESR, in addition to a parallel capacitor which represents the parasitic capacitance of the coil due to its windings. Fig. 3.15 shows the circuit representation for this case. The total reflected impedance is given by

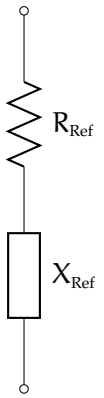

Fig. 3.14: The components of the total reflected impedance for the ideal case

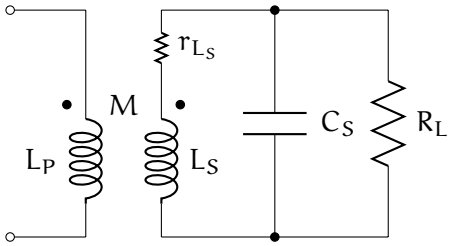

Fig. 3.15: Circuit representation for a non ideal secondary coil

$$Z_{Ref} = \frac{X_M^2}{r_{L_S} + jX_{L_S} - \dfrac{jX_{C_S}R_L}{R_L - jX_C}} = \frac{X_M^2(R_L - jX_{C_S})}{R_L r_{L_S} - jX_{C_S}r_{L_S} + jX_{L_S}R_L + X_{L_S}X_{C_S} - jX_{C_S}R_L}. \tag{3.50}$$

If $X_{C_S} = X_{L_S}$ then the total reflected impedance is now equal to

$$\begin{aligned} Z_{Ref} = \frac{X_M^2(R_L - jX_{C_S})}{R_L r_{L_S} + X_{C_S}^2 - jX_{C_S}r_{L_S}} &= \frac{X_M^2(R_L - jX_{C_S})(R_L r_{L_S} + X_{C_S}^2 + jX_{C_S}r_{L_S})}{(R_L r_{L_S} + X_{C_S}^2)^2 + X_{C_S}^2 r_{L_S}^2} \\ &= \frac{X_M^2(R_L r_{L_S} + X_{C_S}^2 + jX_{C_S}r_{L_S})(R_L - jX_{C_S})}{X_{C_S}^4 + X_{C_S}^2(2R_L r_{L_S} + r_{L_S}^2) + R_L^2 r_{L_S}^2}. \end{aligned} \tag{3.51}$$

Taking the real part of the total reflected impedance gives

$$\text{real}\{Z_{Ref}\} = \frac{X_M^2(X_{C_S}^2 R_L + R_L^2 r_{L_S} + X_{C_S}^2 r_{L_S})}{X_{C_S}^4 + X_{C_S}^2(2R_L r_{L_S} + r_{L_S}^2) + R_L^2 r_{L_S}^2}. \tag{3.52}$$

The real part of the total reflected impedance can be represented as the sum of two resistances; R_{Ref} and r_{Ref} to represent the reflected resistances of the load and ESR of the coil respectively. Resistances R_{Ref} and r_{Ref} are given by

$$R_{Ref} = \frac{X_M^2 X_{C_S}^2 R_L}{X_{C_S}^4 + X_{C_S}^2(2R_L r_{L_S} + r_{L_S}^2) + R_L^2 r_{L_S}^2} \tag{3.53}$$

$$r_{Ref} = \frac{X_M^2 r_{L_S}(R_L^2 + X_{C_S}^2)}{X_{C_S}^4 + X_{C_S}^2(2R_L r_{L_S} + r_{L_S}^2) + R_L^2 r_{L_S}^2}. \tag{3.54}$$

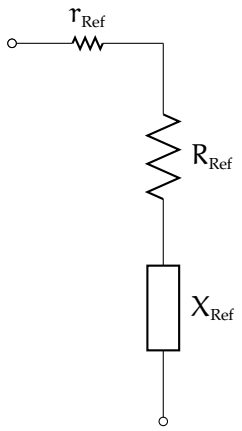

Fig. 3.16: The components of the total reflected impedance for a non-ideal coil operating at its resonant frequency

Taking the imaginary part of the total reflected impedance gives

$$X_{Ref} = \text{imag}\{Z_{Ref}\} = -\frac{X_M^2 X_{Cs}^3}{X_{Cs}^4 + X_{Cs}^2(2R_L r_{Ls} + r_{Ls}^2) + R_L^2 r_{Ls}^2}. \tag{3.55}$$

Reactance X_{Ref} can be referred to as the reflected reactance of the mutual inductance and the parasitic parallel capacitor. Consequently, the total reflected impedance can be represented as shown in Fig. 3.16. Since the real part of the total reflected impedance now consists of two resistances, the power received at the secondary coil will be shared amongst them. Therefore the efficiency for this case is given by

$$\eta = \frac{R_{Ref}}{R_{Ref} + r_{Ref}} \tag{3.56}$$

C. Non-ideal coil with an external parallel capacitor

The resonant frequency of a non-ideal coil is determined by its self inductance and its parasitic capacitance. It may be practically difficult to design a coil to have a specific resonant frequency. Instead, an external capacitor is often used to set the resonant frequency of the coil to a certain value as described in Sec. 3.3. Fig. 3.17 shows the circuit representation for this case. Resistor r_{Cs} represents the ESR of the external capacitor. The value of the parasitic capacitance of coil is assumed to much smaller than that of the external capacitor, therefore it can be omitted. The total reflected impedance is given by

$$\begin{aligned} Z_{Ref} &= \frac{X_M^2}{r_{Ls} + jX_{Ls} + \dfrac{R_L(r_{Cs} - jX_{Cs})}{R_L + r_{Cs} - jX_{Cs}}} \\ &= \frac{X_M^2(R_L + r_{Cs} - jX_{Cs})}{r_{Ls}R_L + r_{Ls}r_{Cs} - jX_{Cs}r_{Ls} + jX_{Ls}R_L + jX_{Ls}r_{Cs} + X_{Ls}X_{Cs} + R_L - jX_{Cs}R_L}. \end{aligned} \tag{3.57}$$

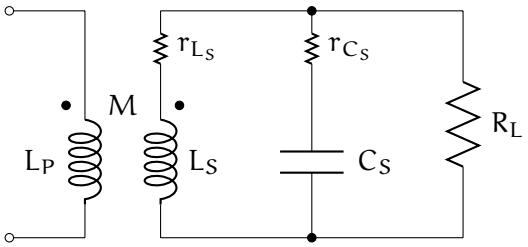

Fig. 3.17: A parallel resonant secondary with non ideal components

If $X_{C_S} = X_{L_S}$ then the total reflected impedance is now equal to

$$Z_{Ref} = \frac{X_M^2(R_L + r_{C_S} - jX_{C_S})}{a + jb} \tag{3.58}$$

where

$$a = R_L(r_{L_S} + r_{C_S}) + r_{L_S}r_{C_S} + X_{L_S}X_{C_S} \tag{3.59}$$

$$b = R_L(X_{L_S} - X_{C_S}) + X_{L_S}r_{C_S} - X_{C_S}r_{L_S}. \tag{3.60}$$

Equation 3.58 can be rewritten as

$$\begin{aligned} Z_{Ref} &= \frac{X_M^2(R_L + r_{C_S} - jX_{C_S})(a - jb)}{a^2 + b^2} \\ &= \frac{X_M^2\,(R_L a + r_{L_S} a - jX_{C_S} a - jR_L b - jr_{C_S} b - X_{C_S} b)}{a^2 + b^2}. \end{aligned} \tag{3.61}$$

Taking the real part of the total reflected impedance gives

$$\text{real}\{Z_{Ref}\} = \frac{X_M^2\,(R_L a + r_{L_S} a - X_{C_S} b)}{a^2 + b^2}. \tag{3.62}$$

The real part of the total reflected impedance can be represented as the sum of two resistances; R_{Ref} and r_{Ref}. Resistances R_{Ref} represents the reflected resistance of the load and resistance r_{Ref} represents the reflected resistance of the ESRs of the coil and the external capacitor. Resistances R_{Ref} and r_{Ref} are given by

$$R_{Ref} = \frac{X_M^2 X_{C_S}^2 R_L}{a^2 + b^2} \tag{3.63}$$

$$r_{Ref} = \frac{X_M^2(R_L^2(r_{L_S} + r_{C_S}) + 2R_L r_{L_S} r_{C_S} + R_L r_{C_S}^2 + r_{L_S} r_{C_S}^2 + X_{C_S}^2 r_{L_S})}{a^2 + b^2}. \tag{3.64}$$

Taking the imaginary part of the total reflected impedance gives

$$\text{imag}\{Z_{Ref}\} = \frac{X_M^2\,(-X_{C_S} a - R_L b - r_{C_S} b - X_{C_S} b)}{a^2 + b^2}. \tag{3.65}$$

The imaginary part of the total reflected impedance can be represented as the sum of two reactances; X_{Ref} and x_{Ref}. Reactance X_{Ref} represents the reflected reactance of the mutual inductance, the secondary coil and the external capacitor. Reactance x_{Ref}

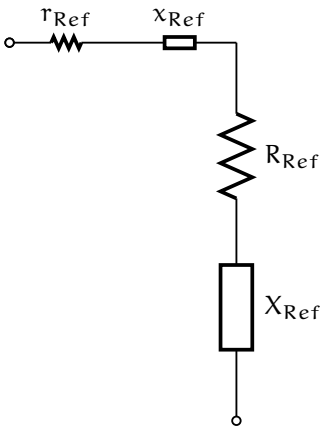

Fig. 3.18: The components of the total reflected impedance for a non-ideal coil with an external capacitor

represents the reflected reactance of the ESRs of the coil and the external capacitor. Reactances R_{Ref} and r_{Ref} are given by

$$X_{Ref} = \frac{X_M^2(R_L^2(X_{C_S} - X_{L_S}) - X_{L_S}X_{C_S}^2)}{a^2 + b^2} \tag{3.66}$$

$$x_{Ref} = \frac{X_M^2(2X_{C_S}R_L r_{C_S} - X_{L_S}r_{C_S}^2)}{a^2 + b^2} \tag{3.67}$$

Consequently, the total reflected impedance can represented as shown in Fig. 3.18. Therefore the efficiency for this case is given by

$$\eta = \frac{R_{Ref}}{R_{Ref} + r_{Ref}} \tag{3.68}$$

3.4.3 *Load and Frequency Variation Effects On The Reflected Impedances*

This section shows the effect of varying the load and the frequency on the total reflected impedance based on an implemented inductive link. The primary coil consists of two layers each having four turns of 18 AWG magnet wire and a diameter of 8 cm. The secondary coil consists of a single layer of four turns of 20 AWG magnet wire with a diameter of 7 cm. The measured inductance and ESR of both coils are plotted in Fig. 3.19. The measured mutual inductances and the calculated coupling coefficients as a function of the separation distance and frequency are plotted in Fig. 3.20. Both self and mutual inductance measurements were taken using a PSM1700 PsimetriQ phase sensitive multimeter. The dimensions of the designed coils were chosen to achieve a higher coupling coefficient at large separation distances. This allows power to be transferred efficiently and therefore the operation of an IPT system can be validated at a wide operation range. In addition, the measurement error of the separation distance is reduced as the coils are moved further or closer apart. Using Eqs. 3.63-3.67,

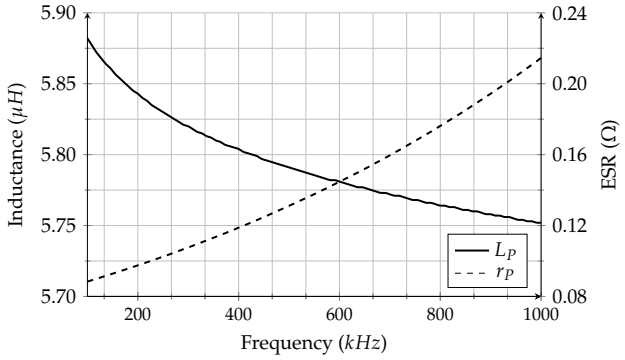

(a) primary coil

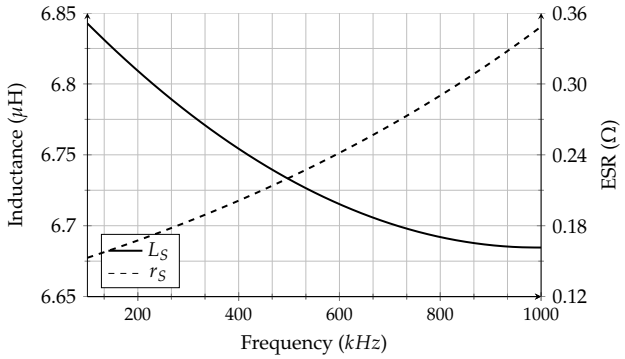

(b) secondary coil

Fig. 3.19: Measured self inductances and ESR of the primary and secondary coils (10kHz steps)

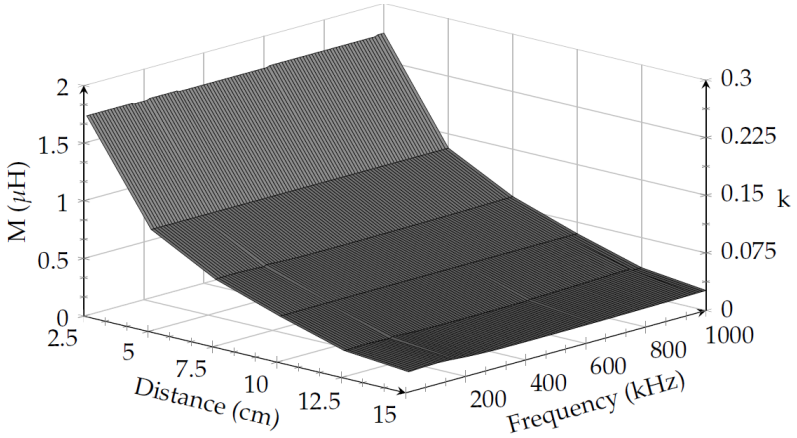

Fig. 3.20: Measured mutual inductance (2.5cm & 10kHz steps)

the values of resistances R_{Ref} and r_{Ref} are calculated as the load resistance R_L and the frequency are swept from 0 Ω to 2 kΩ and 100 kHz to 1 MHz respectively. Fig. 3.21 shows the calculated reflected resistances of the load and ESRs as a function of the load and resonant frequency. The resonant capacitor's ESR and reactance are set to be equal to the inductor's ESR and reactance respectively for each frequency according to the following equation

$$C_s = \frac{1}{\omega^2 L_S} = \frac{1}{(2\pi)^2 f^2 L_S}. \tag{3.69}$$

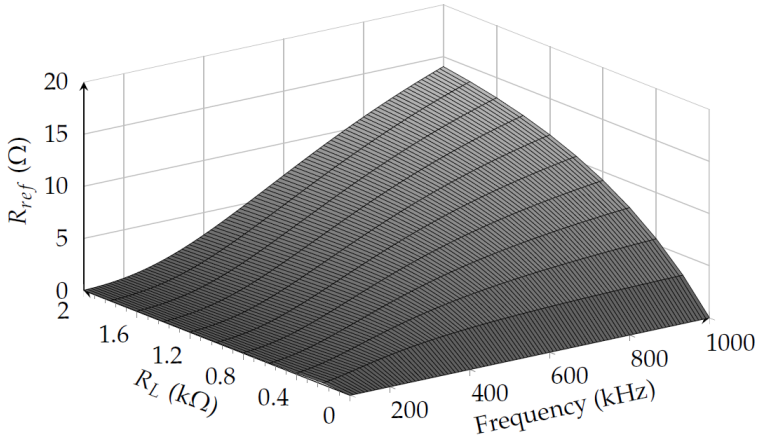

(a) R_{Ref}

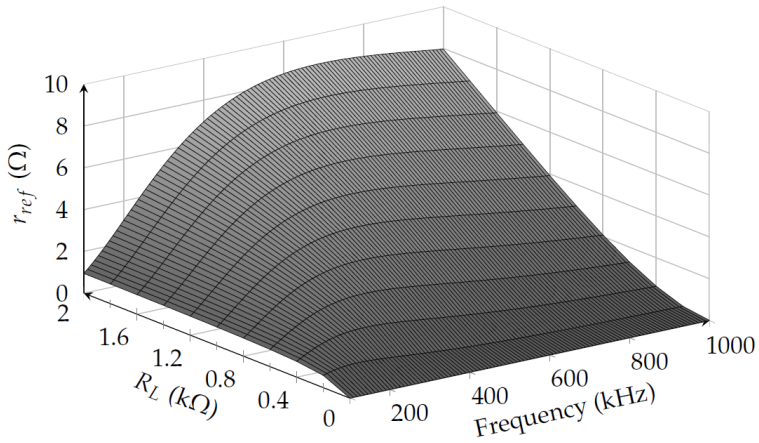

(b) r_{Ref}

Fig. 3.21: The calculated reflected resistance R_{Ref} & r_{Ref} as a function of load resistance and resonant frequency

It can be noticed from Fig. 3.21 that at low load values, or a higher load resistance, and high resonant frequencies, R_{Ref} is larger than r_{Ref} and most of the power that is received in the secondary coil will be dissipated in the load. As the load and resonant frequency decrease, r_{Ref} has a more significant value and a large portion of the power received in the secondary coil will be dissipated as heat in the ESRs of the coil and the parallel capacitor. The maximum difference between R_{Ref} and r_{Ref} corresponds to the maximum power efficiency of the secondary coil side. Consequently, it can be concluded that power can be transferred at higher efficiencies and large separation distances at low load values and high resonant frequencies. However, due to practical limitations, the maximum frequency that can be used is limited by the losses in the MOSFET gate driving circuitry and the switching losses in the primary coil driver. Fig. 3.22a shows the total values of the calculated reflected impedances R_{Ref} and r_{Ref} based on Eqs. 3.63 & 3.64 when the operating frequency shifts from the resonant frequency of the secondary coil. The measured total reflected impedances is plotted in Fig. 3.22b for comparison. It is assumed that the resonant frequency is fixed at 800

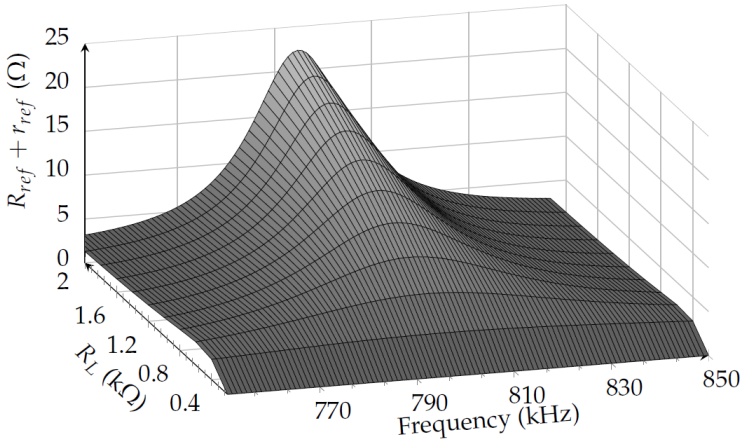

(a) The calculated total reflected impedances

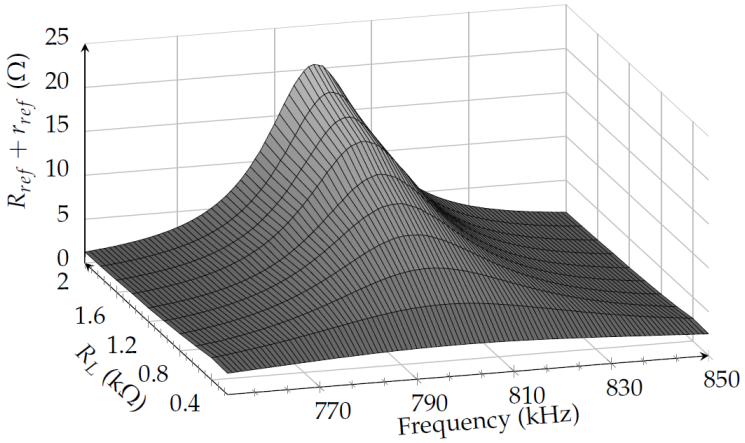

(b) The measured total reflected impedances (200 Ω and 10 kHz steps)

Fig. 3.22: The total reflected impedance for a fixed resonant frequency of 800 kHz as a function of frequency and load resistance

kHz and the distance between the coils is 5 cm corresponding to a coupling coefficient of 0.11. The calculated total reflected impedances values are in good agreement with those measured.

3.5 CONCLUSIONS

This chapter discussed the principle of operation of inductive links from a circuit point of view. The reflected impedance concept was introduced as a circuit analysis method to represent the secondary coil circuit by an equivalent impedance as seen by the power source. It was shown that by using resonance, the reflected impedance of the secondary coil circuitry is maximised. This allows for power to be transferred efficiently especially at higher separation distances.

The parallel resonant secondary configuration was analysed in further details. The reflected impedance was calculated for several configurations based on the non-ideal characteristics of the coil. The reflected impedance was then divided into several components each representing the reflected impedance of a certain element in the secondary coil circuitry. This simplifies the process of determining the amount of power each element receives from the total power received at the secondary coil. Finally, the effect of varying the load and frequency on the reflected impedances was presented based on an implemented inductive link.

4

RESONANT DC/AC INVERTERS

4.1 INTRODUCTION

The current flowing in the primary coil of an inductive link has to be alternating in order to generate an alternating magnetic field to induce a voltage in the secondary coil. Producing an AC current from a DC voltage requires the use of a DC/AC inverter. Inductive links may require large amounts of power to be delivered at high efficiencies. Therefore, certain types and classes of switched-mode DC/AC inverters can only meet this requirement.

Inductive links are generally operated at resonance or near resonance, therefore the driving current of the primary coil has to be sinusoidal. Creating a DC/AC inverter with a sinusoidal output current requires the use of passive networks consisting of capacitors and inductors. The switching frequency of the switching elements of a DC/AC inverter is chosen to be equal to or a harmonic of the resonant frequency of these passive networks. The switches role is to 'chop' the DC supply voltage or current to create a square wave power signal. The square wave signal is applied to the passive networks which then filters out all its frequency components except those that match the resonant frequency of the passive network. DC/AC inverters that utilise passive resonant networks are referred to as resonant inverters. Since these resonant inverters are also switched-mode circuits, they can achieve various zero-voltage and zero-current switching conditions by carefully choosing the values of the passive networks' components, the switching frequency and its duty cycle. Resonant DC/AC inverters can have a theoretical efficiency of 100 %, although practically this may not be achieved due to the nonidealities in the switches and the ohmic losses of the passive components. A typical efficiency range for resonant inverters is between 85-95 %.

Extensive research is devoted to developing efficient resonant DC/AC inverters and numerous circuits can be found in literature. All of these inverters have been classi-

fied into classes depending on the switching conditions of the voltages and currents developed across the switching devices. Most of the inverters that have been used for inductive links fall under two main classes;Class D and Class E. In this chapter, an overview of Class D inverters will be given that will briefly describe their principle of operation and show the different circuit configuration that fall under this class. An extensive review and analysis of Class E inverters is then followed that will cover their principle of operation, different circuit configurations and performance analysis. Other classes of DC/AC inverters will be discussed briefly towards the end of the chapter. The chapter ends with a summary and comparison of the presented classes and their circuit configurations.

4.2 DEFINITIONS

The following definitions are associated with the modelling and analysis of the inverters that will be presented in this chapter

- Switching Frequency ω
  The switching frequency refers to the frequency at which the switches are turned ON and OFF. It can be either supplied from an external signal source such as a function generator, or generated using an oscillator. Since the switching signal is the main driving or 'forcing' signal of the converter, the fundamental frequency components of all other voltage and current signals in the converter will be equal to it.

- Resonant frequency ω_o
  In order to create resonance, the load network of an inverter should consists of at least one capacitor and one inductor. Therefore the resonant frequency of the inverter is given by

$$\omega_o = \frac{1}{\sqrt{LC}} \tag{4.1}$$

  for a series RLC network and

$$\omega_o = \sqrt{\frac{1}{LC} - \frac{1}{C^2R^2}} \tag{4.2}$$

  for a parallel RLC network. The switching frequency does not necessarily has to be equal to the resonant frequency. Different modes of operation can be obtained by operating the inverter at switching frequencies above, below and equal to the resonant frequency.

- Characteristic Impedance Z_o
  The characteristic impedance of the inverter's resonant network is given by

$$Z_o = \sqrt{\frac{L}{C}} = \omega L = \frac{1}{\omega C}. \tag{4.3}$$

- Loaded Quality Factor Q_L
  The loaded quality factor is defined as the ratio of the maximum energy stored in the resonant network to the amount of energy dissipated in the load R_L per one cycle of the switching frequency of the inverter. The loaded quality factor in inverters is used to indicate how close is the voltage or current in the load network to an ideal sinusoidal signal. Theoretically, an infinite loaded quality factor will only result in an ideal sinusoidal signal. However, a minimum value of approximately 10 is generally assumed to be high enough to result in a sinusoidal signal with less than 1 % of distortion. The loaded quality is given by

$$Q_L = \frac{\omega_s L}{R_L} \tag{4.4}$$

  for a series RLC network and

$$Q_L = \frac{R_L}{\omega_s L} \tag{4.5}$$

  for a parallel RLC network.

- Power-Output Capability c_p
  The power-output capability in DC/AC inverters can be defined as the ratio of the output power produced when the peak voltage and the peak current of the inverter's switches is 1 V and 1 A respectively to the number of switches of the inverter. The power-output capability is given by

$$c_p = \frac{P_o}{N V_{DSMAX} I_{DSMAX}} \tag{4.6}$$

  where P_o is the output power, V_{DSMAX} is peak voltage across the inverter's switches, I_{DSMAX} is the peak current in the inverter's switches and N is the number of switches used in the inverter. The power-output capability of an inverter can be used as an indication of cost. For a given output power, an inverter with a low power-output capability requires switches with high voltage and current ratings, whereas an inverter with a high power-output capability may require switches with lower voltage and current ratings. Therefore the higher the power-output capability of and inverter, the lower the implementation cost and vice versa.

4.3 CLASS D INVERTERS

The Class D resonant inverter [58, 59] is probably the first option that an engineer would opt for when designing a DC/AC inverter. It is one of the most widely used classes in DC/AC inverters thanks to its simple principle of operation, high power efficiency and wide operating range. Therefore, it has been extensively used as the primary coil driver in inductive links [32, 53, 60–67]. Class D inverters consist of a pair or more of switches operating in a complementary manner and a passive resonant network. Class D resonant inverters can only achieve either ZVS or ZCS and therefore can be further classified into the following two groups [68]:

- Voltage-Fed Class D ZVS Resonant Inverters
  The inverters in this category are powered directly from a DC voltage supply and employ a series resonant network. The switching action of the switches converts the DC voltage voltage into a series of voltage pulses which then are filtered by the resonant network to produce a sinusoidal output. Since a series resonant network is used, the output of the inverter is a sinusoidal voltage. Hence, the inverters in this group can be represented as an AC voltage source.

- Current-Fed Class D ZCS Resonant Inverters
  The inverters in this category are powered directly from a DC current supply and employ a parallel resonant network. The switching action of the switches converts the DC current supply into a series of current pulses which then are filtered by the resonant network to produce a sinusoidal output. Since a parallel resonant network is used, the output of the inverter is a sinusoidal current. Hence, the inverters in this group can be represented as an AC current source.

4.3.1 *Half-Bridge Class D ZVS Inverter*

Fig. 4.1a shows the basic circuit of a half-bridge Class D ZVS inverter in its simplest form. The circuit consists of two switches Q_1 and Q_2, inductor L and capacitor C form a resonant series network and the resistor R_L represents the load resistance. The switches are driven in a complementary manner at a switching frequency and generally at a duty cycle ratio of 0.5. The output current is sinusoidal provided that the loaded quality factor of the series resonant circuit is large at the switching frequency. Although a single inductor and capacitor are shown, other network configurations can be obtained by using multiple passive components. The main advantage of this configuration is that the maximum voltage developed across the switches is equal to the

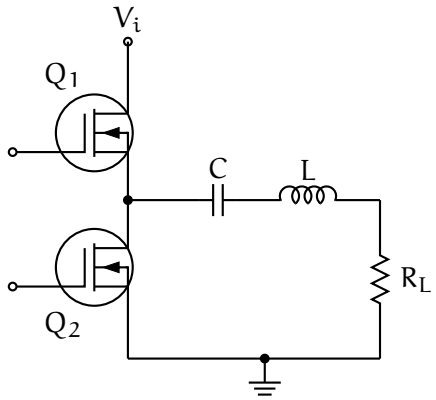

Fig. 4.1: The half-bridge Class D ZVS inverter

DC supply voltage (V_i). This allows the inverter to operate at high DC voltages such as 170 V and 310 V which are obtained by rectifying the mains AC supply [68].

The basic circuit configuration in Fig. 4.1 is widely used in numerous applications other than IPT such as audio amplifiers and electronic ballasts. Due to its popularity, many researchers and engineers refer to this configuration when mentioning the Class D inverter. Therefore, the description and analysis of this configuration will be considered in this section.

A. Analysis

The analysis begins with the assumption that the loaded quality factor of the series load network is high enough such that current in it sinusoidal, and the switching frequency has 50 % duty cycle ratio. The load network's current can be represented as

$$I_o(\omega t) = i_m \sin(\omega t - \phi) \tag{4.7}$$

where i_m is the amplitude of the output current and ϕ is the phase of the output current relative to the switching signal which is equal to the impedance angle of the load network.

The switching action of switches Q_1 and Q_2 presents a voltage square wave signal to the series load signal that alternates between V_i and zero at a frequency equal to the switching frequency. Fig. 4.2 shows the equivalent circuit of the Class D inverter which can be used to continue with the analysis. The input voltage to the load network is

$$V_n(\omega t) = V_{DS2}(\omega t) = \begin{cases} V_i, & \text{for } 0 \leqslant \omega t < \pi \\ 0, & \text{for } \pi \leqslant \omega t < 2\pi \end{cases}. \tag{4.8}$$

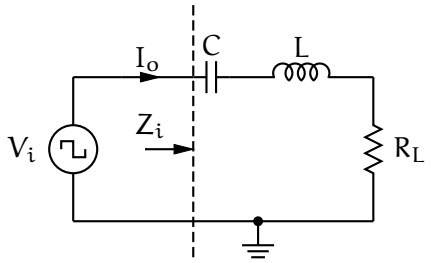

Fig. 4.2: Equivalent circuit of the Class D ZVS inverter

Hence, the maximum voltage across both switches is equal to V_i. The general method to analysing such circuits is to use the Fourier series. Therefore, the input voltage to the load network can be represented by its Fourier components

$$V_n(\omega t) = V_i \left(\frac{1}{2} + \frac{2}{\pi} \sum_{n=1}^{\infty} \frac{\sin\left((2n-1)\omega t\right)}{2n-1} \right). \tag{4.9}$$

The fundamental component of the input voltage to the load network is

$$V_{n1}(\omega t) = v_m \sin \omega t \tag{4.10}$$

where

$$v_m = \frac{2V_i}{\pi} \approx 0.6366 V_i. \tag{4.11}$$

Based on the assumption that the current in the load network is sinusoidal, the input impedance of the load network at a certain switching frequency is

$$Z_i = R_L + j\omega L + \frac{1}{j\omega C} = R\left[1 + jQ_L\left(\frac{\omega}{\omega_o} - \frac{\omega_o}{\omega}\right)\right] \tag{4.12}$$

$$= Z_o\left[\frac{R}{Z_o} + j\left(\frac{\omega}{\omega_o} - \frac{\omega_o}{\omega}\right)\right]. \tag{4.13}$$

The input impedance can be expressed as a phaser

$$Z_i = z_m \angle \phi \tag{4.14}$$

where

$$z_m = |Z_i| = Z_o\sqrt{\left(\frac{R_L}{Z_o}\right)^2 + \left(\frac{\omega}{\omega_o} - \frac{\omega_o}{\omega}\right)^2} = Z_o\sqrt{\frac{1}{Q_L^2} + \left(\frac{\omega}{\omega_o} - \frac{\omega_o}{\omega}\right)^2} \tag{4.15}$$

and

$$\phi = \tan^{-1}\left[Q_L\left(\frac{\omega}{\omega_o}\right) - \left(\frac{\omega_o}{\omega}\right)\right]. \tag{4.16}$$

Consequently, the magnitude of the current in the load network at a certain switching frequency is

$$i_m = \frac{v_m}{z_m} \tag{4.17}$$

and the output voltage across the load is

$$V_{R_L}(\omega t) = I_o R_L = i_m R_L \sin(\omega t - \phi). \tag{4.18}$$

The currents in switches Q_1 and Q_2 are

$$I_{DS1}(\omega t) = \begin{cases} i_m \sin(\omega t - \phi), & \text{for } 0 \leqslant \omega t < \pi \\ 0, & \text{for } \pi \leqslant \omega t < 2\pi \end{cases} \tag{4.19}$$

and

$$I_{DS2}(\omega t) = \begin{cases} 0, & \text{for } 0 \leqslant \omega t < \pi \\ -i_m \sin(\omega t - \phi), & \text{for } \pi \leqslant \omega t < 2\pi \end{cases}. \tag{4.20}$$

respectively. Hence, the maximum value of the currents in both switches is equal to i_m.

The DC input current I_i of the inverter is equal to average value of the current in switch Q_1, i.e.

$$\begin{aligned} I_i &= \frac{1}{2\pi}\int_0^{2\pi} I_{DS1}(\omega t)d\omega t = \frac{i_m}{2\pi}\int_0^{\pi} \sin(\omega t - \phi)d\omega t \\ &= \frac{2V_i \cos^2\phi}{\pi^2 R_L} = \frac{2V_i R_L}{\pi^2 z_m^2} = \frac{i_m}{\pi\sqrt{1 + Q_L^2\left(\frac{\omega}{\omega_o} - \frac{\omega_o}{\omega}\right)^2}}. \end{aligned} \tag{4.21}$$

For an ideal Class D inverter the output power is equal to the input power

$$P_o = P_i = V_i I_i = \frac{2V_i^2 R_L}{\pi^2 z_m}. \tag{4.22}$$

If the inverter is operating at a switching frequency equal to the resonant frequency, the output power is given by

$$P_o = P_i = \frac{2V_i^2 R_L}{\pi^2 R_L^2} \approx 0.2026\frac{V_i^2}{R_L}. \tag{4.23}$$

The maximum current in the switches is

$$I_{DSMAX} = i_m = \frac{4V_i}{\pi R_L} \tag{4.24}$$

and the output-power capability is given by

$$c_p = \frac{P_o}{2V_{DSMAX} I_{DSMAX}} = \frac{V_i I_i}{2V_{DSMAX} I_{DSMAX}} = \frac{1}{2\pi} \approx 0.1592 \tag{4.25}$$

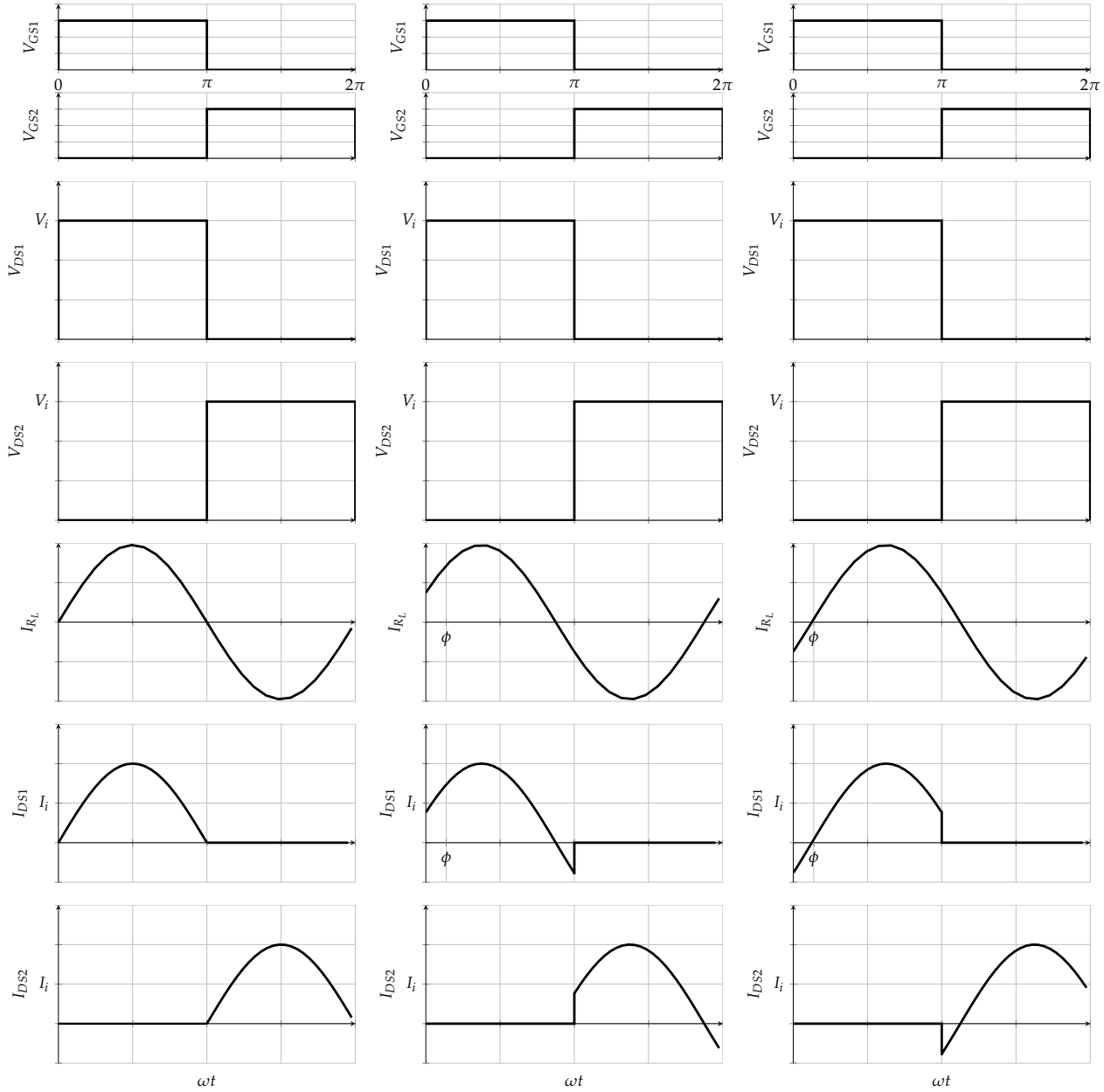

(a) Operation at $f_s = f_o$ (b) Operation at $f_s < f_o$ (c) Operation at $f_s > f_o$

Fig. 4.3: Voltage and current waveforms of the basic Class D ZVS inverter for different switching frequencies

B. Modes of operation

Fig. 4.3 shows the voltage and current waveforms associated with basic half-bridge Class D ZVS inverter. The Class D inverter can operate at three modes; at resonance, below resonance and above resonance depending on the switching frequency:

- Operation at resonance

The Class D inverter operates at resonance when the switching frequency is equal to the resonant frequency of the load network. Fig. 4.3a shows the voltage and cur-

rent waveforms associated with this mode of operation. The current I_o in the load network is in phase with the fundamental voltage component of the load network, therefore $\phi = 0$. The series resonant circuit can be considered as a resistive load.

The Class D inverter in this mode has theoretical efficiency of 100 % since the switches are turned ON and OFF at zero voltages and zero currents. Practical implementation can achieve efficiencies exceeding 90 % since the losses due to switching are minimised and the losses due to the reverse-recovery effect of the body diodes of the switches are not existent.

- Operation below resonance

The Class D inverter operates below resonance when the switching frequency is less than the resonant frequency of the load network. Fig. 4.3b shows the voltage and current waveforms associated with this mode of operation. The current I_o in the load network leads the fundamental voltage component of the load network by a certain phase ϕ. The series resonant circuit can be considered as a capacitive load.

In this mode, the Class D inverter will have a theoretical operating efficiency of 100 % since the switches are turned ON and OFF at zero voltages. However, the practical limitations of the switches can prevent from achieving high efficiencies. This is mainly due to the switching delay times of the switches and the reverse-recovery effect of their body diode [58, 60] (assuming MOSFET switches). Referring to Fig. 4.3b, consider the case when Q_1 is ON and Q_2 is OFF. The current in Q_1 is negative at the end of its ON period. Due to the turn-OFF time of Q_1 and its gate driving circuitry, the current will be directed to its body diode. As Q_2 begins to turn ON, current is diverted from the body diode of Q_1 to the drain of Q_2. Once the current of the body diode of Q_1 reaches zero, the reverse-recovery effect takes place causing current to flow from the voltage source through the body diode of Q_1 and the drain channel of Q_2. Therefore, for a short period time, the voltage supply is shorted to ground which leads to a large current spike to flow through both switches. The current spike can be many times larger than the maximum current ratings of the switches resulting in excessive losses and eventually failure. Therefore for this reason, the operation of Class D inverters below their resonant frequency is not recommended.

- Operation above resonance

The Class D inverter operates above resonance when the switching frequency is higher than the resonant frequency of the load network. Fig. 4.3c shows the voltage and current waveforms associated with this mode of operation. The current I_o in the load network lags the fundamental voltage component of the load network by a certain phase ϕ. The series resonant circuit can be considered as a inductive load.

Similarly to the previous operation modes, the Class D inverter will have a theoretical operating efficiency of 100 % since the switches are turned ON and OFF at zero voltages. The practical limitations of the switches, mainly the reverse-recovery effect of the body diode, are minimised in this mode. Therefore Class D inverter can achieve efficiencies exceeding 90 % in this mode. Referring to Fig. 4.3c, consider the case when Q_1 is ON and Q_2 is OFF. The current in Q_1 is positive at the end of its ON period. As Q_1 begins to turn OFF, current will diverted to the body diode of Q_2 and eventually to the drain channel of Q_2 as Q_2 switches ON. The voltage source is not shorted to ground in this period provided that there is a certain dead-time between the gating driving signals of Q_1 and Q_2. As a result, no current spikes occur in Q_1 and Q_2 and therefore efficient operation can be achieved. The only losses in this mode are the turn OFF losses of the switches and conduction losses in their body diodes, however they are insignificant [58].

4.3.2 *Class D Push-pull ZVS Inverter*

Another popular implementation of the Class D inverter is to use dual voltage sources; one positive and one negative. In the basic configuration analysed in the previous section, the voltage applied to the load network had a peak-to-peak value of V_i. Output power can be increased by using a second voltage supply as shown in Fig. 4.4a to cause the voltage applied to the load network to swing between the two voltage supplies and thus having a peak-to-peak value of $2V_i$. The positive and negative voltage sources can be either supplied using two independent sources or using a centre tapped transformer as shown in Fig. 4.4b. The analysis of this configuration is similar to that of the basic configuration in the previous section. Referring to Fig. 4.4, the loaded quality factor of the load network is assumed to be large enough such that its current is sinusoidal as given in Eq. 4.7 and the impedance of the load network is given in Eqs. 4.14-4.16. The input voltage to the load network for this configuration is

$$V_n(\omega t) = \begin{cases} V_i, & \text{for } 0 \leqslant \omega t < \pi \\ -V_i, & \text{for } \pi \leqslant \omega t < 2\pi \end{cases}. \tag{4.26}$$

Hence, the maximum voltage across both switches is equal to $2V_i$. The magnitude of the fundamental component of the input voltage is given by

$$V_m = \frac{4}{\pi} V_i \approx 1.2732 V_i. \tag{4.27}$$

The magnitude of the load network's current i_m can calculated using Eq. 4.17 and the current in the switches is given in Eqs. 4.19-4.20. The DC input current supplied from the positive voltage source is

$$I_{i+} = \frac{1}{2\pi}\int_0^{2\pi} I_{DS1}(\omega t)d\omega t = \frac{4V_i R_L}{\pi^2 z_m^2} \tag{4.28}$$

and the DC input current supplied from the negative voltage source is

$$I_{i-} = \frac{1}{2\pi}\int_0^{2\pi} I_{DS2}(\omega t)d\omega t = \frac{-4V_i R_L}{\pi^2 z_m^2}. \tag{4.29}$$

Therefore the total power delivered to the load is

$$P_o = V_i I_{i+} - V_i I_{i-} = 2V_i I_{i+} = \frac{8V_i^2 R_L}{\pi^2 z_m^2} \tag{4.30}$$

which is four times more than the total power delivered to load in the basic configuration.

This configuration can be operated at several modes based on the switching frequency as discussed in the basic configuration previously. If the inverter is operating at a switching frequency equal to the resonant frequency, the output power is given by

$$P_o = P_i = \frac{8V_i^2 R_L}{\pi^2 R_L^2} \approx 0.8106\frac{V_i}{R_L}. \tag{4.31}$$

The maximum current in the switches is

$$I_{DSMAX} = i_m = \frac{2V_i}{\pi R_L} \tag{4.32}$$

and the output-power capability is given by

$$c_p = \frac{P_o}{2V_{DSMAX}I_{DSMAX}} = \frac{V_i I_i}{2V_{DSMAX}I_{DSMAX}} = \frac{1}{2\pi} \approx 0.1592 \tag{4.33}$$

4.3.3 *H-Bridge Class D ZVS Inverter*

The H-bridge Class D ZVS inverter is another configuration of the Class D inverter. Two more switches are added as shown in Fig. 4.5 forming two pairs of switches; Q_1-Q_4 and Q_2-Q_3, that are driven in a complementary manner. The operation principle remains the same to that of the basic half-bridge configuration. The H-bridge Class D inverter delivers the same amount of power to the load as the push-pull Class D inverter, however it eliminates the need to use two supplies or a centre-tapped transformer. The analysis of this configuration is the exactly the same as that of the

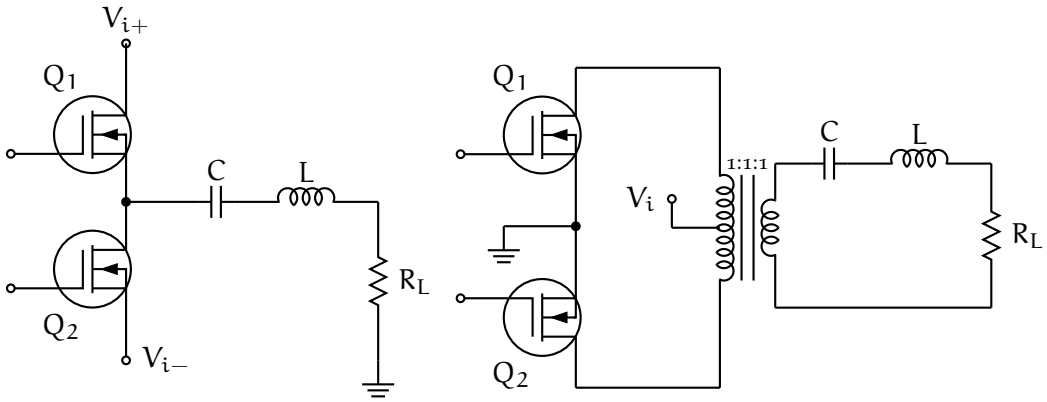

(a) with a positive and negative voltage source

(b) transformer-coupled

Fig. 4.4: The Class D push-pull ZVS inverter

dual supply Class D inverter described previously with exception that the maximum voltage across the switches is V_i. The H-bridge configuration is widely used in recent inductive links that operate at power levels exceeding 1 kW [32, 62, 64, 65].

The addition of the two switches allows for more control methods to regulate the performance and operation of this configuration. A widely used control method to adjust the output power is phase control where the four gate driving signals to the switches are shifted by a certain phase from each other. This alters the input voltage to the load network and therefore varying the power delivered to the load. More details about phase shift control can be found in [58].

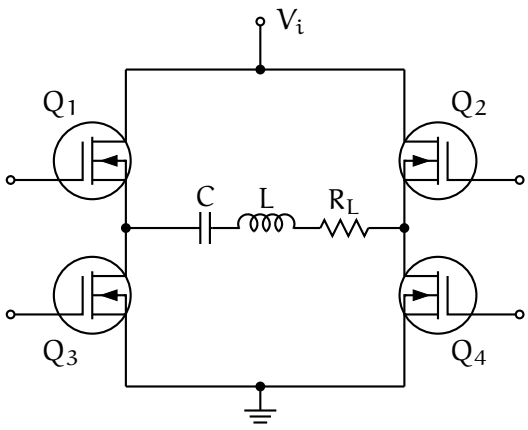

Fig. 4.5: The H-Bridge Class D ZVS inverter

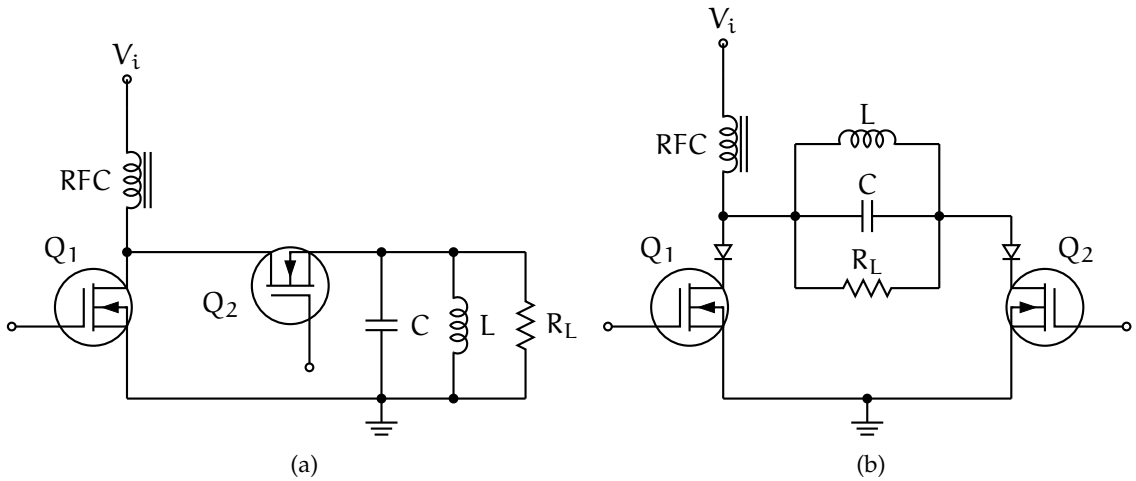

Fig. 4.6: The basic Class D ZCS inverter

4.3.4 *Class D ZCS Inverter*

The Class D configurations discussed previously were all fed by a voltage source. It is also possible to feed the Class D inverter a current source by using a choke (RFC) after the voltage supply. In this way, ZCS will be achieved instead of ZVS. Fig. 4.6a shows a basic configuration of the Class D ZCS inverter first introduced in [69]. Although this particular circuit configuration is seldom used since it can be practically difficult to drive switch Q_2 because its source terminal is neither grounded nor connected to the drain of Q_1, therefore a pulse transformer or an opto-isolator is required. Fig. 4.6b shows the same configuration but now the source terminal of switch Q_2 is grounded. This eliminates any driving issues but additional diodes are required to be connected in series with both switches to avoid their body diodes from conducting. The principle of operation of the Class D ZCS inverter is very similar to that of their ZVS counterparts. The Class D ZCS inverter presents a current square wave signal to a parallel load network that alternates between I_i and zero at a frequency equal to the switching frequency and a duty cycle ratio of 0.50. For further simplification, the analysis will only consider the mode of operation when the switching frequency is equal to the resonant frequency of the load network. Fig. 4.7 shows the equivalent circuit of this configuration. The loaded quality factor of the parallel network is assumed to be high enough such that the current in the load resistance is sinusoidal. The load resistance's current can be represented as:

$$I_{R_L}(\omega t) = i_m \sin \omega t, \quad \omega = \omega_o. \tag{4.34}$$

The input current to the load network is

$$I_n(\omega t) = \begin{cases} I_i, & \text{for } 0 \leqslant \omega t < \pi \\ 0, & \text{for } \pi \leqslant \omega t < 2\pi \end{cases}. \tag{4.35}$$

Hence, the maximum current in both switches is equal to I_i. The input current to the load network can be represented by its Fourier components

$$I_n(\omega t) = I_i \left(\frac{1}{2} + \frac{2}{\pi} \sum_{n=1}^{\infty} \frac{\sin\left((2n-1)\omega t\right)}{2n-1} \right) \tag{4.36}$$

The fundamental component of the input current to the load network is

$$I_{n1}(\omega t) = I_{R_L}(\omega t) = i_m \sin \omega t. \tag{4.37}$$

where

$$i_m = \frac{2I_i}{\pi} \approx 0.6366 I_i. \tag{4.38}$$

The fundamental component of the input current is equal to load resistance's current because the parallel inductor and capacitor will have an infinite resistance and therefore behave as an open circuit to this particular frequency component. Consequently, the input impedance is

$$Z_i = R_L. \tag{4.39}$$

The voltages across switches Q_1 and Q_2 are

$$V_{DS1}(\omega t) = \begin{cases} i_m R_L \sin \omega t, & \text{for } 0 \leqslant \omega t < \pi \\ 0, & \text{for } \pi \leqslant \omega t < 2\pi \end{cases} \tag{4.40}$$

and

$$V_{DS2}(\omega t) = \begin{cases} 0, & \text{for } 0 \leqslant \omega t < \pi \\ -i_m R_L \sin \omega t, & \text{for } \pi \leqslant \omega t < 2\pi \end{cases}. \tag{4.41}$$

respectively. The input voltage V_i is equal to the average voltage across Q_1

$$V_i = \frac{1}{2\pi} \int_0^{2\pi} V_{DS1}(\omega t) d\omega t = \frac{i_r R_L}{2\pi} \int_0^{\pi} \sin \omega t d\omega t = \frac{i_r R_L}{\pi}. \tag{4.42}$$

Consequently, for a certain input voltage the input current is

$$I_i = \frac{\pi^2 V_i}{2R_L} \tag{4.43}$$

and the maximum voltage across the switches is πV_i.

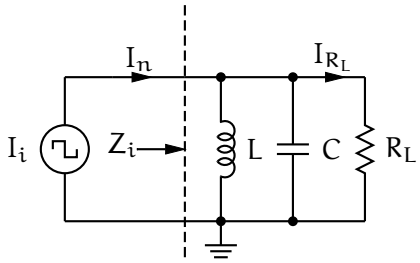

Fig. 4.7: Equivalent circuit of the Class D ZCS inverter

For an ideal Class D ZCS inverter the output power is equal to the input power

$$P_o = P_i = V_i I_i = \frac{\pi^2 V_i^2}{2R_L} \approx 4.9348 \frac{V_i^2}{R_L} \tag{4.44}$$

and the power-output capability is

$$c_p = \frac{P_o}{2V_{DSMAX} I_{DSMAX}} = \frac{V_i I_i}{2V_{DSMAX} I_{DSMAX}} = \frac{1}{2\pi} \approx 0.1592 \tag{4.45}$$

Fig. 4.8 shows the voltage and current waveforms associated with this configuration

4.3.5 *Class D Push-Pull ZCS Inverter*

The Class D push-pull ZCS configuration [58, 70] is similar to its push-pull ZVS counterpart in terms of construction and principle of operation. Fig 4.9 shows two possible circuits for this configuration. In Fig. 4.9a the input current I_i is splits in two by the coupled inductors as it enters the load network. The coupled inductors each have a an inductance of L and form the inductance part of the load network. An additional inductor could also be connected in parallel. In Fig. 4.9 the load network is fed from two current sources via two chokes connected to one voltage source.

The Class D push-pull ZCS inverter requires several bulky magnetic components such as the chokes and the coupled inductors which increase the weight and cost of the inverter. In addition, the maximum voltage developed across the switches is about three times more than the input voltage. For these reasons, the Class D push-pull ZCS inverter is used in inductive links that operate at power levels between below 1 kW [45]. The analysis of this configuration is based on the analysis of the basic ZCS configuration. It is also assumed that the loaded quality factor of the load network is high and that switching frequency is equal to the resonant frequency of the load network. Referring to Fig. 4.9a, the input current enters the load network and splits to two

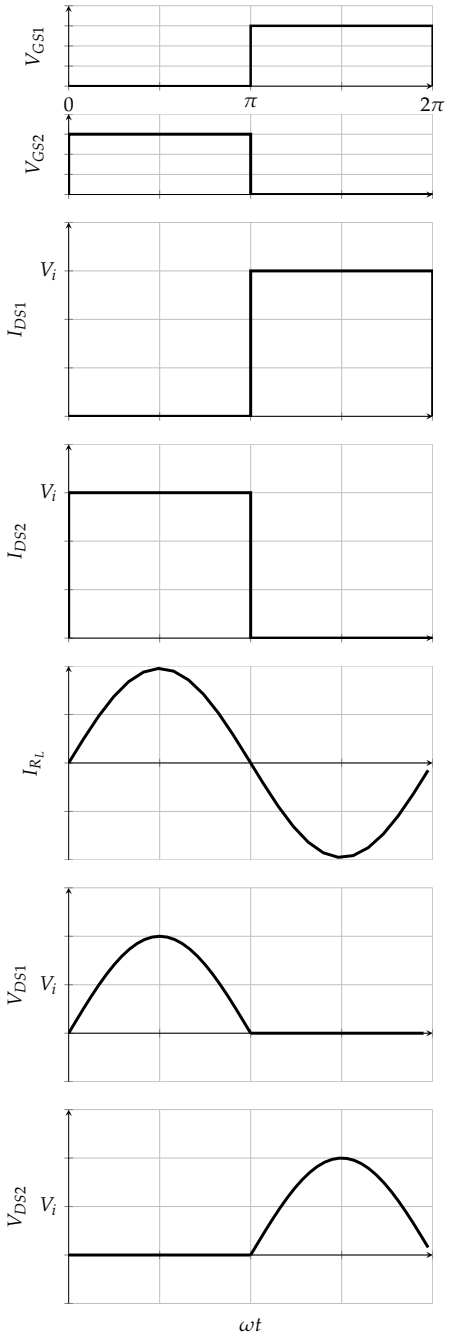

Fig. 4.8: Voltage and current waveforms of the basic Class D ZCS inverter

equal currents that flow in the upper and lower coupled inductors, it can be described by

$$I_n(\omega t) = \begin{cases} \frac{I_i}{2}, & \text{for } 0 \leqslant \omega t < \pi \\ -\frac{I_i}{2}, & \text{for } \pi \leqslant \omega t < 2\pi \end{cases}. \tag{4.46}$$

The magnitude of the fundamental component of the input current to the load network is

$$i_r = \frac{2I_i}{\pi} \approx 0.6366 I_i \tag{4.47}$$

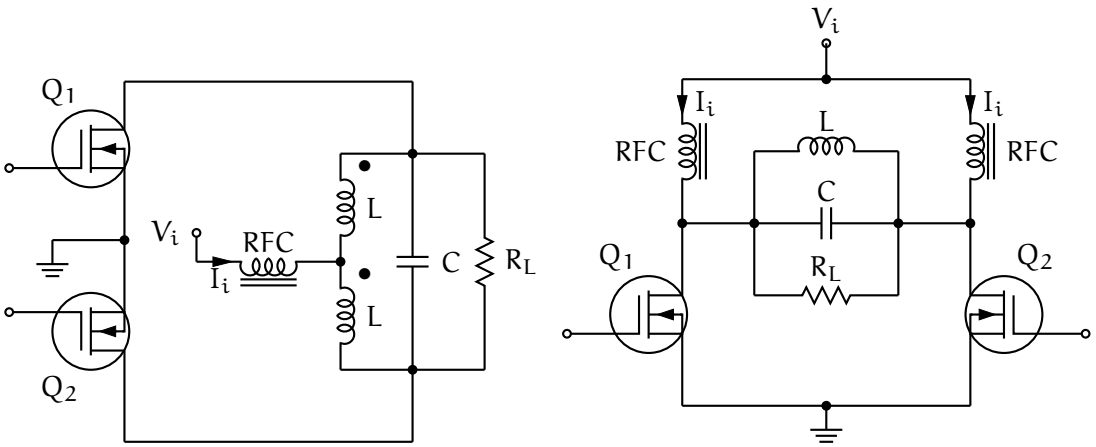

(a) Split inductor configuration (b) Bridge configuration

Fig. 4.9: The Class D Push-Pull ZCS inverter

and the voltages across the switches are given in Eqs. 4.40-4.41. Consequently, the input current is

$$I_i = \frac{\pi^2 V_i}{2R_L} \tag{4.48}$$

and the maximum voltage across the switches is πV_i. For an ideal inverter the output power is

$$P_o = P_i = V_i I_i = \frac{\pi^2 V_i^2}{2R_L} \approx 4.9348 \frac{V_i^2}{R_L} \tag{4.49}$$

and the power-output capability is

$$c_p = \frac{P_o}{2V_{DSMAX} I_{DSMAX}} = \frac{V_i I_i}{2V_{DSMAX} I_{DSMAX}} = \frac{1}{2\pi} \approx 0.1592 \tag{4.50}$$

4.4 CLASS E INVERTERS

The Class E Inverter was introduced by the Sokals in 1975 [71]. It consists of a single switch and a double-tuned output load network that contains a parallel and series tuned LC tank. Not only can the Class E inverter operate at ZVS, the voltage across the switch has a zero slope at the instant at which it is turned ON. This is referred to as zero-voltage derivative switching (ZVDS). Due to this feature, the switch can be 'softly' switched ON and that leads to less switching losses allowing the inverter to operate efficiently in the MHz region. The Class E Inverter is also capable of delivering more power to a load compared to other inverters. This makes it suitable to drive weekly coupled inductive links since they require high driving currents.

This section will provide an extensive review on the different configurations of the Class E inverter. Detailed mathematical analysis and performance investigation will

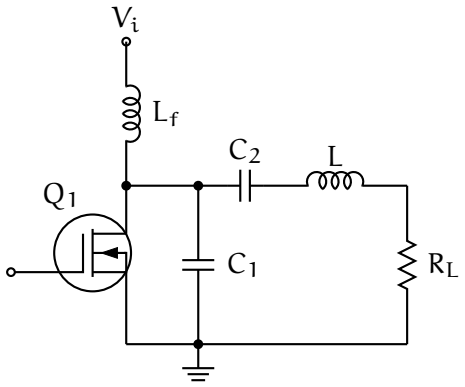

Fig. 4.10: Basic configuration of a current-fed Class E ZVS and ZVDS inverter

be performed on each configuration. Class E inverters are generally more complex to analyse than other inverter classes such as Class D. Two analysis approaches are often used; the analytical approach and the state-space representation approach. The analytical approach is limited to a certain operating region and is based on several assumptions. However, it can give an early insight on the inverter's behaviour. The majority of the analysis of Class E inverters that can be found in the literature is based on the analytical approach. An extensive analysis of Class E inverters using the analytical approach can be found in [58, 70] and the references therein. The state-space representation approach may require complex matrix manipulation and a numerical solver. However, it can cover a wider operating range and is more accurate than the analytical approach. Both approaches will be considered in this section.

4.4.1 *The Class E ZVS and ZVDS Inverter*

Fig. 4.10 shows the basic configuration of a Class E ZVS and ZVDS inverter. The circuit consists of one low-side switch with its source terminal grounded thus simplifying the gate driving circuitry. The circuit also consists of four passive elements. Inductance L_f is referred to as the DC-feed inductance. For this particular configuration, it is assumed that the DC-feed inductance is large enough such that current flowing in it is a DC current. Capacitor C_1 is referred to as the shunt capacitor. Capacitor C_2 and inductor L form a series resonant network and R_L represents the load resistance. If the Class E inverter is used as a coil driver, then inductance L can represent the inductance of the primary coil of the inductive link and R_L can represent the reflected impedance. This configuration is the only Class E configuration that has been used in inductive links [51, 53, 67, 72–77]

Fig. 4.11 shows an equivalent circuit which will be used for the analysis. The operation of interest is only under optimum switching conditions which are ZVS and ZVDS.

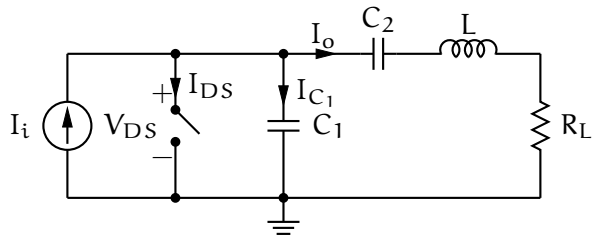

Fig. 4.11: Equivalent circuit of the basic Class E inverter

Assuming the switch is turned ON at $\omega t = 0$, the optimum switching conditions can be described by

$$V_{DS}(0) = 0 \tag{4.51}$$

$$\frac{dV_{DS}(\omega t)}{d\omega t}_{\omega t=0} = 0. \tag{4.52}$$

The analysis is performed under the following assumptions:

- The switch is an ideal switch with a zero ON resistance.
- The DC-feed inductance (L_f) is large enough such that current flowing in it is a DC current.
- The loaded quality factor (Q_L) of the output network consisting of L, C_2 and R_L is higher than 5 such that the current flowing through it can be assumed to be sinusoidal [78].
- The duty cycle of the switching signal is at 50 %.

The current I_o flowing through the output network is sinusoidal and is given by

$$I_o = i_m \sin(\omega t + \phi) \tag{4.53}$$

where i_m is the amplitude of the output current and ϕ is its phase with reference to switching signal. Applying KCL on the switch's drain node results in the following equation

$$I_i + I_o = I_{DS}(\omega t) + I_{C_1}(\omega t) \tag{4.54}$$

where I_i is the DC current of the DC-feed inductance, I_{DS} is the switch's drain current and I_{C_1} is the shunt capacitance's (C_1) current. Based on the switching signal, the switch is assumed to be ON in the period $0 \leqslant \omega t < \pi$ and OFF in the period $\pi \leqslant \omega t < 2\pi$. During the first period $0 \leqslant \omega t < \pi$, the switch is ON therefore

$$V_{DS}(\omega t) = 0 \tag{4.55}$$

$$I_{C_1}(\omega t) = 0. \tag{4.56}$$

The switch's drain current is given by

$$I_{DS}(\omega t) = I_i + i_m \sin(\omega t + \phi). \tag{4.57}$$

During the second period $\pi \leqslant \omega t < 2\pi$, the switch is OFF therefore

$$I_{DS}(\omega t) = 0. \tag{4.58}$$

The current through the shunt capacitor C_1 is given by

$$I_{C_1}(\omega t) = I_i + i_m \sin(\omega t + \phi). \tag{4.59}$$

The voltage across the switch is equal to

$$V_{DS}(\omega t) = \frac{1}{\omega C_1}\int_{\pi}^{2\pi} I_{C_1}(\omega t)d\omega t = \frac{1}{\omega C_1}\int_{\pi}^{2\pi} [I_i + i_m \sin(\omega t + \phi)]d\omega t \tag{4.60}$$

$$\frac{1}{\omega C_1}(I_i(\omega t - \pi) - i_m(\cos(\omega t + \phi) + \cos\phi)). \tag{4.61}$$

Applying the ZVS condition ($V_{DS}(2\pi) = 0$) in Eq. 4.61 results in

$$i_m = \frac{I_i \pi}{2\cos\phi}. \tag{4.62}$$

By substituting Eq. 4.62 in Eq. 4.57, the switch's current can be written as

$$I_{DS}(\omega t) = I_i - I_i \frac{\pi}{2\cos\phi}\sin(\omega t + \phi) \quad \text{for } 0 \leqslant \omega t < \pi. \tag{4.63}$$

Similarly, by substituting Eq. 4.62 in Eq. 4.59, the current through the parallel capacitor can be written as

$$I_{C_1}(\omega t) = I_i - I_i \frac{\pi}{2\cos\phi}\sin(\omega t + \phi) \quad \text{for } \pi \leqslant \omega t < 2\pi. \tag{4.64}$$

Using Eq. 4.62, Eq. 4.61 becomes

$$V_{DS}(\omega t) = \frac{I_i}{\omega C}\left(\omega t - \frac{3\pi}{2} - \frac{\pi}{2\cos\phi}[\cos(\omega t + \phi)]\right) \quad \text{for } \pi \leqslant \omega t < 2\pi. \tag{4.65}$$

Applying the ZVDS condition ($dV_{DS}/d\omega t = 0$ at $\omega t = 2\pi$) in Eq. 4.65, the following equation is obtained

$$\tan\phi = -\frac{2}{\pi} \tag{4.66}$$

from which ϕ is approximately is

$$\phi \approx -0.5669 \text{ rad} = -32.48°. \tag{4.67}$$

Equation 4.62 then becomes

$$i_m = -\frac{\sqrt{\pi^2 + 4}}{2} I_i \approx -1.8621 I_i. \tag{4.68}$$

Since the DC voltage across the choke is always zero, the input voltage supplied to the inverter V_i is equal to the average value of the switch's drain voltage

$$V_i = \frac{I_i}{2\pi\omega C_1}\int_0^{2\pi} V_{DS}(\omega t)d\omega t = \frac{I_i}{2\pi}\int_\pi^{2\pi}\left(\omega t - \frac{3\pi}{2} - \frac{\pi}{2\cos\phi}[\cos(\omega t+\phi)]\right)d\omega t. \tag{4.69}$$

Substituting Eq. 4.66 in Eq. 4.69

$$I_i = \pi\omega C_1 V_i \tag{4.70}$$

consequently,

$$i_m = -\frac{\sqrt{\pi^2+4}}{2}\pi\omega C_1 V_i. \tag{4.71}$$

Rewriting the current and voltage equations and normalising them by dividing by V_i and I_i respectively

$$\frac{I_{DS}(\omega t)}{I_i} = \begin{cases} 1+\dfrac{\sqrt{\pi^2+4}}{2}\sin(\omega t+\phi) & \text{for } 0 \leqslant \omega t < \pi \\ 0 & \text{for } \pi \leqslant \omega t < 2\pi \end{cases} \tag{4.72}$$

$$\frac{I_{C_1}(\omega t)}{I_i} = \begin{cases} 0 & \text{for } 0 \leqslant \omega t < \pi \\ 1+\dfrac{\sqrt{\pi^2+4}}{2}\sin(\omega t+\phi) & \text{for } \pi \leqslant \omega t < 2\pi \end{cases} \tag{4.73}$$

$$\frac{I_o(\omega t)}{I_i} = \frac{\sqrt{\pi^2+4}}{2}\sin(\omega t+\phi) \tag{4.74}$$

$$\frac{V_{DS}(\omega t)}{V_i} = \begin{cases} 0 & \text{for } 0 \leqslant \omega t < \pi \\ \pi\left(\omega t - \dfrac{3\pi}{2} - \dfrac{\pi}{2}\cos\omega t - \sin\omega t\right) & \text{for } \pi \leqslant \omega t < 2\pi \end{cases}. \tag{4.75}$$

The maximum current in the switch is determined by differentiating Eq. 4.72 and setting it to zero

$$\frac{dI_{DS}(\omega t)}{d\omega t} = -I_i\frac{\sqrt{\pi^2+4}}{2}\cos(\omega t+\phi) = 0. \tag{4.76}$$

By solving the above equation the time at which peak of the switch's current occurs at is

$$\omega t_{I_{DS(MAX)}} = \frac{3\pi}{2} - \phi \approx 2.138 \text{ rad} = 122.48^\circ \tag{4.77}$$

and the normalised maximum value of the switch's current is

$$I_{DS(MAX)} = I_i\left(\frac{\sqrt{\pi^2+4}}{2}+1\right) \approx 2.862 I_i. \tag{4.78}$$

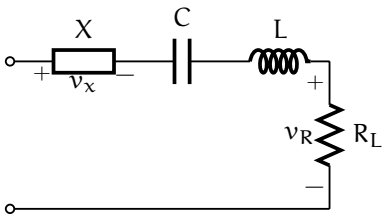

Fig. 4.12: Circuit representation of the output network

Similarly, the maximum voltage across the switch is determined by differentiating Eq. 4.75 and setting it to zero

$$\frac{V_{DS}(\omega t)}{d\omega t} = \pi V_i \left(1 + \frac{\pi}{2\cos\phi}\sin(\omega t + \phi)\right) = 0. \tag{4.79}$$

By solving the above equation the time at which peak of the switch's voltage occurs at is

$$\omega t_{V_{DS(MAX)}} = 3\pi - 2\phi \approx 4.275 = 244.96° \tag{4.80}$$

and the normalised maximum value of the switch's voltage is

$$V_{DS(MAX)} = 2\pi(\pi - \phi)V_i \approx 3.562V_i. \tag{4.81}$$

To continue with the analysis, the impedance of the output network has to be calculated. The output network can be represented as shown in Fig. 4.12. It consists of the load resistance R_L, an inductor capacitor pair that are in resonance at the switching frequency and an unknown impedance $j\omega X$. The current in the output network is sinusoidal but the voltage across it is not sinusoidal. The voltage across the series resonant inductor capacitor pair is zero and the voltage across the load resistance is

$$v_R(\omega t) = -i_m R_L \sin(\omega t + \phi) = -v_m \sin(\omega t + \phi). \tag{4.82}$$

The voltage across the unknown impedance is

$$v_X(\omega t) = -i_m \omega X \cos(\omega t + \phi) = v_{xm}\cos(\omega t + \phi). \tag{4.83}$$

Since the current in the output network is sinusoidal, the sum of the voltages across the load and the unknown impedance is equal to the fundamental component of the switch's drain voltage

$$V_{DS1}(\omega t) = v_R + v_X = v_m \sin(\omega t + \phi) + v_{xm}\cos(\omega t + \phi). \tag{4.84}$$

By using Fourier trigonometric series formula, the amplitude of the voltages across the load and the unknown impedance are equal to

$$\begin{aligned} v_m &= i_m R_L = \frac{1}{\pi}\int_0^{2\pi} V_{DS}(\omega t)\sin(\omega t+\phi)d\omega t \qquad (4.85)\\ &= \frac{1}{\pi}\int_\pi^{2\pi} V_i\pi\left(\omega t-\frac{3\pi}{2}-\frac{\pi}{2\cos\phi}\cos(\omega t+\phi)\right)\sin(\omega t+\phi)d\omega t \\ &= \frac{4}{\sqrt{\pi^2+4}}V_i \approx 1.074V_i \qquad (4.86)\end{aligned}$$

$$\begin{aligned} v_{xm} &= i_m\omega X = \frac{1}{\pi}\int_0^{2\pi} V_{DS}(\omega t)\cos(\omega t+\phi)d\omega t \qquad (4.87)\\ &= \frac{1}{\pi}\int_\pi^{2\pi} V_i\pi\left(\omega t-\frac{3\pi}{2}-\frac{\pi}{2\cos\phi}\cos(\omega t+\phi)\right)\cos(\omega t+\phi)d\omega t \\ &= \frac{\pi(\pi^2-4)}{4\sqrt{\pi^2+4}}V_i. \qquad (4.88)\end{aligned}$$

From Eq. 4.86, the power delivered to the load is

$$P_o = \frac{1}{2}\frac{v_m^2}{R_L} = \frac{8}{\pi^2+4}\frac{V_i^2}{R_L} \qquad (4.89)$$

and the power-output capability is

$$c_p = \frac{P_o}{V_{DS(MAX)}I_{DS(MAX)}} = \frac{V_i I_i}{V_{DS(MAX)}I_{DS(MAX)}} = \frac{1}{\pi(\pi-\phi)\sqrt{\pi^2+4}+2} \approx 0.0981. \qquad (4.90)$$

The optimum values of the components of the Class E inverter can now be calculated. Using Eq. 4.62 and Eq. 4.86 the value of the shunt capacitor C_1 is

$$C_1 = \frac{\frac{4}{\sqrt{\pi^2+4}}V_i}{\frac{\pi^2+4}{2}\pi\omega R_L V_i} = \frac{8}{\pi(\pi^2+4)\omega R_L} \approx \frac{0.1836}{\omega R_L}. \qquad (4.91)$$

Likewise, using Eq. 4.62 and Eq. 4.88 the unknown impedance $j\omega X$ is

$$\omega X = \frac{v_{xm}}{i_m} = \frac{\frac{\pi(\pi^2-4)}{4\sqrt{\pi^2+4}}V_i}{\frac{\pi^2+4}{2}\pi\omega C_1 V_i} = \frac{\pi^2-4}{2(\pi^2+4)\omega C_1} \qquad (4.92)$$

and the inductance X is

$$X = \frac{\pi^2-4}{2(\pi^2+4)\omega^2 C_1} \approx \frac{0.2116}{\omega^2 C_1}. \qquad (4.93)$$

The value of the resonant inductor is

$$L = \frac{Q_L R_L}{\omega}. \qquad (4.94)$$

Using Eq. 4.91 and Eq. 4.93 the value of capacitor C_2 is

$$C_2 = \frac{1}{\omega(Q_L R_L - \omega X)} \approx \frac{1}{\omega R_L(Q_L - 1.1525)}. \qquad (4.95)$$

Using Eq. 4.91 and Eq. 4.70 the DC input current can be written as

$$I_i = \frac{8}{\pi^2 + 4}\frac{V_i}{R_L} \approx 0.5768\frac{V_i}{R_L} \tag{4.96}$$

From Eqs. 4.72-4.75, the voltage and current waveforms can be plotted and are shown in Fig. 4.13.

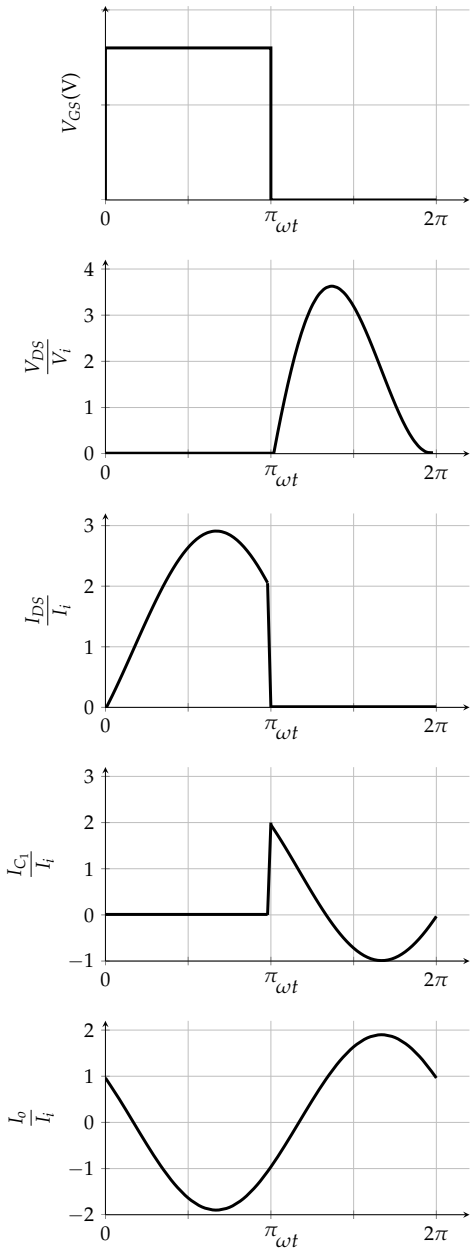

Fig. 4.13: Normalised voltage and current waveforms associated with the Class E operating at optimum switching conditions

4.4.2 *Class E push-pull ZVS and ZVDS Inverter*

Similar to Class D push-pull inverters, a Class E push-pull inverter can be constructed by using two identical Class E inverters as shown in Fig. 4.14a. Switches Q_1 and Q_2 are switched in a complementary manner. The output current (I_o) in the Class E push-pull is twice the output current of the single Class E inverter. Therefore, the output power is quadrupled.

The principle of operation and analysis of the Class E push-pull inverter is exactly the same as the single Class E inverter [79]. Therefore, the assumptions and the design equations in the previous section can be applied here. The Class E push-pull inverter can be represented by two separate and identical circuits as shown Fig. 4.14b. It can be seen that the equivalent circuit is the same as that of the single Class E inverter of Fig. 4.11. Due to the push-pull operation, the impedances of the load network consisting of R_L, L and C_2, in addition to the input and output currents, for each equivalent circuit are now halved. Using Eqs. 4.91 and 4.95, the values of capacitors C_1 and C_2 are

$$C_1 = 2 \times \frac{8}{\omega R_L \pi(\pi^2+4)} \approx 2 \times \frac{0.1836}{\omega R_L} = \frac{0.3672}{\omega R_L} \tag{4.97}$$

$$C_2 = \frac{1}{2} \times \frac{1}{\omega(Q_L R_L - \omega X)} \approx \frac{1}{\omega 2 R_L (Q_L - 1.1525)}. \tag{4.98}$$

From Eq. 4.96, the sum of the DC input currents to the two equivalent circuits represents the DC input current to the push-pull inverter, i.e.

$$I_i = 2 \times 2 \times \frac{8}{\pi^2+4}\frac{V_i}{R_L} \approx 2.3072\frac{V_i}{R_L}. \tag{4.99}$$

Consequently the total output power of the Class E push-pull inverter is

$$P_o = P_i = \frac{32}{\pi^2+4}\frac{V_i^2}{R_L} \approx 2.3072\frac{V_i^2}{R_l} \tag{4.100}$$

which is four times more than that of a single Class E inverter at the same-power output capability which is given in 4.90. The power-output capability is

$$c_p = \frac{P_o}{2V_{DS(MAX)}I_{DS(MAX)}} = \frac{V_i I_i}{V_{DS(MAX)}I_{DS(MAX)}} = \frac{1}{\pi(\pi-\phi)\sqrt{\pi^2+4}+2} \approx 0.0981. \tag{4.101}$$

4.4.3 *Class E Inverter with Finite DC-feed Inductance*

In the basic configuration of the Class E inverter shown in Fig. 4.10, the DC-feed inductance L_f was assumed to be large enough, or infinite, such that the current in it is a DC

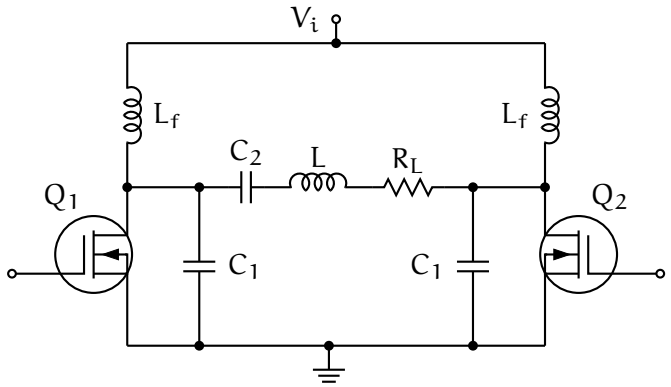

(a) practical circuit

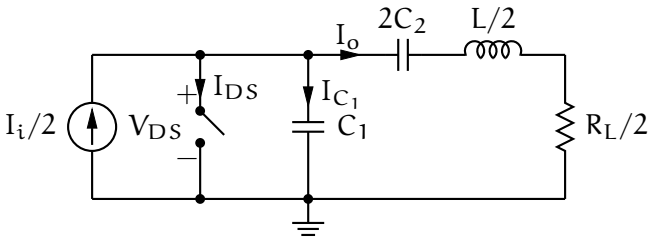

(b) equivalent cricuit, one of two

Fig. 4.14: The Class E ZVS and ZVDS push-pull inverter

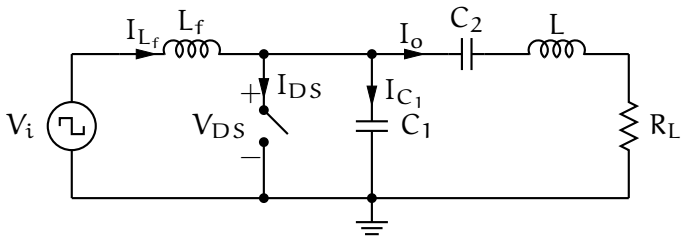

Fig. 4.15: Equivalent circuit of the Class E inverter with finite DC-feed inductance

current. It is possible to use a finite DC-feed inductance as described in [80–82]. This allows the Class E inverter to operate over a larger load range with a broader output power capability. In this section, the effect of using a finite DC-feed inductance on the performance of the basic Class E inverter is investigated. The Class E inverter with finite DC-feed inductance was first used in inductive links in this research [73].

The same assumptions that were applied in the analysis of the basic Class E configuration will be applied here. Fig. 4.15 shows an equivalent circuit of the Class E inverter with a finite DC-feed inductance. Applying KCL at the switch's drain node results in the following equation

$$I_{L_f}(\omega t) = I_{DS}(\omega t) + I_{C_1}(\omega t) + I_o(\omega t). \tag{4.102}$$

Similarly, applying KVL at the switch's drain node results in the following equation

$$V_i - V_{DS}(\omega t) = V_{L_f}(\omega t) = \omega L_f \frac{dI_{L_f}(\omega t)}{d\omega t}. \tag{4.103}$$

For the period $0 \leqslant \omega t < \pi$, the switch is ON, therefore

$$V_{DS}(\omega t) = 0 \tag{4.104}$$

$$I_{C_1}(\omega t) = 0 \tag{4.105}$$

$$V_{L_f}(\omega t) = V_i = \omega L_f \frac{dI_{L_f}(\omega t)}{\omega t}. \tag{4.106}$$

The DC-feed inductor's current is

$$I_{L_f}(\omega t) = \frac{1}{\omega L_f}\int_0^{\omega t} V_i \, d\omega t + I_{L_f}(0) = \frac{V_i}{\omega L_f}\omega t + I_{L_f}(0). \tag{4.107}$$

The switch's drain current is given by

$$I_{DS}(\omega t) = I_{L_f}(\omega t) - I_o(\omega t) = I_{L_f}(\omega t) - i_m \sin(\omega t + \phi). \tag{4.108}$$

Since the switch's drain current is zero before it is switched ON, the initial value of the DC-feed inductor's current is

$$I_{DS}(0) = I_{L_f}(0) - i_m \sin\phi. \tag{4.109}$$

Hence,

$$I_{L_f}(0) = i_m \sin\phi. \tag{4.110}$$

Therefore Eq. 4.107 and Eq. 4.108 become

$$I_{L_f}(\omega t) = \frac{V_i}{\omega L_f}\omega t + i_m \sin\phi \quad \text{for } 0 \leqslant \omega t < \pi \tag{4.111}$$

and

$$I_{DS}(\omega t) = \frac{V_i}{\omega L_f}\omega t - i_m[\sin(\omega t + \phi) - \sin\phi] \quad \text{for } 0 \leqslant \omega t < \pi \tag{4.112}$$

respectively. For the period $\pi \leqslant \omega t < 2\pi$, the switch is switched OFF, therefore

$$I_{DS}(\omega t) = 0. \tag{4.113}$$

The voltage across the DC-feed inductor is

$$V_{L_f}(\omega t) = V_i - V_{DS}(\omega t) = \omega L \frac{dI_{L_f}(\omega t)}{d\omega t}. \tag{4.114}$$

The current through the parallel capacitor can found by differentiating Eq. 4.114

$$I_{C_1}(\omega t) = -\omega C \frac{dV_{DS}(\omega t)}{d\omega t} = \omega^2 L_f C_1 \frac{d^2 I_{L_f}(\omega t)}{d\omega t^2}. \tag{4.115}$$

According to Eq. 4.102, the DC-feed inductor's current is

$$I_{L_f}(\omega t) = I_{C_1}(\omega t) + I_o(\omega t) = i_m \sin(\omega t + \phi) - \omega^2 L_f C_1 \frac{d^2 I_{L_f}(\omega t)}{d\omega t^2}. \tag{4.116}$$

Rearranging the above equation and normalising with respect to i_m

$$\omega^2 L_f C_1 \frac{d^2 \frac{I_{L_f}}{i_m}(\omega t)}{d\omega t^2} + \frac{I_{L_f}}{i_m}(\omega t) - \sin(\omega t + \phi) = 0. \tag{4.117}$$

Equation 4.117 is a linear non-homogeneous second-order differential equation which has the following general solution

$$\frac{I_{L_f}}{i_m}(\omega t) = \alpha \sin(q\omega t) + \beta \cos(q\omega t) + \frac{q^2 \sin(\omega t + \phi)}{q^2 - 1}, \quad q \neq 1 \tag{4.118}$$

where

$$q = \frac{1}{\omega\sqrt{L_f C_1}} \tag{4.119}$$

and the coefficients α and β are to be determined from the initial conditions of the ON period, i.e.

$$I_{L_f}(\pi^+) = I_{L_f}(\pi^-) = \frac{V_i \pi}{\omega L_f} + i_m \sin\phi \tag{4.120}$$

and

$$\frac{i_{L_f}(\pi^+)}{d\omega t} = \frac{i_{L_f}(\pi^-)}{d\omega t} = \frac{V_i}{\omega L_f}. \tag{4.121}$$

Normalising the initial conditions with respect to i_m

$$\frac{I_{L_f}}{i_m}(\pi^+) = \frac{\pi}{p} + \sin\phi \tag{4.122}$$

$$\frac{i'_{L_f}}{i_m}(\pi^+) = \frac{1}{p} \tag{4.123}$$

where

$$p = \frac{\omega L_f i_m}{V_i}. \tag{4.124}$$

Consequently the coefficients α and β are:

$$\alpha = \frac{1}{q^2 - 1}\left(q\cos(q\pi)\cos\phi + (2q^2 - 1)\sin(q\pi)\sin\phi\right) + \frac{\pi}{p}\sin(q\pi) + \frac{1}{qp}\cos(q\pi), \quad q \neq 1 \tag{4.125}$$

$$\beta = \frac{1}{q^2 - 1}\left(-q\sin(q\pi)\cos\phi + (2q^2 - 1)\cos(q\pi)\sin\phi\right) + \frac{\pi}{p}\cos(q\pi) - \frac{1}{qp}\sin(q\pi), \quad q \neq 1. \tag{4.126}$$

Using Eqs. 4.114 and 4.124, the normalised voltage across the switch with respect to the input voltage is

$$\frac{V_{DS}(\omega t)}{V_i} = 1 - p\frac{d\frac{I_{L_f}}{i_m}(\omega t)}{d\omega t}$$
$$= 1 - \alpha qp\cos(q\omega t) + \beta qp\sin(q\omega t) - \frac{q^2 p}{q^2-1}\cos(\omega t + \phi), \quad q \neq 1. \tag{4.127}$$

For the specific case when $q = 1$, which occurs when the circuit of the DC-feed inductance L_f and the shunt capacitor C_1 is tuned to the switching frequency, the DC-feed inductor's current is derived by substituting $q = 1$ in Eq. 4.118 and resolving the differential equation with the initial conditions defined in Eqs. 4.122 and 4.123. The following equation is produced

$$\frac{i_{L_f}}{i_m}(\omega t) = \frac{1}{2}\big(\sin\phi\cos\phi + \pi\cos(\omega t+\phi)\omega t\cos(\omega t+\phi)\big)$$
$$-\sin\phi\cos(\omega t) - \frac{1}{p}\big(\sin(\omega t) + \pi\cos(\omega t)\big), \quad q = 1 \tag{4.128}$$

and the normalised voltage across the MOSFET is

$$\frac{v_{DS}(\omega t)}{V_i} = -\frac{3p}{2}\sin\phi\sin(\omega t) + \frac{p}{2}(\pi - \omega t)\sin(\omega t+\phi)$$
$$+\cos(\omega t) - \pi\sin(\omega t) + 1, \quad q = 1. \tag{4.129}$$

The DC supply current is found by averaging the DC-feed inductor's current over the period 0 to 2π which is also equal to average of the switch's current,

$$I_i = \frac{1}{2\pi}\int_0^{2\pi} I_{L_f}(\omega t)d\omega t = \frac{1}{2\pi}\int_0^{\pi} I_{DS}(\omega t)d\omega t \tag{4.130}$$
$$= \frac{1}{2\pi}\int_0^{2\pi}\left(\frac{V_i}{\omega L_f}\omega t - i_m[\sin(\omega t+\phi) - \sin\phi]\right)d\omega t$$
$$= \frac{i_m}{2\pi}\int_0^{\pi}\left(\frac{1}{p}\omega t - \sin(\omega t+\phi) + \sin\phi\right)d\omega t$$
$$= \frac{i_m}{2\pi}\left(\frac{\pi^2}{2p} - 2\cos\phi + \pi\sin\phi\right). \tag{4.131}$$

In an ideal Class E inverter there are no losses in the circuit, therefore all the power supplied by the power source is consumed in the load R_L, thus

$$P_{in} = P_{out}$$
$$V_i I_i = \frac{{v_R}^2}{2R_L} = \frac{1}{2}{i_m}^2 R_L. \tag{4.132}$$

Rearranging the above equation and using Eq. 4.131

$$\frac{v_R}{V_i} = \frac{2I_i}{i_m} = \frac{1}{\pi}\left(\frac{\pi^2}{2p} - 2\cos\phi + \pi\sin\phi\right). \tag{4.133}$$

Therefore the DC resistance seen by the voltage source is

$$R_{DC} = \frac{V_i}{I_o} = R_L \Big/ \frac{1}{2\pi^2}\left(\frac{\pi^2}{2p} - 2\cos\phi + \pi\sin\phi\right)^2. \tag{4.134}$$

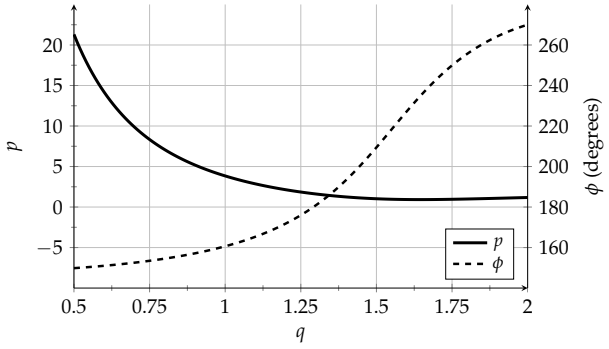

Fig. 4.16: The solved optimum parameters p and ϕ versus q

The normalised DC-feed inductor and the parallel capacitor with respect to the load resistance can be defined using Eqs. 4.119, 4.124 and 4.133 as

$$\frac{\omega L_f}{R_L} = p \Big/ \left(\frac{\pi}{2p} - \frac{2}{\pi} \cos\phi + \sin\phi \right) \tag{4.135}$$

$$\omega C_1 R_L = \frac{R_L}{q^2 \omega L_f}. \tag{4.136}$$

Substituting the ZVS and ZVDS conditions (i.e. $V_{DS} = 0$ and $dV_{DS}/d\omega t = 0$ at $\omega t = 2\pi$) in Eq. 4.127 results in the following two equations

$$1 - Aqp\cos(2\pi q) + Bqp\sin(2\pi q) - \frac{q^2 p}{q^2 - 1}\cos\phi = 0, \quad q \neq 1 \tag{4.137}$$

$$Aq^2 p\sin(2\pi q) + Bq^2 p\cos(2\pi q) + \frac{q^2 p}{q^2 - 1}\sin\phi = 0, \quad q \neq 1. \tag{4.138}$$

Equations 4.137 and 4.138 can be solved numerically as a function of q. Fig. 4.16 shows solved values of p and ϕ. Appendix A.1.1 includes the MATLAB code to be obtain these solutions The value of the residual impedance is

$$X = \frac{v_{xm}}{i_m} = R_L \frac{v_{xm}}{v_m}. \tag{4.139}$$

Therefore the normalised residual impedance is

$$\frac{X}{R_L} = \frac{v_{xm}}{v_m} \tag{4.140}$$

where v_m and v_{xm} are the first two quadrature Fourier components given in Eqs. 4.85 and 4.87. The value of the resonant inductor L is

$$L = \frac{Q_L R_L}{\omega} \tag{4.141}$$

and the value of capacitance C is

$$C = \frac{1}{\omega^2 L}. \tag{4.142}$$

Therefore the actual value of capacitor C_2 is

$$C_2 = \frac{1}{\omega(Q_L R_L - \omega X)}. \tag{4.143}$$

Using Eqs. 4.135, 4.136 and 4.140, the normalised impedances of L_f, C_1 and X can be plotted against q as shown in Fig. 4.17.

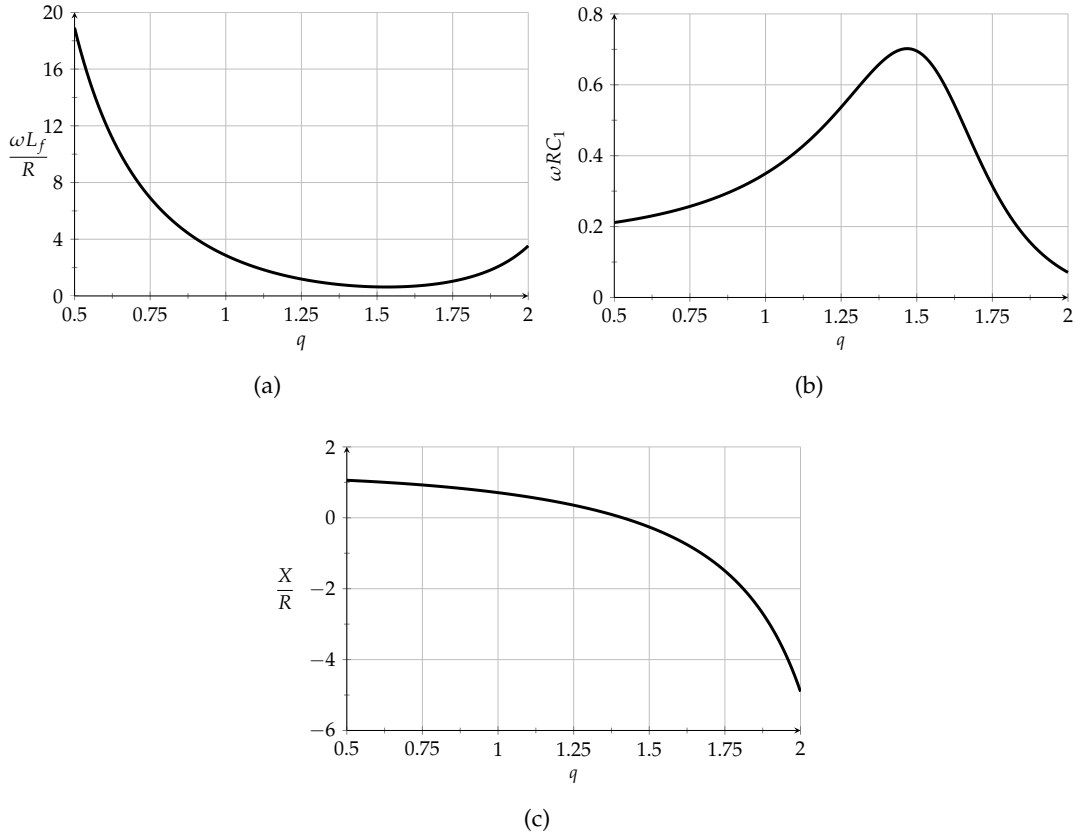

Fig. 4.17: The calculated normalised impedances versus q.

Finally, the normalised voltages and normalised currents of the inverter for both ON and OFF periods can be written as

$$\frac{I_{DS(\omega t)}}{I_i} = \begin{cases} 2\pi \dfrac{\dfrac{1}{p}\omega t - \sin(\omega t + \phi) + \sin\phi}{\dfrac{\pi^2}{2p} - 2\cos\phi + \pi\sin\phi} & \text{for } 0 \leqslant \omega t < \pi \\ 0 & \text{for } \pi \leqslant \omega t < 2\pi \end{cases} \tag{4.144}$$

$$\frac{I_{L_f}(\omega t)}{I_i} = \begin{cases} 2\pi \dfrac{\frac{1}{p}\omega t + \sin\phi}{\frac{\pi^2}{2p} - 2\cos\phi + \pi\sin\phi} & \text{for } 0 \leqslant \omega t < \pi \\ 2\pi \dfrac{A\sin(q\omega t) + B\cos(q\omega t) + \dfrac{q^2\sin(\omega t+\phi)}{q^2-1}}{\frac{\pi^2}{2p} - 2\cos\phi + \pi\sin\phi},\ q \neq 1 & \text{for } \pi \leqslant \omega t < 2\pi \\ 2\pi \dfrac{\frac{1}{2}\big(\sin\phi\cos\phi + \pi\cos(\omega t+\phi)\omega t\cos(\omega t+\phi)\big)\ldots}{\frac{\pi^2}{2p} - 2\cos\phi + \pi\sin\phi}, & \\ \ldots - \sin\phi\cos(\omega t) - \frac{1}{p}\big(\sin(\omega t) + \pi\cos(\omega t)\big), \quad q = 1 & \text{for } \pi \leqslant \omega t < 2\pi \end{cases} \tag{4.145}$$

$$\frac{I_o(\omega t)}{I_i} = \frac{2\pi}{\frac{\pi^2}{2p} - 2\cos\phi + \pi\sin\phi}\sin(\omega t + \phi) \tag{4.146}$$

$$\frac{V_{DS}(\omega t)}{V_i} = \begin{cases} 0 & \text{for } 0 \leqslant \omega t < \pi \\ 1 - Aqp\cos(q\omega t) + Bqp\sin(q\omega t) & \\ \qquad -\dfrac{q^2p}{q^2-1}\cos(\omega t+\phi), q \neq 1 & \text{for } \pi \leqslant \omega t < 2\pi\,. \\ -\dfrac{3p}{2}\sin\phi\sin(\omega t) + \dfrac{p}{2}(\pi - \omega t)\sin(\omega t+\phi) & \\ \qquad +\cos(\omega t) - \pi\sin(\omega t) + 1, q = 1 & \text{for } \pi \leqslant \omega t < 2\pi \end{cases} \tag{4.147}$$

The maximum values of the voltage and current of the switch can be obtained by differentiating Eq. 4.144 and Eq. 4.147 and setting the derivatives equal to zero. Fig. 4.18 shows the maximum values of the voltage and current of the switch in addition to the power output capability as a function of q. The dashed lines represents the values when $q = 0$ which corresponds to an infinite DC-feed inductance. When $q = 0$ the inverter becomes the basic Class E inverter described previously. The values in Fig. 4.18 were obtained using Chebfun2 and the code is included in Appendix A.1.1.

Referring to Figs. 4.17 and 4.18, a particular operating point of interest is when $q = 1.412$. At this point, the switching frequency is equal to the resonant frequency of the load network since the residual impedance X is zero. Also, the inverter's output power is at a maximum and the current stress in the switch is at its lowest resulting in lower ohmic losses in the switch, thereby increasing the efficiency. The range when $q > 1.412$ is not recommended to operate at since the inverter delivers less power at higher voltage and current stresses resulting in poor efficiencies.

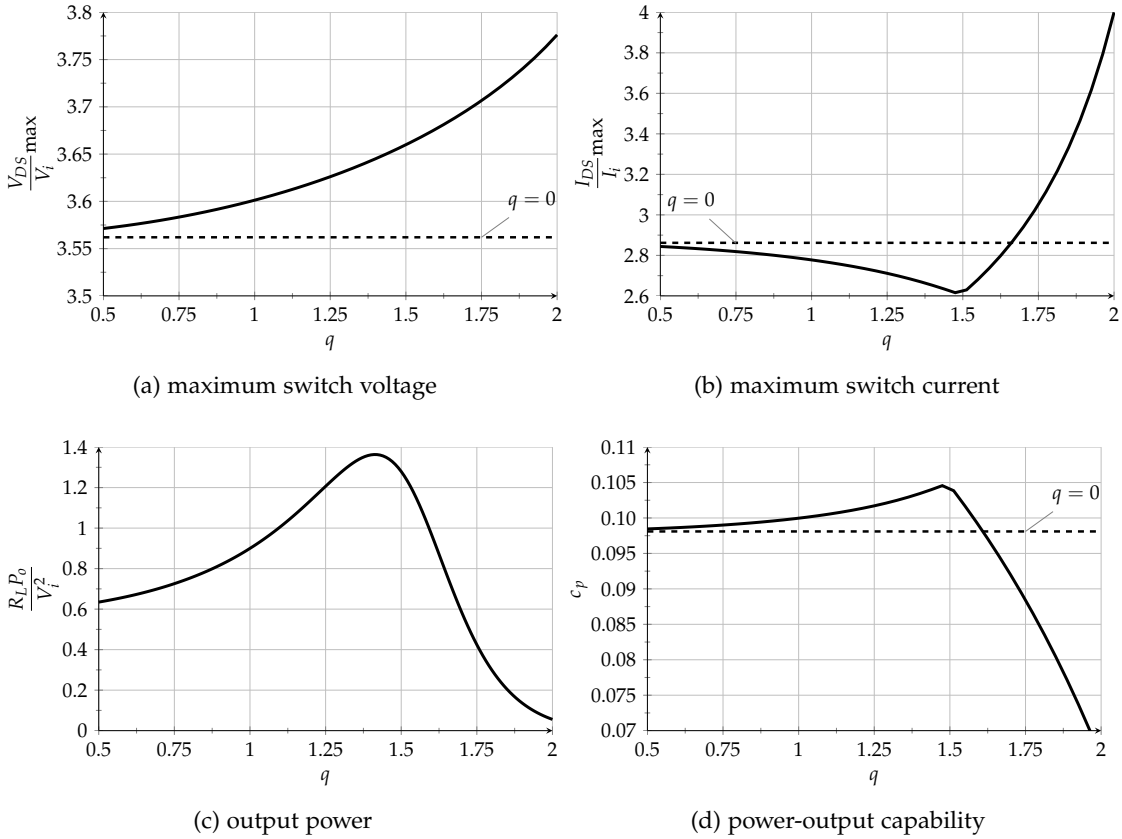

(a) maximum switch voltage

(b) maximum switch current

(c) output power

(d) power-output capability

Fig. 4.18: Calculated parameters showing the inverter's performance as a function of q

The optimum normalised impedances in Fig. 4.17 can be represented by an approximated set of analytical equations to simplify the design process. By using the MATLAB Curve Fitting toolbox, the following set of equations were obtained

$$\frac{\omega L_f}{R_L}(q) = ae^{bq} + ce^{dq} + ee^{fq} \tag{4.148}$$

$$\omega R C_1(q) = \frac{aq^3 + bq^2 + cq + d}{q^2 + eq + f} \tag{4.149}$$

$$\frac{X}{R_L}(q) = \frac{aq + b}{q^2 + cq + d}. \tag{4.150}$$

The values of the coefficients a to f are shown in Table. 4.1. The residual plots are shown in Fig. 4.19 compared with the residuals of another proposed set of equation in [83].

4.4.4 *State-space Modelling*

In this section, a state-space modelling approach will be taken to analyse the basic configuration of the Class E inverter that was shown in Fig. 4.10. The analytic approach used previously was mainly based on the assumptions that the duty cycle of

Table 4.1: Values of the coefficients for Eqs. 4.148-4.150

	$\frac{\omega L_f}{R_L}$	$\omega R C_1$	$\frac{X}{R_L}$
a	1.7294×10^{3}	-23.5985×10^{-3}	-17.7797
b	-13.2617	154.1969×10^{-3}	25.1152
c	34.7455×10^{-6}	-415.9449×10^{-3}	-11.2378
d	5.7554	424.6084×10^{-3}	20.6048
e	98.6020	-3.1012	-
f	-3.5552	2.4996	-

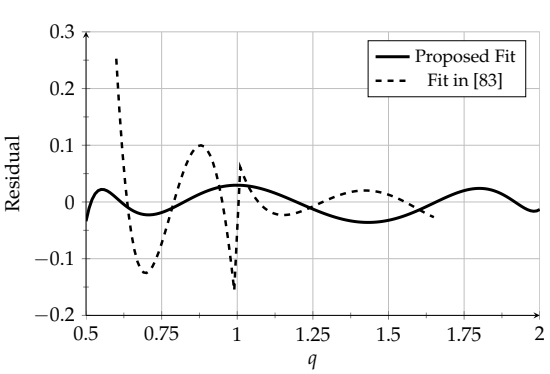

(a) residual of Eq. 4.148

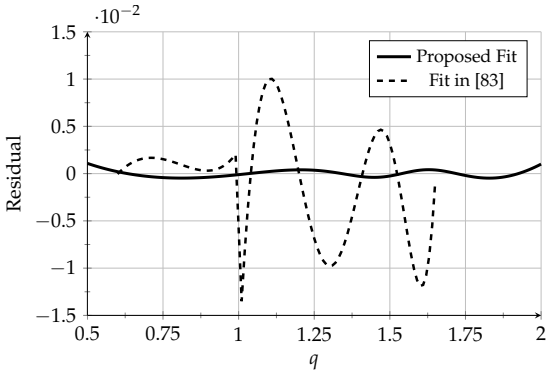

(b) residual of Eq. 4.149

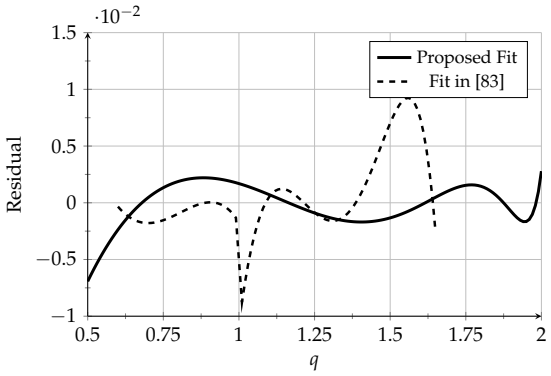

(c) residual of Eq. 4.150

Fig. 4.19: Residual plots of Eqs. 4.148-4.150

the switching frequency is 0.50 and the loaded quality factor of the output network is large. Although the analytical approach can be used to analyse the Class E inverter for different duty cycles and low or finite quality factors, it can be very complicated and can become less intuitive as can be seen in [84]. The state-space modelling approach with the aid of a computer provides a more accurate analysis and can simplify the design process significantly. In addition, it allows Class E inverter to be analysed at different duty cycles.

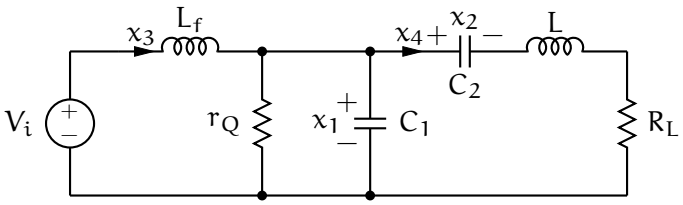

Fig. 4.20: Equivalent circuit of the Class E inverter for state-space representation

Fig. 4.20 shows an improved equivalent circuit representation of the basic Class E inverter that was initially shown in Fig. 4.10. The improvement lies in including a resistor r_Q to represent the resistance of the switch. Resistor r_Q can be either equal to the ON resistance of the switch when the switch is ON or the OFF resistance of the switch when it is OFF. The equivalent circuit has two operating intervals depending on the condition of the switch. The first interval, denoted by ON, represents the Class E inverter when the switch is ON. The second interval, denoted by OFF, represents the Class E inverter when the switch is OFF. Assuming that the Class E inverter is operating at steady-state conditions., the ON and OFF intervals can be defined as follows for each period of the switching signal

$$\begin{aligned} \text{ON interval} \qquad & 0 \leqslant \omega t \leqslant 2\pi D,\ r_Q = r_{ON} \\ \text{OFF interval} \qquad & 0 \leqslant \omega t \leqslant 2\pi(1-D),\ r_Q = r_{OFF} \end{aligned}$$

where D is the duty cycle ratio defined as the ratio of turn ON time to the period of the switching frequency of the switch gate drive signal. Resistors r_{ON} and r_{OFF} represent the ON and OFF resistances of the switch respectively. The equivalent circuit is a piecewise linear system and can be described by the following general state-space representation for the ON

$$\dot{\mathbf{x}}_{ON}(\omega t) = A_{ON}\mathbf{x}(\omega t) + B_{ON}\mathbf{u}(\omega t) \tag{4.151}$$

$$\mathbf{y}_{ON}(\omega t) = C_{ON}\mathbf{x}(\omega t) + D_{ON}\mathbf{u}(\omega t) \tag{4.152}$$

and for the OFF interval

$$\dot{\mathbf{x}}_{OFF}(\omega t) = A_{OFF}\mathbf{x}(\omega t) + B_{OFF}\mathbf{u}(\omega t) \tag{4.153}$$

$$\mathbf{y}_{OFF}(\omega t) = C_{OFF}\mathbf{x}(\omega t) + D_{OFF}\mathbf{u}(\omega t) \tag{4.154}$$

where $\mathbf{x}$ is the state vector and contains the following four voltage and current state variables

$$\mathbf{x}(\omega t) = \begin{bmatrix} x_1(\omega t) \\ x_2(\omega t) \\ x_3(\omega t) \\ x_4(\omega t) \end{bmatrix} = \begin{bmatrix} V_{DS}(\omega t) \\ v_{C_2}(\omega t) \\ I_{L_f}(\omega t) \\ I_o(\omega t) \end{bmatrix}. \tag{4.155}$$

and $\mathbf{u}(\omega t)$ is unit step function defined as

$$\mathbf{u}(\omega t) = \begin{cases} 1 & \omega t \geqslant 0 \\ 0 & \omega t < 0 \end{cases}. \tag{4.156}$$

$\mathbf{y}$ is the output vector, C is the output matrix and Đ is the feedthrough matrix. Using KVL and KCL, the following set of equations can be obtained

$$x_3 = \frac{x_1}{r_Q} + \dot{x_1}\omega C_1 + x_4 \tag{4.157}$$

$$x_4 = \dot{x_2}\omega C_2 \tag{4.158}$$

$$V_i = \dot{x_3}\omega L_f + x_1 \tag{4.159}$$

$$x_1 = x_2 + \dot{x_4}\omega L + x_4 R_L \tag{4.160}$$

Normalising the impedances with respect to R_L, the current state variables with respect to I_i and the voltage states variables with respect V_i, Eqs. 4.157-4.160 become

$$\dot{x}_{n1} = \frac{x_{n1}}{\omega R_L C_1 \frac{r_Q}{R_L}} + \frac{x_{n3}}{\omega R_L C_1} - \frac{x_{n4}}{\omega R_L C_1} \tag{4.161}$$

$$\dot{x}_{n2} = \frac{x_{n4}}{\omega R_L C_2} \tag{4.162}$$

$$\dot{x}_{n3} = -\frac{x_{n1}}{\frac{\omega L_f}{R_L}} + \frac{1}{\frac{\omega L_f}{R_L}} \tag{4.163}$$

$$\dot{x}_{n4} = \frac{x_{n1}}{Q_L} - \frac{x_{n2}}{Q_L} - \frac{x_{n4}}{Q_L} \tag{4.164}$$

where the subscript n denotes a normalised state variable and Q_L is the loaded quality factor given in Eq. 4.4. Based on Eqs. 4.161-4.164, the normalised A, B, C and Đ matrices for both ON and OFF intervals are given by

$$A_{ON} = \begin{bmatrix} \frac{1}{\omega R_L C_1 \frac{r_{ON}}{R_L}} & 0 & \frac{1}{\omega R_L C_1} & -\frac{1}{\omega R_L C_1} \\ 0 & 0 & 0 & \frac{1}{\omega R_L C_2} \\ -\frac{1}{\frac{\omega L_f}{R_L}} & 0 & 0 & 0 \\ \frac{1}{Q_L} & -\frac{1}{Q_L} & 0 & -\frac{1}{Q_L} \end{bmatrix} \tag{4.165}$$

$$A_{OFF} = \begin{bmatrix} \frac{1}{\omega R_L C_1 \frac{r_{OFF}}{R_L}} & 0 & \frac{1}{\omega R_L C_1} & -\frac{1}{\omega R_L C_1} \\ 0 & 0 & 0 & \frac{1}{\omega R_L C_2} \\ -\frac{1}{\frac{\omega L_f}{R_L}} & 0 & 0 & 0 \\ \frac{1}{Q_L} & -\frac{1}{Q_L} & 0 & -\frac{1}{Q_L} \end{bmatrix} \tag{4.166}$$

$$B_{ON} = B_{OFF} = B = \begin{bmatrix} 0 \\ 0 \\ \frac{1}{\frac{\omega L_f}{R_L}} \\ 0 \end{bmatrix} \tag{4.167}$$

$$C_{ON} = C_{OFF} = C = \begin{bmatrix} 1 & 0 & 0 & 0 \\ 0 & 1 & 0 & 0 \\ 0 & 0 & 1 & 0 \\ 0 & 0 & 0 & 1 \end{bmatrix} \tag{4.168}$$

$$Đ_{ON} = Đ_{OFF} = \begin{bmatrix} 0 \\ 0 \\ 0 \\ 0 \end{bmatrix}. \tag{4.169}$$

The general solution to Eqs. 4.151 and 4.152 is given by

$$\mathbf{x}(\omega t) = \mathbf{x_n}(\omega t) + \mathbf{x_f}(\omega t). \tag{4.170}$$

Function $\mathbf{x_n}$ is the natural response matrix, or the zero-input response matrix, and is equal to

$$\mathbf{x_n}(\omega t) = e^{A\omega t}\mathbf{x}(0) \tag{4.171}$$

where e is the matrix exponential function and $\mathbf{x}(0)$ is the initial condition matrix. Function $\mathbf{x_f}$ is the forced response matrix, or the zero-state response matrix, and is equal to

$$\mathbf{x_f}(\omega t) = \int_0^{\tau} e^{A(\omega t-\tau)} B\mathbf{u}(\tau) d\tau = A^{-1}\left(e^{A\omega t} - \mathbf{I}\right) B. \tag{4.172}$$

where $\mathbf{I}$ is the 4×4 identity matrix and e is the matrix exponential function. The initial condition matrix $x(0)$ can be determined by applying the continuity conditions of the voltages across C_1 and C_2 and the currents in L_f and L as the inverter transitions from the ON interval to the OFF interval and from the OFF interval to the ON interval as follows

$$\mathbf{x}_{ON}(0) = \mathbf{x}_{OFF}(\omega t)\Big|_{\omega t=2\pi(1-D)} \tag{4.173}$$

$$\mathbf{x}_{OFF}(0) = \mathbf{x}_{ON}(\omega t)\Big|_{\omega t=2\pi D}. \tag{4.174}$$

It is noted that the state-space equations (Eqs. 4.161-4.164) and the general solution equation (Eq. 4.170) represent a periodic system. By substituting Eqs. 4.171-4.174 in 4.170, the initial conditions for all periods of the switching signal are equal to

$$\begin{bmatrix} \mathbf{x}_{ON}(2\pi_m) \\ \mathbf{x}_{OFF}(2\pi_m) \end{bmatrix} = \begin{bmatrix} -e^{A_{ON}2\pi D} & \mathbf{I} \\ \mathbf{I} & -e^{A_{OFF}2\pi(1-D)} \end{bmatrix}^{-1} \begin{bmatrix} A_{ON}^{-1}(e^{A_{ON}2\pi D} - \mathbf{I}) \\ A_{OFF}^{-1}(e^{A_{OFF}2\pi(1-D)} - \mathbf{I}) \end{bmatrix} B \quad \text{for } m = 0, 1, 2, \ldots \tag{4.175}$$

For optimal switching conditions, the initial conditions of the following states for all periods of the switching signal should be

$$x_{1ON}(2\pi m) = 0 \quad \text{for } m = 0, 1, 2, \ldots \tag{4.176}$$

$$x_{3ON}(2\pi m) - x_{4ON}(2\pi m) = 0 \quad \text{for } m = 0, 1, 2, \ldots \tag{4.177}$$

Eq. 4.176 corresponds to the ZVS condition whereas Eq. 4.177 corresponds to the ZVDS condition. Eqs. 4.176-4.177 allow for two unknown parameters to be solved for. In order to compare the state-space analysis approach with the analytical analysis approach, the two unknown parameters that will be solved, for a given D and Q_L, are $\omega R_L C_1$ and $\omega R_L C_2$. Fig. 4.21 shows several numerically calculated parameters of the basic Class E inverter. It was assumed that the DC-feed inductance is very large ($\approx \infty$), r_{ON} is very small (≈ 0), r_{OFF} is very large ($\approx \infty$) and the duty cycle is 0.50. Also shown are the same parameters that were obtained using the closed form equations of the analytical approach in Sec. 4.4.1 for comparison. It can be seen that the parameters that were calculated numerically via the state-space approach converges to those of the analytical approach at higher Q_L values. The state-space modelling approach also shows the parameters for lower Q_L values which cannot be obtained using the closed-form equations of the analytical approach since it is only limited to higher Q_L values. The MATLAB code for obtaining these parameters is in Appendix A.1.2.

4.4.5 *Sub-optimum Operation*

In the previous sections, the Class E inverter was analysed for optimum switching conditions. The normalised values of its components, mainly $\omega R_L C_1$ and $\omega R_L C_2$, were calculated to satisfy the ZVS and ZVDS conditions. These values are only valid for a certain load resistance. In many applications, and specifically in inductive links, the resistance representing load is not constant and will vary over a certain range while the Class E inverter is operating. Therefore, the Class E inverter will no longer operate at its optimum switching conditions. However, the Class E inverter can still achieve a 100 % theoretical efficiency by achieving only ZVS. In this case the Class E inverter is said to be operating at a sub-optimum switching condition. The load resistance range at which the Class E inverter operates in its sub-optimum switching condition is given by [85]

$$0 \leqslant R_L \leqslant R_{Lopt} \tag{4.178}$$

The criteria in Eq. 4.178 could be represented as

$$0 \leqslant s \leqslant 1 \tag{4.179}$$

where

$$s = \frac{R_L}{R_{Lopt}}. \tag{4.180}$$

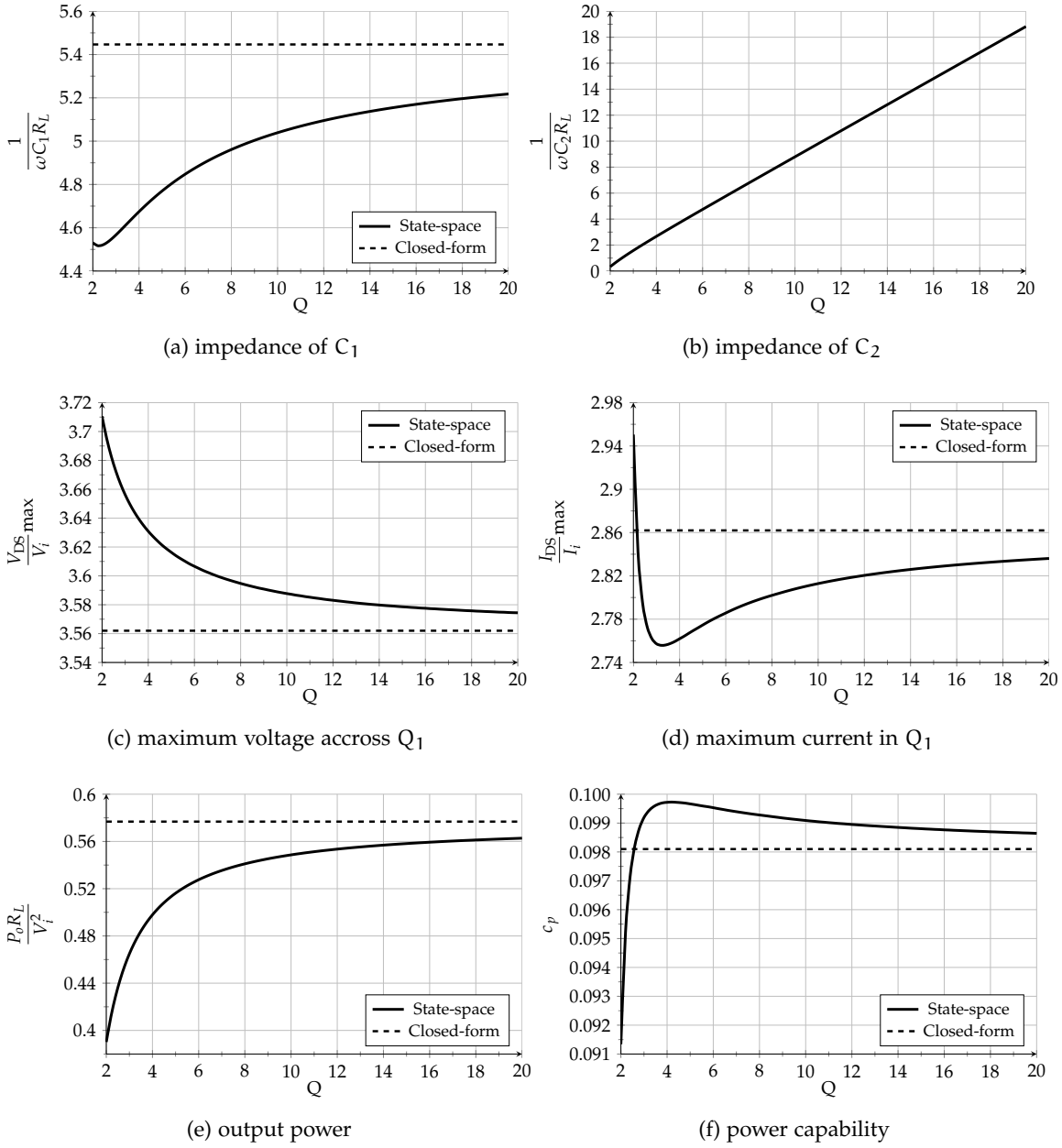

(a) impedance of C_1

(b) impedance of C_2

(c) maximum voltage accross Q_1

(d) maximum current in Q_1

(e) output power

(f) power capability

Fig. 4.21: Variation of normalised values and parameters with Q_L

Operating at a sub-optimum condition means that the Class E inverter cannot achieve ZVDS. Therefore, the current in the switch could be either negative or positive when the switch is turned ON. As a result, the Class E inverter behaves much like a Class D inverter. The criteria in Eq. 4.178 was reached using an analytical approach [85]. Although it is useful in terms of determining the load range for lossless operation, it does not show how the variation in load resistance affects the parameters of the Class E inverter such as maximum voltage and current of the switch, in addition to the output power capability. There hasn't been an attempt to provide a clear general characterization of the variation in load resistance on the performance of the Class E inverter since the criteria was first published in 1986.

The state-space modelling approach presented in Sec. 4.4.4 can be used to provide further insight on the performance of the Class E inverter operating in a sub-optimum switching condition. In order to achieve this, the normalised A matrices in Eqs. 4.165-4.167 become

$$A_{ON} = \begin{bmatrix} \frac{1}{\omega R_{Lopt} C_1 \frac{r_{ON}}{R_{Lopt}}} & 0 & \frac{1}{\omega R_{Lopt} C_1} & -\frac{1}{\omega R_{Lopt} C_1} \\ 0 & 0 & 0 & \frac{1}{\omega R_{Lopt} C_2} \\ -\frac{1}{\frac{\omega L_f}{R_{Lopt}}} & 0 & 0 & 0 \\ \frac{1}{Q_{opt}} & -\frac{1}{Q_{opt}} & 0 & -\frac{s}{Q_{opt}} \end{bmatrix} \tag{4.181}$$

$$A_{OFF} = \begin{bmatrix} \frac{1}{\omega R_{Lopt} C_1 \frac{r_{OFF}}{R_{Lopt}}} & 0 & \frac{1}{\omega R_L C_1} & -\frac{1}{\omega R_{Lopt} C_1} \\ 0 & 0 & 0 & \frac{1}{\omega R_{Lopt} C_2} \\ -\frac{1}{\frac{\omega L_f}{R_{Lopt}}} & 0 & 0 & 0 \\ \frac{1}{Q_{opt}} & -\frac{1}{Q_{opt}} & 0 & -\frac{s}{Q_{opt}} \end{bmatrix} \tag{4.182}$$

$$B_{ON} = B_{OFF} = B = \begin{bmatrix} 0 \\ 0 \\ \frac{1}{\frac{\omega L_f}{R_{Lopt}}} \\ 0 \end{bmatrix} \tag{4.183}$$

where the Q_{opt} is the loaded quality factor for the optimum load resistance, i.e.

$$Q_{opt} = \frac{\omega L}{R_{L_{opt}}} \tag{4.184}$$

Since in most cases the Class E inverter is initially designed to operate at optimum load resistance, the values of C_1 and C_2 are those that will result in optimum operation. Following the analysis in the previous section, for sub-optimal operation to occur, only the initial condition given in Eq. 4.173 is valid. This allows for only one parameter to be solved for. In fact, the only parameter that could be solved is the duty cycle since all other parameter and component values are known for the optimum switching conditions case.

Fig. 4.22 shows how the performance of Class E inverter is affected as the load changes from zero to R_{Lopt} for several values of Q_{opt}. The duty cycle, maximum switch voltage and output current increase as the load resistance decreases towards zero, whereas the power-output capability increases as the load resistance increases towards R_{Lopt}. Although it may seem that operating the Class E inverter in a at sub-optimum switching condition may be preferred since it delivers more power, the increasing

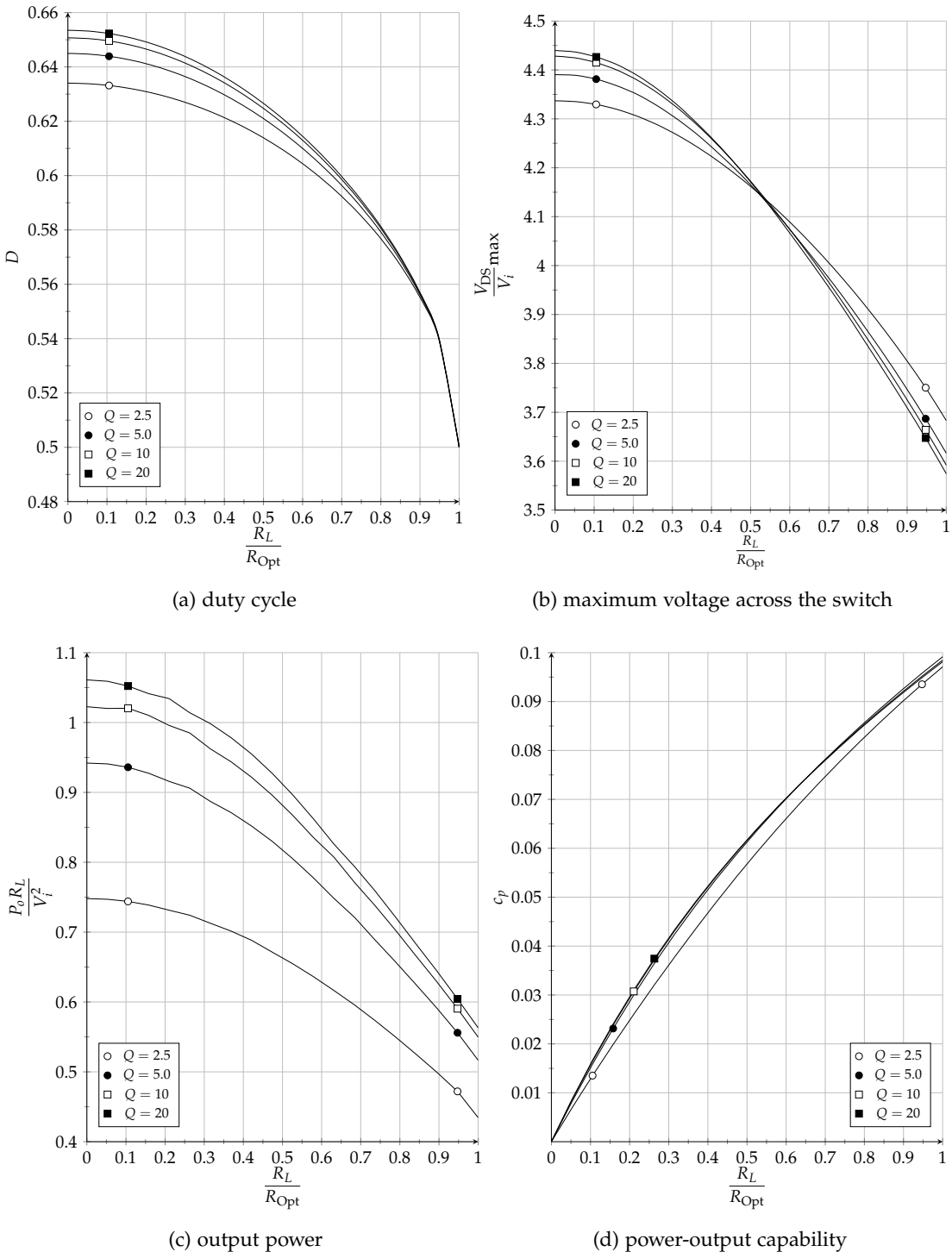

(a) duty cycle

(b) maximum voltage across the switch

(c) output power

(d) power-output capability

Fig. 4.22: Variation of normalised values and parameters with load resistance

voltage stresses of the switch may practically limit the amount of power that can be delivered to the load and may result in lower efficiencies. Appendix A.1.3 includes the MATLAB code to obtain these plots. Fig. 4.23 show the voltage and current waveforms of the switch for two different load values at $Q_{opt} = 10$. It can be seen that the peaks of the switch's voltage and current increase as the load resistance decreases from its optimum value to 75 % and then to 25 %. The fact that the duty cycle increases with a

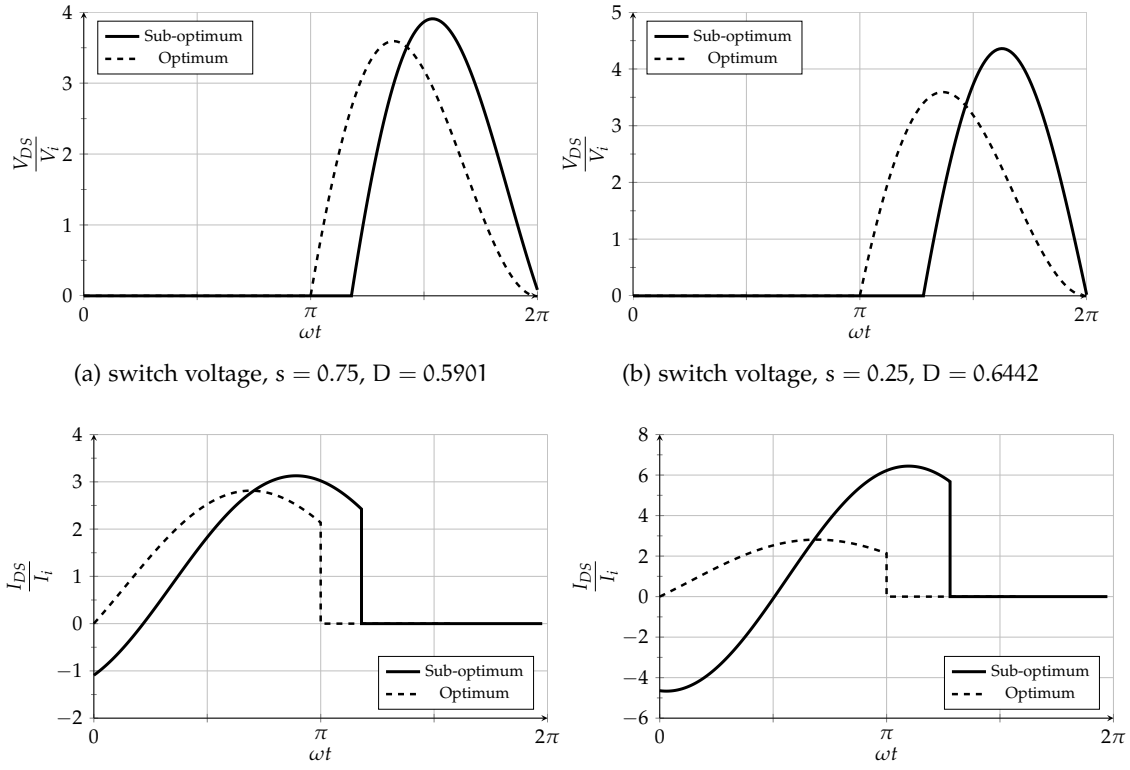

(a) switch voltage, s = 0.75, D = 0.5901

(b) switch voltage, s = 0.25, D = 0.6442

(c) switch current, s = 0.75, D = 0.5901

(d) switch current, s = 0.25, D = 0.6442

Fig. 4.23: Voltage and current waveforms of the switch for $Q_{opt} = 10$

decreasing load resistance does not necessarily mean that the actual duty cycle of the switching signal to the switch should be varied. If the switch is a MOSFET, then its body diode will conduct once the MOSFET's voltage crosses zero volts. Therefore the actual duty cycle of the switching could remain at 0.50, therefore simplifying the gate driving circuitry.

4.5 OTHER CLASSES AND CONFIGURATIONS

As stated in the beginning of this chapter, the majority of the inverters that have been used as primary coil drivers in inductive links have been either Class D or Class E. Other classes or configurations of inverters can still be used as primary coil drivers, however they may not be as powerful and efficient as Class D or Class E. This section provides a brief review of certain inverters that are similar in operation to Class D and Class E inverters and discusses their suitability to be used as primary coil drivers.

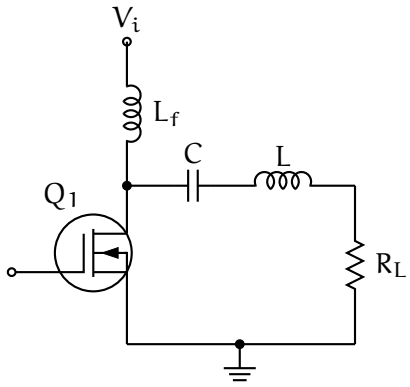

Fig. 4.24: The Class E ZCS and ZDCS inverter

4.5.1 *Class E Current-switching Inverter*

Fig. 4.24 show the circuit diagram of a Class E current-switching inverter in its simplest form [86]. The construction of the inverter is similar to that of a Class E voltage-switching inverter. However it achieves ZCS and ZDCS conditions rather than ZVS and ZDVS conditions. The DC-feed inductance in Class E current-switching inverters is always finite, therefore its value has an effect on the inverter's performance. The load network consists of a series resonant network. The inductor L could represent the inductance of the primary coil of an inductive link and resistor R_L could represent the reflected resistance. The inverter is usually operated at a switching frequency below the resonant frequency of the load network.

The Class E current-switching inverter has a theoretical efficiency of 100 %, however practical issues, such as switch output capacitance and parasitics in the board layout, can affect its performance and prevent it from achieving a high efficiency. The inverter is more prone to damage if the ZCS condition is not met since large voltage spikes could occur across the switch [58].

The output power of the Class E current-switching is given by [58]

$$P_o = \frac{8}{\pi^2(\pi^2+4)}\frac{V_i^2}{R_L} \approx 0.05844\frac{V_i^2}{R_L} \tag{4.185}$$

which is about ten times less than that of a basic Class E voltage-switching inverter. Therefore it can be concluded that the Class E current-switching inverter may not be suitable to be used as a primary coil driver due to its low output power capability and low practical efficiency.

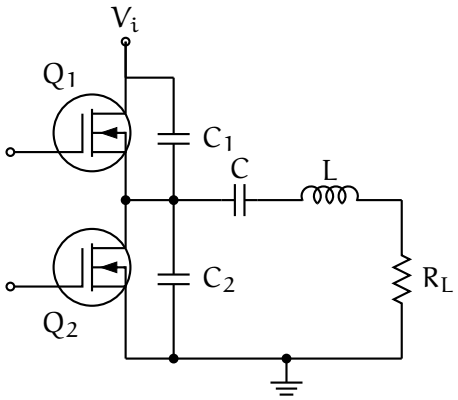

Fig. 4.25: The Class DE inverter

4.5.2 *Class DE Inverters*

Class DE inverters join Class D and Class E inverter together by providing the benefits of each class in one inverter [58]. Fig. 4.25 shows the circuit diagram of a basic Class DE inverter. The maximum voltages across the switches is the same as that of a basic voltage switching Class D inverter. The addition of capacitors in parallel with the switches allows it to operate at ZVS and ZDVS conditions similar to a Class E inverter. The load network consists of a series resonant network. The inductor L could represent the inductance of the primary coil of an inductive link and resistor R_L could represent the reflected resistance.

In Class DE inverters the switches are switched ON in a complementary manner with certain deadtime periods. This means that both switches could be OFF at a certain time. Therefore the duty cycle of the switching signals is usually below 0.50. Class DE inverters have a theoretical efficiency of 100 % and practical implementations could obtain efficiencies above 90 %. The output power of a Class DE inverter is given by [58]

$$P_o = \frac{1}{2\pi^2}\frac{V_i^2}{R_L} \approx 0.05066\frac{V_i^2}{R_L} \tag{4.186}$$

which is about ten times less than that of a basic Class E voltage-switching inverter. Therefore it can be concluded that this inverter can be used in low power inductive links such as wireless power for medical implants. For it to be used high power applications, the input voltage will have to be increased significantly which generally may not be a practical solution.

4.6 CONCLUSIONS

This chapter presented a review of switched-mode resonant DC/AC inverters. The main classes reported in literature that have been used in inductive links are Class D and Class E. Both classes meet the requirements of inductive links in terms of power and efficiency. Class D inverters have the lowest voltage and current stresses but they consist of two or four switches, therefore component layout, heat dissipation and gate driving circuity require further consideration. Whereas Class E inverters have higher voltage and current stresses, however they can deliver more power and can only consist of a single switch. In addition, the source terminal of the switch in a Class E inverter is connected to ground therefore simplifies the gate driving circuitry.

Class D inverters are more tolerant to variations in the load; they can maintain their efficient operation over a certain range above and below the nominal load value. Whereas Class E inverters are less tolerant to variations in load; they can maintain their efficient operation for load resistance values that are lower than their optimum load value. In addition, the voltage and current stresses increase as the load resistance decreases. Therefore a switch with a maximum voltage rating of at least four times the input voltage may be required if the Class E inverter is to be operated in a sub-optimum switching condition.

Power regulation in inductive links is an important issue, especially in applications where the load and distance between the coils varies continuously. Neither Class D or Class E inverters have good output regulation. For instance, as the coils of an inductive links are brought closer to each other, the reflected impedance of the secondary coil will increase and the output power of both classes will then decrease. If the coils are further apart, the reflected impedance will decrease and the output power of both classes will increase. In order to keep the output power of a Class D or a Class E inverter relatively constant over a certain load range, certain control methods will have to be introduced. For Class D inverters, output power can be controlled by adjusting the frequency of the switching signal [60] or using phase control as mentioned in Sec. 4.3.3. Controlling the output power of a Class E inverter can be done by varying the switching frequency, however it is less dynamic and usually done on a trial and error basis as performed in [85]. A novel control method for Class E inverters will be presented in the following chapter that involves using saturable reactors.

Table 4.2 lists all the inverters that have been discussed in this chapter and provides a comparison between them in terms of output power, maximum voltages and currents in each inverter, number of switches, power-output capability and power control methods.

Table 4.2: Summary and comparison between the resonant inverter classes and configurations

Inverter Class	Output Power	Max. Switch Voltage	Max. Switch Current	No. of Switches	Power-Output Capability c_p	Power Control Methods
Half-Bridge Class D ZVS	$\frac{2V_i^2 R_L}{\pi^2 R_L^2\left[1+\frac{\omega^2 L^2}{R_L^2}\left(\frac{\omega}{\omega_o}-\frac{\omega_o}{\omega}\right)^2\right]}$, $\frac{2V_i^2}{\pi^2 R_L}\approx 0.2026\frac{V_i^2}{R_L}$ at $\omega=\omega_o$	V_i	max= $\frac{2V_i}{\pi R_L}\approx 0.6366\frac{V_i}{R_L}$ at $\omega=\omega_o$	2	≈ 0.1592 at $\omega=\omega_o$	PWM DC supply
Push-Pull Class D ZVS	$\frac{8V_i^2}{\pi^2 R_L}\approx 0.8106\frac{V_i^2}{R_L}$	$2V_i$	$\frac{4V_i}{\pi R_L}\approx 1.2732\frac{V_i}{R_L}$	2	≈ 0.1592 at $\omega=\omega_o$	-
H-Bridge Class D ZVS	$\frac{8V_i^2 R_L}{\pi^2 Z_o^2\left[\left(\frac{R_L}{Z_o}\right)^2+\left(\frac{\omega}{\omega_o}-\frac{\omega_o}{\omega}\right)^2\right]}$, $\frac{8V_i^2}{\pi^2 R_L}\approx 0.8106\frac{V_i^2}{R_L}$ at $\omega=\omega_o$	V_i	max= $\frac{4V_i}{\pi R_L}\approx 1.2732\frac{V_i}{R_L}$ at $\omega=\omega_o$	4	≈ 0.0796 at $\omega=\omega_o$	PWM Phase shift control DC Supply
Class D ZCS	$\frac{\pi^2 V_i^2}{2R_L}\approx 4.9348\frac{V_i^2}{R_L}$	$\pi V_i\approx 3.1416V_i$	$\frac{\pi^2 V_i}{2R_L}\approx 4.9348\frac{V_i}{R_L}$	2	≈ 0.1592 at $\omega=\omega_o$	-
Push-Pull Class D ZCS	$\frac{\pi^2 V_i^2}{2R_L}\approx 4.9348\frac{V_i^2}{R_L}$	$\pi V_i\approx 3.1416V_i$	$\frac{\pi^2 V_i}{4R_L}\approx 2.4674\frac{V_i}{R_L}$	2	≈ 0.1592 at $\omega=\omega_o$	-
Class E ZVS & ZVDS	$\frac{8V_i^2}{(\pi^2+4)R_L}\approx 0.5768\frac{V_i^2}{R_L}$	$2\pi(\pi-\phi)V_i$ $\approx 3.5619V_i$	$\approx 1.6508\frac{V_i}{R_L}$	1	≈ 0.0981	DC supply
Push-Pull Class E ZVS & ZVDS	$\frac{32V_i^2}{(\pi^2+4)R_L}\approx 2.3072\frac{V_i^2}{R_L}$	$2\pi(\pi-\phi)V_i$ $\approx 3.5619V_i$	$\approx 3.3016\frac{V_i}{R_L}$	2	≈ 0.0981	DC supply
Finite DC-Feed Ind. Class E	max $\approx 1.365\frac{V_i^2}{R_L}$ at $q=1.412$	$\approx 3.647V_i$ at $q=1.412$	$\approx 3.6151\frac{V_i}{R_L}$ at $q=1.412$	1	≈ 0.1034 at $q=1.412$	DC supply
Class E ZCS & ZDCS	$\frac{8V_i^2}{\pi^2(\pi^2+4)R_L}\approx 0.05844\frac{V_i^2}{R_L}$	$\left(\frac{\sqrt{\pi^2+4}}{2}+1\right)V_i$ $\approx 2.8621V_i$	$\approx 3.562I_i$	1	≈ 0.0981	DC supply
Class DE ZVS & ZVDS	$\frac{V_i^2}{2\pi^2 R_L}\approx 0.0507\frac{V_i^2}{R_L}$	V_i	$\frac{V_i}{\pi R_L}\approx 0.3183\frac{V_i}{R_L}$	2	-	DC supply

5

DESIGN AND OPTIMIZATION OF CLASS E PRIMARY COIL DRIVERS

5.1 INTRODUCTION

This chapter will discuss the application of Class E inverters as primary coil drivers in inductive links. The chapter begins by modelling and analysing a system consisting of a Class E ZVS and ZVDS inverter and the inductive link designed in Chapter 3. Two different analysis approaches are considered; an analytical approach provides an initial view on how the system operates under ideal assumptions, then a state-space modelling approach is taken to provide a more accurate analysis of the system while considering practical limitations and non-idealities. An investigation is performed on how the Class E inverter's performance is affected as the load and distance between the coils of the inductive link are varied.

Based on the performed investigation, several tuning methods are suggested to allow the Class E inverter to operate at optimum switching conditions over a wide load range. The tuning methods will be derived based on the analytical and the state-space analysis approaches. Extensive experimental results will be presented to show the implementation of the proposed tuning methods.

5.2 MODELLING AND ANALYSIS OF AN INDUCTIVE LINK WITH A CLASS E DRIVER

5.2.1 *Design*

The Class E inverter was chosen as the primary coil driver due to its simplicity, high efficiency and high power delivering capability as discussed in Chapter 4. Fig. 5.1 shows the circuit diagram of a Class E inverter driving an inductive link. The Class E

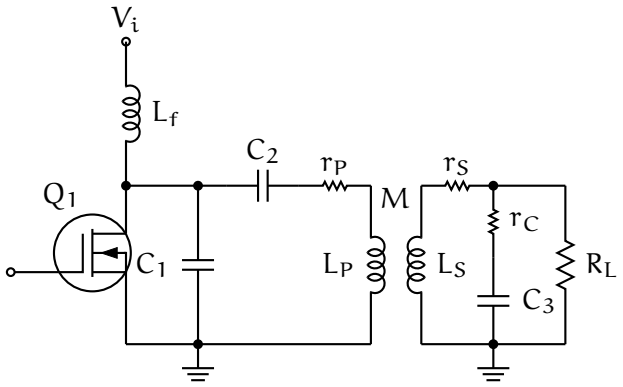

Fig. 5.1: Class E inverter as the primary driver for an inductive link

inverter is the ZVS and ZVDS configuration discussed in Sec. 4.4 and the inductive link is of a parallel resonant secondary configuration as discussed in Sec. 3.4.3. The inductance of the primary coil along with capacitor C_2 form the Class E inverter's load network. Inductor L_S represents the secondary coil and M is the mutual inductance between the primary and secondary coils. Capacitor C_3 is connected in parallel with L_S and its value is chosen to set the resonant frequency of the secondary coil to be equal to the switching frequency of the Class E inverter. Resistor R_L represents the load's resistance and resistors r_P, r_S and r_C represent the ESR of the primary coil, the secondary coil and capacitor C_3.

5.2.2 *Analysis Using the Analytical Approach*

The analysis of the Class E inverter that will be presented here takes into consideration the reflected impedance of the inductive link. The equivalent circuit diagram of the Class E inverter including the reflected impedances of the inductive is shown in Fig. 5.2. The output load network of the Class E inverter now consists of the primary coil inductance L_P and its ESR, the reflected impedances of the secondary coil at a certain coupling coefficient and a residual impedance X. Capacitance C, the primary coil inductance and the imaginary components of the reflected impedance are tuned to the switching frequency. The residual impedance may or may not be a physical component, it is assumed in this analysis that the residual impedance and capacitance C form a physical capacitor and is referred to as C_2.

The analysis will be based on the following assumptions:

- The MOSFET is an ideal switch whose ON resistance is zero, and its turn ON and OFF times are zero.

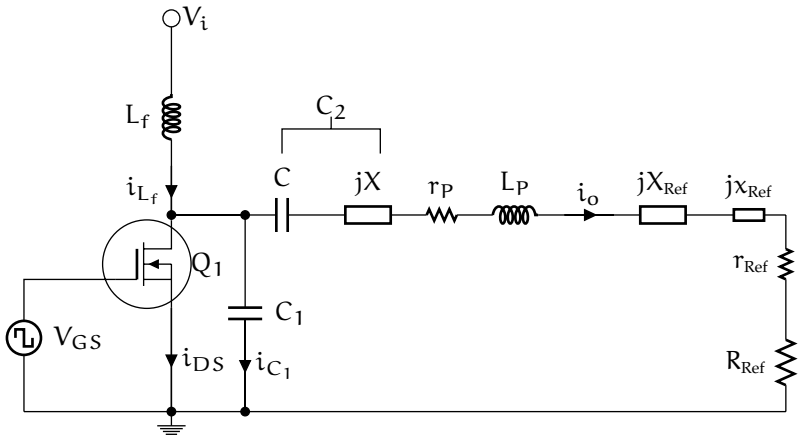

Fig. 5.2: Equivalent circuit of the Class E inverter circuit including the reflected impedances of the inductive link

- The loaded quality factor of the series load network is high enough such that the current flowing through it (I_o) is sinusoidal and is equal to

$$I_o(\omega t) = i_m \sin(\omega t + \phi). \tag{5.1}$$

- The duty cycle of the MOSFET gate drive signal is 50%.

Case I: Infinite DC-feed inductance

It will be initially assumed that the DC-feed inductance L_f is infinite for simplification. Therefore the current flowing in L_f is a DC current equal to I_i. In addition, the Class E inverter is to be operated at optimum switching conditions. In this case the analysis is similar to that of the Class E inverter with infinite DC-feed inductance in Sec. 4.4.1. Therefore Eqs. 4.54-4.88 remain the same since the current in the load network is assumed to be sinusoidal. Only Eqs. 4.89-4.96 can be altered to include the additional components in the load network. The loaded quality factor in this case is

$$Q_L = \frac{\omega L_P}{R_T} \tag{5.2}$$

where

$$R_T = R_{Ref} + r_{Ref} + r_P. \tag{5.3}$$

From Eq. 4.89 the total power supplied to the resistive elements of the inverter is

$$P_i = \frac{8}{\pi^2 + 4}\frac{V_i^2}{R_T} = \frac{1}{2} i_m^2 R_T \tag{5.4}$$

and the total delivered to the reflected resistive corresponding to the load (R_{Ref}) is

$$P_o = \frac{1}{2} i_m^2 R_{Ref}. \tag{5.5}$$

Hence, the efficiency of the Class E inverter with infinite DC-feed inductance and the inductive link is

$$\eta = \frac{P_o}{P_i} = \frac{R_{Ref}}{R_T}. \tag{5.6}$$

From Eqs. 4.91-4.96 the value of capacitor C_1 is

$$C_1 = \frac{8}{\pi(\pi^2+4)\omega R_T} \approx \frac{0.1836}{\omega R_T} \tag{5.7}$$

and the unknown inductance X is

$$X = \frac{\pi^2-4}{2(\pi^2+4)\omega^2 C_1} \approx \frac{0.2116}{\omega^2 C_1}. \tag{5.8}$$

From Eq. 4.94 the value of the primary coil's inductance is

$$L_P = \frac{Q_L R_T}{\omega}, \tag{5.9}$$

the value of capacitor C_2 is

$$C_2 = \frac{1}{\omega(Q_L R_T - \omega X)} \approx \frac{1}{\omega R_T (Q_L - 1.1525)}, \tag{5.10}$$

and the DC input current is

$$I_i = \frac{8}{\pi^2+4}\frac{V_i}{R_L} \approx 0.5768\frac{V_i}{R_T}. \tag{5.11}$$

Case II: Finite DC-feed inductance

In this case it is assumed that the DC-feed inductance is finite. Therefore its values will affect the performances of the Class E inverter and the inductive link. In addition, the Class E inverter is to be operated at optimum switching conditions. The analysis in this case is similar to that of the Class E inverter with finite DC-feed inductance in Sec. 4.4.3. Therefore Eqs. 4.102-4.131 and Eqs. 4.144-4.147 remain the same since the current in the load network is assumed to be sinusoidal. Beginning with power relations, the power supplied by the power source is consumed in the reflected resistances (R_{Ref} and r_{Ref}) and the ESR of the primary coil r_P

$$P_i = \frac{8}{\pi^2+4}\frac{V_i^2}{R_T} = \frac{1}{2} i_m^2 R_T \tag{5.12}$$

and the total power delivered to the reflected resistors corresponding to the load (R_{Ref}) is

$$P_o = \frac{1}{2} i_m^2 R_{Ref}. \tag{5.13}$$

Hence, the efficiency of the Class E inverter with finite DC-feed inductance and the inductive link is

$$\eta = \frac{P_o}{P_i} = \frac{R_{Ref}}{R_T}. \tag{5.14}$$

From Eq. 4.134 the DC resistance seen by the voltage source is

$$R_{DC} = \frac{V_i}{I_o} = R_T \Big/ \frac{1}{2\pi^2}\left(\frac{\pi^2}{2p} - 2\cos\phi + \pi\sin\phi\right)^2. \tag{5.15}$$

The normalised DC-feed inductor and the shunt capacitor with respect to the resistance R_T can be defined using Eqs. 4.119, 4.124 and 4.133 by

$$\frac{\omega L_f}{R_T} = p \Big/ \left(\frac{\pi}{2p} - \frac{2}{\pi}\cos\phi + \sin\phi\right) \tag{5.16}$$

$$\omega R_T C_1 = \frac{R_T}{q^2 \omega L_f}. \tag{5.17}$$

where q and p are given in Eqs 4.119 and 4.124 respectively. From Eqs. 4.140-4.143 the value of the primary coil's inductance L_P is

$$L = \frac{Q_L R_T}{\omega} \tag{5.18}$$

and the value of capacitance C is

$$C = \frac{1}{\omega(\omega L_P + X_{Ref} + x_{Ref})}. \tag{5.19}$$

Therefore the actual value of C_2 is

$$C_2 = \frac{1}{\frac{1}{C} + \omega X_b}. \tag{5.20}$$

5.2.3 *Analysis Using the State-space Representation Approach*

The equivalent circuit of the Class E inverter along and the inductive link is shown in Fig. 5.3 for state-space representation. The switch's resistance r_Q is represented by resistances r_{ON} and r_{OFF} for the ON and OFF intervals respectively. The equivalent circuit is a piecewise linear system and can be described by general state-space representation given in Eqs 4.151-4.154 for each ON and OFF intervals

$$\dot{\mathbf{x}}_{ON}(\omega t) = A_{ON}\mathbf{x}(\omega t) + B_{ON}\mathbf{u}(\omega t) \tag{5.21}$$

$$\mathbf{y}_{ON}(\omega t) = C_{ON}\mathbf{x}(\omega t) + Đ_{ON}\mathbf{u}(\omega t) \tag{5.22}$$

$$\dot{\mathbf{x}}_{OFF}(\omega t) = A_{OFF}\mathbf{x}(\omega t) + B_{OFF}\mathbf{u}(\omega t) \tag{5.23}$$

$$\mathbf{y}_{OFF}(\omega t) = C_{OFF}\mathbf{x}(\omega t) + Đ_{OFF}\mathbf{u}(\omega t) \tag{5.24}$$

where $\mathbf{x} = [x_1, x_2, x_3, x_4, x_5, x_6]^T$ is the state vector. The states x_1, x_2, x_3 represent the voltage across the shunt capacitor C_1, the voltage across the series capacitor C_2 and the voltage across the resonant capacitor C_S for both ON and OFF intervals respectively. The states x_4, x_5, x_6 represent the current of the DC-feed inductance L_f, the current

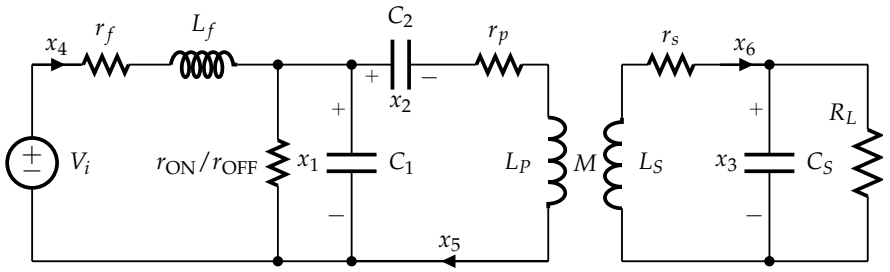

Fig. 5.3: Equivalent circuit of the Class E inverter and the inductive link for both ON and OFF intervals

of the primary coil L_p and the current of the secondary coil L_s for both ON and OFF intervals respectively. Resistance r_f represents the ESR of the DC-feed inductor. The input vector $\mathbf{u}(\omega t)$ is equal to the unit step function defined in Eq. 4.156. The ON interval's domain is defined as $0 \leqslant \omega t \leqslant 2\pi D$, whereas the domain for the OFF interval is defined as $0 \leqslant \omega t \leqslant 2\pi(1-D)$. Using KVL and KCL, the following equations can be obtained

$$V_i = x_4 r_f + \dot{x}_4 L_f + x_1 \tag{5.25}$$

$$x_5 = C_2 \dot{x}_2 \tag{5.26}$$

$$x_6 = \dot{x}_3 C_S + \frac{x_3}{R_L} \tag{5.27}$$

$$V_i = x_4 r_f + \dot{x}_4 L_f + x_1 \tag{5.28}$$

$$x_4 = \frac{x_1}{r_Q} + \dot{x}_1 C_1 + x_5 \tag{5.29}$$

$$x_1 = x_2 + x_5 r_p + \dot{x}_5 L_p - \dot{x}_6 M \tag{5.30}$$

$$\dot{x}_5 M = \dot{x}_6 L_S + x_6 r_s + x_3. \tag{5.31}$$

Using Equ. 5.30 & 5.31, the derivative states $\dot{x_5}$ and $\dot{x_6}$ can be written as

$$\dot{x_5} = \frac{1}{L_p L_s - M^2}\left(x_1 L_s - x_2 L_s - x_3 M - x_5 L_s r_p - x_6 M r_s\right) \tag{5.32}$$

$$\dot{x_6} = \frac{1}{L_p L_s - M^2}\left(x_1 M - x_2 M - x_3 L_p - x_5 M r_p - x_6 L_p r_s\right). \tag{5.33}$$

Based on Eqs. 5.25-5.29 and Eqs. 5.32-5.33, the matrices A, B, C and Đ for both ON and OFF intervals are given by

$$A_{ON} = \begin{bmatrix} -\frac{1}{\omega r_{ON} C_1} & 0 & 0 & \frac{1}{\omega C_1} & -\frac{1}{\omega C_1} & 0 \\ 0 & 0 & 0 & 0 & \frac{1}{\omega C_2} & 0 \\ 0 & 0 & -\frac{1}{\omega R_L C_S} & 0 & 0 & \frac{1}{\omega C_S} \\ -\frac{1}{\omega L_f} & 0 & 0 & -\frac{r_f}{\omega L_f} & 0 & 0 \\ \frac{\omega L_s}{\omega^2(L_p L_s - M^2)} & -\frac{\omega L_s}{\omega^2(L_p L_s - M^2)} & -\frac{\omega M}{\omega^2(L_p L_s - M^2)} & 0 & -\frac{\omega L_s r_p}{\omega^2(L_p L_s - M^2)} & -\frac{\omega M r_s}{\omega^2(L_p L_s - M^2)} \\ \frac{\omega M}{\omega^2(L_p L_s - M^2)} & -\frac{\omega M}{\omega^2(L_p L_s - M^2)} & -\frac{\omega L_p}{\omega^2(L_p L_s - M^2)} & 0 & -\frac{\omega M r_p}{\omega^2(L_p L_s - M^2)} & -\frac{\omega L_p r_s}{\omega^2(L_p L_s - M^2)} \end{bmatrix} \tag{5.34}$$

$$A_{OFF} = \begin{bmatrix} -\frac{1}{\omega r_{OFF} C_1} & 0 & 0 & \frac{1}{\omega C_1} & -\frac{1}{\omega C_1} & 0 \\ 0 & 0 & 0 & 0 & \frac{1}{\omega C_2} & 0 \\ 0 & 0 & -\frac{1}{\omega R_L C_S} & 0 & 0 & \frac{1}{\omega C_S} \\ -\frac{1}{\omega L_f} & 0 & 0 & -\frac{r_f}{\omega L_f} & 0 & 0 \\ \frac{\omega L_s}{\omega^2(L_p L_s - M^2)} & -\frac{\omega L_s}{\omega^2(L_p L_s - M^2)} & -\frac{\omega M}{\omega^2(L_p L_s - M^2)} & 0 & -\frac{\omega L_s r_p}{\omega^2(L_p L_s - M^2)} & -\frac{\omega M r_s}{\omega^2(L_p L_s - M^2)} \\ \frac{\omega M}{\omega^2(L_p L_s - M^2)} & -\frac{\omega M}{\omega^2(L_p L_s - M^2)} & -\frac{\omega L_p}{\omega^2(L_p L_s - M^2)} & 0 & -\frac{\omega M r_p}{\omega^2(L_p L_s - M^2)} & -\frac{\omega L_p r_s}{\omega^2(L_p L_s - M^2)} \end{bmatrix} \tag{5.35}$$

$$B_{ON} = B_{OFF} = B = \begin{bmatrix} 0 & 0 & 0 & \frac{V_i}{\omega L_f} & 0 & 0 \end{bmatrix}^T \tag{5.36}$$

$$C_{ON} = C_{OFF} = C = \begin{bmatrix} 1 & 0 & 0 & 0 & 0 & 0 \\ 0 & 1 & 0 & 0 & 0 & 0 \\ 0 & 0 & 1 & 0 & 0 & 0 \\ 0 & 0 & 0 & 1 & 0 & 0 \\ 0 & 0 & 0 & 0 & 1 & 0 \\ 0 & 0 & 0 & 0 & 0 & 1 \end{bmatrix} \tag{5.37}$$

$$Đ_{ON} = Đ_{OFF} = Đ = \begin{bmatrix} 0 & 0 & 0 & 0 & 0 & 0 \end{bmatrix}^T. \tag{5.38}$$

From Eq. 4.170 the solution to Eqs. 5.21-5.24 for each ON and OFF intervals can be written in the form

$$\mathbf{x}(\omega t) = \mathbf{x_n}(\omega t) + \mathbf{x_f}(\omega t) = e^{A\omega t}\mathbf{x}(0) + A^{-1}(e^{A\omega t} - \mathbf{I})B \tag{5.39}$$

where $\mathbf{x_n}$ is the natural response matrix given in Eq. 4.171, $\mathbf{x_f}$ is the forced response matrix given in Eq. 4.172, $\mathbf{x}(0)$ is the initial condition matrix and $\mathbf{I}$ is a 6×6 identity matrix. The initial conditions are determined by applying the continuity conditions of the voltages across C_1, C_2 and C_S and the currents of L_f, L_p and L_s when the circuit transitions from the ON state to the OFF state, hence the following equations are obtained

$$\mathbf{x}_{ON}(0) = \mathbf{x}_{OFF}(\omega t)\Big|_{\omega t = 2\pi(1-D)} \tag{5.40}$$

$$\mathbf{x}_{OFF}(0) = \mathbf{x}_{ON}(\omega t)\Big|_{\omega t = 2\pi D}. \tag{5.41}$$

It is noted that the state-space equations (Eqs. 5.25-5.33) and the general solution equation (Eq. 5.39) represent a periodic system. By substituting Eqs. 5.40-5.41 in 5.39, the initial conditions for all periods of the switching signal are equal to

$$\begin{bmatrix} \mathbf{x}_{ON}(2\pi_m) \\ \mathbf{x}_{OFF}(2\pi_m) \end{bmatrix} = \begin{bmatrix} -e^{A_{ON}2\pi D} & \mathbf{I} \\ \mathbf{I} & -e^{A_{OFF}2\pi(1-D)} \end{bmatrix}^{-1} \begin{bmatrix} A_{ON}^{-1}(e^{A_{ON}2\pi D} - \mathbf{I}) \\ A_{OFF}^{-1}(e^{A_{OFF}2\pi(1-D)} - \mathbf{I}) \end{bmatrix} B \quad \text{for } m = 0, 1, 2, \ldots \tag{5.42}$$

For optimal switching conditions, the initial conditions of the following states for all periods of the switching signal should be

$$x_{1ON}(2\pi m) = 0 \quad \text{for } m = 0, 1, 2, \ldots \tag{5.43}$$

$$x_{4ON}(2\pi m) - x_{5ON}(2\pi m) = 0 \quad \text{for } m = 0, 1, 2, \ldots \tag{5.44}$$

As discussed in Sec. 4.4.4, Eq. 5.43 corresponds to the ZVS condition whereas Eq. 5.44 corresponds to the ZVDS condition. The two equations allow for two unknown parameters to be solved for. The following design example elaborates more on this

5.2.4 *Design Example*

The following design example will demonstrate the design process of a Class E inverter as the primary coil driver for an inductive link. The design process will rely on both the analytical and the state-space representation approaches, in addition to certain equations from Chapter 4.

A Class E inverter with finite DC-feed inductance is required to drive the inductive link with specifications mentioned in Sec. 3.4.3 at a frequency of 800 kHz. The load of the inductive link is set at 47 Ω and is required to operate at 10 W. The coils of the inductive link are separated by a distance of 5 cm which corresponds to a mutual inductance of approximately 1 µH and a coupling coefficient of approximately 0.20. Assume $q = 1$ and neglect the ESR of the DC-feed inductor for simplicity.

Referring to Fig. 5.3, the only unknown component values for this design example are L_f, C_1 and C_2. The duty cycle of the switching frequency will be set at 50 % for maximum power-output capability and minimum voltage and current stresses as discussed in Sec. 4.4.5. From Eq. 4.119, the DC-feed inductance can be represented as

$$\omega L_f = \frac{1}{q^2 \omega C_1} = \frac{1}{\omega C_1} \tag{5.45}$$

The switch will be the IRF540 MOSFET which has a drain resistance (r_{ON}) of 0.15 Ω at a 5 V gate voltage. Its OFF resistance (r_{OFF}) is assumed to be infinite. The only unknown values are now C_1 and C_2. Their values can now be obtained by numerically solving Eqs.5.43-5.44. The MATLAB code for obtaining the values of C_1 and C_2 is included in Appendix A.2.1, their solved values are 40.65 nF and 7.51 nF respectively. Consequently, the value of L_f is 0.974 µH.

The next step is to determine the input voltage. From Eq. 5.3, the total resistance (R_T) of the output load network of the Class E inverter is

$$R_T = R_{Ref} + r_{Ref} + r_P = 1.0177 + 0.0221 + 0.17 = \ 1.210\,\Omega.$$

Therefore the expected efficiency of the inductive link is

$$\eta = \frac{R_{Ref}}{R_T} = 84.11\,\%.$$

The loaded quality factor of the Class E inverter's output network is

$$Q_L = \frac{\omega L_P}{R_T} = 23.93. \tag{5.46}$$

The loaded quality factor is higher than 5 therefore the current in the load network can be assumed to be sinusoidal [78]. The Class E inverter is required to deliver 10 W therefore the magnitude of the current in the load network is

$$i_m = \sqrt{\frac{2P_o}{R_T}} = 4.066\,\text{A}. \tag{5.47}$$

Referring to Fig. 4.16, p is equal to 3.84 when q = 1. From Eq. 4.124 the input voltage is

$$V_i = \frac{\omega L_f i_m}{p} = 5.183\,\text{V}. \tag{5.48}$$

Fig. 5.4 shows the PSPICE simulation results for this design example. It can be seen that the switch is operating at optimum switching conditions since the switch is turned ON at zero voltage and its current increases from zero. The magnitude of the current in the primary coil is close to the expected value of 4.066 A. The maximum voltage at the load is 31.822 V therefore the power delivered to the load is 10.772 W. The overall efficiency of the Class E inverter and the inductive link is 83.92 % which is an excellent agreement with the expected efficiency.

5.2.5 *Performance Investigation*

In certain IPT applications the distance between the coils and their alignment may not be fixed and can continuously vary. For instance, the alignment of the coils in an

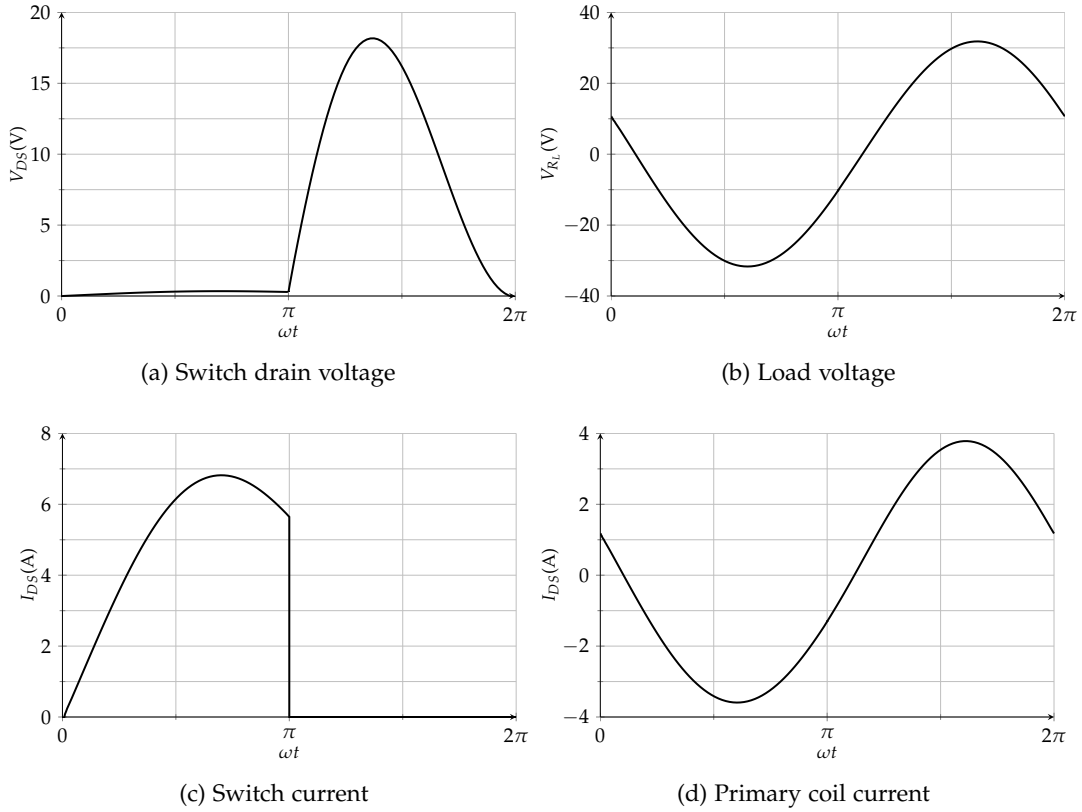

(a) Switch drain voltage

(b) Load voltage

(c) Switch current

(d) Primary coil current

Fig. 5.4: Simulation results showing the voltages and currents of interest for the design example in Sec. 5.2.4

IPT system for charging electric vehicles depends on the position of the vehicle when it parks. Therefore the coupling coefficient varies with time and so do the reflected impedances. Since Class E inverters operate at optimum switching conditions at a certain load value, any variations in the load or the reflected impedances from their optimum values will cause the Class E inverter to either operate at sub-optimum or non-optimum switching conditions. Operating in these switching conditions may be inefficient due to the increased voltage and current stresses throughout the inverter as shown in Sec. 4.4.5 and discussed in further details in [87].

Fig. 5.5 shows the simulated waveforms of the switch's drain voltage and current of the Class E inverter designed in the previous example. The waveforms illustrate how the variation of the coupling coefficient affects the Class E inverter. The waveforms for optimum operation are shown in dashed lines for comparison. In Figs. 5.5a & 5.5c, the coupling coefficient is decreased from its optimum value of 0.20 to 0.10 to simulate a decreased distance between the coils. Therefore the reflected impedances are less than their optimum values. In this case the Class E inverter is operating at a sub-optimum switching condition as discussed in Sec. 4.4.5. The switch turns ON at a negative voltage causing its body diode to conduct which may degrade the overall efficiency. The switch's drain voltage is increased which implies that a switch with a high voltage

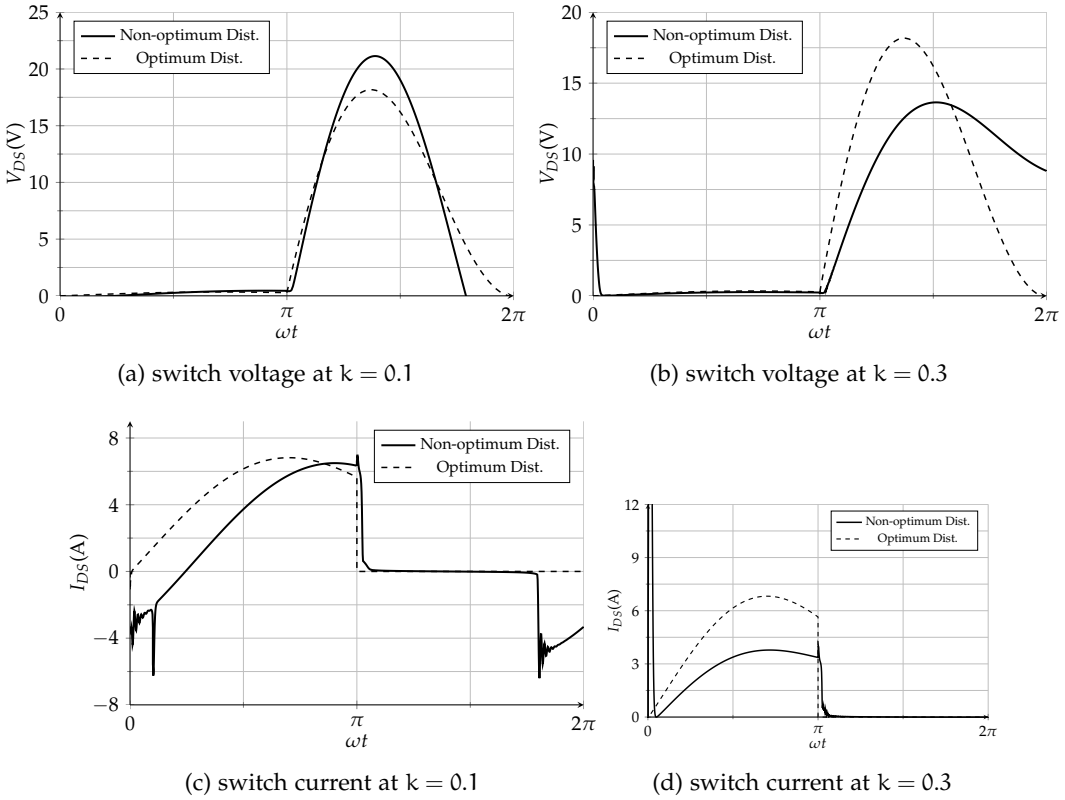

(a) switch voltage at k = 0.1

(b) switch voltage at k = 0.3

(c) switch current at k = 0.1

(d) switch current at k = 0.3

Fig. 5.5: Effect of changing the distance between the primary and secondary coils on the performance of the inverter

rating may be required. In Figs. 5.5b & 5.5d, the coupling coefficient is increased from its optimum value of 0.20 to 0.30 to simulate an increased distance between the coils. Therefore the reflected impedances are now larger than their optimum values and the Class E inverter now operates at non-optimum switching conditions. The switch in this case turns ON at a positive voltage causing a large current to flow through its drain channel. The initial current that flows in the drain channel can surpass the switch's maximum ratings and may cause irreversible damage.

5.2.6 *Developing Tuning Methods and Requirements*

It was shown that the variation of the coupling coefficient between the primary and the secondary coils of the inductive link, due to a change of the distance between the coils, will alter the operation of the Class E inverter from its optimal switching conditions. It is therefore necessary to recalculate the values of its components as the coupling coefficient changes to ensure optimum switching operation. Due to practical considerations, it is not desirable to replace the components of the Class E inverter for every change that occurs in the coupling coefficient. Using mechanically variable components such as variable capacitors or inductors may be in efficient and will slow

the response of the inverter since they require manual adjustment. Therefore a tuning method will have to be developed that will allow the Class E inverter to be electronically tuned while in operation. Tuning methods based on impedance transformation [88–91], impedance network switching [92, 93] and phase control and load modulation [94–97] have been proposed. These methods allow the Class E inverter to operate in optimal and sub-optimal switching conditions, achieving zero-voltage and zero-voltage derivative switching regardless of the load value. However, these methods may not be applicable to resonant inductive links due to the complexity of the load and the reflected impedances. Furthermore, including additional components in series with the primary coil is undesirable since this increases the ESR and hence an increase in ohmic power losses. Therefore the following sections will be devoted to developing novel tuning methods that will allow the Class E inverter to be electronically tuned to operate at optimum switching conditions as the reflected impedances of an inductive link vary due to a change in the separation distance or misalignment.

Achieving the two optimum switching conditions, ZVS and ZVDS, implies that at least two operating parameters and/or component values should be controlled. The parameters that can be controlled are the duty cycle of the switching signal and its frequency. In addition, the values of the DC-feed inductor L_f, capacitors C_1 and C_2 could also be varied. The following sections will begin by discussing the possibility of creating an electronically tunable element. Then, tuning methods will be derived based on the analytical and state-space modelling approaches. Simulation and experimental results will be presented to show validity of the developed tuning methods. A Class E inverter was designed specifically for each tuning method to drive the inductive link in Sec. 3.4.3. This shows the possible range of operation of the each developed tuning method and at which circuit configurations they work best.

5.3 SATURABLE REACTORS AS ELECTRONIC TUNING ELEMENTS

The term 'electronic tuning' implies that a system can be tuned to operate at a specific condition by the application of a voltage or current control signal. In electric circuits this refers to adjusting the value of a physical property of a circuit element, such as the capacitance of a capacitor or the inductance of an inductor, via a voltage or current signal. In most applications that make use of electronic tuning, only one circuit element is adjusted to tune the complete system. An example of such an application is in digital radio tuners where radio channels are tuned in using digital input rather than performing mechanical adjustments.

The most common controllable circuit elements are varactors (varicaps). Varactors are essentially PN diodes where the capacitance of their junction can be adjusted

by applying a voltage across their terminals. Therefore they can be referred to as voltage-controlled capacitors. Varactors can only operate at voltage levels that don't exceed 100 mV therefore they might not be suitable to be used in Class E inverters since voltage levels throughout the inverter can reach up to tens or hundreds of volts. Varactors are used in every modern radio and mobile device.

Saturable reactors which are also know as 'Magnetic Ampifiers (Mag-Amp)' or 'Transductors' are basically AC/AC transformers that consist of a primary winding and a secondary winding wound on a magnetic core. They are somewhat similar to a transistor in terms of control where a small change in current in one winding leads to a relatively large change in current in the other. The saturable reactor achieves this by supplying a low DC current (several hundreds of milliamps) to one winding (referred to as the control or signal winding), this will cause the magnetic core's permeability to decrease (i.e. limiting the number of magnetic flux lines) and therefore effectively changing the impedance of the other winding (referred to as the controlled or power winding). Consequently, saturable reactors can be referred to as current-controlled inductors. Unlike varactors, saturable reactors can operate at voltage and current levels that can reach up to several hundreds of volts and amperes respectively which makes them the only suitable tunable element to be used in Class E inverters.

Fig. 5.6 illustrates a simple example on how a saturable reactor can be used as a light dimmer. Detailed description on saturable reactors and their applications can be found in [98].

5.3.1 *Magnetic Cores*

The type of magnetic core used for the saturable reactor affects the analysis and performance of a circuit. The two types of magnetic cores that can be used are ferrite cores and iron powder cores. Ferrite cores are used in RF low power circuits since they have less eddy-current losses [99, 100]. However, their high permeability limits the amount of DC bias current that can flow in the primary windings. Since the Class E inverter has a non-zero average DC input current, unwanted saturation may occur if a ferrite core is used. In addition, their high hysteresis levels makes the calculation of their primary winding inductance, that is adjusted by control windings, difficult. Iron powder cores can be used for frequencies up to 2 MHz since they can suffer from high eddy-current losses. Due to their lower permeability compared to ferrite cores, the inductance of primary windings is stable against high DC bias currents and frequency variations [99, 100]. Inductance calculations are simplified and can be estimated accurately since they have low hysteresis levels. Iron powder cores are manufactured with

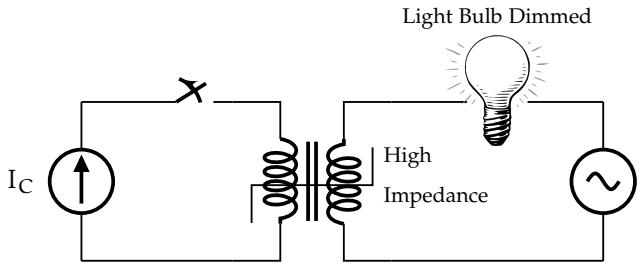

(a) When the switch is open no current flows in the control winding, the core is unsaturated and the controlled windings will have a high impedance which will limit the current flowing through the light bulb and therefore it is dimmed

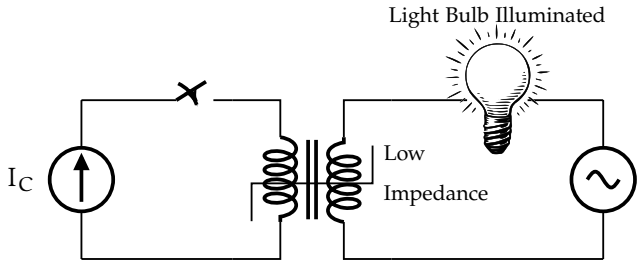

(b) The switch is closed allowing DC current to flow through the control windings causing the core to saturate and therefore lowering the imepdance of the controlled windings. More current flows through the light bulb and more light is produced

Fig. 5.6: A simple example demonstrating the application of a saturable reactor as an electronic switch

different ratios of iron, nickel, molybdenum ferrous and silicon, distributed air gaps are also included.

5.3.2 *Design Trade-offs*

After choosing the magnetic core type to be used in the saturable reactor, it is necessary to determine the number of turns of the primary windings and the control windings. Beginning with the primary windings, since the DC-feed inductance current has a non-zero average DC component and high frequency AC components, it is therefore preferable that the primary windings have a low number of turns to minimise ohmic losses. On the other hand, higher turns give a higher DC-feed inductance which allows for a wider control range. The control windings should consist of tens to hundreds of turns in order to inject sufficient magnetic flux into the core to alter the inductance of the primary windings. A high number of turns implies that less DC current levels will be required to control the inductance, therefore simpler control circuits can be

built and less power is dissipated in the windings. However, due to the high turn ratio between the control and the primary windings and the large current levels in the primary windings, voltages in the range of hundreds to kilovolts can be induced in the control windings. These excessive voltage levels may cause undesirable arcing and can exceed the breakdown voltage of the insulation of the control windings. Therefore, a suitable number of turns must be chosen to allow for a safe operation.

To neutralise the effect of the induced the voltage in the control windings on the control circuitry, two saturable reactors are often used. Their primary windings are connected in series which doubles the overall inductance, whereas their control windings are connected in an antiphase manner to effectively cancel or minimise the total induced voltage.

5.4 TUNING THE CLASS E INVERTER WITH INFINITE DC-FEED INDUCTANCE

The first tuning method will be introduced for the basic Class E inverter with infinite DC-feed inductance. Referring to Fig. 5.1, the parameters and component values that can be controlled are the switching frequency and capacitors C_1 and C_2. The duty cycle cannot be controlled since it has been assumed to be set at 0.50. From Eqs. 5.7 and 5.10, the value of capacitor C_1 is only affected by the total reflected resistance whereas capacitor C_2 is only affected by the inductance of the primary coil of the inductive link. Therefore the value of capacitor C_2 cannot be controlled. Consequently, only the switching frequency and the value of capacitor C_1 can be controlled to achieve optimum switching operation.

5.4.1 *Frequency and C_1 control*

The proposed tuning method relies on varying the switching frequency and capacitor C_1. As discussed previously, adjusting the value of a capacitor may not be practically feasible. By connecting a saturable reactor in parallel with capacitor C_1, the reactance of C_1 can be controlled indirectly by adjusting the control current of the saturable reactor. Fig. 5.7 shows the Class E inverter including a saturable reactor L_{Sat} connected in parallel with capacitor C_1. The capacitor connected in series with the saturable reactor is a DC blocking capacitor. By varying the reactance of the saturable reactor and the switching frequency, the Class E inverter can now be tuned to achieve optimum switching conditions after a change in the reflected impedance occurs.

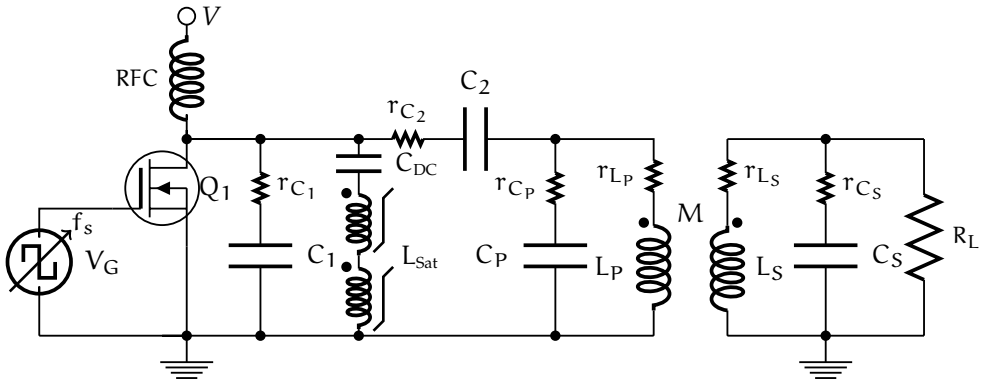

Fig. 5.7: The Class E inverter including a saturable reactor for tuning

The proposed tuning method involves varying L_{Sat} and the switching frequency only while keeping C_2 at a fixed value. Since the switching frequency is varied, the secondary coil of the inductive will not be operating at resonance, instead it will be operating at near resonance as described in Sec. 3.4.1. The required switching frequency and the value of capacitance C_1 are calculated by setting C_2 as a constant in Eq. 5.10 and solving for the switching frequency. The following equation is produced

$$L_P^2 C_2 - 2.08\omega^2 R_T L_P C_2 - \omega L_P + 0.66 R_T = 0. \tag{5.49}$$

The above equation can be solved numerically and the value of the required capacitance C_1 can then be calculated from Eq. 5.7.

5.4.2 *Experimental Verification*

A. Implementation

The proposed tuning method was implemented on a Class E inverter designed to driver the inductive link specified in Sec. 3.4.3. The resonant frequency of the inductive link is 800 kHz. The coil separation range varies from 5 cm to 13 cm. The load connected to the secondary coil of the inductive link varies from 400 Ω to 2 kΩ. The value of capacitor C_2 was set at 5.34 nF. This value was chosen since it was possible to obtain using standard capacitor values. Fig. 5.8 shows values of capacitance C_1 and switching frequency that are required to achieve optimum switching conditions as a function of the load resistance and the coupling coefficient. The values were obtained by solving Eq. 5.49.

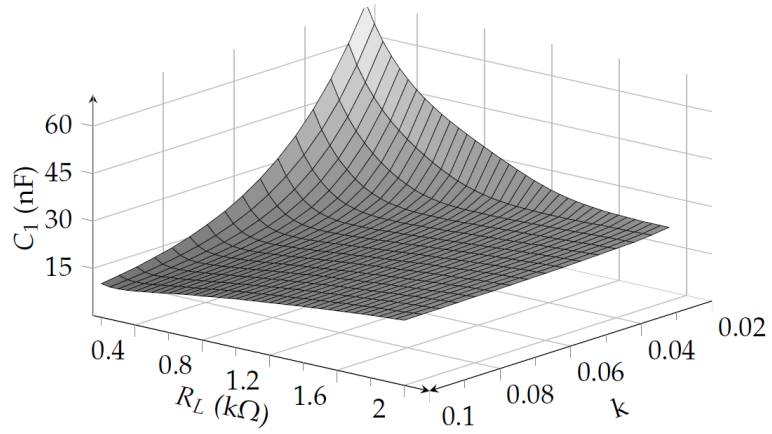

(a) C_1

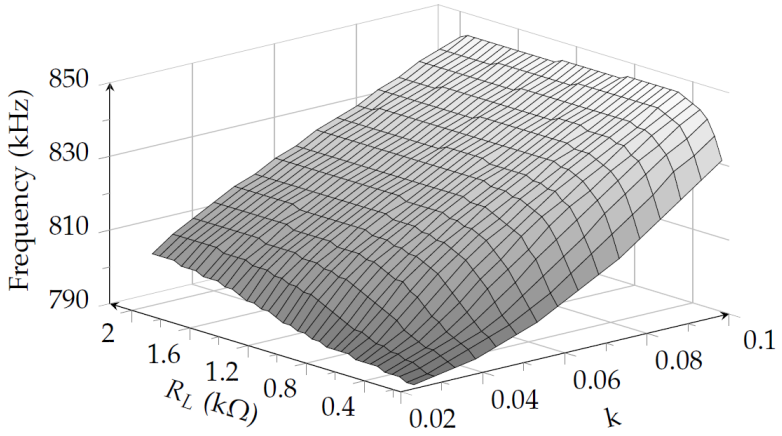

(b) Switching frequency

Fig. 5.8: C_1 and switching frequency variation as a function of the load resistance and coupling coefficient

B. Hardware Setup

The circuit of the Class E inverter shown in Fig. 5.7 was constructed with values and parameters shown in Table. 5.1. Switch Q_1 is a STP40NF10 MOSFET from STMicroelectronics driven via an EL7154 MOSFET driver from Intersil. The circuit configuration of the saturable reactor L_{Sat} is shown in Fig. 5.9. The saturable reactor consisted of two toroidal transformers connected in series with each other. Their primary windings were connected in phase, whereas their secondary or control windings were connected in an antiphase manner to cancel the voltage induced by the current in the primary windings. The two toroids were wound on a TX22/14/6.4-3C90 ferromagnetic core from Ferroxcube which had a specified effective cross section area Ae of 24.8 mm², an effective magnetic path length Le of 54.2 mm, a relative permeability Ue of 2300 and an inductance factor Al of 1400 nH/Turn^2. The control windings of both toroids consisted of 50 turns giving a total inductance of 6.6 mH and the primary windings consisted of 3 turns giving a total inductance of 25.2 µH for each toroid. The DC

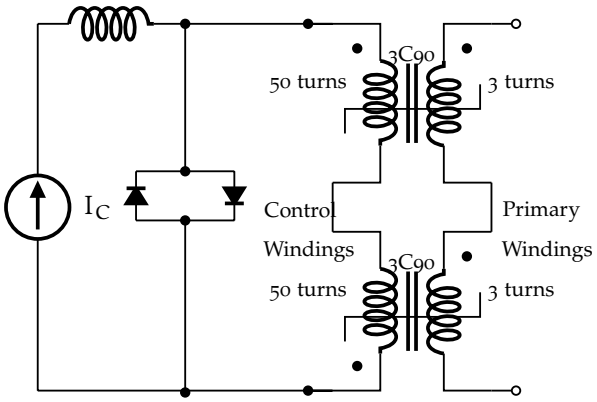

Fig. 5.9: Saturable reactor circuit configuration

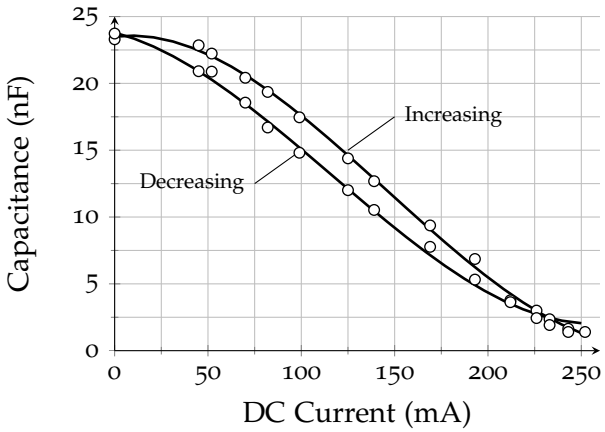

Fig. 5.10: The measured variation of Capacitance C_1 at 800 kHz as a function of the saturable reactor's DC current applied to its control windings

control current (I_C) applied to the control windings ranged from 0 mA for maximum inductance to 500 mA for minimum inductance. Fig. 5.10 shows the measured effective capacitance of C_1 when the saturable reactor was connected in parallel with it as a function of the DC control current. Hysteresis can be observed since the core of the saturable reactor is ferromagnetic. A photograph of the complete setup is shown in Fig. 5.11. The chosen values of the inverter allow it to operate in optimum switching conditions with a 180 mA I_C for a nominal load of 1 kΩ at a nominal distance of 12 cm corresponding to a coupling coefficient of 0.035.

5.4.3 *Implementation of the proposed tuning method*

To test the dependence of the Class E inverter on the reflected impedances, the distance between the coils is decreased from its nominal value of 12 cm to 5 cm in 1 cm steps for three different load values; 470 Ω, 1 kΩ and 2 kΩ. For every step, the Class E

Table 5.1: Values and ranges of several parameters of the Class E inverter and the inductive link measured at 800 kHz

	Component/Parameter	Value
Inductive Link	L_P / r_P	5.76 µH / 0.17 Ω
	L_S / r_S	6.69 µH / 0.28 Ω
	C_S / r_{C_S}	5.92 nF / 0.25 Ω
	Resonant Frequency f_o	800 kHz
	R_{Load}	0-2 kΩ
	Mutual Inductance (M) Range	0.17 - 1.73 µH
	Coupling Coefficient (k) Range	0.02 - 0.1
	Coils' Separation Range	2.5-15 cm
Class E Inverter	**Component/Parameter**	**Value**
	MOSFET	STP40NF10
	Gate Driver	TC1412
	Input Voltage	15 V
	C_1	24 nF
	C_2	5.34 nF
	C_{DC}	0.47 µF
	RFC	1 mH
	Switching Frequency Range f_s	790 - 845 kHz
	Duty Cycle	50 %
Saturable Reactors	**Component/Parameter**	**Value**
	Core Type	3C90
	No. of Cores	2
	Primary No. turns per core	4
	Secondary No. turns per core	70
	Control Current Range I	0.00 - 0.5 A
	L_{Sat} Range	4 - 50.4 µH

inverter was retuned to achieve optimum switching conditions by adjusting the frequency and the saturable reactor's DC current according to Fig. 5.8. Fig. 5.12 and 5.13 show the measured power received to the loads and the overall efficiency respectively. Simulation results obtained in PSPICE are included for comparison. The Class E inverter was able to operate over a larger coil separation distance for lower loads with less variation in received power. The overall efficiency of the IPT system includes that of the MOSFET driver, the Class E inverter, the saturable reactor's primary coil and the inductive link. The efficiency is maintained at a relatively constant level for lower

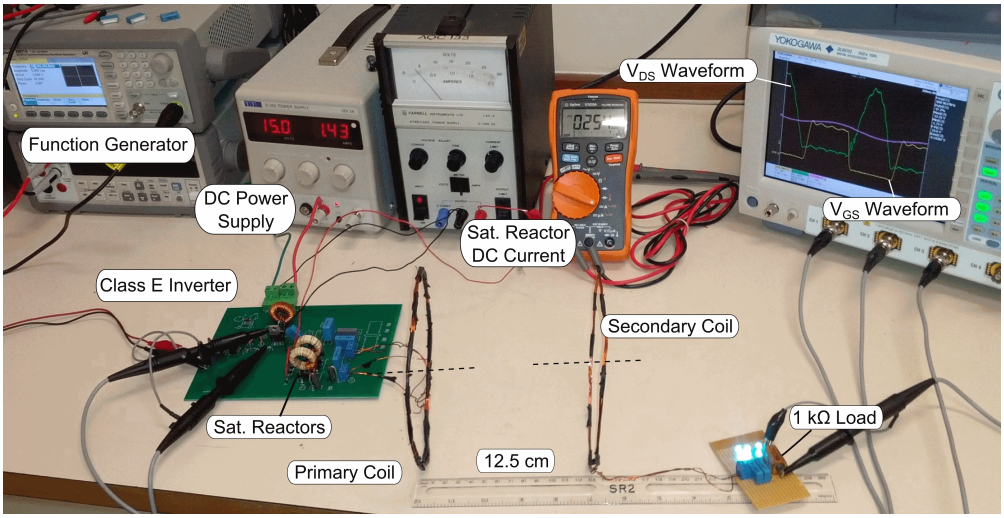

Fig. 5.11: Experimental setup of the WPT system

loads but at reduced values. Discrepancies between the simulated and measured results are mainly due to the instability of the passive components' tolerance to large current values and temperature variations.

Figs. 5.14 and 5.15 show the switching frequencies and the saturable reactor's DC current that were required to achieve optimum operation for each step. Both are a linear function of distance or the coupling coefficient as predicted in Fig. 5.8. The difference between the calculated switching frequencies and the required switching frequencies were mainly due to the unaccounted nonlinear operation of the saturable reactor's primary windings. Although the control windings of the saturable reactor were connected in an antiphase manner, the imperfection of the windings will cause a certain amount of voltage to be induced in the control windings. Therefore more DC current was injected to achieve the required effective capacitance compared to what was initially measured in Fig. 5.10.

Fig. 5.16 shows the waveforms of the switch's drain voltage and gate signal of the Class E inverter for three different coil separation distances with a constant load resistance of 1 kΩ. Fig. 5.16a shows the inverter working in optimal switching conditions at a distance of 12 cm without requiring any tuning ($I_C = 180$ mA) at a switching frequency of 800 kHz. In Fig. 5.16, the distance between the coil is decreased to 5 cm. It can be observed that the Class E inverter is operating in a non-optimal switching condition since the MOSFET is now being switched ON at a non-zero drain voltage. The gate voltage is distorted due to the high current spike that occurs once the switch turns ON. In Fig. 5.16c, the saturable reactor's DC current was increased to 370 mA and the frequency was increased to 826 kHz. It can be noticed that the Class E inverter is now operating at optimal switching conditions. Therefore the tuning method described in Sec. 5.4.1 has been successfully validated.

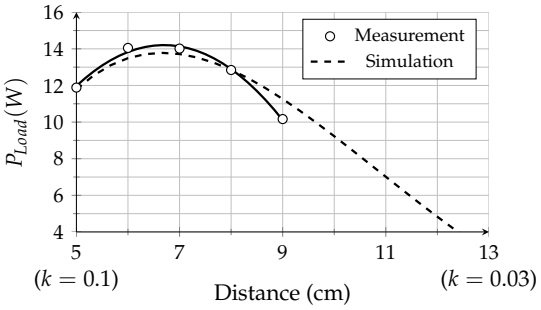

(a) $R_L = 470\ \Omega$

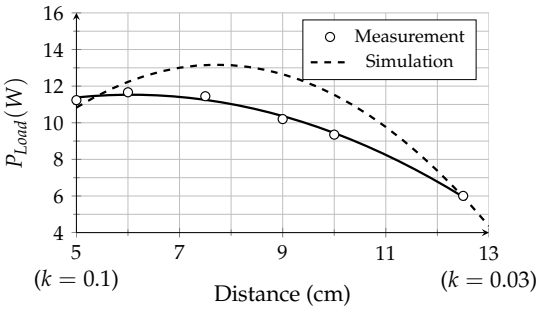

(b) $R_L = 1\ k\Omega$

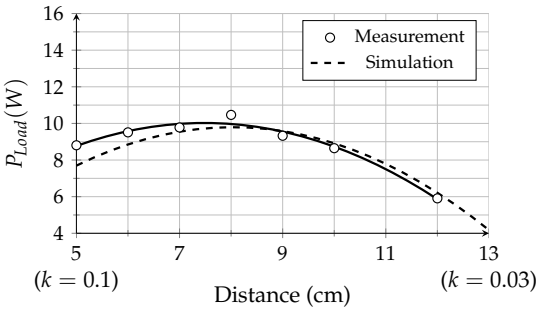

(c) $R_L = 2\ k\Omega$

Fig. 5.12: Received power against coil separation distance for three different load values

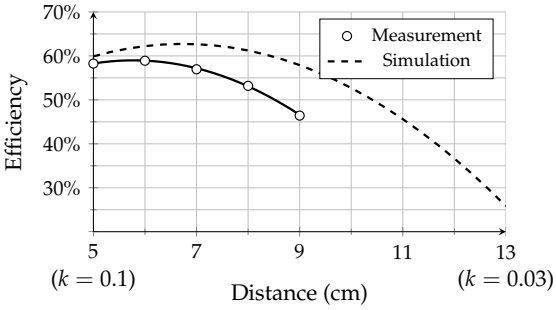

(a) $R_L = 470\ \Omega$

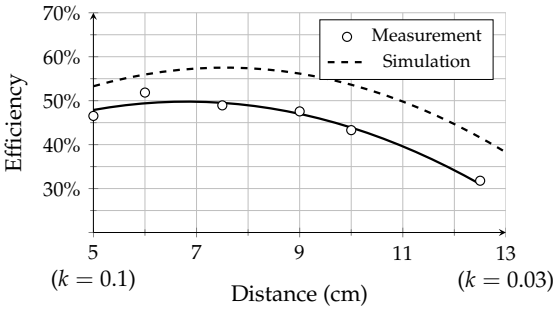

(b) $R_L = 1\ k\Omega$

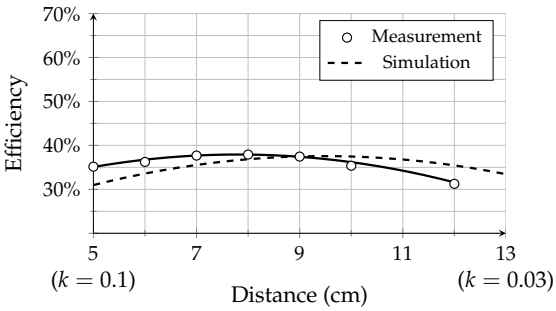

(c) $R_L = 2\ k\Omega$

Fig. 5.13: Overall efficiency against coil separation distance for three different load values

5.5 TUNING THE CLASS E INVERTER WITH FINITE DC-FEED INDUCTANCE

The tuning method that will be introduced in this section will be based on the analytical analysis performed in Sec. 5.2.2 for the Class E inverter with finite DC-feed inductance. The value of the DC-feed inductor affects the performance of the Class E inverter; it can determine whether or not the Class E inverter will operate at optimum switching conditions. Therefore the proposed tuning method replaces the finite DC-feed inductance with a saturable reactor.

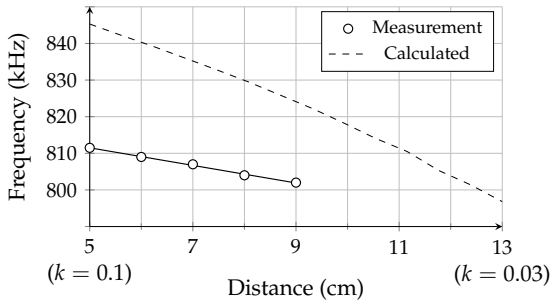

(a) $R_L = 470\ \Omega$

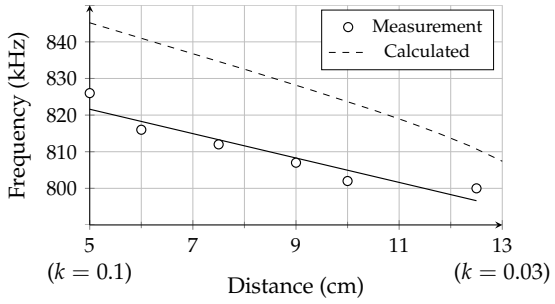

(b) $R_L = 1\ k\Omega$

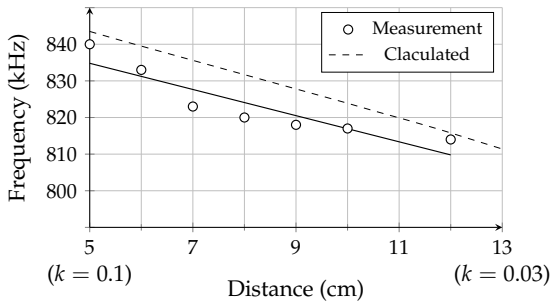

(c) $R_L = 2\ k\Omega$

Fig. 5.14: Switching frequency against coil separation distance for three different load values

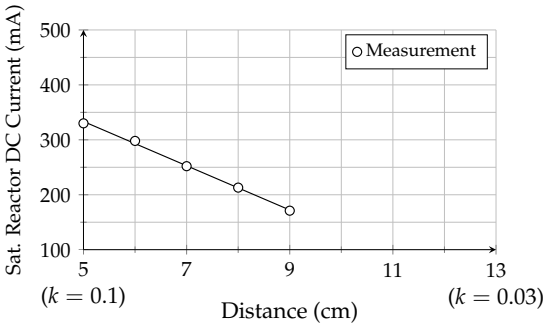

(a) $R_L = 470\ \Omega$

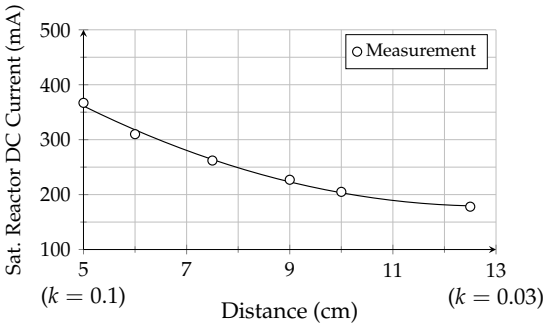

(b) $R_L = 1\ k\Omega$

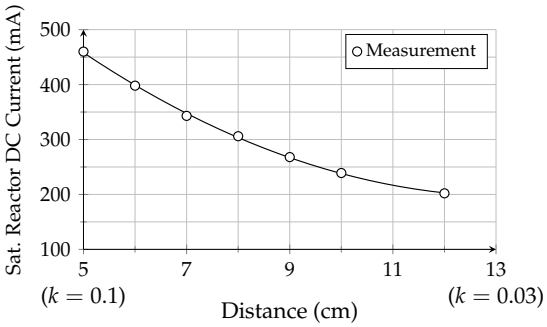

(c) $R_L = 2\ k\Omega$

Fig. 5.15: Saturable reactors' DC current against coil separation distance for three different load values

5.5.1 *Frequency and* L_f *control*

Referring to Eqs. 5.16-5.20, the passive elements of the Class E inverter with finite DC-feed inductance L_f, C_1 and C_2 are set for a specific reflected impedance at a certain switching frequency. The reflected impedance itself varies according to the distance, or the coupling coefficient, between the primary and secondary coils of the inductive link and the switching frequency. It is necessary to recalculate the values of the passive elements that will allow the Class E inverter to operate at optimum switching conditions as the coupling coefficient changes. The aim here will be to find

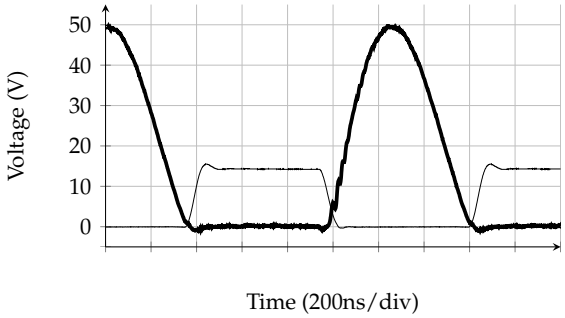

(a) Optimum switching operation at 12 cm

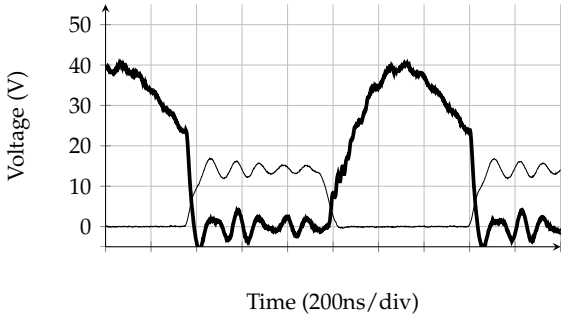

(b) Untuned non-optimum switching at operation at 5 cm

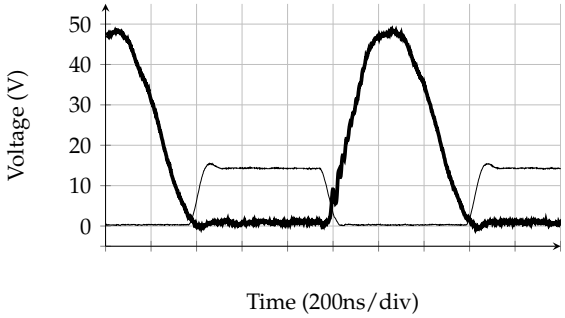

(c) Tuned optimum switching at 5 cm

Fig. 5.16: Class E inverter waveforms according variation in coil separation distance (V_{DS} in bold and V_{GS} in light lines respectively)

the values of the switching frequency and the DC-feed inductance as the coupling coefficient varies while keeping the values of C_1 and C_2 fixed. To achieve this, we begin by substituting Eq. 5.16 in Eq. 5.17 which produces the following equation

$$q^2 p R_t(\omega, k) X_{C_1} - \left(\frac{\pi}{2p} - \frac{2}{\pi} \cos\phi + \sin\phi \right) = 0. \tag{5.50}$$

The residual impedance X can be represented as the difference between the impedance of the primary coil, the imaginary components of the reflected impedances and the impedance of the series capacitor C_2 as follows

$$X = X_{L_p}(\omega) - X_{C_2} + X_{Ref}(\omega, k) + x_{Ref}(\omega, k). \tag{5.51}$$

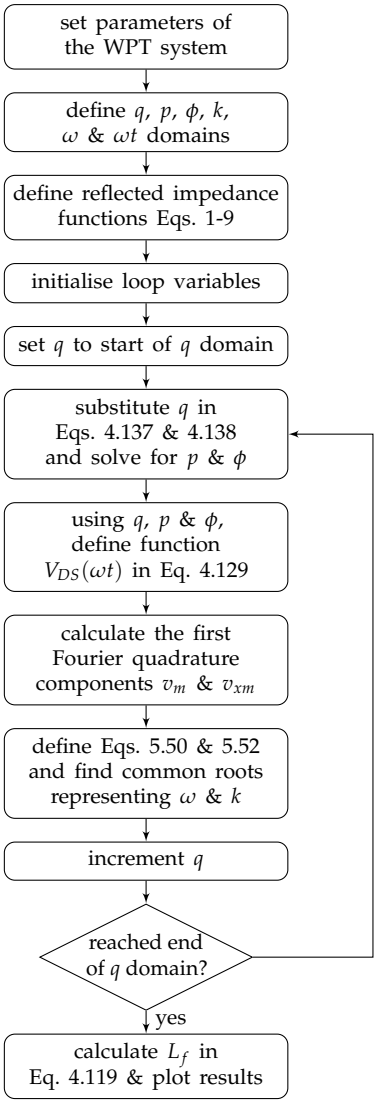

Fig. 5.17: Flowchart of the solution method to calculate the optimum values of the switching frequency and the DC-feed inductance as the coupling coefficient varies

Substituting Eq. 5.51 in Eq. 4.140 results in the following equation

$$X_{L_P}(\omega) + X_{Ref}(\omega, k) + x_{Ref}(\omega, k) - X_{C_2}(\omega) - R_T(\omega, k)\frac{v_{xm}}{v_m} = 0. \tag{5.52}$$

The optimum values of the switching frequency and the coupling coefficient can be found by finding the common roots for Eqs. 5.50 and 5.52 for specific values of q, p and ϕ. The optimum value of the DC-feed inductance can then be calculated by substituting the obtained optimum values of the switching frequency and the coupling coefficient in Eq. 4.119. Fig. 5.17 shows a flowchart of a solution method which can be used to calculated the optimum values. The solution method is an iterative process that provides an exact solution. Other simpler design equations represented by second-order and third-order polynomial approximations [83] can be used but they can be less accurate.

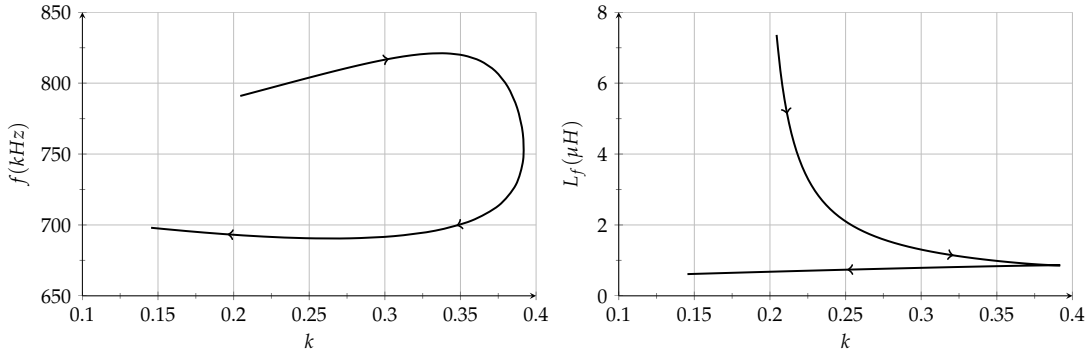

(a) Switching frequency (b) DC-feed inductance

Fig. 5.18: The numerical solutions of Eqs. 5.50 and 5.52 for the WPT system specified in Table. 8.1

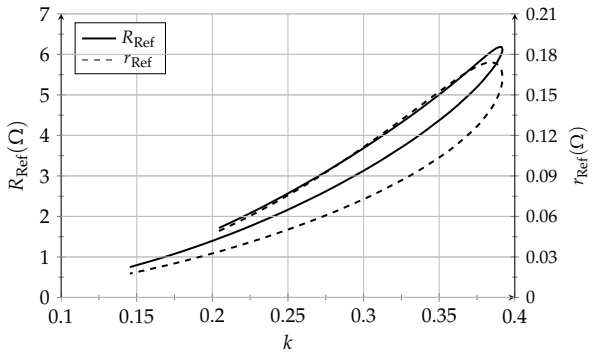

Fig. 5.19: Variation of R_{Ref} and r_{Ref} as the coupling coefficient changes

5.5.2 *Optimisation*

The application of this solution method was demonstrated on a Class E inverter designed to drive the inductive link in Sec. 3.4.3. The load connected to the secondary coil was fixed at 47 Ω. The coupling coefficient varies from a minimum of 0.10 when the primary and secondary coils are separated by a distance of 5 cm to a maximum of 0.4 when the coils are closer at a separation distance of 1 cm. This separation distance range was chosen to provide a different operating range than that of the tuning method presented in the previous section. The values of capacitors C_1 and C_2 were set at 22 nF and 7.9 nF respectively. Fig. 5.18 shows the solutions for the switching frequency and the DC-feed inductance against the coupling coefficient. The solutions were obtained by programming the solution method in Fig. 5.17 in MATLAB using Chebfun2 [101, 102]. The complete code is included in Appendix A.2.2.

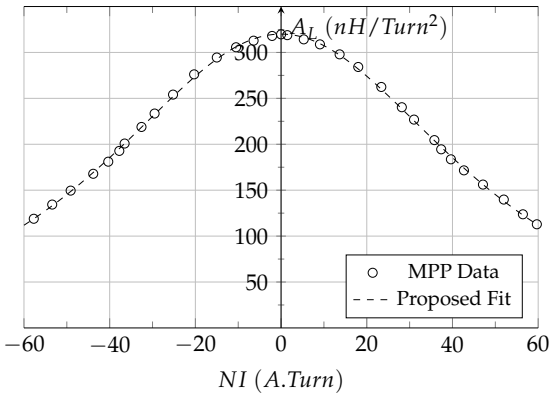

Fig. 5.20: MPP 550 data and proposed fit [103]

A. Modelling the saturable reactor

The magnetic core that was used form to the saturable reactors for this tuning method is the 50202A MPP toroidal core from Magentics Inc. The core has an initial relative permeability of 550, an effective cross-section area of 22.1 mm^2 and an effective length of 50.9 mm. Fig. 5.20 shows a plot of the DC bias performance of the MPP core used obtained from the core manufacturer's datasheet [103]. The vertical axis represent the inductance factor in nanohenries per $turn^2$, the horizontal axis represents the magnetoforce in ampere-turns The following equation is proposed to provide an accurate fit for the data:

$$A_L = 320\text{sech}(0.02854NI) \times 10^{-9} \tag{5.53}$$

where A_L is the inductance factor, N is the number of turns and I is the DC current in the turns.

The permeability of magnetic cores is not constant, it varies with frequency, the density of the magnetic flux and temperature. According to the manufacturer's specifications for the MPP core used [104], the permeability decreases to about 50 % of its initial value at frequencies approaching 1 MHz. Conversely, the permeability increases to a peak of about 20 % for AC flux density values of 0.1 T. The relative permeability is 550 when the core's temperature is 20 °C and increases by approximately 0.1 % per degree Celsius. Since inductance is directly proportional to the permeability, the inductance of the primary windings can be multiplied by a factor representing the increase or decrease of the core's permeability. Therefore, by using Eq. 5.53, the overall DC-feed inductance, which consists of two identical series connected saturable reactors, as a function of the current in the control windings can be written as

$$L_f = 2 \times 320rN_p^2\text{sech}(0.02854N_cI_c) \times 10^{-9} \tag{5.54}$$

where r is the reduction factor of the core's permeability, N_p is the number of turns of the primary windings, N_c is the number of turns in the control windings and I_c is the DC controlling current.

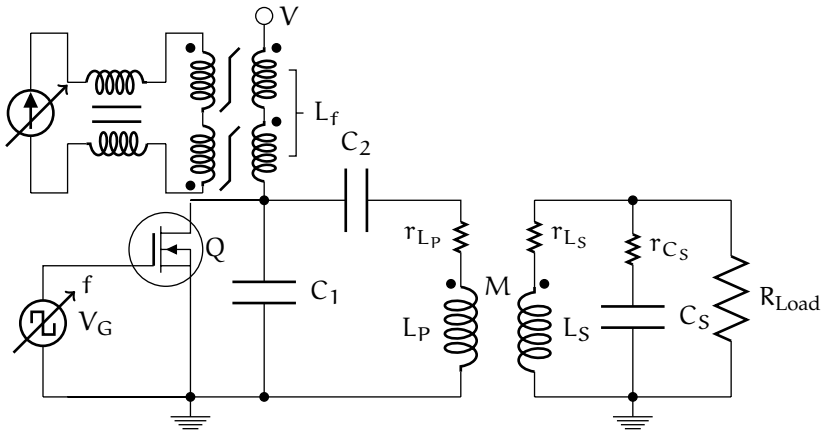

Fig. 5.21: Class E inverter with an inductive link and a controlled DC-finite inductance

Equation 5.54 was used to determine the control current that was required to adjust the DC-feed inductance to retune the Class E inverter.

B. Hardware setup

The implemented circuit of the Class E inverter with the saturable reactors is shown in Fig. 5.21. The DC-feed inductance consists of two saturable reactors connected in series. The control windings are connected to a variable DC current source through a RFC choke. Based on initial measurements and experimental results, the reduction factor of the permeability of the saturable reactors' cores is assumed to be 65 % at an operating temperature of 65 °C. The specifications and values of the inductive link, Class E inverter and the saturable reactors are summarised in Table. 5.2.

C. Implementing the proposed tuning method

Depending on the coupling coefficient of the coupled coils, the amount of DC current injected in the secondary side of the transformers, along with the switching frequency, were varied to retune the Class E inverter into operating at optimum switching conditions as the coils were displaced. Based on the solutions presented in Fig. 5.50, the values of the switching frequency that are close to the resonant frequency of the inductive link, which is 800 kHz, and the corresponding DC-feed inductance were chosen to be verified. Fig. 5.22 shows the measured DC control current, the calculated DC-feed inductance and the switching frequencies as the coupling coefficient of the coil varied. The experimental results are in good agreement with the numerical solutions. Fig. 5.22c shows the measured power received to the load which was connected to the secondary coil of the inductive link, as well as the overall system efficiency which includes that of the inductive link losses, the Class E inverter losses, the MOSFET

Table 5.2: Values and ranges of several parameters of the Class E inverter and the inductive link measured at 800 kHz

	Component/Parameter	Value
Inductive Link	L_P / r_P	5.76 µH / 0.17 Ω
	L_S / r_S	6.69 µH / 0.28 Ω
	C_S / r_{C_S}	5.92 nF / 0.25 Ω
	Resonant Frequency f_o	800 kHz
	R_{Load}	47 Ω
	Mutual Inductance (M) Range	1.37 - 2.23 µH
	Coupling Coefficient (k) Range	0.22 - 0.36
	Coils Radial Displacement Range (d)	0 - 2.5 cm
	Coils Separation Dist. (h)	2.5 cm
	Component/Parameter	**Value**
Class E Inverter	MOSFET	STP40NF10
	Gate Driver	TC1412
	Input Voltage	8 V
	C_1 / r_{C_1}	22 nF / 0.15 Ω
	C_2 / r_{C_2}	7.9 nF / 0.15 Ω
	Switching Frequency Range f_s	790 - 820 kHz
	Duty Cycle	48 %
	Component/Parameter	**Value**
Saturable Reactors	Core Type	MPP 550 [103]
	No. of Cores	2
	Primary No. turns per core	2.5
	Secondary No. turns per core	70
	Permeability reduction factor r	0.65
	Control Current Range I	0.00 - 1.00 A
	L_f Range	2.56 - 0.88 µH

gate driver losses, the saturable reactors' core losses and the ohmic losses in the secondary windings of the saturable reactors. The received power was kept at a relatively constant level of 10 W throughout the displacement range with a peak occurring at a coupling coefficient of 0.30. The overall efficiency is reduced when the coupled coils are closer to each other at higher coupling coefficients and is maintained at a constant level as the coils are further apart at lower coupling coefficients. Therefore, for the chosen values of the inductive link and the Class E inverter, the proposed tuning method is suited for reduced coupling coefficients and at higher radial displacements of the

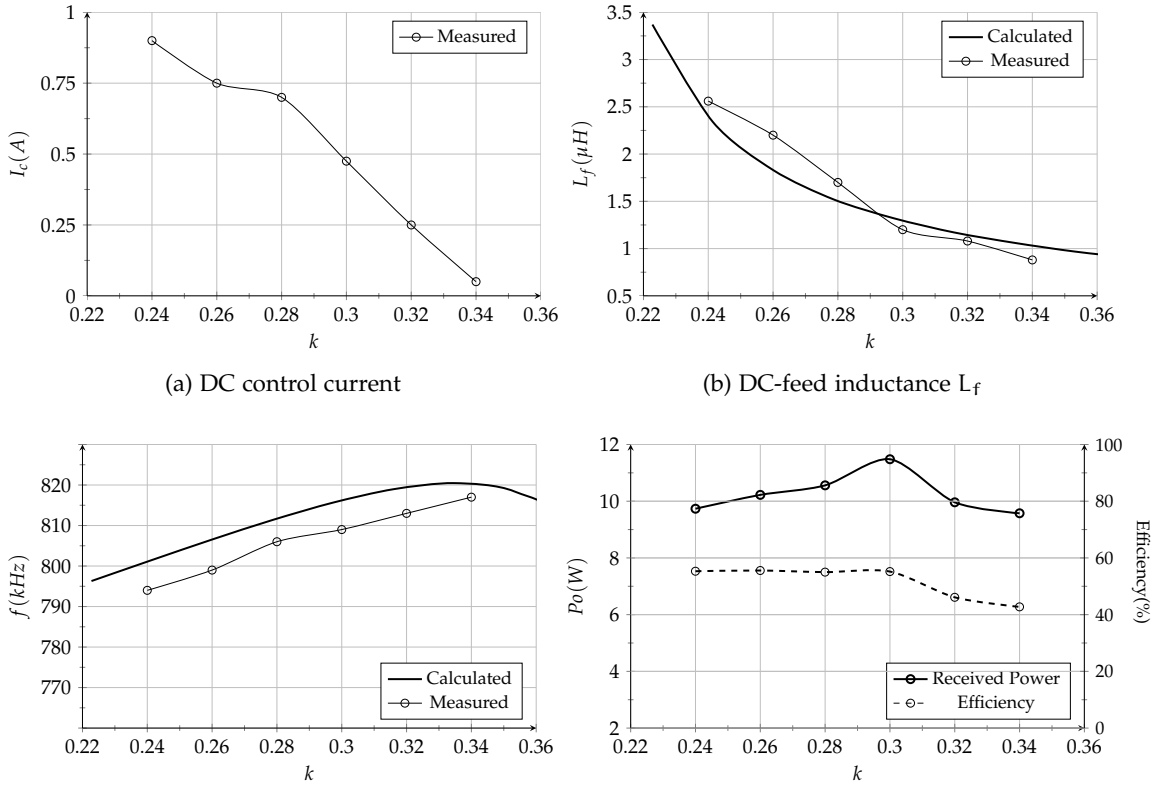

(a) DC control current

(b) DC-feed inductance L_f

(c) Switching frequencies

(d) Recieved power and overall system efficiency

Fig. 5.22: Calculated and measured parameters of the Class E inverter. Tuning is performed as the coupling coefficient varies

coupled coils. Fig. 5.23 shows the experimental waveforms of the MOSFET's drain voltage, the voltage of the load at the secondary coil, the voltage across one saturable reactor's control windings and the current of the saturable reactor's primary windings. In Fig. 5.23a the inverter is operating at optimum switching conditions when the primary coils are aligned with each other. The coupling coefficient is 0.34, the DC control current is 0.9 A and the switching frequency is 818 kHz. In Fig. 5.23b. the coils are radially displaced from each other by a distance of 2.5 cm, corresponding to a coupling coefficient of 0.24, while maintaining the same DC control current and switching frequency. Since the coupling and the reflected impedances have now changed, the inverter no longer operates at optimum switching conditions since the MOSFET is being switched ON at a non-zero voltage. In Fig. 5.23 the inverter is retuned and is now operating at optimum switching conditions by decreasing the DC control current to 0.05 A and the switching frequency to 795 kHz. Therefore, the proposed tuning method of controlling the DC-feed inductance and the switching frequency has been successfully verified allowing the Class E inverter to operate safely and efficiently over a certain coil misalignment range.

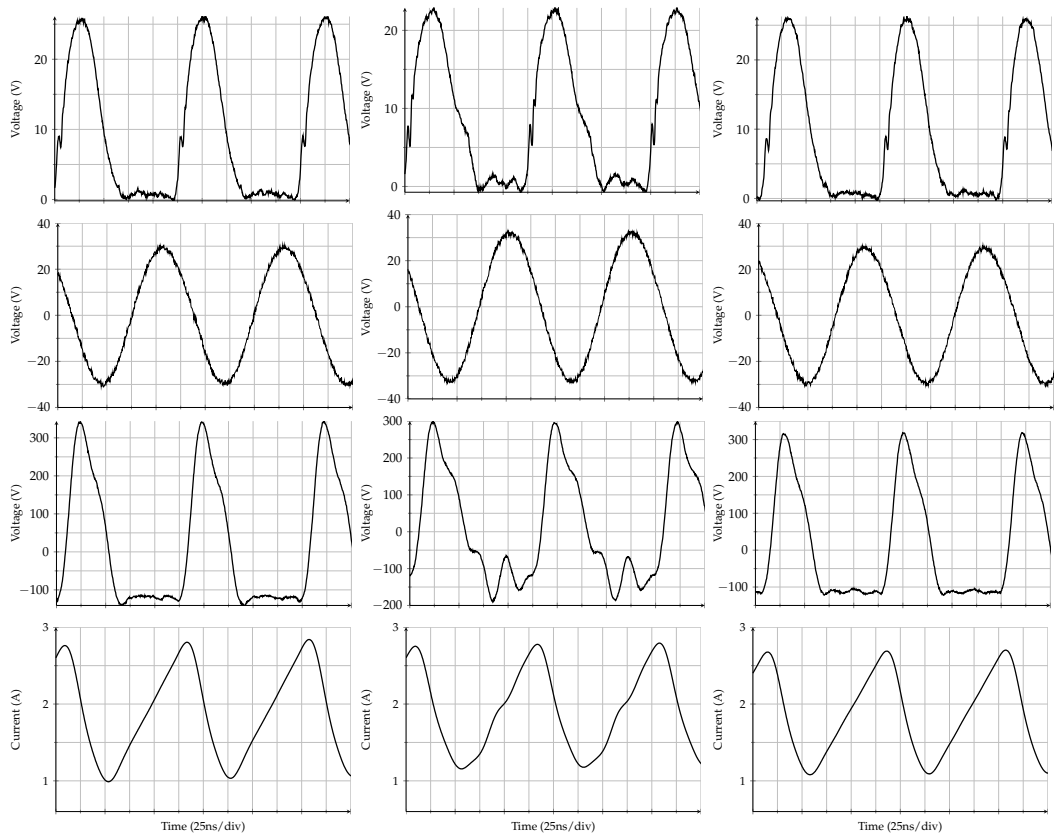

(a) Tuned optimum switching operation at $k = 0.34$

(b) Non-optimum switching operation at $k = 0.24$

(c) Retuned optimum switching operation at $k = 0.24$

Fig. 5.23: Experimental waveforms of the implemented WPT system at different coupling coefficients demonstrating the proposed tuning method. First waveform is the MOSFET's drain voltage V_{DS}, second is the load voltage at the secondary coil, third is voltage across the control windings of one saturable reactor and the fourth is the current in the DC-feed inductance I_{L_f} (primary windings of the saturable reactors)

5.6 TUNING METHODS BASED ON STATE-SPACE MODELLING

The tuning methods presented in Secs. 5.4 and 5.5 both relied on adjusting the switching frequency of the Class E inverter. Although optimum switching operation was achieved, the variation in the switching frequency can degrade the efficiency of the inductive link especially if the coils are designed to have a large quality factor at their resonant frequency. In addition, adjusting the switching frequency may be undesirable if a resonant rectifier, such as a Class D rectifier or a Class E rectifier, is used at the receiving coil. Therefore the tuning method that will be presented in this section allow for the duty cycle of the switching signal to be controlled rather than the frequency. This tuning method will be based on the state-space representation approach presented in Sec. 5.2.3 and will be applied for the Class E inverter designed previously in Sec. 5.5.

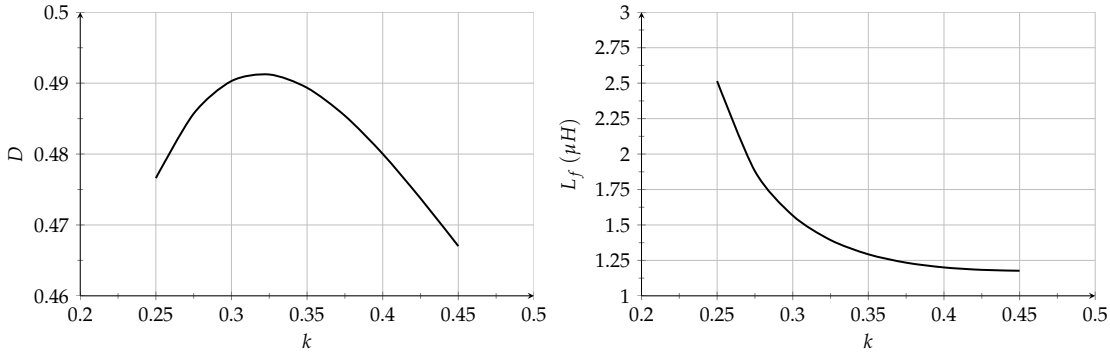

Fig. 5.24: Solutions of the duty cycle and the DC-feed inductance

5.6.1 *Duty cycle and* L_f *control*

The aim will be to find the values of the duty cycle and the DC-feed inductance as the coupling coefficient varies while keeping the values of C_1 and C_2 fixed. Using Eqs. 5.42-5.44, the values of the duty cycle and L_f can be numerically solved for different values of the coupling coefficient. Fig. 5.24 shows the solutions of the duty cycle and L_f which exist in the coupling coefficient range from 0.2 to 0.45. No other solutions exist outside this particular coupling coefficient range. The code for obtaining the duty cycle and the value of L_f was programmed in MATLAB and is included in the Appendix A.2.3.

5.6.2 *Simulink modelling*

Fig. 5.25 shows a simulation model constructed in MATLAB Simulink. The model allows for the Class E inverter and the inductive link to be simulated as a system over one switching period. The simulation model is divided into two independent submodels; one to simulate the system for the ON interval and the other for the OFF interval. Each submodel is based on the 'State-space model' block and is only simulated over its predefined interval. This can be achieved using the 'Enable' block. The ON submodel is activated over the interval $0 \rightarrow 2\pi D$ and the OFF submodel is activated over the interval $2\pi D \rightarrow 2\pi$. The outputs of both models are combined to obtain the voltage and current waveforms of the system over the entire switching period.

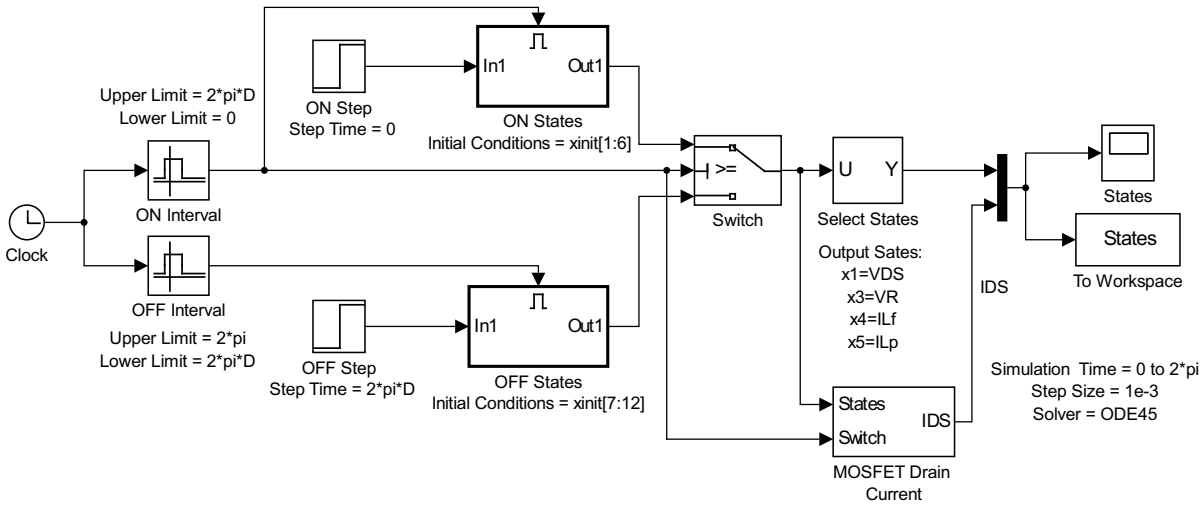

(a) entire model

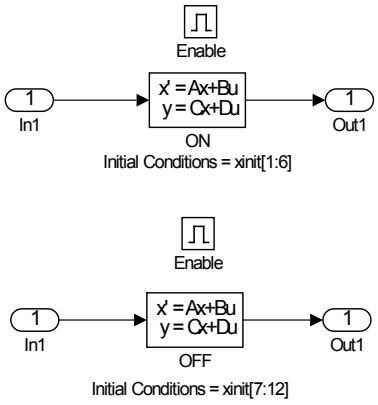

(b) the 'ON States' and 'OFF States' sub blocks

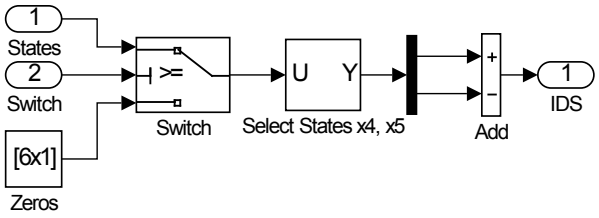

(c) the 'MOSFET Drain Current' sub block

Fig. 5.25: Simulink model

5.6.3 *Implementation of the proposed tuning method*

The tuning method was implemented as follows. The coils of the inductive link were initially kept at an initial separation distance of 2.5 cm and were brought closer to each other in steps of 0.25 cm to a distance 0.5 cm. The duty cycle and the control current of the magnetic amplifiers are varied according to Fig. 5.24 to achieve optimum switching conditions over the coupling coefficient range. Fig. 5.26 shows several measured parameters. In Fig. 5.26a, the measured values of the duty cycle that were required to achieve optimum switching operation are compared with the solved values shown in Fig. 5.24. The discrepancies are due to finite rise and fall times of the MOSFET and the MOSFET driver. Fig. 5.26b shows the values of the DC control current of the magnetic amplifier. Figs. 5.26c-g show the variation of voltages and current throughout the inverter over the entire coupling coefficient range. The input power and the transmitted power are plotted in Fig. 5.26h. A peak occurs at a distance of 1.25 cm

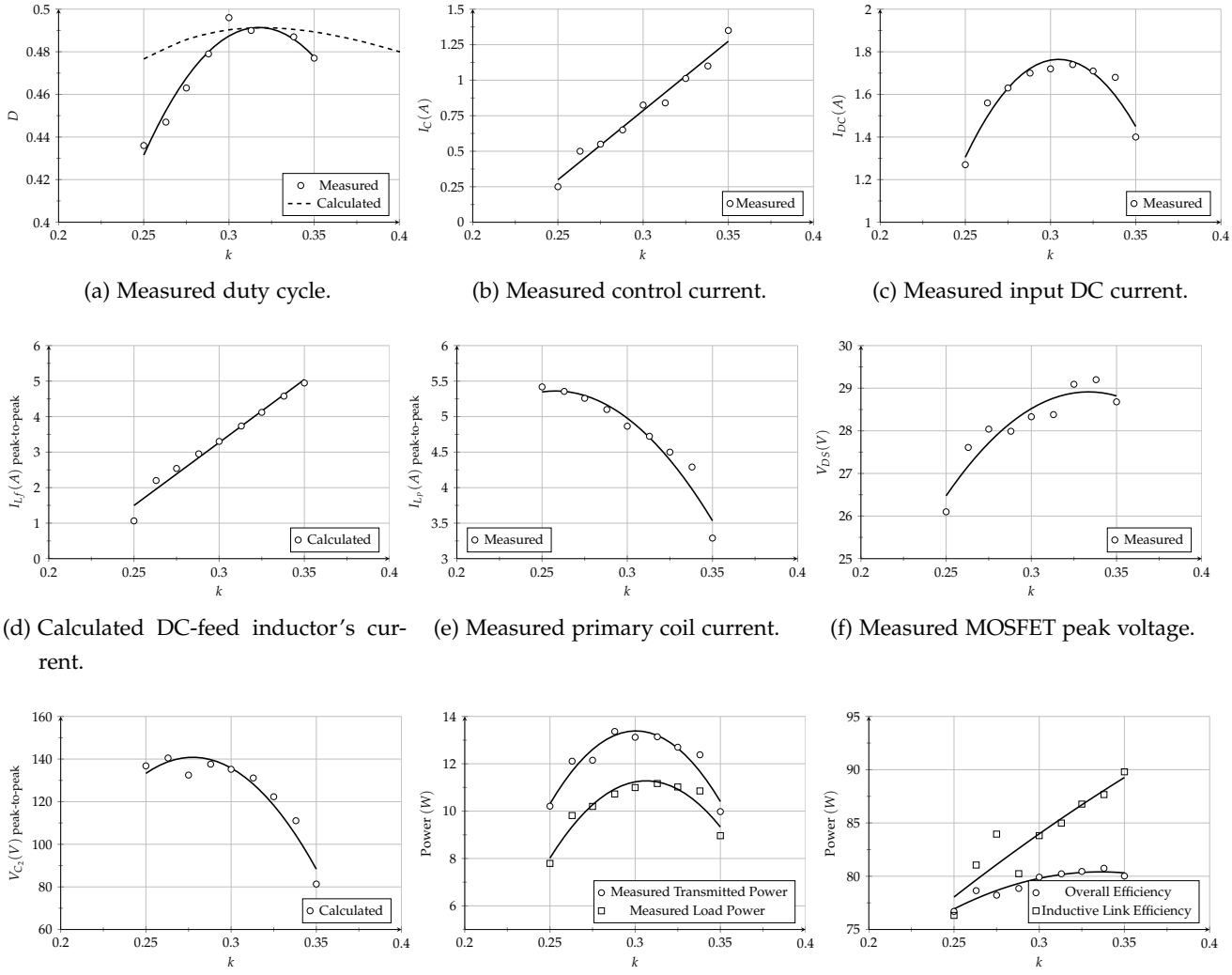

(a) Measured duty cycle.

(b) Measured control current.

(c) Measured input DC current.

(d) Calculated DC-feed inductor's current.

(e) Measured primary coil current.

(f) Measured MOSFET peak voltage.

(g) Calculated voltage of C_2.

(h) Measured power.

(i) Calculated Efficiencies

Fig. 5.26: Measured and calculated parameters, voltages and currents over a certain coupling coefficient range.

corresponding to a coupling coefficient value of 0.3. The calculated overall system efficiency, i.e. DC-to-load, and the calculated efficiency of the inductive link are shown in Figs. 5.26h and 5.26i respectively. The efficiency of the inductive link increases as the coils are brought closer to each other since the reflected impedance of the load becomes more significant than that of the ESR of the coils. The overall efficiency increases as the coils are brought closer and remains relatively constant at 80 % for larger coupling coefficient values.

The experimental waveforms of the voltages and currents throughout the Class E inverter and the inductive link are shown in Figs. 5.27 and 5.28 respectively. In Fig. 5.27a and Fig. 5.28a, the inverter is operating at optimum switching conditions achieving ZVS and ZVDS. The separation distance is 1.25 cm corresponding to a coupling coefficient of 0.3, the DC control current is 0.85 A, the duty cycle of the switching sig-

nal is 49.5 % and the power delivered to the load is 11.75 W. Theoretical waveforms are also plotted and are in good agreement with the experimental waveforms. In Fig. 5.27b and Fig. 5.28b, the coils are brought closer to each other to a separation distance of 0.75 cm corresponding to a coupling coefficient of 0.35 while maintaining the same DC control current and duty cycle. Since the coupling coefficient has now changed, the Class E inverter no longer operates at optimum switching conditions since the MOSFET is being switched ON at a non-zero voltage as can be seen in the figures. The non-optimum switching conditions result in distortion of the voltage and current waveforms. This causes excessive losses in the form of heat and reduces the amount of power that can be delivered over the load which in this case is now 7.70 W. In Fig. 5.27c and Fig. 5.28c, the inverter is retuned and is now operating at optimum switching conditions by decreasing the duty cycle of the switching signal to 48.0 % and increasing the DC control current to 1.35 A. Theoretical waveforms are also plotted and are found to match the new experimental waveforms. The power delivered to load has now increased to 8.92 W. Therefore, the proposed tuning method of controlling the duty cycle of the switching frequency and DC-feed inductance has been successfully verified allowing the Class E inverter to operate safely and efficiently over a certain coil displacement range.

5.7 CONCLUSIONS

This chapter discussed the application of Class E inverters as primary coil drivers in inductive links. Analysis was performed using the analytical approach and the state-space representation approach to calculate the parameters and component values of the Class E inverter for a pre-specified inductive link. The performance of Class E inverters was investigated. It was shown that a variation in the coupling coefficient between the coils of an inductive link can significantly affect the switching conditions of the Class E inverter. As a result, several novel tuning methods were proposed to electronically tune Class E inverters during operation to achieve optimum switching conditions as the coupling coefficient varies. The tuning methods rely on using saturable reactors as controlled elements. Extensive experimental results were presented showing the successful implementation of the proposed tuning methods on various configurations of the Class E inverter.

The proposed tuning methods provide the basis for developing control and tuning algorithms that can achieve automatic tuning as variations occur in the coupling coefficient of an inductive link.

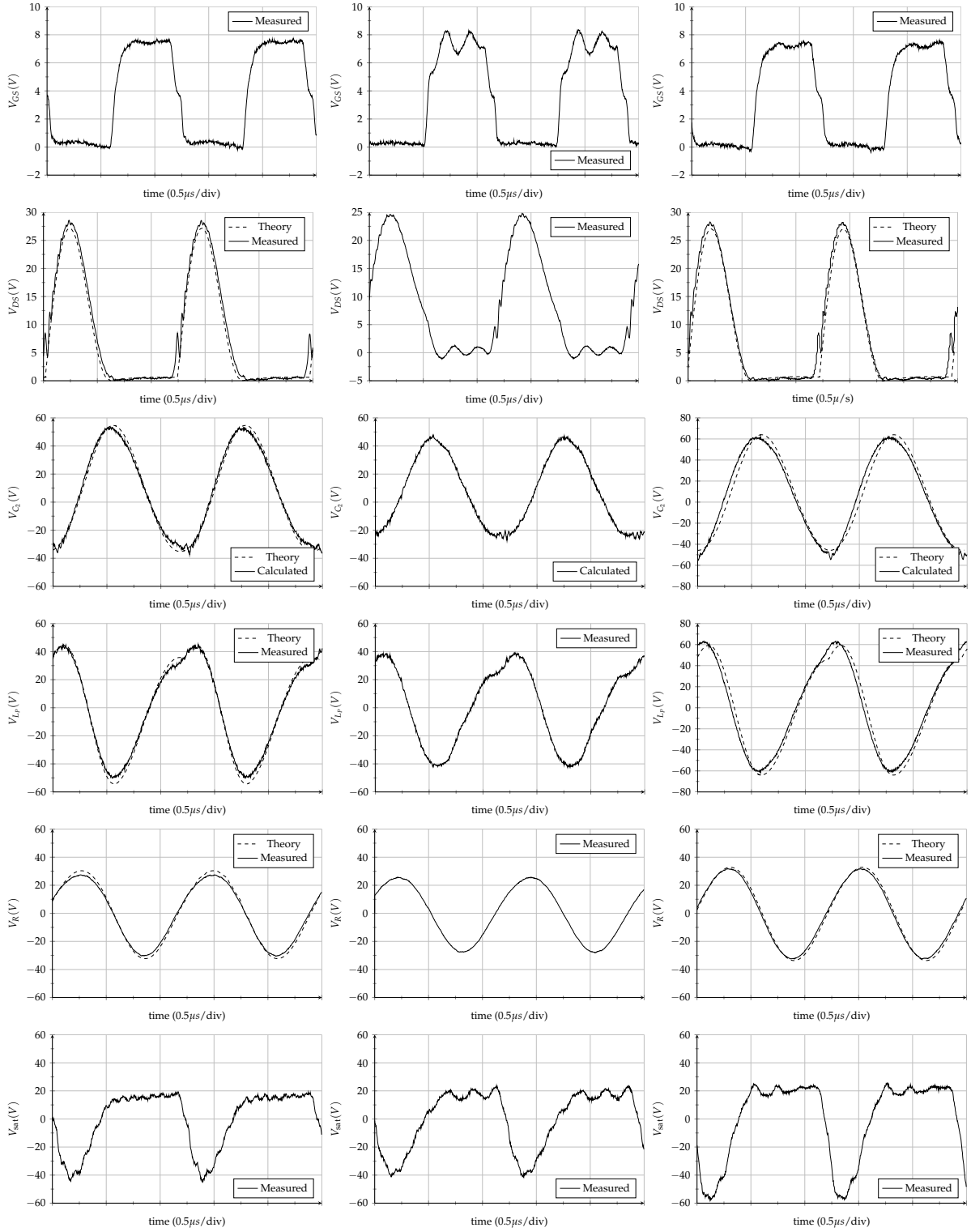

(a) Tuned optimum operation at k = 0.25.

(b) Untuned non-optimum operation at k = 0.35.

(c) Retuned optimum operation at k = 0.35.

Fig. 5.27: Voltage waveforms of the implemented WPT system at different coupling coefficients demonstrating the proposed tuning method representing the MOSFET's gate driving signal V_{GS}, the MOSFET's drain voltage V_{DS}, the voltage across the series capacitor V_{C_2}, the voltage across the primary coil V_{L_P}, the output voltage at the load V_R and the voltage developed across the control windings of one of the magnetic amplifier V_{sat}.

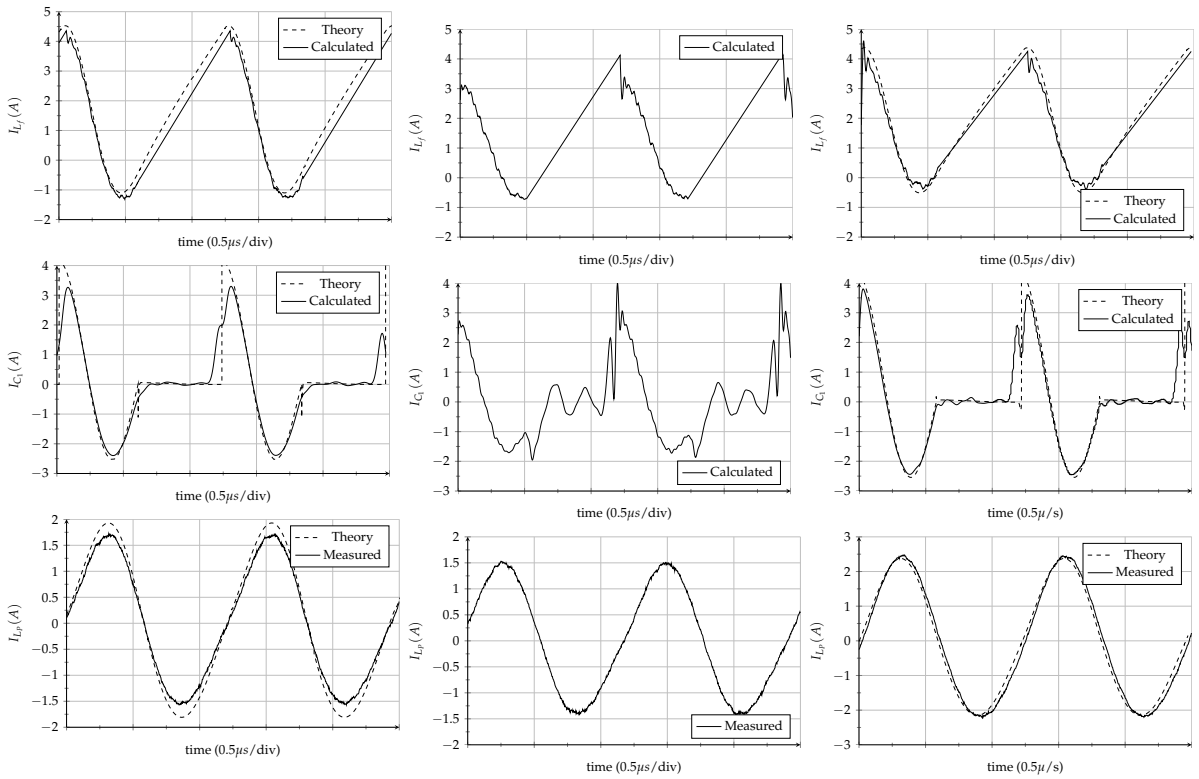

(a) Tuned optimum operation at $k = 0.25$.

(b) Untuned non-optimum operation at $k = 0.35$.

(c) Retuned optimum operation at $k = 0.35$.

Fig. 5.28: Current waveforms of the implemented WPT system at different coupling coefficients demonstrating the proposed tuning method representing the DC-feed inductor's current I_{L_f}, the shunt capacitor's current I_{C_1} and the primary coil's current I_{L_P}.

6

AC/DC RECTIFIERS IN IPT SYSTEMS

6.1 INTRODUCTION

The analysis of the inductive links and primary coil drivers were performed under the assumption that the load connected to the secondary coil was a pure resistive AC load. Most applications nowadays are considered DC loads which are either represented by a resistor or a current sink. To deliver the received power to a DC load requires the use of a AC/DC rectifier. AC/DC rectification is extensively studied and well described in literature. As a matter of fact, every electronic power device that is powered from an AC voltage source such as the mains voltage in our homes must contain a rectifier.

Whilst most of recent published work in inductive power transfer (IPT) technology focuses on the design and optimization issues of the resonant inductive coils [45, 61, 105–107] and the transmitting coil driver [73–75], there has been little research in high frequency, high efficiency rectifiers for IPT applications and their impact on the overall performance of an IPT system. In previous work, the load connected to the secondary coil of the inductive link has either been an AC load in the form of a resistor [73–75, 107, 108], or a DC load connected through an AC/DC rectifier. Since DC loads are more common than AC loads, more research into rectifiers that are suitable for IPT systems is required.

The majority of AC/DC rectifiers that have been used in recent publications about IPT systems are either traditional half-wave rectifiers [77] or bridge rectifiers [32, 51, 106]. The main losses that occur in the rectifiers are due to the forward voltage drop of the rectifying elements and their switching losses. Synchronous rectifiers based on a bridge configuration can improve the overall efficiency in IPT systems. However timing and control of the four switches may be difficult especially at high resonant frequencies [60]. In addition, traditional half-wave rectifiers and bridge rectifiers have a non-sinusoidal input current and can cause a non-sinusoidal current to flow out

of the secondary resonant circuit of the inductive link. This affects the performance and efficiency of the primary coil driver since most primary coil drivers operate at resonance and generate a sinusoidal driving current.

In the following sections the use of the traditional half-wave and full-wave rectifiers in IPT and their affect on resonant DC/AC inverters, particularly the Class E inverter, will be discussed. Then, Class D and Class E rectifiers are introduced and a certain configuration of each will be proposed to be used with the inductive link designed in Sec. 3.4.3. Mathematical analysis based on the state-space representation approach will be performed to derive certain parameters. Extensive experimental results will be shown to demonstrate their performance and to show their efficient operation.

6.1.1 *Definitions*

The following definitions are associated with analysis and modelling of the rectifiers that will be presented in the chapter:

- Switching frequency ω
  The angular switching frequency of the rectifier ω is equal to the angular switching frequency of the primary coil driver

- Resonant frequency ω_o
  The resonant frequency of the resonant section of the rectifier (if any) is
  $$\omega_o = \frac{1}{\sqrt{LC}} \tag{6.1}$$
  where L and C represent the inductance and capacitance of its resonant section

- Characteristic impedance Z_o
  The characteristic impedance of the resonant section of the rectifier formed by L and C
  $$Z_o = \sqrt{\frac{L}{C}} \tag{6.2}$$

- the ratio of the rectifier's resonant frequency to the switching frequency
  $$q = \frac{\omega_o}{\omega} = \frac{1}{\omega\sqrt{LC}} \tag{6.3}$$

- Normalised load R_L
  $$R_{norm} = \frac{R_L}{Z} \tag{6.4}$$
  where R_L represents the resistance of the load to the rectifier

- Input voltage source
  The voltage source for voltage-driven rectifiers is assumed to be sinusoidal and is given by

$$V_i(\omega t) = v_m \sin(\omega t + \phi) \tag{6.5}$$

  where v_m is the magnitude of the input voltage.

- Input current source
  The input current for current-driven rectifiers is assumed to be sinusoidal and is given by

$$I_i(\omega t) = i_m \sin(\omega t + \phi) \tag{6.6}$$

  where i_m is the magnitude of the input current

- Power Factor (PF)
  The power factor is defined as the ratio of the real power to the apparent power at the input of a rectifier and is given by [109]

$$PF = \frac{\sum_{n=1}^{\infty} P_n}{V_{RMS} I_{RMS}} = \frac{\sum_{n=1}^{\infty} V_n I_n \cos\phi_n}{\sqrt{\sum_{n=1}^{\infty} V_n^2}\sqrt{\sum_{n=1}^{\infty} I_n^2}} \tag{6.7}$$

  where P_n is the power of the nth harmonic, V_{RMS} and I_{RMS} are the RMS values of the source voltage and current respectively, V_n and I_n are the RMS values of the nth harmonic of the source's voltage and current respectively, and ϕ_n is the phase shift between the voltage and current of the $n$the harmonic. The power factor can be used as an indication of how reactive the reflected impedance of the rectifier is for different loading conditions as seen from the receiving and transmitting coils of a resonant IPT system.

- Total Harmonic Distortion (THD)
  The THD is defined as the ratio of the sum of the powers of all harmonic components to the power of the fundamental frequency. For a voltage-driven rectifier the THD in its input current is given by

$$THD = \frac{\sqrt{\sum_{n=2}^{\infty} V_n^2}}{V_1} = \sqrt{\left(\frac{V_{RMS}}{V_{1RMS}}\right)^2 - 1}. \tag{6.8}$$

  For a current-driven rectifier the THD in its input voltage is given by

$$THD = \frac{\sqrt{\sum_{n=2}^{\infty} I_n^2}}{I_1} = \sqrt{\left(\frac{I_{RMS}}{I_{1RMS}}\right)^2 - 1}. \tag{6.9}$$

The THD can determine the compatibility of a certain rectifier with a resonant inductive link. A value close to zero indicates that the rectifier's input voltage or current is close to an ideal sine wave and therefore can be compatible with resonant inductive links. Whereas an increasing value indicates that the rectifiers input voltage and current is highly non-linear and therefore not suitable to be used in resonant inductive links.

6.2 TRADITIONAL RECTIFIERS

The AC voltage induced in the secondary coil cannot be applied directly to a DC load such as a motor or a battery, AC/DC rectification is therefore required. The majority of the rectifiers that are used today and that are applied to inductive links fall under two categories; half-wave rectifiers and full-wave rectifiers. A brief discussion will be provided on these categories of AC/DC rectifiers with the assumption that the AC voltage to be rectified is pure sinusoidal.

6.2.1 *Half-Wave Rectifiers*

Since an AC voltage signal alternates between a positive voltage value and a negative voltage value, a half wave rectifier simply allows the positive part of the AC voltage signal to pass to the load while blocking the negative part, or alternatively, passing the negative part and blocking the positive part. A widely popular circuit that achieves half-wave rectification is shown in Fig. 6.1 using a single diode. A capacitor with a very large capacitance is added to average the pulses into a constant DC voltage. Ideally the value of the rectified DC output voltage should be equal to the peak voltage of the AC voltage signal if the time constant of the added capacitor and the load is large compared to the period of the AC voltage. The rectified DC output voltage should also be flat, i.e. without any voltage ripples. Practically, due to the forward voltage drop of the diode and the limited capacitance of the capacitor, the rectified DC output voltage will not be equal to the peak of the AC voltage and will contain voltage ripples as illustrated in Fig. 6.3. To overcome this issue, large capacitors with a low ESR should be used. The diode could also be replaced by a Schottky diode and even with a controlled switch such as a MOSFET. If a MOSFET is used, then the rectifier is referred to as a 'synchronous' rectifier since the MOSFET driving signals have to be synchronised with input AC voltage.

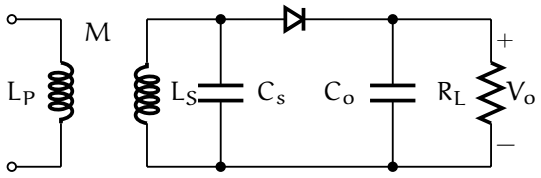

(a) inductive link with a half-wave rectifier

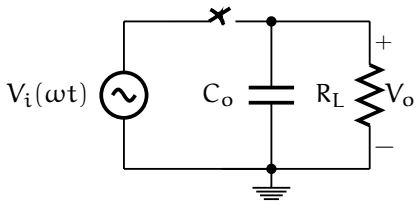

(b) equivalent circuit

Fig. 6.1: A half-wave rectifier using a single diode

The RMS value of the unaveraged output voltage of the half-wave rectifier with an ideal diode ($V_f = 0$) is given by

$$V_{oRMS} = \sqrt{\frac{1}{T}\int_0^T V_i^2(\omega t)d\omega t} = \sqrt{\frac{1}{2\pi}\int_0^\pi (v_m \sin(\omega t))^2 d\omega t} = \frac{v_m}{2} \tag{6.10}$$

and its averaged output voltage is given by

$$V_o = \frac{1}{T}\int_0^T V_i(\omega t)d\omega t = \frac{1}{2\pi}\int_0^\pi v_m \sin(\omega t)d\omega t = \frac{v_m}{\pi} \approx 0.3183 v_m \tag{6.11}$$

6.2.2 *Full-Wave Rectifiers*

Instead of blocking the negative part of the AC voltage signal, a full-wave rectifier not only passes the positive part but also converts the negative parts into a positive voltage. Consequently, the full-wave rectifier needs a smaller capacitor compared to that of the half-wave rectifier and also the voltage ripples on the rectified DC output voltage are smaller. Fig. 6.2 shows the widely popular full-wave bridge rectifier. The circuit of the bridge rectifier consists of four diodes or switching devices. The value of the rectified DC output voltage is reduced since the forward voltage drop is doubled due to the additional diodes. However, replacing the diodes with MOSFETs overcomes this issue.

The RMS value of the unaveraged output voltage of the full-wave rectifier with ideal diodes ($V_f = 0$) is given by

$$V_{oRMS} = \sqrt{\frac{1}{T}\int_0^T V_i^2(\omega t)d\omega t} = \sqrt{\frac{1}{\pi}\int_0^\pi (v_m \sin(\omega t))^2 d\omega t} = \frac{v_m}{\sqrt{2}} \approx 0.7071 v_m \tag{6.12}$$

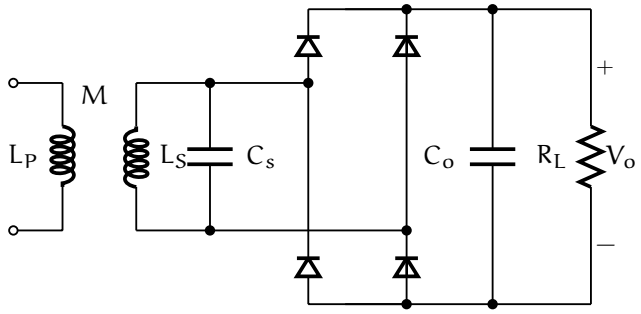

(a) inductive link with a h-bridge full-wave rectifier

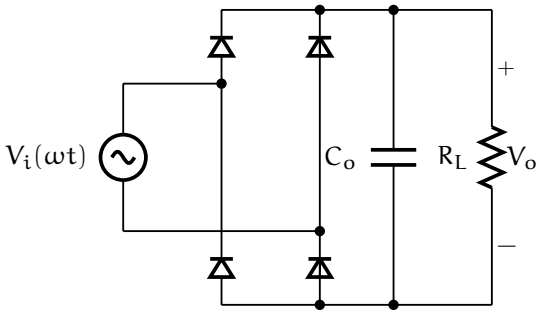

(b) equivalent circuit

Fig. 6.2: A full-wave H-bridge rectifier

and its averaged output voltage is given by

$$V_o = \frac{1}{T}\int_0^T V_i(\omega t)d\omega t = \frac{1}{\pi}\int_0^\pi v_m \sin(\omega t)d\omega t = \frac{2v_m}{\pi} \approx 0.6366 v_m \tag{6.13}$$

Fig. 6.3 shows the voltage waveforms that are associated with the half-wave and full-wave rectifiers.

6.2.3 *Performance Investigation*

In order to investigate the suitability of the traditional rectifiers in inductive links, it is necessary to look into their input current waveform. Fig. 6.4 shows the typical input voltage and current waveforms of the full-bridge rectifier in Fig. 6.2. Due to the output-filter capacitor, the rectifier draws current when the instantaneous voltage of the supply exceeds the voltage across the capacitor. Therefore the input current is a sequence of high current pules that occur at the positive and negative peaks of the input voltage. The resulting current spikes are nonsinusoidal and have a harmonic content. Consequently, the voltage supply operates at a very low power factor and at a high current THD factor. A low power factor affects the inductive link by detuning its resonant frequency and therefore limits the amount of power that is delivered to the load as discussed. Power factor ratios between 0.5 to 0.7 are common for the full-wave bridge rectifier [110].

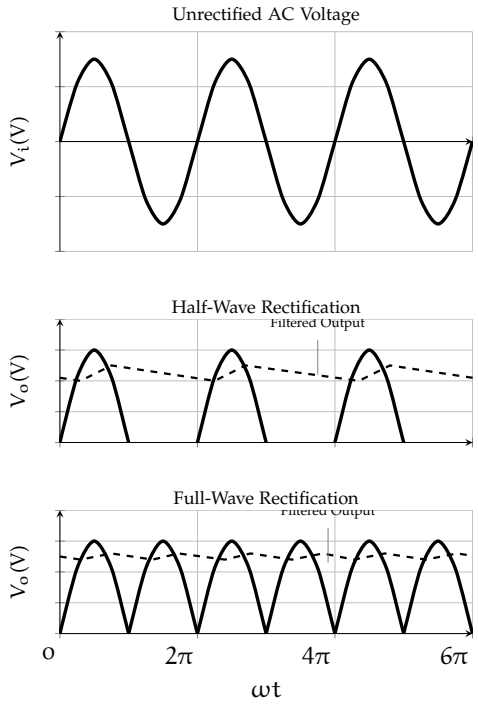

Fig. 6.3: Half-wave and full-wave rectification waveforms

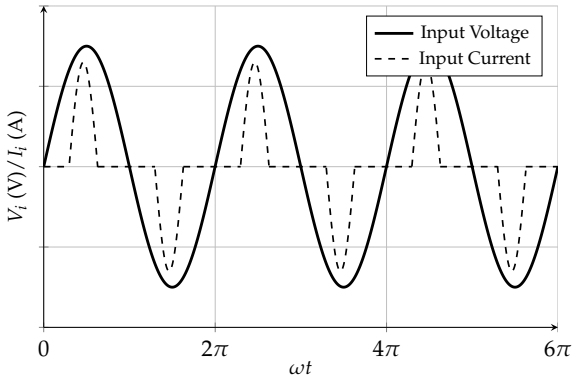

Fig. 6.4: Typical input voltage and input current waveforms of an H-bridge full-wave rectifier with an output filter capacitor

The THD of the input current of a rectifier has a higher impact on the overall performance of an inductive link and its primary coil driver than the power factor. The fact that resonant inverters are optimised to generate a sinusoidal output current at a certain load value makes them less tolerant to variations in load, as in the case for the Class E inverter. Each harmonic of the input current of the rectifier can correspond to a certain impedance. Therefore a high harmonic content can result in a large number of impedances which distort the output current of a resonant inverter. Fig. 6.5 shows the typical harmonic content of the input current for an H-bridge full-wave rectifier, THD factors are generally above 50 %. Power factor corrections circuits and input filters can be used to improve the power factor and the THD, however they can increase the size and complexity of the rectifier in addition to degradation of the overall system

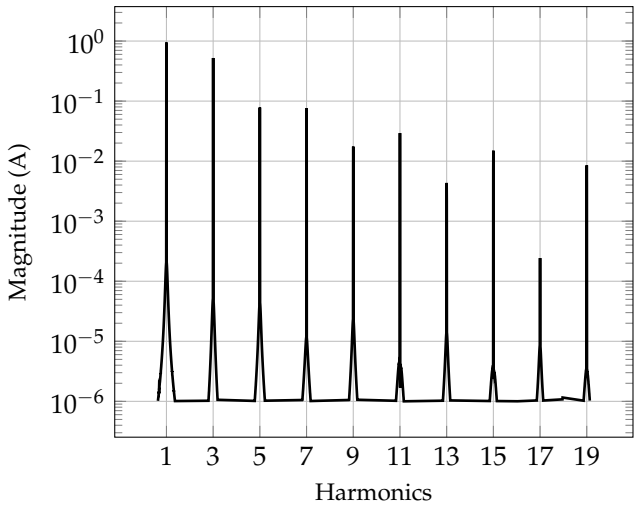

Fig. 6.5: Typical harmonic content of the input current of an H-bridge full-wave rectifier with an output-filter capacitor

efficiency. Nevertheless, the H-bridge full-wave rectifier has been used in IPT systems due to their simple principle of operation and low voltage stresses. For further information about half-wave and full-wave rectifiers, including extensive modelling and analysis, refer to [110].

6.3 CLASS D RECTIFIERS

Class D rectifiers [111–113] can be thought of as the dual of Class D inverters. Much like the traditional rectifiers, Class D rectifiers can convert a sinusoidal voltage or current into a DC voltage or current. Their main advantage is that the input voltage or current to the rectifier is a square wave, therefore the power factor and the THD are enhanced which makes them compatible with Class D and Class E resonant inverters.

Class D rectifiers are similar in construction to the traditional rectifiers. They are further classified into two subclasses [111]; Class D current-driven rectifiers and Class D voltage-driven rectifiers. The Class D current-driven rectifier rectifies a sinusoidal input current into a DC output voltage, whereas a Class D voltage-driven rectifier rectifies a sinusoidal input voltage into a DC output current. Figs. 6.6 and 6.7 show several configurations of both subclasses and their equivalent circuits. Fig. 6.8 shows the voltage and current waveforms that are associated with the Class D voltage-driven and current-driven rectifiers.

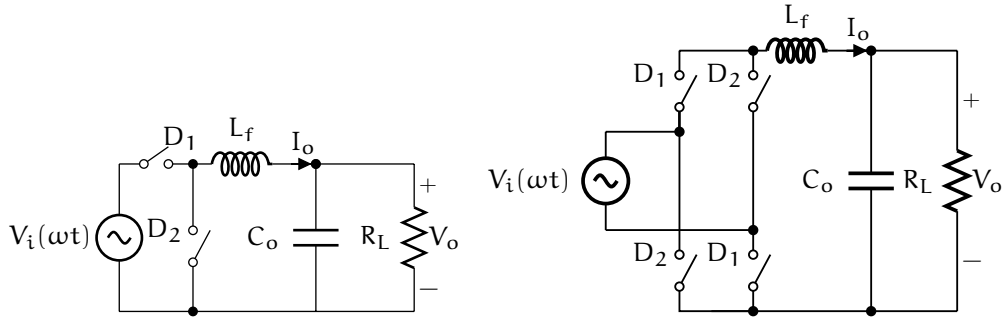

(a) half-wave Class D voltage-driven recitifer (b) full-wave Class D voltage-driven recitifer

Fig. 6.6: Class D voltage-driven rectifiers in inductive links

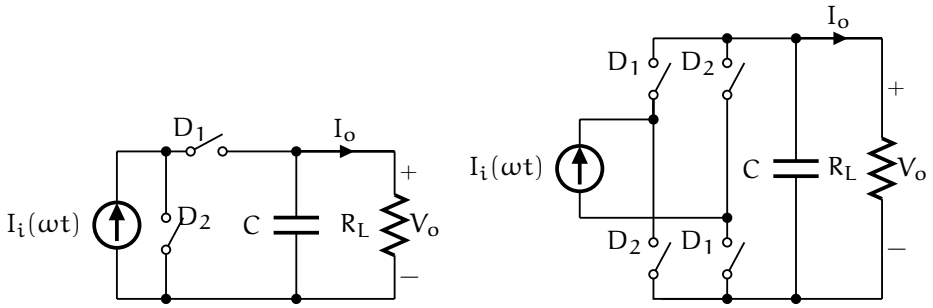

(a) half-wave Class D current-driven recitifer (b) full-wave Class D current-driven recitifer

Fig. 6.7: Class D current-driven rectifiers in inductive links

6.3.1 *Analysis of Class D Voltage-driven Rectifiers*

The voltage and current relationships will be derived for the half-wave Class D voltage-driven rectifier in Fig, 6.6a, in addition to the power factor and the THD. The analysis will be based on an analytical approach and will be based on the following assumptions:

- The input voltage is sinusoidal.
- The inductance of the inductor L is large enough such that the current (I_o) flowing through it is a DC current.
- The capacitance of the capacitor C is large enough such that the output voltage (V_o) across is it is a DC voltage.
- The diodes are ideal switches with a zero forward voltage drop and a zero ON resistance.

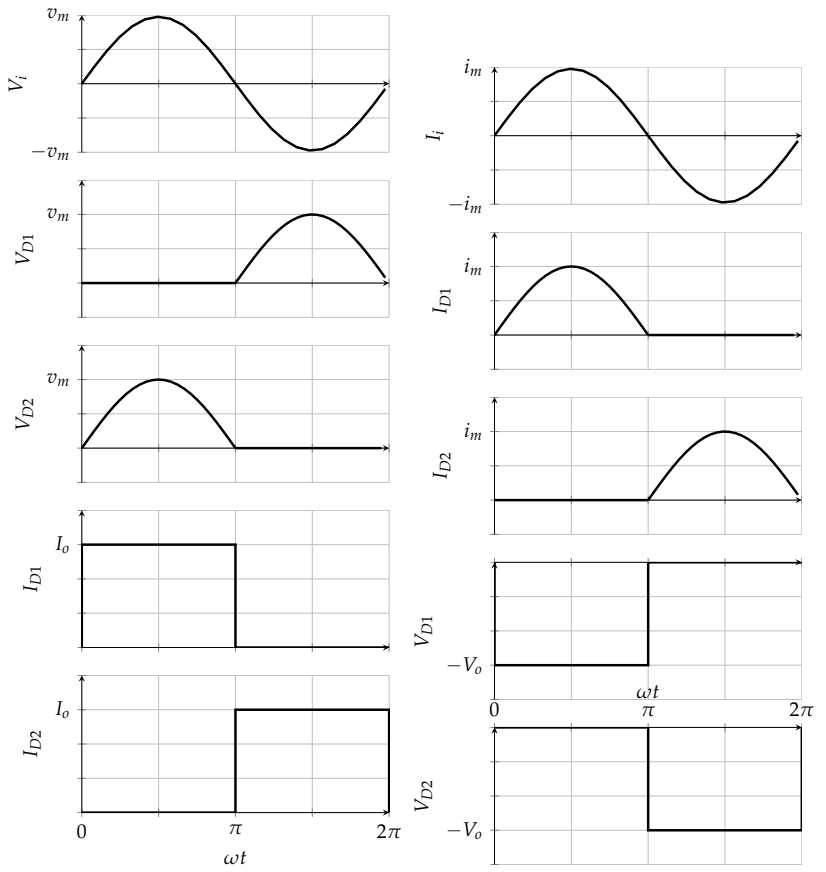

(a) voltage-driven Class D rectifiers (b) current-driven Class D rectifiers

Fig. 6.8: Voltage and current waveforms of Class D rectifiers

Referring to the voltage and current waveforms in Fig. 6.8a, the currents in the diodes are

$$I_{D_1}(\omega t) = \begin{cases} I_o, & \text{for } 0 \leqslant \omega t < \pi \\ 0, & \text{for } \pi \leqslant \omega t < 2\pi \end{cases} \tag{6.14}$$

$$I_{D_2}(\omega t) = \begin{cases} 0, & \text{for } 0 \leqslant \omega t < \pi \\ I_o, & \text{for } \pi \leqslant \omega t < 2\pi \end{cases}. \tag{6.15}$$

The voltage across the diodes is

$$V_{D_1}(\omega t) = \begin{cases} 0, & \text{for } 0 \leqslant \omega t < \pi \\ -v_m \sin \omega t, & \text{for } \pi \leqslant \omega t < 2\pi \end{cases} \tag{6.16}$$

$$V_{D_2}(\omega t) = \begin{cases} v_m \sin \omega t, & \text{for } 0 \leqslant \omega t < \pi \\ 0, & \text{for } \pi \leqslant \omega t < 2\pi \end{cases}. \tag{6.17}$$

Hence the output voltage is equal to the average voltage of diode D_2

$$V_o = \frac{1}{2\pi}\int_0^{2\pi} V_{D_2}(\omega t)d\omega t = \frac{1}{2\pi}\int_0^{\pi} v_m \sin\omega t = \frac{v_m}{\pi}. \tag{6.18}$$

Consequently, the output current is given by

$$I_o = \frac{V_o}{R_L} = \frac{v_m}{\pi R_L}. \tag{6.19}$$

The RMS value of the input voltage is given by

$$V_{iRMS} = \frac{v_m}{\sqrt{2}}. \tag{6.20}$$

Therefore the AC-to-DC voltage gain can be represented as

$$M_v = \frac{V_o}{V_{iRMS}} = \frac{\sqrt{2}V_o}{v_m} = \frac{\sqrt{2}}{\pi}. \tag{6.21}$$

It can be noticed from Eqs. 6.18 and 6.21 that for the Class D voltage-driven rectifiers the output voltage is independent of the load value.

The input current (I_i) to the rectifier is equal to diode's D_1 current

$$I_i(\omega t) = I_{D_1}(\omega t) = \begin{cases} I_o, & \text{for } 0 \leqslant \omega t < \pi \\ 0, & \text{for } \pi \leqslant \omega t < 2\pi \end{cases}. \tag{6.22}$$

The RMS value of the input current is

$$I_{iRMS} = \sqrt{\frac{1}{2\pi}\int_0^{2\pi} I_i^2(\omega t)d\omega t} = \sqrt{\frac{1}{2\pi}\int_0^{\pi} I_o^2 d\omega t} = \frac{I_o}{\sqrt{2}}. \tag{6.23}$$

The fundamental component of the input current is

$$i_{m1} = \frac{1}{\pi}\int_0^{2\pi} I_i(\omega t)\sin(\omega t)d\omega t = \frac{1}{\pi}\int_0^{\pi} I_o \sin(\omega t)d\omega t = \frac{2I_o}{\pi} \tag{6.24}$$

and its RMS value is given by

$$i_{m1RMS} = \frac{i_{m1}}{\sqrt{2}} = \frac{\sqrt{2}I_o}{\pi}. \tag{6.25}$$

From Fig. 6.8a it can be assumed that the fundamental component of the input current is in phase with the input voltage. Since the input voltage is sinusoidal therefore the input power contains only the fundamental component

$$P_i = \frac{1}{2}v_m i_{m1}. \tag{6.26}$$

Considering the assumption that the diodes are ideal implies that the output power is equal to the input power, therefore input power can expressed as

$$P_i = P_o = \frac{V_o^2}{R_L} = I_o^2 R_L = \frac{v_m^2}{\pi^2 R_L} \tag{6.27}$$

Using Eqs. 6.19 and 6.24 the input resistance of the rectifier is

$$R_i = \frac{v_m}{i_{m1}} = \frac{v_m \pi}{2I_o} = \frac{\pi^2}{2} R_L \approx 4.9348 R_L. \tag{6.28}$$

From Eqs. 6.7, 6.24 and 6.25 the power factor of the half-wave Class D voltage-driven rectifier is

$$PF = \frac{V_{iRMS} i_{m1RMS}}{V_{iRMS} I_{iRMS}} = \frac{2}{\pi} \approx 0.6366. \tag{6.29}$$

Using Eqs, 6.9, 6.23 and 6.25 the THD factor of the the half-wave Class D voltage-driven rectifier is

$$THD = \sqrt{\left(\frac{I_{iRMS}}{i_{m1RMS}}\right)^2 - \left(\frac{I_o}{2 i_{m1RMS}}\right)^2 - 1} = \sqrt{\left(\frac{\pi}{2}\right)^2 - \left(\frac{\pi}{2\sqrt{2}}\right)^2 - 1} \approx 0.4834. \tag{6.30}$$

The maximum voltage across the diodes is v_m and their maximum current is I_o, therefore the power-output capability is

$$cp = \frac{P_o}{2 V_{DMAX} I_{DMAX}} = \frac{V_o I_o}{2 V_{DMAX} I_{DMAX}} = \frac{1}{2\pi} \approx 0.1592. \tag{6.31}$$

6.3.2 *Analysis of Class D Current-driven Rectifiers*

The voltage and current relationships will be derived for the half-wave Class D current-driven rectifier in Fig. 6.6b, in addition to the power factor and the THD. The analysis will be based on an analytical approach and will be based on the following assumptions:

- The input current is sinusoidal.
- The capacitance of the capacitor C is large enough such that the output voltage (V_o) across is it is a DC voltage.
- The diodes are ideal switches with a zero forward voltage drop and a zero ON resistance.

Referring to the voltage and current waveforms in Fig. 6.8b, the currents in the diodes are

$$I_{D_1}(\omega t) = \begin{cases} i_m \sin(\omega t), & \text{for } 0 \leqslant \omega t < \pi \\ 0, & \text{for } \pi \leqslant \omega t < 2\pi \end{cases} \tag{6.32}$$

$$I_{D_2}(\omega t) = \begin{cases} 0, & \text{for } 0 \leqslant \omega t < \pi \\ -i_m \sin(\omega t), & \text{for } \pi \leqslant \omega t < 2\pi \end{cases}. \tag{6.33}$$

The voltage across the diodes is

$$V_{D_1}(\omega t) = \begin{cases} 0, & \text{for } 0 \leqslant \omega t < \pi \\ -V_o, & \text{for } \pi \leqslant \omega t < 2\pi \end{cases} \tag{6.34}$$

$$V_{D_2}(\omega t) = \begin{cases} V_o, & \text{for } 0 \leqslant \omega t < \pi \\ 0, & \text{for } \pi \leqslant \omega t < 2\pi \end{cases}. \tag{6.35}$$

Hence the output current is equal to the average current of diode D_1

$$I_o = \frac{1}{2\pi}\int_0^{2\pi} I_{D_1}(\omega t)d\omega t = \frac{1}{2\pi}\int_0^{\pi} i_m \sin \omega t = \frac{i_m}{\pi}. \tag{6.36}$$

Consequently, the output voltage is given by

$$V_o = I_o R_L = \frac{i_m R_L}{\pi}. \tag{6.37}$$

The RMS value of the input current is given by

$$I_{iRMS} = \frac{i_m}{\sqrt{2}}. \tag{6.38}$$

Therefore the AC-to-DC current gain can be represented as

$$M_c = \frac{I_o}{I_{iRMS}} = \frac{\sqrt{2}I_o}{i_m} = \frac{\sqrt{2}}{\pi}. \tag{6.39}$$

Similar to their voltage-driven counterparts, it can be noticed from Eqs. 6.36 and 6.39 that for the Class D voltage-driven rectifiers the output current is independent of the load value. The input voltage (V_i) to the rectifier is equal to the voltage of diode D_2

$$V_i(\omega t) = V_{D_2}(\omega t) = \begin{cases} V_o, & \text{for } 0 \leqslant \omega t < \pi \\ 0, & \text{for } \pi \leqslant \omega t < 2\pi \end{cases}. \tag{6.40}$$

The RMS value of the input voltage is

$$V_{iRMS} = \sqrt{\frac{1}{2\pi}\int_0^{2\pi} V_i^2(\omega t)d\omega t} = \sqrt{\frac{1}{2\pi}\int_0^{\pi} V_o^2 d\omega t} = \frac{V_o}{\sqrt{2}}. \tag{6.41}$$

The fundamental component of the input current is

$$v_{m1} = \frac{1}{\pi}\int_0^{2\pi} V_i(\omega t)\sin(\omega t)d\omega t = \frac{1}{\pi}\int_0^{\pi} V_o \sin(\omega t)d\omega t = \frac{2V_o}{\pi} \tag{6.42}$$

and its RMS value is given by

$$v_{m1RMS} = \frac{v_{m1}}{\sqrt{2}} = \frac{\sqrt{2}V_o}{\pi}. \tag{6.43}$$

From Fig. 6.8b it can be assumed that the fundamental component of the input voltage is in phase with the input current. Since the input current is sinusoidal, the input power contains only the fundamental component

$$P_i = \frac{1}{2} v_{m1} i_m. \tag{6.44}$$

Considering the assumption that the diodes are ideal implies that the output power is equal to the input power, therefore input power can expressed as

$$P_i = P_o = \frac{V_o^2}{R_L} = I_o^2 R_L = \frac{i_m^2 R_L}{\pi^2} \tag{6.45}$$

Using Eqs. 6.37 and 6.42 the input resistance of the rectifier is

$$R_i = \frac{v_{m1}}{i_m} = \frac{2V_o}{\pi i_m} = \frac{2}{\pi^2} R_L \approx 0.2026 R_L. \tag{6.46}$$

From Eqs. 6.7, 6.42 and 6.43 the power factor of the half-wave Class D current-driven rectifier is

$$PF = \frac{v_{m1RMS} I_{iRMS}}{V_{iRMS} I_{iRMS}} = \frac{2}{\pi} \approx 0.6366 \tag{6.47}$$

which is the same as that of it voltage-driven counterpart. The power factor can be improved to 0.9001 by connecting the rectifier to the voltage source through a transformer and a DC blocking capacitor to remove the DC component of the input voltage as shown in [112].

Using Eqs, 6.9, 6.23 and 6.25 the THD factor of the the half-wave Class D voltage-driven rectifier is

$$THD = \sqrt{\left(\frac{I_{iRMS}}{i_{m1RMS}}\right)^2 - \left(\frac{I_o}{2i_{m1RMS}}\right)^2 - 1} = \sqrt{\left(\frac{\pi}{2}\right)^2 - \left(\frac{\pi}{2\sqrt{2}}\right)^2 - 1} \approx 0.4834. \tag{6.48}$$

The maximum voltage across the diodes is V_o and their maximum current is i_m, therefore the power-output capability is

$$cp = \frac{P_o}{2V_{DMAX} I_{DMAX}} = \frac{V_o I_o}{2V_{DMAX} I_{DMAX}} = \frac{1}{2\pi} \approx 0.1592. \tag{6.49}$$

6.3.3 *Performance Investigation of Class D Voltage-driven Rectifiers*

Here the performance of a Class D voltage-driven rectifiers in inductive links will be investigated by taking into consideration the presence of the inductive link.

Fig. 6.9 shows the circuit diagram of the half-wave Class D voltage-switching rectifier in an IPT system with a parallel resonant secondary configuration. The rectifier consist of two diodes, D_1 and D_2, a DC filter inductor L_f and output capacitor C_o.

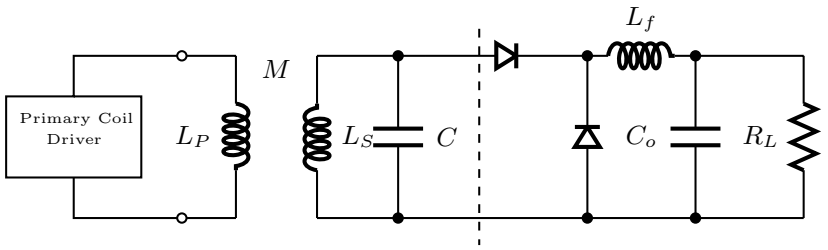

Fig. 6.9: Circuit representation of an IPT system with a Class D half-wave voltage-switching rectifier

The load is represented by a resistance R_L. The inductive link consists of a primary coil represent by an inductance L_P, the secondary coil represented by an inductance L_S and their mutual inductance M. Capacitor C is connected in parallel with the secondary coil to create resonance or near-resonance operation. The inductive link is driven by a sinusoidal DC/AC inverter such as a Class D or Class E inverter, and the rectifier is driven by the voltage induced at the secondary coil. Fig. 6.10 shows the voltage and current waveforms that are associated with the Class D rectifier in this particular application.

A. Assumptions

The modelling and analysis will be performed here will based on the following assumptions:

1. The diodes are ideal; they have zero threshold voltage, a zero ON resistance, an infinite OFF resistance and a zero junction capacitance.

2. The quality factor of the secondary coil is high enough such that its equivalent series resistance is negligible.

3. The filter inductance L_f is large enough such that the output current I_o is DC and consequently the output voltage V_o is DC.

4. The driving current of the primary coil is sinusoidal and consequently the voltage induced in the secondary coil V_i is also sinusoidal. The induced voltage is given by

$$V_i(\omega t) = v_m \sin(\omega t + \phi) \tag{6.50}$$

where v_m is the magnitude of the induced voltage and ϕ is its phase with reference to the current of diode D_1.

5. Since the induced voltage is sinusoidal, the ON duty cycle for both diodes is 0.50.

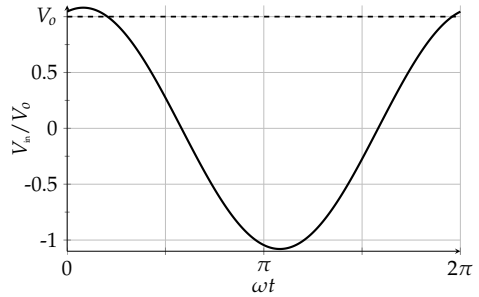

(a) V_i

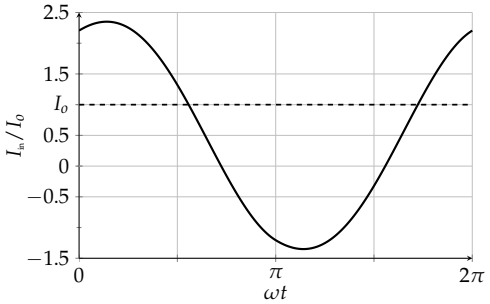

(b) I_i

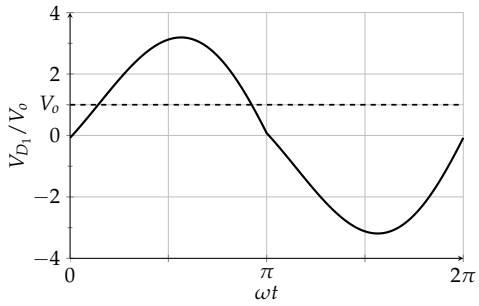

(c) V_{D_1}

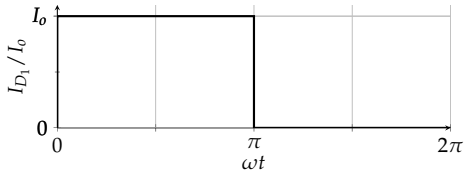

(d) I_{D_1}

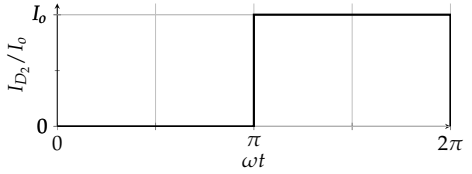

(e) I_{D_2}

Fig. 6.10: Voltage and current waveforms associated with the half-wave Class D voltage-switching rectifier in an inductive link with a parallel resonant secondary coil configuration

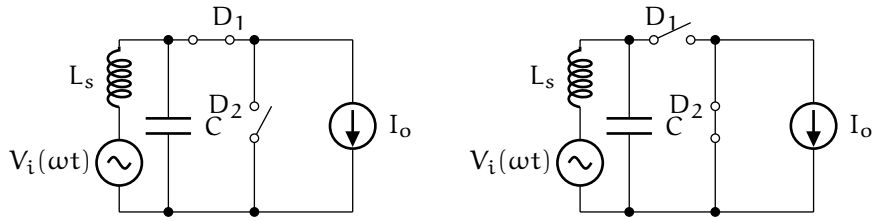

(a) equivalent during the period $0 \leqslant \omega t < \pi$ (b) equivalent during the period $\pi \leqslant \omega t < 2\pi$

Fig. 6.11: Equivalent circuits of the Class D rectifier

B. Operation outside resonance

The Class D rectifier can be represented by the equivalent circuits in Fig. 6.14 depending the on the conduction of the diodes. Diode D_1 is ON and diode D_2 is OFF for the period $0 \leqslant \omega t < \pi$. Diode D_1 is OFF and diode D_2 is ON for the period $\pi \leqslant \omega t < 2\pi$. The analysis will only consider the near-resonance operation of the rectifier, i.e. $q_{eq}1$. This is due to the fact that perfect resonant operation, i.e. $q = 1$, is practically difficult to practically achieve due to the tolerance of the components of the circuit. In addition, operating near-resonance is sometimes preferred to allow for power regulation as demonstrated in [60, 73–75].

For the period $0 \leqslant \omega t < \pi$, by applying KVL and KCL in Fig. 6.14a, the following equations can be obtained

$$v_m \sin(\omega t + \phi) = \omega L \frac{dI_i(\omega t)}{d\omega t} + V_C(\omega t) \tag{6.51}$$

$$I_i(\omega t) = \omega C \frac{dV_C(\omega t)}{d\omega t} + I_o. \tag{6.52}$$

Substituting Eq. 6.51 in Eq. 6.52 and normalising with the respect to the magnitude of the input voltage v_m and the output current I_o

$$p \cos(\omega t + \phi) = \frac{1}{q^2} \frac{d^2 I_i(\omega t)_{norm}}{d\omega t^2} + I_i(\omega t)_{norm} - 1 \tag{6.53}$$

where

$$p = \frac{v_m \omega C}{I_o}. \tag{6.54}$$

Eq. 6.53 is a linear non-homogeneous second-order differential equation which has the following general solution

$$I_i(\omega t)_{norm} = \frac{q^2 p}{q^2 - 1} \cos(\omega t + \phi) + A_1 \cos(q\omega t) + B_1 \sin(q\omega t) - 1, \qquad q \neq 1 \tag{6.55}$$

where the coefficients A_1 and B_1 are to be determined by satisfying the equation's boundary conditions.

For the period $\pi \leqslant \omega t < 2\pi$, by applying KVL and KCL in Fig. 6.14b, the following equations can be obtained

$$v_m \sin(\omega t + \phi) = \omega L \frac{dI_i(\omega t)}{d\omega t} + V_C(\omega t) \tag{6.56}$$

$$I_i(\omega t) = \omega C \frac{dV_C(\omega t)}{d\omega t}. \tag{6.57}$$

Substituting Eq. 6.56 in Eq. 6.57 and normalising with the respect to the magnitude of the input voltage v_m and the output current I_o,

$$p \cos(\omega t + \phi) = \frac{1}{q^2} \frac{d^2 I_i(\omega t)_{norm}}{d\omega t^2} + I_i(\omega t)_{norm} \tag{6.58}$$

Eq. 6.58 is a linear second-order differential equation which has the following general solution

$$I_i(\omega t)_{norm} = \frac{q^2 p}{q^2 - 1} \cos(\omega t + \phi) + A_2 \cos(q\omega t) + B_2 \sin(q\omega t), \qquad q \neq 1 \tag{6.59}$$

where the coefficients A_2 and B_2 are to be determined by satisfying the equation's boundary conditions. The current and voltage continuity conditions of inductor L and capacitor C respectively can be described by

$$I_i(\pi^-)_{norm} = I_i(\pi^+)_{norm} \tag{6.60}$$

$$I_i(0^+)_{norm} = I_i(2\pi^-)_{norm} \tag{6.61}$$

$$\left.\frac{dI_i(\omega t)_{norm}}{d\omega t}\right|_{\omega t = \pi^-} = \left.\frac{dI_i(\omega t)_{norm}}{d\omega t}\right|_{\omega t = \pi^+} \tag{6.62}$$

$$\left.\frac{dI_i(\omega t)_{norm}}{d\omega t}\right|_{\omega t = 0^+} = \left.\frac{dI_i(\omega t)_{norm}}{d\omega t}\right|_{\omega t = 2\pi^-}. \tag{6.63}$$

By using Eqs. 6.60-6.63, the coefficients A_1, A_2, B_1 and B_2 can be determined and are given by

$$A_1 = -\frac{1}{2}, \qquad q \neq 1 \tag{6.64}$$

$$A_2 = -\frac{1}{2} + \cos(\pi q), \qquad q \neq 1 \tag{6.65}$$

$$B_1 = -\frac{1}{2} \tan(\frac{\pi q}{2}), \qquad q \neq 1 \tag{6.66}$$

$$B_2 = \sin(\pi q) - \frac{1}{2} \tan(\frac{\pi q}{2}), \qquad q \neq 1. \tag{6.67}$$

Consequently, the normalised input current can be represented as

$$I_i(\omega t)_{norm} = \begin{cases} \dfrac{q^2 p}{q^2 - 1} \cos(\omega t + \phi) + A_1 \cos(q\omega t) + B_1 \sin(q\omega t) - 1, \quad q \neq 1 \\ \qquad\qquad \text{for } 0 \leqslant \omega t < \pi \\ \dfrac{q^2 p}{q^2 - 1} \cos(\omega t + \phi) + A_2 \cos(q\omega t) + B_2 \sin(q\omega t), \qquad q \neq 1 \\ \qquad\qquad \text{for } \pi \leqslant \omega t < 2\pi \end{cases}. \tag{6.68}$$

The normalised voltage across capacitor C can be represented as

$$V_C(\omega t)_{norm} = \begin{cases} \frac{q^2}{q^2-1}\sin(\omega t+\phi) + \frac{A_1}{qp}\sin(q\omega t) - \frac{B_1}{qp}\cos(q\omega t) & q \neq 1 \\ & \text{for } 0 \leqslant \omega t < \pi \\ \frac{q^2}{q^2-1}\sin(\omega t+\phi) + \frac{A_2}{qp}\sin(q\omega t) - \frac{B_2}{qp}\cos(q\omega t) & q \neq 1 \\ & \text{for } 0 \leqslant \omega t < \pi \end{cases} . \tag{6.69}$$

The voltages across diodes D_1 and D_2 are given by

$$V_{D_1}(\omega t) = \begin{cases} 0 & \text{for } 0 \leqslant \omega t < \pi \\ -V_C(\omega t) & \text{for } \pi \leqslant \omega t < 2\pi \end{cases} \tag{6.70}$$

$$V_{D_2}(\omega t) = \begin{cases} V_C(\omega t) & \text{for } 0 \leqslant \omega t < \pi \\ 0 & \text{for } \pi \leqslant \omega t < 2\pi \end{cases} \tag{6.71}$$

and their currents are given by

$$I_{D_1}(\omega t) = \begin{cases} I_o & \text{for } 0 \leqslant \omega t < \pi \\ 0 & \text{for } \pi \leqslant \omega t < 2\pi \end{cases} \tag{6.72}$$

$$I_{D_2}(\omega t) = \begin{cases} 0 & \text{for } 0 \leqslant \omega t < \pi \\ I_o & \text{for } \pi \leqslant \omega t < 2\pi \end{cases} . \tag{6.73}$$

The phase ϕ can be determined from Eq. 6.69 when $V_C = 0$ at $\omega t = 0$, resulting in the following equation

$$\sin(\phi) + \frac{1}{q^2-1}\sin(\phi) - \frac{B_1}{qp} = 0 \tag{6.74}$$

therefore the phase ϕ is equal to

$$\phi = \begin{cases} \sin^{-1}\left(\frac{B_1(q^2-1)}{q^3 p}\right) & \text{for } q > 1 \\ \pi - \sin^{-1}\left(\frac{B_1(q^2-1)}{q^3 p}\right) & \text{for } q < 1 \end{cases} . \tag{6.75}$$

The output current is equal to the average of the input current during the period 0 to π

$$I_o = \frac{1}{\pi}\int_0^{\pi} I_i(\omega t)\, d\omega t. \tag{6.76}$$

Substituting Eqs. 6.55, 6.64 & 6.66 in Eq. 6.76 gives

$$1 = \frac{1}{\pi}\left(\pi - \frac{2q^2 p}{q^2-1}\sin(\phi) - \frac{1}{q}\tan\left(\frac{\pi q}{2}\right)\right) \tag{6.77}$$

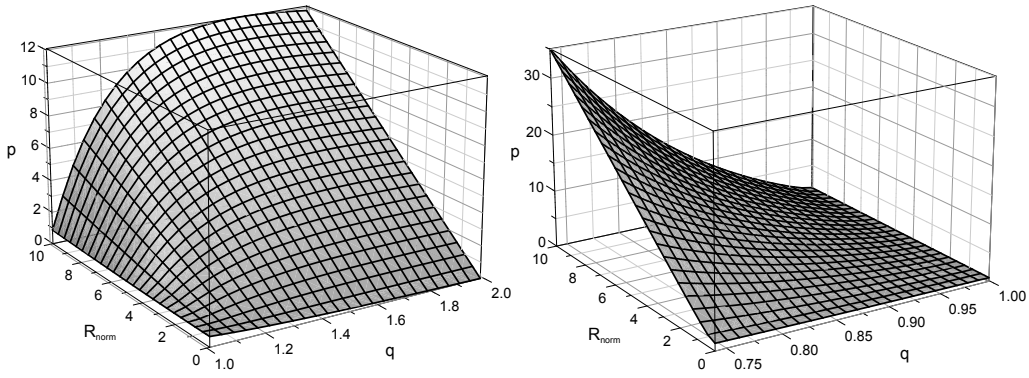

(a) for $1 < q \leqslant 2$ (b) for $0.75 \leqslant q < 1$

Fig. 6.12: Variation of p with q and R_{norm}

which simplifies to

$$\frac{2q^2p}{q^2-1}\sin(\phi)+\frac{1}{q}\tan\left(\frac{\pi q}{2}\right)=0. \tag{6.78}$$

The output voltage is equal to the average voltage across diode D_2

$$V_o = I_o R_L = \frac{1}{2\pi}\int_0^{\pi} V_C(\omega t)\,d\omega t. \tag{6.79}$$

Using Eqs. 6.54 & 6.69, the above equations can be represented by

$$\frac{q^2p}{\pi(q^2-1)}\cos(\phi)=\omega R_L C. \tag{6.80}$$

Eq. 6.80 can also be represented as

$$R_{Lnorm}=\frac{q^3p}{\pi(q^2-1)}\cos(\phi). \tag{6.81}$$

From Eqs. 6.78 & 6.81 the value p can also be represented as

$$p=\frac{(q^2-1)}{2q^3}\sqrt{(2\pi R_{Lnorm})^2+\tan^2\left(\frac{\pi q}{2}\right)}. \tag{6.82}$$

Eq. 6.82 along with Eq. 6.54 allow for determining the output current and voltage for a given load resistance and input voltage. Figs. 6.12 & 6.13 show how p and ϕ vary with q and R_{norm}.

Using Fourier series, the normalised magnitude of the input current harmonics are

$$|I_{inn}| = \sqrt{a_n^2+b_n^2} \tag{6.83}$$

where

$$a_n = \frac{1}{\pi}\int_0^{\pi} I_i(\omega t)\cos\left(n(\omega t+\phi)\right)d\omega t \tag{6.84}$$

$$b_n = \frac{1}{\pi}\int_0^{\pi} I_i(\omega t)\sin\left(n(\omega t+\phi)\right)d\omega t \tag{6.85}$$

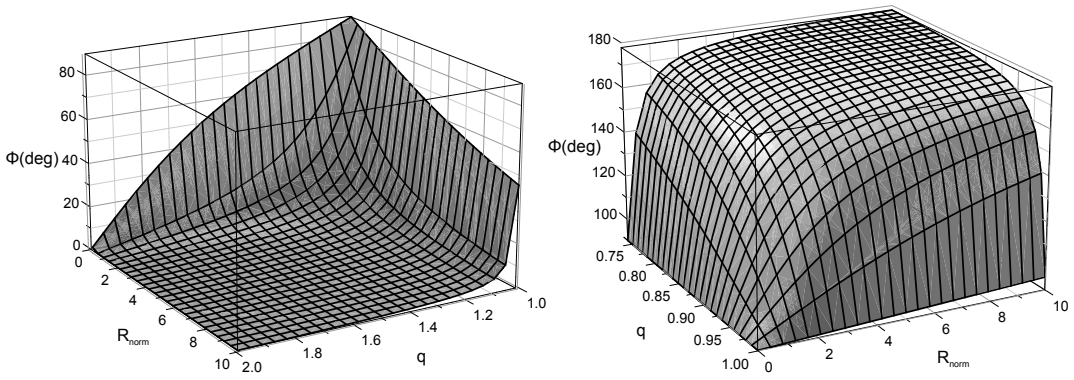

(a) for $1 < q \leqslant 2$ (b) for $0.75 \leqslant q < 1$

Fig. 6.13: Variation of ϕ with q and R_{norm}

Table 6.1: Input current harmonics for the out of resonance operation ($q \neq 1$)

n	$\lvert I_{inn}\rvert_{norm}$	$\tan(\phi_n)$
1st	$\left\lvert\frac{q^2}{\pi(q^2-1)}\sqrt{4+\pi^2p^2-4\pi p\sin\phi}\right\rvert$	$\frac{\pi}{2}p\sec\phi-\tan\phi$ (4th qdr.)
2nd	0	0
3rd	$\left\lvert\frac{2q^2}{3\pi(q^2-9)}\right\rvert$	$\tan(3\phi)$ (3rd qdr.)
4th	0	0
5th	$\left\lvert\frac{2q^2}{5\pi(q^2-25)}\right\rvert$	$\tan(5\phi)$ (4th qdr.)

and the phase of each harmonic with respect to the phase of the input voltage is

$$\phi_n = \tan^{-1}\left(\frac{a_n}{b_n}\right) \tag{6.86}$$

Table 6.1 lists the equations for the first three odd harmonics. It can be noticed that the first harmonic is dominant and the 3rd and 5th harmonics are several orders of magnitude less. Therefore it can be assumed that the input current for the Class D rectifier operating out of resonance is near sinusoidal.

C. *Equivalent circuit*

The rectifier can be represented by an equivalent input impedance consisting of a resistance representing the load and a reactance. Since the input voltage to the rectifier has been assumed to be sinusoidal, the input impedance of the rectifier corresponds to that of the first harmonic only. From Table 6.1, and Eq. 6.54, the input impedance of the rectifier is

$$Z_i = R_i + jX_i = \frac{v_m}{I_{i1}} = \frac{qpZ_o}{I_{i1_{norm}}}\angle -\phi_1. \tag{6.87}$$

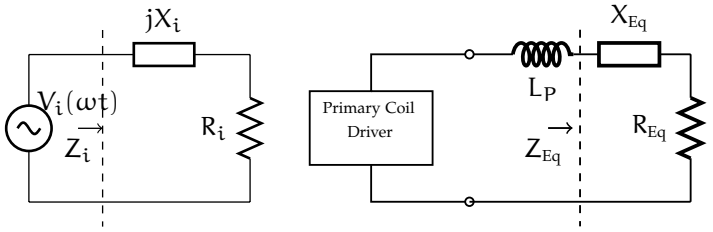

(a) input impedance (b) equivalent circuit of the inducitve link and the rectifier

Fig. 6.14: Equivalent circuits of the Class D rectifier

The input resistance is equal to

$$R_i = \frac{\pi p(q^2-1)Z_o}{q\sqrt{4+\pi^2p^2-4\pi p\sin(\phi)}}\frac{1}{\sqrt{1+\left(\frac{\pi}{2}p\sec(\phi)+\tan(\phi)\right)^2}} \tag{6.88}$$

and the input reactance is equal to

$$X_i = \frac{\pi p(q^2-1)Z_o}{q\sqrt{4+\pi^2p^2-4\pi p\sin(\phi)}} - \frac{\frac{\pi}{2}p\sec(\phi)+\tan(\phi)}{\sqrt{1+\left(\frac{\pi}{2}p\sec(\phi)+\tan(\phi)\right)^2}}. \tag{6.89}$$

The input reactance of the Class D rectifier is inductive when $q > 1$ and capacitive when $q < 1$. The input impedance of the Class D rectifier along with the inductive link can be further replaced by an equivalent impedance as seen by the primary coil driver. Since $V_i = jX_M I_P$, where X_M is the reactance of the mutual inductance and I_P is the output current of the primary coil driver, the equivalent impedance of the inductive link and the Class D rectifier can be described by

$$Z_{eq} = R_{eq} + jX_{eq} = \frac{X_M^2}{R_i + jX_i} \tag{6.90}$$

where R_{eq} is equivalent resistance corresponding to the load resistance and is given by

$$R_{eq} = \frac{X_M^2 R_i}{R_i^2 + X_i^2} \tag{6.91}$$

and X_{eq} is equivalent reactance corresponding to the mutual inductance and input reactance of the rectifier and is given by

$$X_{eq} = \frac{X_M^2 X_i}{R_i^2 + X_i^2}. \tag{6.92}$$

Fig. 6.14 shows the equivalent circuits of the Class D rectifier and the inductive link. Fig. 6.15 shows the variation of the input resistance of the rectifier R_i with q and R_{norm}.

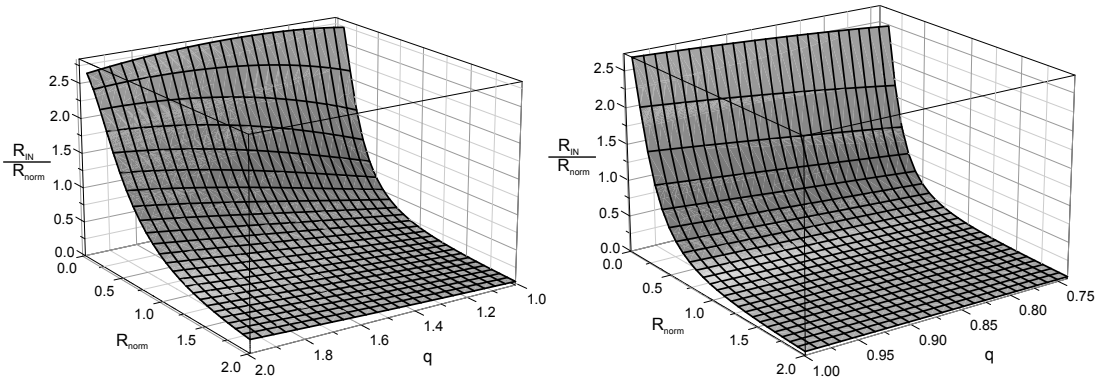

(a) for $1 < q \leqslant 2$ (b) for $0.75 \leqslant q < 1$

Fig. 6.15: Variation of R_i with q and R_{norm}

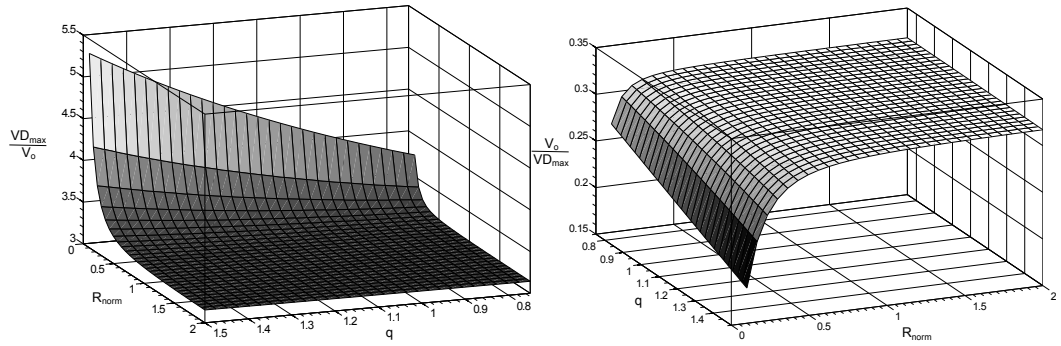

(a) $V_{D\,max}$ (b) output voltage gain

Fig. 6.16: Variation of $V_{D\,max}$ and output voltage gain with q and R_{norm}

D. Output voltage, voltage and current stresses

The maximum current in the diodes is equal to I_o. The maximum voltage across diodes is equal to the maximum voltage across capacitor C. By differentiating Eq. 6.69 and setting it equal to zero, the following equation is obtained

$$\frac{q^2}{q^2-1}\cos(\omega t+\phi)-\frac{1}{2p}\cos(q\omega t)-\frac{1}{2p}\sin(q\omega t)\tan\left(\frac{\pi q}{2}\right)=0. \tag{6.93}$$

Eq. 6.93 can be solved numerically for given values of p and R_{norm}. Fig. 6.16a shows the variation of the maximum voltage across the diodes normalised with respect to the output voltage as q and R_{norm} vary. The induced voltage at the secondary coil V_i cannot be physically measured, the voltage across capacitor C is measured instead. Therefore the gain the rectifier can be represented as the ratio of the output voltage across the load to the voltage across capacitor C. Fig. 6.16b shows the variation of the output voltage with q and R_{norm}.

The analysis was based on the assumption that the diodes and the secondary coil are lossless. In practice, the losses due to conduction of the diodes and ESR of the secondary coil. Therefore the efficiency of the rectifier can be described by

$$\eta \approx \frac{I_o^2 R_L}{I_{in1}^2 r_s + I_o V_f + I_o^2 r_{ON} + I_o^2 r_f + I_o^2 R_L}. \tag{6.94}$$

where r_p represented the ESR of the secondary coil, V_f is the forward voltage drop of the diodes, r_{ON} represented the diodes' ON resistance and r_f represents resistance of the filter inductor.

E. Design Case

This section will describe the design procedure of an IPT system with a Class E DC/AC inverter and a Class D rectifier. The IPT system will operate from a 15 V DC supply and will deliver up to 20 W of power to a load range 10-100 Ω at an 800 kHz switching frequency. Class E inverters operate at optimum switching condition, zero-voltage and zero-derivative switching, only for a certain load value. Therefore the Class E inverter will provide an excellent indication on the accuracy of modelling and analysis performed on the Class D rectifier by monitoring its switching conditions. Class E inverters can also operate at sub-optimum switching conditions, zero-voltage switching, as their load is decreased below its optimum value. Consequently the Class E inverter will be designed to operate at optimum switching conditions for $R_{norm} = Z_o$ and at sub-optimum switching condition for $\frac{1}{2}Z_o < R_{norm} < 3Z_o$.

The inductive coils that will be used here are those designed in Sec. 3.4.3. The distance between the coils will be 5 cm and the measure mutual inductance at this separation distance is 1 µH. The inductive link will be operated near resonance, its resonant frequency will be set at 850 kHz which corresponds to $q = 1.0625$. The value of the parallel capacitor C is therefore equal to 5.4 nF. Three polypropylene capacitors (2.2 nF+2.2 nF+1 nF) will be connected in parallel to minimise losses and current stresses. The characteristic impedance of the rectifier is equal to 34.67 Ω.

Based on the performed analysis of the Class D rectifier, for $q = 1.0625$ and $R_{norm} = Z_o = 34.67\,\Omega$, the values of p and ϕ can be found from Eqs. 6.75 & 6.82 are equal to 0.6419 and 58.16° respectively. From Eqs. 6.88-6.89, the input resistance of the rectifier is 7.396 Ω and its input reactance is -j2.225 Ω which corresponds to a capacitance of 89.413 nF at 800 kHz. From Fig. 6.16, the voltage gain of the rectifier is 31.644 % and the normalised maximum voltages across the diodes is 3.160.

The equivalent impedance of the inductive and the Class D rectifier can now be determined as a function of the mutual inductance of the inductive link. The value of the equivalent impedance for the set separation distance can be found from Eqs. 6.91-6.92.

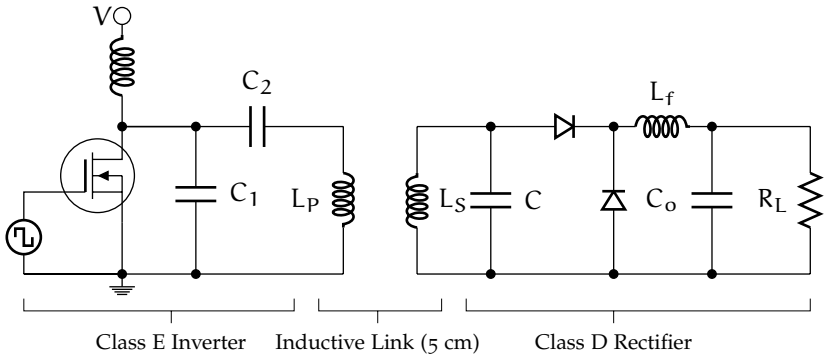

(a) complete circuit

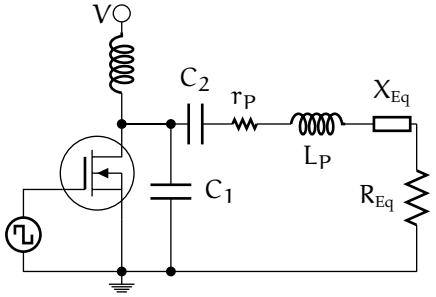

(b) simplified circuit

Fig. 6.17: Complete circuit of an IPT system with a Class E primary driver and a half-wave Class D rectifier

The equivalent resistance is equal to 3.133 Ω and the equivalent reactance is equal to -j0.942 Ω which corresponds to a capacitance of 211.193 nF. The equivalent impedance is then used to design the Class E inverter at optimum switching conditions. Fig. 6.17a shows the complete circuit diagram of the overall IPT system and Fig. 6.17b shows a simplified circuit of the system obtained by replacing the inductive link and the Class D rectifier with their equivalent circuit. The values that need to be determined to complete this design case are capacitors C_1 and C_2 of the Class E inverter. Their values can be found by using the design equations in [73, 89]. The values of C_1 and C_2 are found to be equal to 12.322 nF and 7.661 nF respectively. An IPT system was built based on the design case presented in the previous section. Fig. 6.18 shows a photograph on the experimental setup. Fig. 5.26 shows the measured voltage and current waveforms of the Class D rectifier and the Class E inverter. The theoretical waveforms are plotted for comparison. It can be seen from Fig. 6.19a & 6.19b that measured waveforms of the Class D rectifier are in excellent agreement with theoretical waveforms which confirms the accuracy of the modelling and analysis that was performed. Fig. 6.19c shows the voltage across the MOSFET of the Class E inverter. The particular voltage waveform of the Class E inverter is associated with the optimum switching operation. Therefore this provides further confirmation on the performed modelling and analysis.

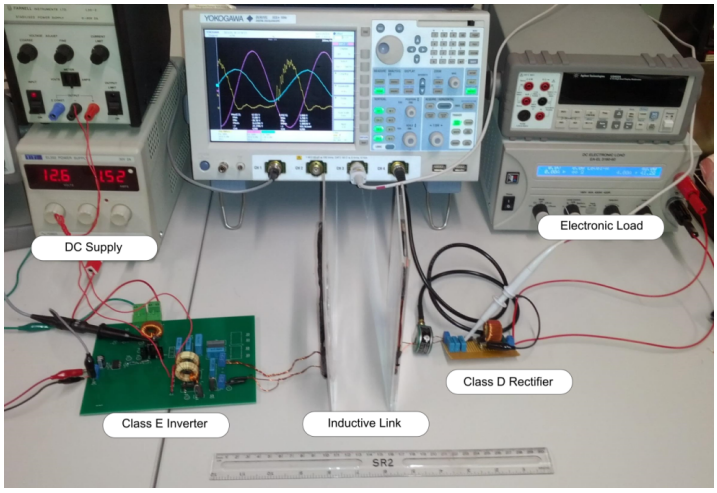

Fig. 6.18: Photograph of the experimental setup

Fig. 6.20 shows the measured variation of the voltage gain of the rectifier and normalised first harmonic of its input current. As predicted in Fig. 6.15, the voltage gain of the rectifier reaches to a constant value of ≈ 0.1 as the load resistance increases. The measured variation of the first harmonic of the input current is in excellent agreement with the theoretical values in Table 6.1.

6.4 CLASS E RECTIFIERS

Class E rectifiers are resonant switching circuits that can operate efficiently at frequencies exceeding 500 kHz. Efficient operation is achieved due to the zero-voltage switching (ZVS), low voltage-slope (dv/dt) switching, zero-current switching (ZCS) and low current-slope (di/dt) switching of the rectifying element. Class E rectifiers have a near sinusoidal input current with low harmonic distortion which makes them compatible with resonant inverters, such as Class D and Class E, that are used as primary coil drivers in IPT systems. Class E rectifiers have been used to form resonant DC-DC converters [114–118] and in power harvesting and power recovery applications [119]. Nonetheless, there appears no report in literature on the use of Class E rectifiers for IPT systems.

This section will provide a brief introduction about Class E rectifiers and their principle of operation. The suitability of Class E resonant rectifiers in inductive links is discussed. An analysis is performed on a Class E voltage-switching rectifier will be performed. The analysis will be based on a piecewise linear state-space representation to model the Class E rectifier including the rectifying diode's forward voltage drop, its ON resistance and the equivalent series resistance of the resonant inductor. Power quality parameters, such as power factor and total harmonic distortion, are calculated

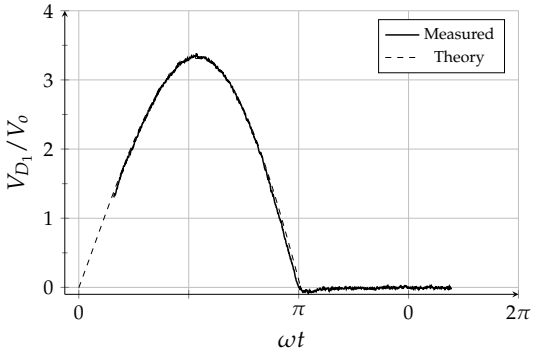

(a) normalised voltage across diode D_1

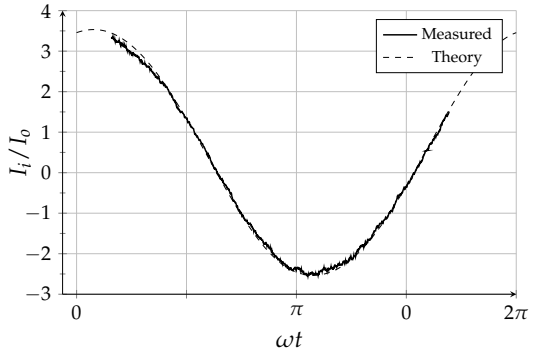

(b) normalised current in the secondary coil

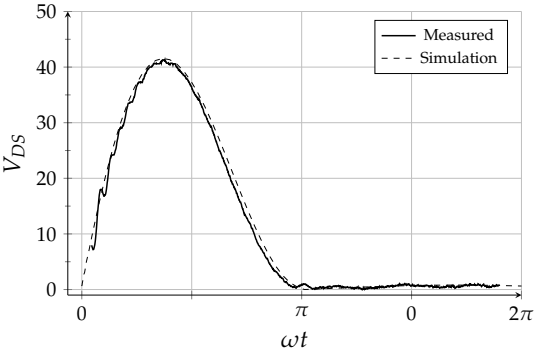

(c) voltage across the MOSFET of the Class E inverter

Fig. 6.19: Measured voltage and current waveforms when $R_{norm} = Z_o$

for different loading conditions. Extensive experimental results based on a 10 W prototype are presented confirming the performed analysis and show the efficient operation of the rectifier. An operating efficiency of 94.43 % has been achieved at a resonant frequency of 800 kHz.

Class E rectifiers were first introduced by Bowman [120] in a patent filled in 1986 to be used in resonant DC/DC converters. Similar to Class D rectifiers, Class E rectifiers can be thought of as the dual of Class E inverters. Class E rectifiers consist of a single rectifying switch for the half-wave rectification configuration and two rectifying switches for the full-wave rectification configuration. Class E rectifiers also contain

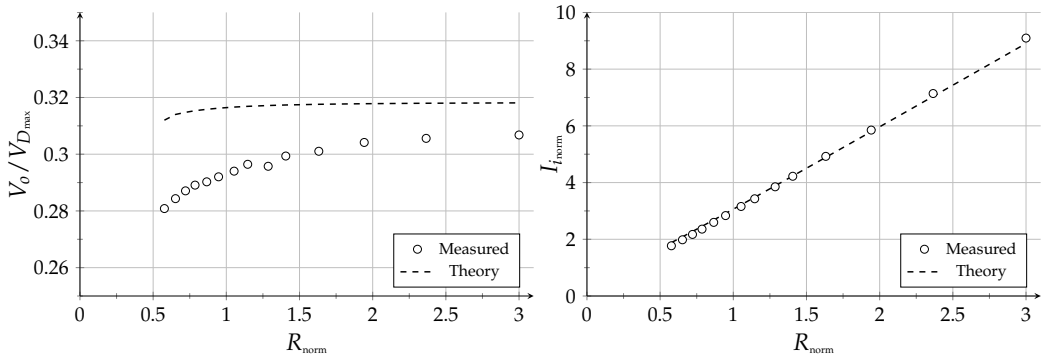

(a) voltage gain (b) magnitude of first harmonic

Fig. 6.20: Measured parameters against normalised load

a passive network that is tuned to the frequency of the input voltage or current signal. The passive network takes into consideration the non-ideal characteristics of the switch, such as output capacitance and parasitic inductance, thus reducing their affect which is the main reason why Class E rectifiers can be operate at frequencies higher than that of Class D and the traditional rectifiers. Similar to Class E inverters, the main disadvantage of Class E rectifiers is the increased voltage stresses across the rectifying switch which is also affected by the load value. However, they can maintain efficient operation over a wider load range. The principle of operation of Class E rectifiers and the different configurations that have been researched are summarised in [109, 121] and the references therein, however a brief overview will be provided in the next subsection.

Figs. 6.21 and 6.22 show a common configuration of half-wave Class E ZVS low dv_d/dt and Class E ZCS low di_d/dt rectifiers respectively. Other configurations and topologies can be obtained as summarised in [109, 121]. The figures also show two versions of each configuration based on the rectifying switch. Rectifiers generally use diodes as the rectifying switch since they do not require any control or gate triggering circuitry therefore simplifying the overall circuit design and implementation. A MOSFET as the rectifying switch can be used instead which result in an improved overall efficiency and performance, however they require control and gate driving circuitry which may increase the complexity of the overall circuit especially at high frequencies.

6.4.1 *Principle of Operation*

Fig. 6.23 shows the typical voltage and current waveforms associated with the half-wave Class E voltage-switching and current-switching rectifiers of Figs. 6.21a and 6.22a.

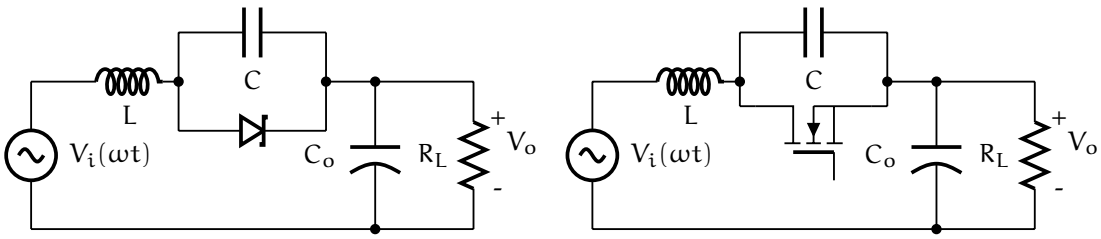

(a) uncontrolled configuration with a diode as the rectifying switch

(b) controlled configuration with a MOSFET as the rectifying switch

Fig. 6.21: Circuit diagram of a half-wave Class E ZVS low dv_d/dt rectifier [109, 122]

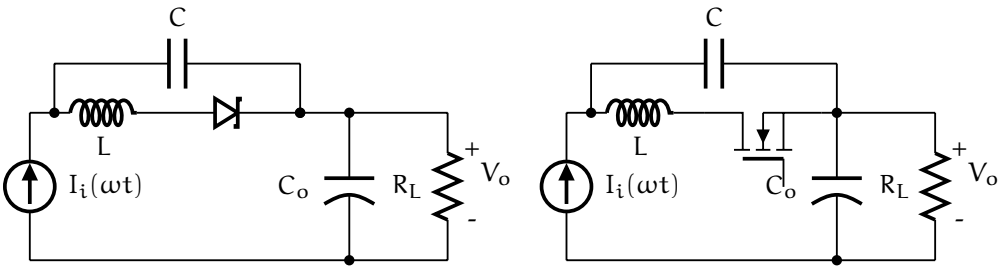

(a) uncontrolled configuration with a diode as the rectifying switch

(b) controlled configuration with a MOSFET as the rectifying switch

Fig. 6.22: Circuit diagram of a half-wave Class E ZCS low di_d/dt rectifier [109]

Both rectifier are driven by a sinusoidal voltage source. Inductor L and capacitor C form the passive network of the rectifiers. Their values are chosen such that their resonant frequency is equal to frequency of the input voltage. Capacitor C_o is a output filter and its value should be large enough such that the output voltage is a DC voltage. Resistance R_L represents the load. The duty cycle of the rectifying switch is assumed to be at 0.50 for the purpose of illustration. The duty cycle is a function of the load resistance as will be shown in the following sections.

Referring to the waveforms in Fig. 6.23a for the Class E voltage-switching rectifier, during the period when the rectifying switch is OFF, the inductor and capacitor form a series resonant LC circuit. The output-filter capacitor can be represented as a short since it has an insignificant impedance. The LC circuit is driven by the input sinusoidal voltage in addition to the output DC voltage. Therefore the voltage across capacitor C, which is equal to the voltage of the rectifying switch, will contain a sinusoidal part plus a ramp. The input current during this period is slightly distorted and contains a sinusoidal part and a ramp current. The output-filter capacitor also discharges its energy into the load during this period. The rectifying switch turns ON when its voltage crosses zero volts. The input current is diverted from capacitor C to the rectifying switch. The input current at this instant is continuous due to inductor L. The circuit now consists of only the inductor which is driven by the input sinusoidal voltage and the output DC voltage. The input current contains a sinusoidal part and ramp current

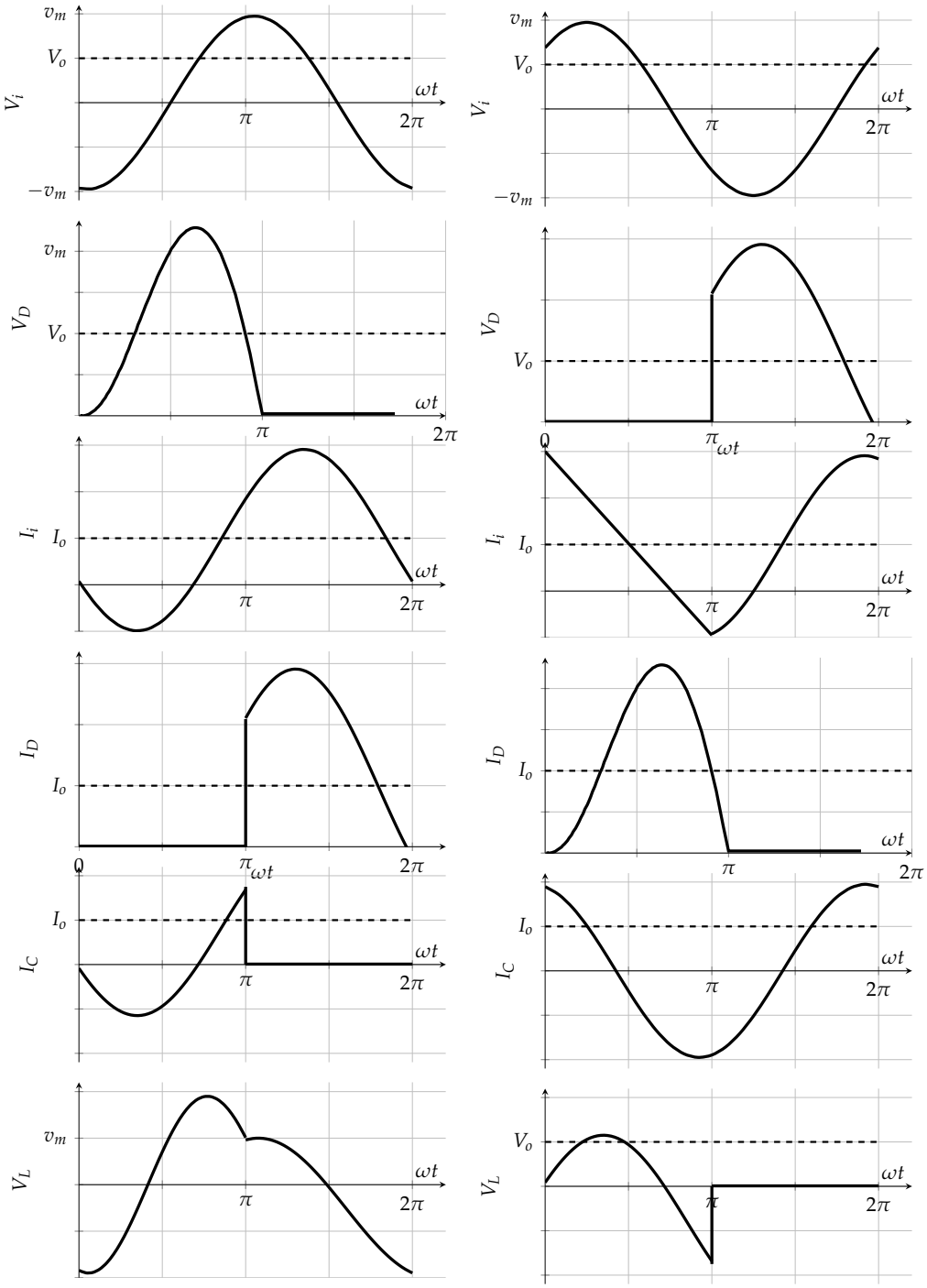

(a) voltage-switching (b) current-switching

Fig. 6.23: Typical voltage and current waveforms associated with half-wave Class E voltage-switching and current-switching rectifiers

and the output-filter capacitor charges during this period. The rectifying switch turns OFF once its current reaches zero amps and its voltage gradually increases from zero volts. In conclusion, the rectifying switch turns ON at a zero voltage and low dV_D/dt and turns OFF at a zero voltage and zero dV_D/dt therefore switching losses are minimised [109]. The main advantage of the Class E voltage-switching rectifier is that the

output capacitance of the rectifying switch is absorbed by capacitor C and hence its degradation affect on the rectifier's performance is significantly reduced. The overall distortion in input current is very low and can be assumed to be sinusoidal.

Referring to the waveforms in Fig. 6.23b for the Class E current-switching rectifier, during the period when the rectifying switch is ON, the inductor and capacitor form a parallel resonant LC circuit. The LC circuit is driven by the input sinusoidal voltage in addition to the output DC voltage. The average voltage across capacitor C is equal to the average output voltage therefore its current contains only a sinusoidal part. The current in the inductor contains a sinusoidal part and a ramp current. The sinusoidal current parts in the LC circuit will be much lower compared to the ramp current since the impedance of the parallel LC circuit is large. The output-filter capacitor charges during this period. The rectifying switch turns OFF once the current in the inductor reaches zero. The circuit now consists of only capacitor C which is driven by the input sinusoidal voltage and the output-filter capacitor discharges its energy into the load. The voltage across the rectifying switch is equal to the voltage across capacitor C therefore it turns ON again once the voltage across it crosses zero volts. The current in the rectifying switch increases from zero amps once it turns ON due to inductor L. In conclusion, the rectifying switch turns ON at a zero current and zero dI_D/dt and turns off at a zero current and low dI_D/dt. The main drawback of the Class E current-switching rectifier is that the output capacitance of the rectifying switch is not considered therefore it can degrade the performance of the rectifier especially at high frequencies. In addition, the input current has a highly distortion factor compared to that of the Class E voltage-switching rectifier.

6.4.2 *Modelling and Analysis of a Class E ZVS, Low* dv/dt *Rectifier*

The circuit of the Class E ZVS low dV_D/dt rectifier in Fig. 6.21a with diode as the rectifying element will be analysed. The equivalent circuits are shown in Figs. 6.24a and b for the ON and OFF periods respectively. The piecewise linear model of a diode is used which consists of a voltage source V_f, representing the forward voltage drop, resistance r_{ON}, representing the diode's ON and resistance r_L represents the ESR of the resonant inductor. The equivalent circuits are a piecewise linear multiple input multiple output time invariant system which can be represented by the following state-space representation for each ON and OFF intervals

$$\dot{\mathbf{x}}(\omega t) = A\mathbf{x}(\omega t) + B\mathbf{u}(\omega t) \tag{6.95}$$

$$\mathbf{y}(\omega t) = C\mathbf{x}(\omega t) + D\mathbf{u}(\omega t) \tag{6.96}$$

where $\mathbf{x} = [x_1, x_2, x_3]^T$ is the state vector. The states x_1, x_2, x_3 represent the current through inductor L, the voltage across capacitor C and the voltage across capacitor

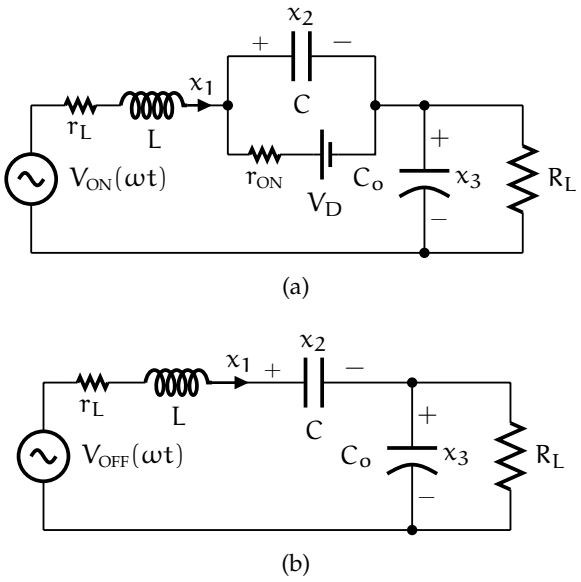

Fig. 6.24: Equivalent circuits (a) ON period (b) OFF period.

C_o for both ON and OFF intervals respectively. The input vector $\mathbf{u} = [u_1, u_2]^T$ where u_1 and u_2 represent the input sinusoidal voltage and the forward voltage drop of the diode respectively. The ON interval's domain is defined as $0 \leqslant \omega t \leqslant 2\pi D$ and the OFF interval's domain is defined as $0 \leqslant \omega t \leqslant 2\pi(1-D)$ where D is the ON duty cycle of the diode. Using KVL and KCL, the matrices A, B, C and D and the input vector, denoted by the subscripts ON and OFF for both intervals are given as

$$A_{ON} = \begin{bmatrix} \frac{-r_L}{\omega L} & \frac{-1}{\omega C} & \frac{-1}{\omega L} \\ \frac{1}{\omega C} & 0 & 0 \\ \frac{1}{\omega C_o} & 0 & \frac{-1}{\omega R_L C_o} \end{bmatrix} \tag{6.97}$$

$$A_{OFF} = \begin{bmatrix} \frac{-r_L}{\omega L} & \frac{-1}{\omega C} & \frac{-1}{\omega L} \\ \frac{1}{\omega C} & \frac{-1}{\omega r_{ON} C} & 0 \\ \frac{1}{\omega} & 0 & \frac{-1}{\omega R_L C_o} \end{bmatrix} \tag{6.98}$$

$$B_{ON} = \begin{bmatrix} B_{1ON} & B_{2ON} \end{bmatrix} = \begin{bmatrix} \frac{1}{\omega L} & 0 \\ 0 & \frac{1}{\omega r_{ON} C} \\ 0 & 0 \end{bmatrix} \tag{6.99}$$

$$B_{OFF} = \begin{bmatrix} B_{1OFF} & B_{2OFF} \end{bmatrix} = \begin{bmatrix} \frac{1}{\omega L} & 0 \\ 0 & 0 \\ 0 & 0 \end{bmatrix} \tag{6.100}$$

$$C_{ON} = C_{OFF} = C = \begin{bmatrix} 1 & 0 & 0 \\ 0 & 1 & 0 \\ 0 & 0 & 1 \end{bmatrix} \tag{6.101}$$

$$Đ_{ON} = Đ_{OFF} = Đ = \begin{bmatrix} 0 & 0 \\ 0 & 0 \\ 0 & 0 \end{bmatrix} \tag{6.102}$$

$$\mathbf{u}_{ON}(\omega t) = \begin{bmatrix} u_{1ON}(\omega t) \\ u_{2ON}(\omega t) \end{bmatrix} = \begin{bmatrix} v_m \sin(\omega t + \phi_{ON}) \\ V_f \end{bmatrix} \tag{6.103}$$

$$\mathbf{u}_{OFF}(\omega t) = \begin{bmatrix} u_{1OFF}(\omega t) \\ u_{2OFF}(\omega t) \end{bmatrix} = \begin{bmatrix} v_m \sin(\omega t + \phi_{OFF}) \\ 0 \end{bmatrix} \tag{6.104}$$

where

$$\phi_{ON} = \phi_o + 2\pi(1 - D) \tag{6.105}$$

$$\phi_{OFF} = \phi_o. \tag{6.106}$$

The solution to Eq. 6.95 for both ON and OFF states is

$$\mathbf{x}(\omega t) = \mathbf{x_n}(\omega t) + \mathbf{x_f}(\omega t). \tag{6.107}$$

Function $\mathbf{x_n}$ is the natural response, or the zero-input response, and is equal to

$$\mathbf{x_n}(\omega t) = e^{A\omega t}\mathbf{x}(0) \tag{6.108}$$

where $\mathbf{x}(0)$ is the initial condition of the states, e is the matrix exponential function. Function $\mathbf{x_f}$ is the forced response, or the zero-state response, and is equal to

$$\begin{aligned} \mathbf{x_f}(\omega t) &= \int_0^{\tau} e^{A(\omega t - \tau)} B\mathbf{u}(\tau) d\tau = \int_0^{\omega t} e^{A(\omega t - \tau)} \begin{bmatrix} B_1 & B_2 \end{bmatrix} \begin{bmatrix} u_1(\tau) \\ u_2(\tau) \end{bmatrix} d\tau \\ &= \int_0^{\omega t} e^{A(\omega t - \tau)} \big(B_1 u_1(\tau) + B_2 u_2(\tau)\big) d\tau \\ &= \big(A^2 + \mathbf{I}\big)^{-1} \Big(e^{A(\omega t} \big(\mathbf{I}\cos(\phi) + A\sin(\phi)\big) \\ &\quad -\mathbf{I}\cos(\omega t + \phi) - A\sin(\omega t + \phi) \Big) B_1 + A^{-1}\big(e^{A\omega t} - \mathbf{I}\big) B_2 \end{aligned} \tag{6.109}$$

where τ is a dummy variable and $\mathbf{I}$ is a 3×3 identity matrix.

The initial conditions of the states can be determined by applying the continuity conditions of the current through L and the voltages across C and C_o when circuit

transitions from the ON state to the OFF state, hence the following equations are obtained

$$\mathbf{x}_{ON}(0) = \mathbf{x}_{OFF}(2\pi(1-D)) \tag{6.110}$$

$$\mathbf{x}_{OFF}(0) = \mathbf{x}_{ON}(2\pi D). \tag{6.111}$$

It is noted that the general solution equation (Eq. 6.107) represents a periodic system. By substituting Eqs. 6.108-6.109 in 6.107, the initial conditions for all periods of the switching signal are equal to

$$\begin{bmatrix} \mathbf{x}_{ON}(2\pi m) \\ \mathbf{x}_{OFF}(2\pi m) \end{bmatrix} = \begin{bmatrix} -e^{A_{ON}2\pi D} & \mathbf{I} \\ \mathbf{I} & -e^{A_{OFF}2\pi(1-D)} \end{bmatrix}^{-1} \begin{bmatrix} \mathbf{x}_{fON}(2\pi D) \\ \mathbf{x}_{fOFF}(2\pi(1-D)) \end{bmatrix} \quad \text{for } m = 0, 1, 2, \ldots \tag{6.112}$$

The values of D and ϕ can be numerically solved for by finding the instants at which the voltage across the diode is equal to zero in both ON and OFF intervals, i.e,

$$x_{2ON}(2\pi m) - V_f = 0 \quad \text{for } m = 0, 1, 2, \ldots \tag{6.113}$$

$$x_{2OFF}(2\pi m) - V_f = 0 \quad \text{for } m = 0, 1, 2, \ldots. \tag{6.114}$$

Fig. 6.25 shows the solved values of D, ϕ and the normalised output DC voltage V_{Onorm} with respect to the peak input voltage for an ideal Class E inverter with $V_f = 0$, $r_{ON} = 0$ and $r_L = 0$. The Matlab code for obtaining these values is included in Appendix A.3.1. The ON duty cycle of diode is high for lower normalised loads and declines as the normalised load increases. The duty cycle at a normalised load of unity is 0.403, it increases by approximately 50 % as the normalised load is reduced to 0.1 and decreases by more than 50 % as the normalised load increases to 10. The normalised output voltage increases as the load increases at lower duty cycles, and decreases as the load is reduced at lower duty cycles. The output voltage is approximately a linear function of the load. The results in Fig. 6.25 agree with the results obtained using the analytical approach in [122], therefore the validity and accuracy of the state-space modelling approach is confirmed. The plots in Fig. 6.25 can be represented by the following best fit functions that have an a maximum error of 5%.

$$D(R_{norm}) \approx 7.440(1.0535R_{norm}^{-0.01295} - 1) \tag{6.115}$$

$$\phi(R_{norm}) \approx -3.256(1.4816R_{norm}^{0.0726} - 1) \tag{6.116}$$

$$\phi(D) \approx 3.535(1.0499D^{0.07262} + 1) \tag{6.117}$$

$$V_{Onorm}(R_{norm}) \approx 0.04726(11.6938R_{norm}^{0.9681} + 1) \tag{6.118}$$

$$V_{Onorm} \approx 0.515(0.3487D^{-1.965} - 1). \tag{6.119}$$

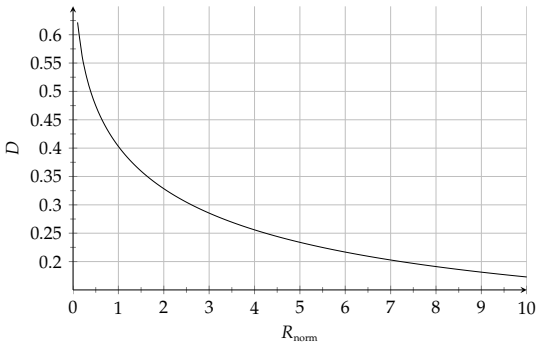

(a) Duty cycle against normalised load

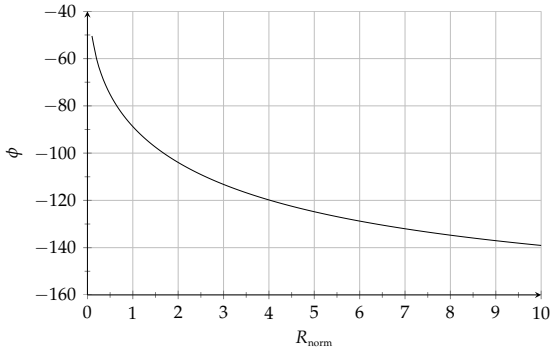

(b) Phase angle against normalised load

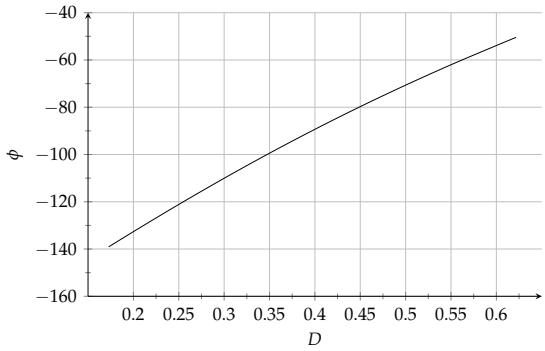

(c) Phase angle against duty cycle

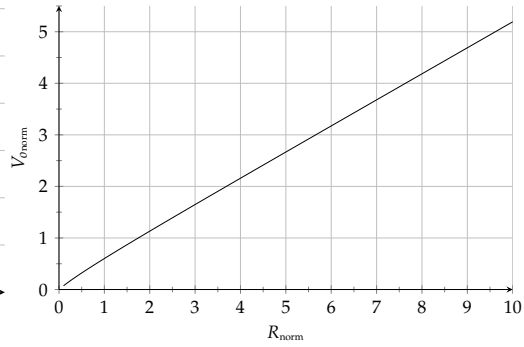

(d) Normalised output voltage against normalised load

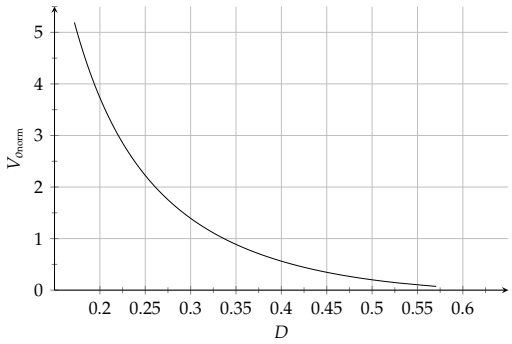

(e) Normalised output voltage against duty cycle

Fig. 6.25: Numerically calculated values.

Fig. 6.26 shows the maximum voltage and current stresses of the rectifying element. Figs. 6.26a and 6.26b show the maximum voltage developed across the rectifying switch normalised with respect to the output voltage as a function of the duty cycle and load respectively. The maximum voltage increases at lower load resistances and higher duty cycle ratios. A higher duty cycle means that the rectifying switch is ON for longer periods which causes a larger amount of energy to be stored in inductor L. As the rectifying switch turns OFF, the inductor releases its energy to the uncharged capacitor C at a high current rate. Hence, the value of $L dI_L/dt$ is large and therefore the voltage across rectifying switch is larger.

Figs. 6.26c and 6.26d show the maximum current of the rectifying switch normalised with respect to the output load current as a function of the duty cycle and load respectively. The maximum current increases at higher load resistances and lower duty cycle rations. A lower duty cycle means that the rectifying switch is OFF for longer periods which leads to a higher charge to build up in capacitor C. Once the rectifying switch turns ON, capacitor C will discharge its energy into the rectifying switch at large value of CdV_D/dt and therefore the maximum current is higher. Fig. 6.26c shows that the maximum current in the rectifying switch decreases at higher duty cycle ratios which is the reason of referring to this configuration of the Class E rectifier as 'low dV/dt'. Figs. 6.26e and 6.26f show the power-output capability as a function of duty cycle and load. The Class E rectifier has a maximum power-output capability at a duty cycle ration of 0.50 and a normalised load resistance value of approximately 0.3884.

6.4.3 *Input Current linearity and Harmonic Content*

It is necessary to investigate the signal quality of the input current of the Class E rectifier in order to determine its performance and suitability to be used in a resonant IPT system. The main parameters of interest are the normalised RMS value of the input current with respect to the output current, the power factor (PF) and the total harmonic distortion of the input current.

A. Input RMS current

The RMS value of the input current, which is equal to that of inductor L, the voltage across capacitor C and the diode and the voltage across the output capacitor C_o can be calculated by evaluating the RMS value of the state vector $X(\omega t)$ in Eq. 6.107 as shown below

$$\begin{bmatrix} I_{LRMS} \\ V_{CRMS} \\ V_{ORMS} \end{bmatrix} = \mathbf{x}_{RMS} = \sqrt{\frac{1}{2\pi}\left(\int_0^{2\pi D} \mathbf{x}_{ON}^{\circ 2}(\omega t)d\omega t + \int_0^{2\pi(1-D)} \mathbf{x}_{OFF}^{\circ 2}(\omega t)d\omega t\right)}. \tag{6.120}$$

Figs. 6.27a and 6.27b show the normalised input RMS current with the respect to the output load current as a function of the duty cycle and the normalised load respectively for the ideal Class E rectifier. The input RMS current is lower for low normalised loads at higher duty cycles. This is because the rectifier behaves more as an inductive load since the diode is ON for most of switching period. The input RMS current increases as the normalised load increases at lower duty cycles since the rectifier operates at resonance and therefore has a reduced input impedance.

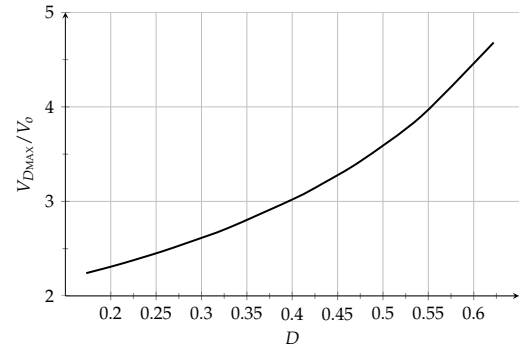

(a) Maximum normalised switch voltage against duty cycle

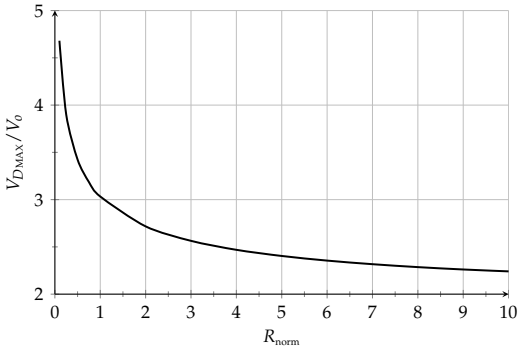

(b) Maximum normalised switch voltage against normalised load

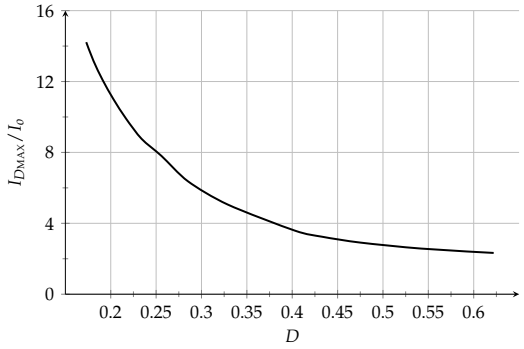

(c) Maximum normalised switch current against duty cycle

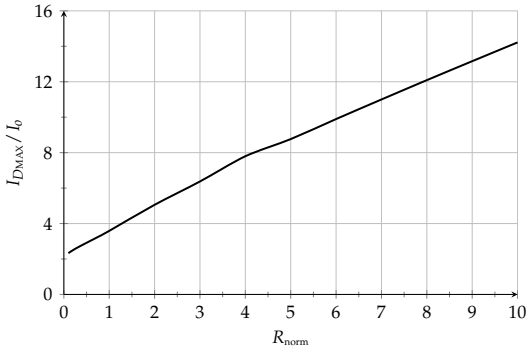

(d) Maximum normalised switch current against normalised load

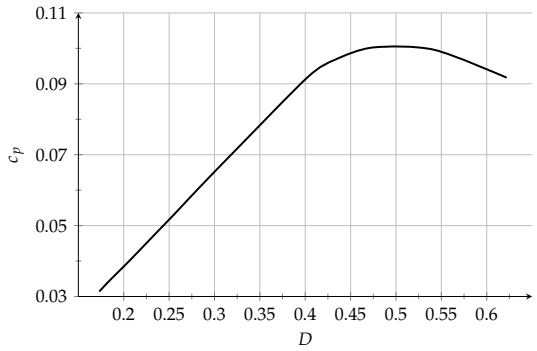

(e) c_p against duty cycle

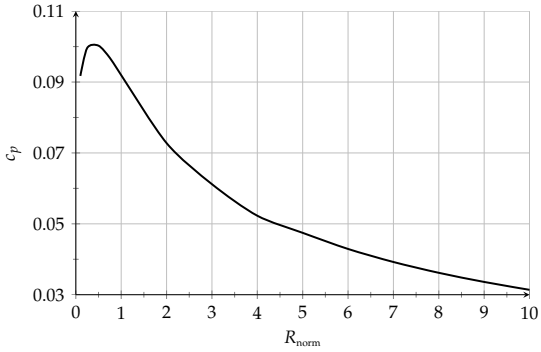

(f) c_p against normalised load

Fig. 6.26: Maximum voltage and current stresses and the corresponding power-output capability

B. Power factor

Class E rectifiers generally present an inductive load to a source, therefore this can detune an IPT system from operating at resonance. Consequently, calculating the power factor can aid in determining the type of compensation required to retune an IPT system to operate at resonance and at which part of the IPT system to include the compensation circuitry. The power factor is defined as the ratio of the real power to

the apparent power at the input of a system. For the Class E rectifier, the power factor can be expressed as

$$PF = \frac{P_i}{v_m I_{RMS}} \tag{6.121}$$

where P_i is the input real power and is equal to the sum of the power delivered to the load, the power lost in the diode's forward voltage and its ON resistance and the power lost due to the ESR of inductor L. Hence, the input real power can be expressed as

$$P_i = \frac{V_{oRMS}}{R_L}\left(V_{oRMS} + V_f + \frac{V_{oRMS}}{R_L} r_{ON}\right) + I_{LRMS}^2 r_L. \tag{6.122}$$

Note that the RMS value of the output voltage is equal to its mean or DC value.

Figs. 6.27c and 6.27d show the variation of the power factor with duty cycle and normalised load respectively for the ideal Class E rectifier. The power factor approaches unity for higher normalised loads at low duty cycles since the diode is switched OFF for most of the switching period. The rectifier operates mostly at resonance and therefore has a higher power factor. The power factor decrease to zero for lower normalised loads at higher duty cycles since the diode is switched ON for most of the switching period. The rectifier behaves more as an inductive circuit and therefore the power factor is reduced. Depending on the load, a passive compensation circuit can be included at the receiver of IPT system for a fixed load or at the transmitter for a variable load.

The Matlab code for calculating the normalised input RMS current and the power factor is included in Appendix A.3.2.

C. *Total harmonic distortion*

As mentioned previously, having a high harmonic content in the input current of the rectifier can disrupt the resonant operation of the transmitting coil driver in a resonant inductive link. The total harmonic distortion of the Class E rectifier is given by

$$THD = \frac{\sqrt{\sum_{n=2}^{\infty} i_{Ln}^2}}{i_{L1}} \tag{6.123}$$

where i_{Ln} represents the input current harmonics and i_{L1} is the fundamental current component of the input current at the resonant frequency. Using the Fourier trigono-

metric series formula, i_{Ln} can be derived by evaluating the harmonic content of the state vector $X(\omega t)$ in Eq. 6.107 as shown below

$$\begin{bmatrix} i_{Ln} \\ v_{cn} \\ v_{C_o n} \end{bmatrix} = \mathbf{x}_n = \left(\mathbf{a}_n^{\circ 2} + \mathbf{b}_n^{\circ 2}\right)^{\circ \frac{1}{2}}. \tag{6.124}$$

The coefficients matrices $\mathbf{a}_n$ and $\mathbf{b}_n$ contain the Fourier coefficients and are equal to

$$\mathbf{a}_n = \frac{1}{\pi}\left(\int_0^{2\pi D} \mathbf{x}_{ON}(\omega t)\cos\left(n\omega t + \phi + 2\pi(1-D)\right)d\omega t + \int_0^{2\pi(1-D)} \mathbf{x}_{OFF}(\omega t)\cos\left(n\omega t + \phi\right)d\omega t\right) \tag{6.125}$$

$$\mathbf{b}_n = \frac{1}{\pi}\left(\int_0^{2\pi D} \mathbf{x}_{ON}(\omega t)\sin\left(n\omega t + \phi + 2\pi(1-D)\right)d\omega t + \int_0^{2\pi(1-D)} \mathbf{x}_{OFF}(\omega t)\sin\left(n\omega t + \phi\right)d\omega t\right) \tag{6.126}$$

Figs. 6.27e and 6.27f show the variation the THD of the input current with duty cycle and normalised load for the ideal Class E rectifier. The THD has a peak value of 10.34 % at a duty cycle of 0.392 and normalised load of 1.10. The THD is reduces when the duty cycle approaches zero or unity since the diode is either ON or OFF for most of the switching period and the effect of the rectifier transitioning from either the ON and OFF states is reduced.

The Matlab code for calculating the THD is included in Appendix A.3.3.

6.4.4 *Experimental Setup and Results*

A Class E rectifier has been built to deliver up to 10 W for a previously designed IPT system [74]. The IPT system, shown in Fig. 6.28, consists of the Class E resonant inverter designed in Sec. 5.4 as the transmitting coil current driver, the inductive specified in Sec. 3.4.3. The transmitting coil and the receiving coil were aligned with each other and separated by a distance of 5 cm. A capacitor was connected across the receiving coil to form a parallel LC tank which is intended to boost the voltage induced at the receiving coil. The parallel LC tank can be represented as a voltage source [109]. The Class E rectifier is connected directly to the receiving coil and a resistive load is connected to the output of the rectifier. A photograph of the complete system is shown in Fig. 6.29. The rectifier was designed to operate at a duty cycle of 0.5 for maximum power capability [122] and its resonant frequency is designed to match the operating

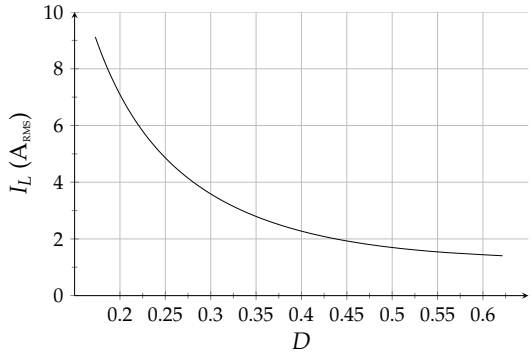

(a) Normalised RMS input current against duty cycle

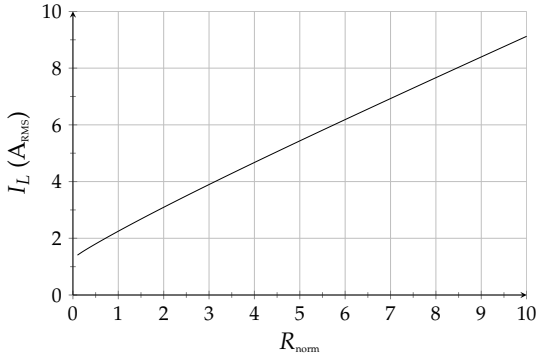

(b) Normalised RMS input current against normalised load

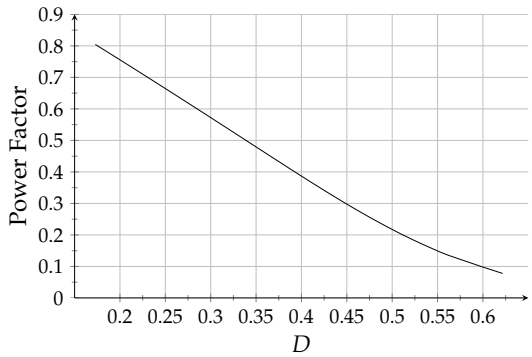

(c) Power factor against duty cycle

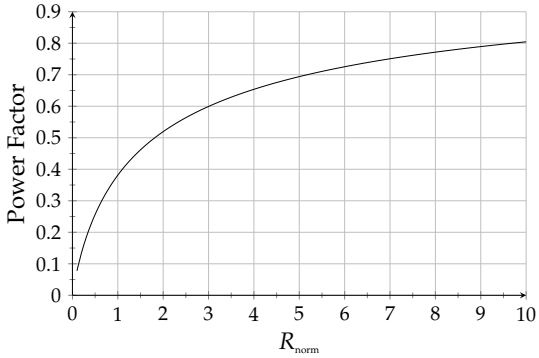

(d) Power factor against normalised load

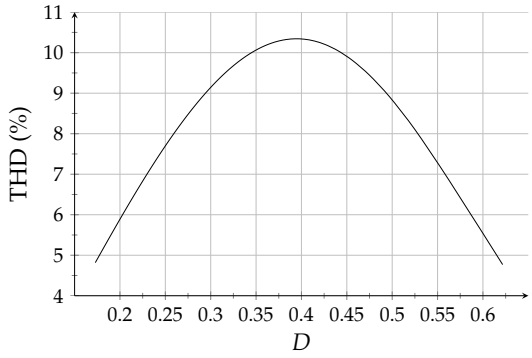

(e) THD against duty cycle

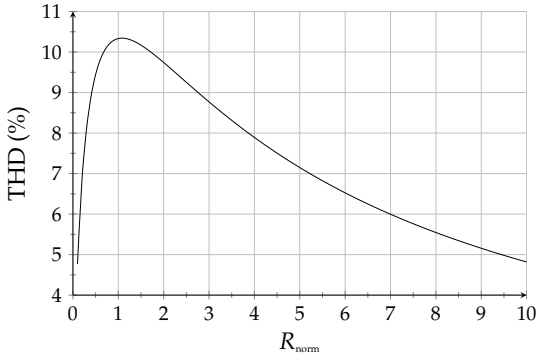

(f) THD against normalised load

Fig. 6.27: Power quality parameters for the ideal Class E rectifier at different duty cycle and normalised load combinations.

frequency of the IPT system which is at 800 kHz. The values of the load resistance R_L is 77.5 Ω, the resonant inductor L is 39.5 µH, the resonant capacitor C is 1 nF and the output capacitor C_o is 1 µF. The Schottky diode used is the SB3100 (100V/3A), its forward voltage drop is 0.3 V and its ON resistance is 0.45 Ω. The resonant inductor consists of 64 turns wound on a T68-7B core from mircometals and its ESR is 0.5 Ω. The input voltage to the IPT system is varied to control the induced voltage that is to be rectified at the receiving coil.

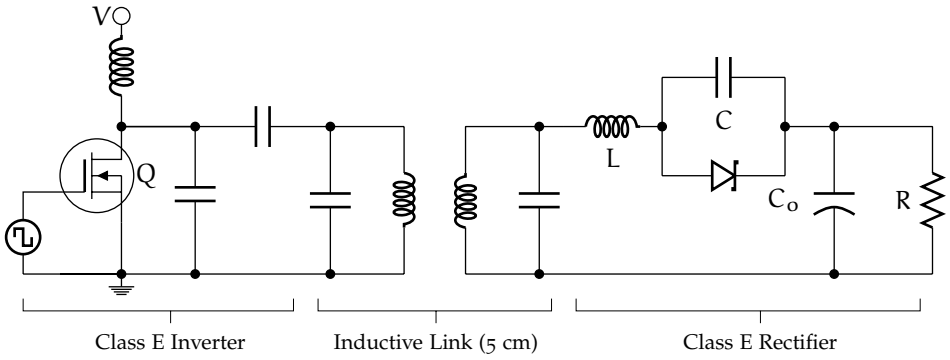

Fig. 6.28: Complete circuit of the IPT system. The circuit consists of a Class E inverter as the transmitting coil current driver, an inductive link with a separation distance of 5 cm and the designed Class E rectifier.

Figs. 6.30a and 6.30b show the measured and calculated output voltage and input RMS current of the rectifier respectively as the input voltage to the rectifier varies from 20 Vpp to 200 Vpp. The power factor measurements and calculations are shown in Fig. 6.30c, the power factor varies slightly over the entire input voltage range. The measured input and output powers and the efficiency of the Class E rectifier are shown in Figs. 6.30d and e respectively. The Class E rectifier has a maximum efficiency of 94.43 % at an input voltage of 100 Vpp and is above 90 % over most of the input voltage range. The calculated variation of the duty cycle is shown in Fig. 6.30f. The calculated values are in good agreement with the measurements confirming the modelling approach.

Fig. 6.31 shows the measured and simulated voltage and current waveforms throughout the rectifier for an input voltage of 200 Vpp. Fig. 6.31a shows the obtained input voltage that is induced at the receiving coil. It can be seen that the input voltage can be considered to be sinusoidal when compared to the reference sinusoidal plot. The obtained and simulated input current is shown in Fig. 6.31b, the input current is a near sinusoidal and contains a DC offset current. The obtained and simulated diode voltage and current waveforms are shown in Figs. 6.31c and d respectively. The ringing observed in diode's current is due to the lead inductances of the diode and the current probe. Fig. 6.31f shows the magnitude of the first four harmonic contents of the obtained and simulated input currents. The THD of the measured input current is 8.84 % compared to a calculated value of 8.89 %. The close match between the obtained and simulated waveforms provides further confirmation of the analysis and the modelling approach.

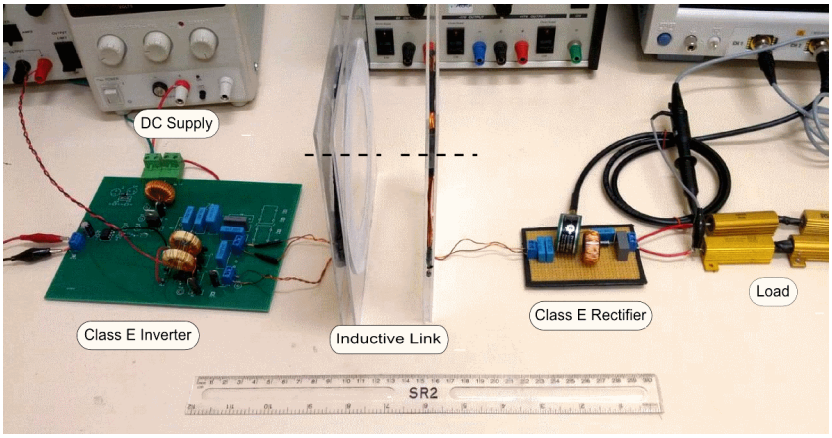

Fig. 6.29: Photograph of the experimental setup showing the various sections of the IPT system. The DC supply of the Class E inverter is varied to control the inducted voltage at the secondary coil of the inductive link.

6.5 CONCLUSIONS

The chapter provided an overview of AC/DC rectifiers that can be possibly used in inductive links. The traditional half-wave and full-wave bridge rectifiers were shown to be not compatible with inductive links that use resonant inverters, especially Class E inverters, as primary coil drivers due to the high harmonic content in their input current. Class D rectifiers were then presented and analysed. It was shown that Class D rectifiers are suitable to be used in inductive links with resonant primary coil drivers.

This chapter also presented a novel analysis for a Class E ZVS, low dv/dt rectifier with a diode as a the rectifying switch. A piecewise linear state-space representation had been used to model the rectifier and to derive various parameters. The accuracy of the model was improved by including the diode's voltage drop, the diodes ON resistance and the ESR of the resonant inductor in the analysis. A novel investigation into the power quality of the Class E rectifier has been conducted by evaluating parameters such as power factor and THD of its input current. Such parameters can aid in determining the performance of the Class E rectifier and its effect on the resonant operation of a IPT system. Experimental results are presented based on a Class E rectifier designed to operate in a resonant IPT system that is capable of delivering up to 10 W. The results are in excellent agreement with numerical calculations and simulations which confirms the analysis and modelling approach. The results obtained show that the designed rectifier operates at efficiencies exceeding 90 % over an input voltage ranging from 40 Vpp to 200 Vpp and having a maximum efficiency of 94.43 %.

In the next chapter, the Class E rectifier will be used to form a Class E^2 resonant DC/DC converter. The diode will be replaced with a MOSFET to increase the rec-

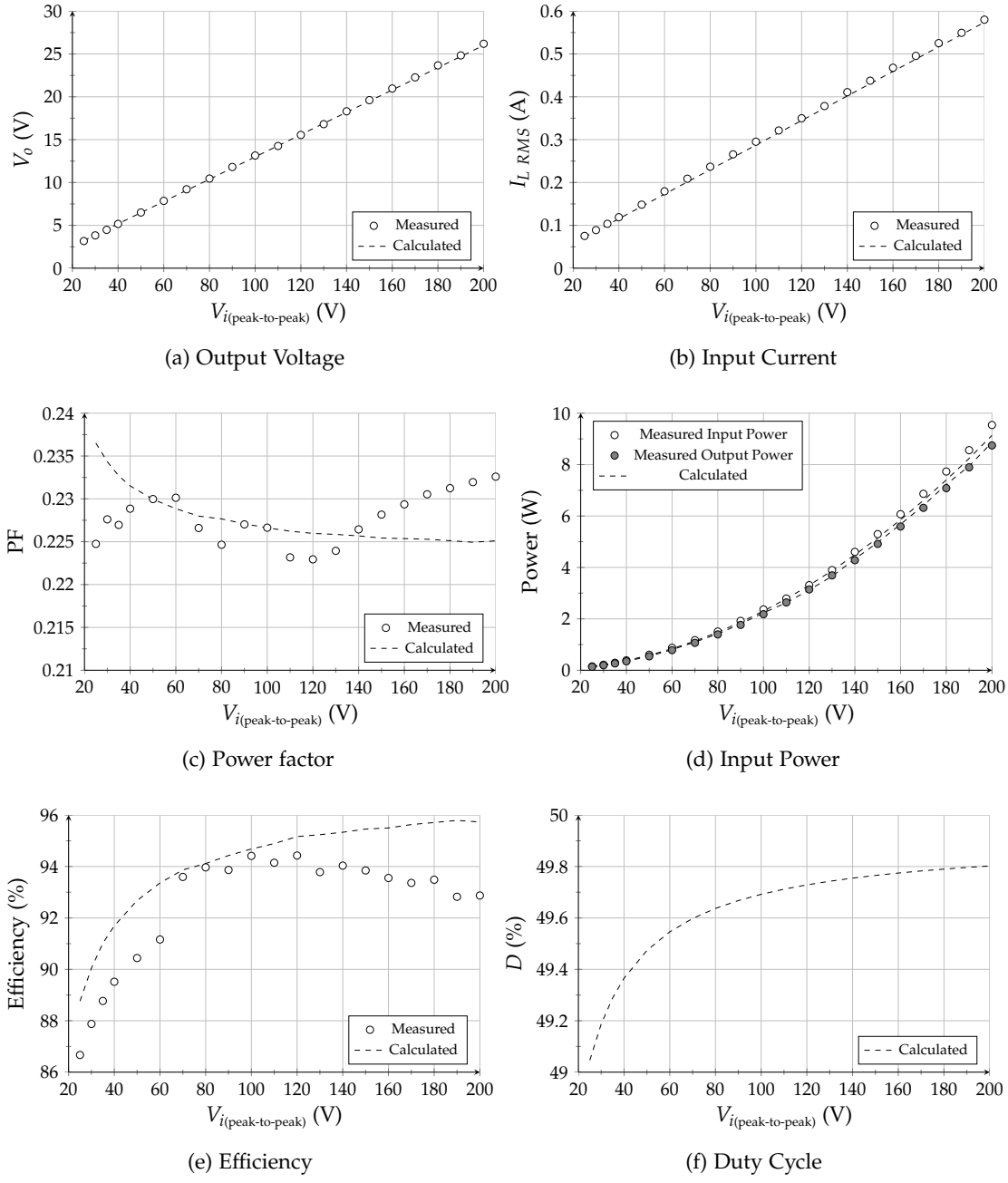

(a) Output Voltage

(b) Input Current

(c) Power factor

(d) Input Power

(e) Efficiency

(f) Duty Cycle

Fig. 6.30: Measured and calculated values of various parameters against input voltage.

tifier's input voltage range and output power capability. In addition to designing a self-powered MOSFET gate driver, timing and control circuitry.

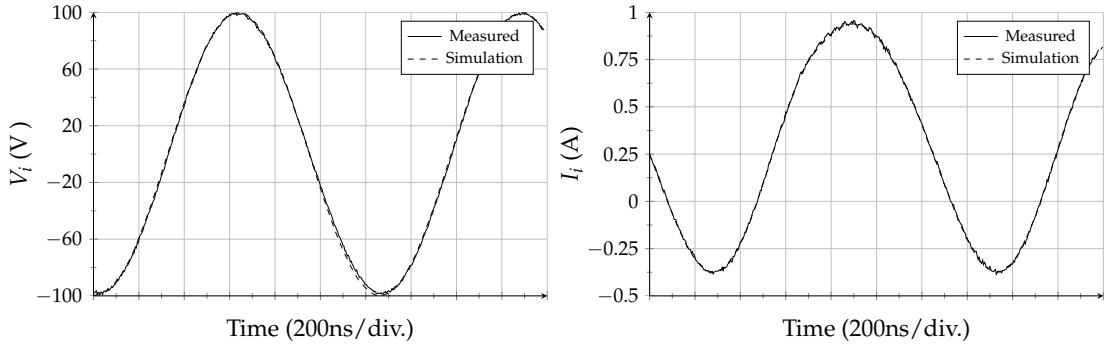

(a) Input voltage

(b) Input current

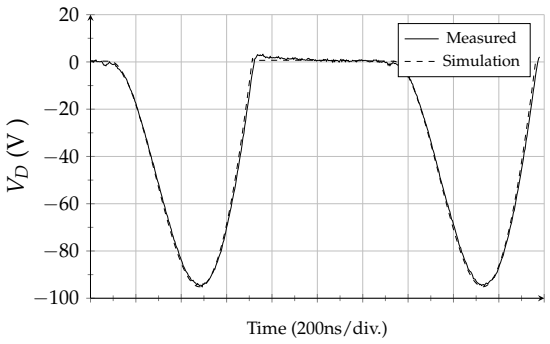

(c) Diode voltage

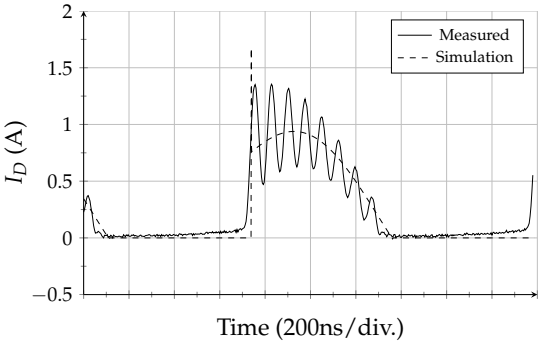

(d) Diode current

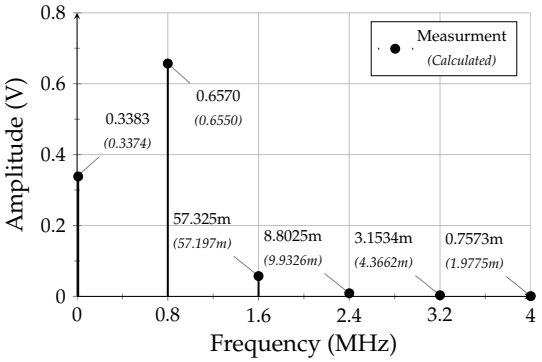

(e) Input current harmonics

Fig. 6.31: Measured and simulated voltages and currents throughout the rectifier for an input voltage of 200 Vpp.

7

CLASS E^2 RESONANT DC/DC CONVERTERS

7.1 INTRODUCTION

Class E inverters and Class E rectifiers can be combined together to form Class E^2 DC/DC resonant converters. These converters can be used to build high frequency, powerful and efficient DC/DC converters. Extensive research has also been carried out on Class E^2 DC/DC converters over the past three decades [78, 85, 97, 116, 123–132]. Therefore, the first aim of this chapter is to take the first step in bringing the Class E^2 converter to inductive links. Second, a novel state-space modelling approach will be used to provide an accurate analysis of the complete system. The previous work in analysing Class E^2 converters has been based on an analytical approach. The analysis assumed that the inverter part of the Class E^2 converter was operating at high Q factor and that the rectifier part could be represented by an equivalent impedance. The experimental results that were obtained were in good agreement with the analytical calculations over certain load ranges, however a more accurate analysis can still be performed to obtain better results over a wider load range.

This chapter is organised as follows. Sec. 7.2 presents the Class E^2 converter. Analysis is carried out based on a 7th order piece-wise linear state-space representation. Sec. 7.3 provides a design example and addresses the effect of coil misalignment and load variation. A comparison is provided between the results obtained from the analysis presented in this chapter with the analytical approach. Sec. 7.4 describes the experimental setup of a Class E^2 converter for an IPT system and discusses the obtained experimental results.

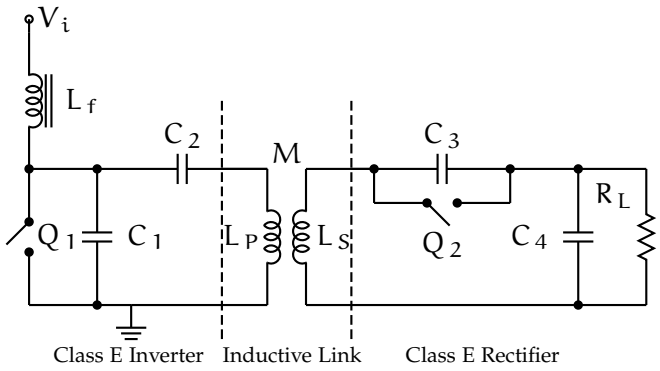

Fig. 7.1: Circuit of the Class E inverter, inductive link and the Class E rectifier

7.2 MODELLING AND ANALYSIS

The Class E^2 converter that will be analysed in this chapter consists of a Class E zero-voltage switching and zero-derivative voltage switching inverter with an infinite DC-feed inductance that was discussed in Sec. 4.4.1, an inductive link consisting of a primary and secondary coils separated by a certain air gap and the Class E ZVS low dv/dt rectifier that was presented in Sec. 6.4.2. Fig. 7.1 shows the complete circuit of the converter. A similar configuration had been used in [125] to design an isolated DC/DC converter. The inverter and rectifier switches are designated by Q_1 and Q_2 respectively, L_f is the DC-feed inductance of the inverter, L_P and L_S represent the inductances of the primary and secondary coils respectively and M is mutual inductance between them. Resistor R_L represents the load. The switches are driven at the same switching frequency ω, though at different duty cycles which will be discussed in the following sections.

7.2.1 *State-space Representation*

The Class E^2 converter in Fig. 7.1 can represented by the equivalent circuit shown in Fig. 7.2. The switches are replaced by resistors r_{Q_1} and r_{Q_2}. Depending on the state of the switches, r_{Q_1} and r_{Q_2} are either equal to their ON or OFF resistances. Resistors r_P and r_S are included to represent the equivalent series resistance (ESR) of the primary and secondary coils respectively. The equivalent circuit can be analysed by the following general state-space representation

$$\dot{\mathbf{x}}(\omega t) = A\mathbf{x}(\omega t) + B\mathbf{u}(\omega t) \tag{7.1}$$

$$\mathbf{y}(\omega t) = C\mathbf{x}(\omega t) + D\mathbf{u}(\omega t) \tag{7.2}$$

where $\mathbf{x}$ is the state vector and contains the following seven voltage and current states variables

$$\mathbf{x}(\omega t) = \begin{bmatrix} v_{C_1}(\omega t) & v_{C_2}(\omega t) & v_{C_3}(\omega t) & v_{C_4}(\omega t) & i_{L_f}(\omega t) & i_{L_P}(\omega t) & i_{L_S}(\omega t) \end{bmatrix}^T \tag{7.3}$$

and $\mathbf{u}$ is the input vector equal to a unit step function. Using KVL and KCL, the matrices A, B, C and D are given as

$$A = \begin{bmatrix} \frac{-1}{\omega C_1 r_{Q_1}} & 0 & 0 & 0 & \frac{1}{\omega C_1} & \frac{-1}{\omega C_1} & 0 \\ 0 & 0 & 0 & 0 & 0 & \frac{1}{\omega C_2} & 0 \\ 0 & 0 & \frac{-1}{\omega C_3 r_{Q_2}} & 0 & 0 & 0 & \frac{1}{\omega C_3} \\ 0 & 0 & 0 & 0 & 0 & 0 & \frac{1}{\omega C_4} \\ \frac{-1}{\omega L_f} & 0 & 0 & 0 & 0 & 0 & 0 \\ \frac{L_S \alpha}{\omega M^2(1-\alpha)} & \frac{-L_P \alpha}{\omega M^2(1-\alpha)} & \frac{-\alpha}{\omega M(1-\alpha)} & \frac{-\alpha}{\omega M(1-\alpha)} & \frac{-\alpha}{\omega M(1-\alpha)} & \frac{L_S \alpha r_p}{\omega M^2(1-\alpha)} & \frac{-\alpha r_s}{\omega M(1-\alpha)} \\ \frac{\alpha}{\omega M(1-\alpha)} & \frac{-\alpha}{\omega M(1-\alpha)} & \frac{-L_P \alpha}{\omega M^2(1-\alpha)} & 0 & 0 & \frac{-\alpha r_p}{\omega M(1-\alpha)} & \frac{L_P \alpha r_s}{\omega M^2(1-\alpha)} \end{bmatrix} \tag{7.4}$$

$$B = \begin{bmatrix} 0 & 0 & 0 & 0 & \frac{1}{\omega L_f} & 0 & 0 \end{bmatrix}^T \tag{7.5}$$

$$C = \mathbf{I} \tag{7.6}$$

$$D = \begin{bmatrix} 0 & 0 & 0 & 0 & 0 & 0 & 0 \end{bmatrix}^T \tag{7.7}$$

where $\mathbf{I}$ is the 7×7 identity matrix and

$$\alpha = \omega^2(L_P L_S - M^2). \tag{7.8}$$

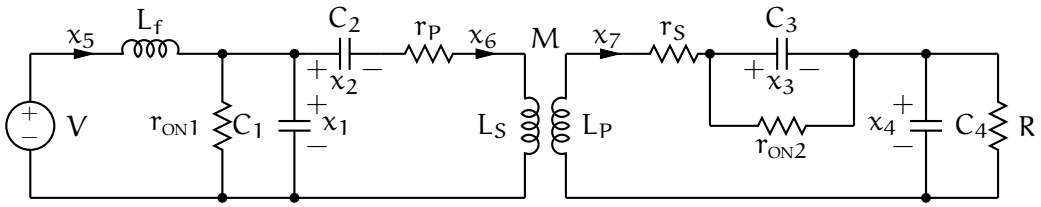

Fig. 7.2: Equivalent circuit model of the Class E^2 converter.

7.2.2 *Switching Periods and Operating Modes*

The Class E^2 converter will have four operating modes depending on the state of the switches. The switches are either ON in which they are represented by their ON resistances, or OFF in which they are represented by their OFF resistances. For simplicity, it is assumed that the OFF resistance of both switches is infinity.

Fig. 7.3 shows the order of the four different modes in one switching period. It is assumed that the inverter is set to operate at a duty cycle ratio of 0.50. The order of the modes can be initially deduced by inspecting the operation of the circuit, however the duration of each mode is yet unknown. The four different operating modes are defined in Table 7.1. The switching period begins in Mode①. In this mode both switches are turned ON and are represented by their ON resistance. At $\omega t = a$, the converter transitions into Mode② and the rectifier's switch is turned OFF. At $\omega t = b$, the converter transitions into Mode③ where the inverter's switch is now turned OFF. At $\omega t = c$, the converters transitions to the final Mode④, where the rectifier's switch is now turned ON and the inverter's is kept OFF. The four modes of operation result in four different A matrices which lead to four different linear state-space representations. The complete model of the converter is now a piecewise linear state-space representation. Fig. 8.5 shows the voltage waveforms of the switches that are associated with this mode sequence. From Fig. 8.5, the duty cycle ratio D_1 of

Table 7.1: Definition of the operating modes of the Class E^2 converter

Mode	Domain	r_{Q_1}	r_{Q_2}
①	$0 < \omega t \leqslant 2\pi a$	r_{ON1}	r_{ON2}
②	$0 < \omega t \leqslant 2\pi(b-a)$	r_{ON1}	∞
③	$0 < \omega t \leqslant 2\pi(c-a)$	∞	∞
④	$0 < \omega t \leqslant 2\pi(1-c)$	∞	r_{ON2}

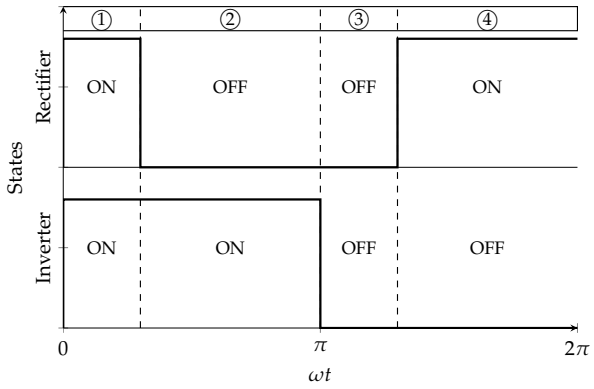

Fig. 7.3: The possible operating modes of the inverter and rectifier for one switching cycle

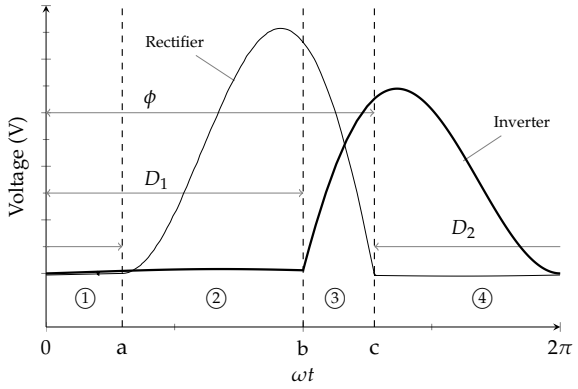

Fig. 7.4: Voltage waveforms of the inverter MOSFETs Q_1 and the rectifier MOSFET Q_2

switch Q_1 is equal to

$$D_1 = \frac{b}{2\pi} \tag{7.9}$$

and the duty cycle ratio D_2 of switch Q_2 is equal to

$$D_2 = \frac{2\pi + a - c}{2\pi}. \tag{7.10}$$

The phase difference ϕ between D_1 and D_2 is equal to

$$\phi = c \tag{7.11}$$

7.2.3 *Determining the Initial Conditions of the States*

The general solution to Eqs. 7.1 and 7.2 is given by

$$\mathbf{x}(\omega t) = \mathbf{x_n}(\omega t) + \mathbf{x_f}(\omega t). \tag{7.12}$$

Function $\mathbf{x_n}$ is the natural response matrix, or the zero-input response matrix, and is equal to

$$\mathbf{x_n}(\omega t) = e^{A\omega t}\mathbf{x}(0) \tag{7.13}$$

where e is the matrix exponential function. $\mathbf{x}(0)$ is the initial condition matrix. Function $\mathbf{x_f}$ is the forced response matrix, or the zero-state response matrix, and is equal to

$$\begin{aligned}\mathbf{x_f}(\omega t) &= \int_0^{\tau} e^{A(\omega t-\tau)}B\mathbf{u}(\tau)d\tau \\ &= A^{-1}\left(e^{A\omega t}-\mathbf{I}\right)B.\end{aligned} \tag{7.14}$$

The initial condition matrix $\mathbf{x}(0)$ for can be determined from the voltages' and currents' continuity conditions as the converter transitions from one mode to the next as follows

$$\mathbf{x}_{①}(0) = \mathbf{x}_{④}(2\pi(1-c)) \tag{7.15}$$

$$\mathbf{x}_{②}(0) = \mathbf{x}_{①}(2\pi(a)) \tag{7.16}$$

$$\mathbf{x}_{③}(0) = \mathbf{x}_{②}(2\pi(b-a)) \tag{7.17}$$

$$\mathbf{x}_{④}(0) = \mathbf{x}_{③}(2\pi(c-b)). \tag{7.18}$$

It is noted that the general solution equation (Eq. 7.12) represents a periodic system. By substituting Eqs. 7.15-7.18 in Eq. 7.12, the initial conditions of all states in all modes for all periods of the switching signal are equal to

$$\begin{bmatrix}\mathbf{x}_{①}(2\pi m)\\ \mathbf{x}_{②}(2\pi m)\\ \mathbf{x}_{③}(2\pi m)\\ \mathbf{x}_{④}(2\pi m)\end{bmatrix} = \begin{bmatrix}-e^{A_{①}2\pi a} & \mathbf{I} & 0 & 0\\ 0 & -e^{A_{②}2\pi(b-a)} & \mathbf{I} & 0\\ 0 & 0 & -e^{A_{③}2\pi(c-b)} & \mathbf{I}\\ \mathbf{I} & 0 & 0 & -e^{A_{④}2\pi(1-c)}\end{bmatrix}\cdot \begin{bmatrix}A_{①}^{-1}(e^{A_{①}2\pi a}-\mathbf{I})\\ A_{②}^{-1}(e^{A_{②}2\pi(b-a)}-\mathbf{I})\\ A_{③}^{-1}(e^{A_{③}2\pi(c-b)}-\mathbf{I})\\ A_{④}^{-1}(e^{A_{④}2\pi(1-c)}-\mathbf{I})\end{bmatrix} B. \quad \text{for } m = 0,1,2,... \tag{7.19}$$

7.2.4 *Solving for Optimum Switching Conditions*

The modelling and analysis has now been completed. The next step is to determine the values of the components and switching periods for each modes that will achieve the optimum switching conditions of the Class E^2 converter. From Fig. 8.5, the inverter's optimum ZVS and ZDS conditions occur in Mode① at $\omega t = 0$. The rectifier's optimum

ZVS conditions occur in Mode② at $\omega t = a$ and in Mode④ at $\omega t = c$. These optimum switching conditions can be written as

$$V_{DS1}(0) = 0 \;\rightarrow\; x_{1①}(0) = 0 \tag{7.20}$$

$$\frac{V_{DS1}(\omega t)}{d\omega t}_{\omega t=0} = 0 \;\rightarrow\; x_{5①}(0) - x_{6①}(0) = 0 \tag{7.21}$$

$$V_{DS2}(2\pi a) = 0 \;\rightarrow\; x_{3②}(0) = 0 \tag{7.22}$$

$$V_{DS2}(2\pi c) = 0 \;\rightarrow\; x_{3④}(0) = 0 \tag{7.23}$$

By using Eqs. 7.19-7.23, a computer program can written to numerically solve for four different component values or parameters. The design example in the following section will discuss this in further details.

7.3 DESIGN CASE

This section will describe the design procedure of a Class E^2 converter prototype for an inductive link. The converter will operate from a 9 V DC supply and will deliver up to 20 W of power to a nominal 10 Ω load at a 200 kHz switching frequency.

7.3.1 *Initial Design*

The design procedure begins with coils of the inductive link. The coils should have a large quality (Q) factor at the switching frequency of the converter for maximum power transfer efficiency. For this reason the primary and secondary coils that will be used are those that are specifically designed for the 'Qi' Wireless Power Consortium standard [133]. Both coils have a maximum DC resistance of 0.1 Ω, an inductance of 24 µH and a Q factor of 230 at 200 kHz [134]. The coils' ESR can be calculated and is equal to 0.137 Ω. With the addition of the connectors' resistance and the DC resistance of the printed circuit board tracks, the total resistance of the coils is approximately 0.25 Ω at 200 kHz. The mutual inductance between the primary and secondary coils can be measured at different separation distances. For a separation distance of 3 mm, the measured mutual inductance is approximately 12 µH which corresponds to a coupling coefficient value of 0.50.

The secondary coil along with capacitor C_3 form the resonant part of the Class E rectifier. Therefore the value of C_3 that will cause the rectifier to resonate at 200 kHz is equal to

$$C_3 = \frac{1}{\omega^2 L_P} = 26.38\,\text{nF} \tag{7.24}$$

The output capacitor C_4 should be large enough to maintain a constant DC voltage. A value of 6.6 µF is found to be suitable. The duty cycle D_2 of switch Q_2 and its phase ϕ with respect to D_1 are the first two parameters that will need to be determined from Eqs. 7.19-7.23.

The DC-feed inductor L_f of the Class E inverter should be large enough to maintain a constant DC current flow. A choke with a 1 mH inductance is used. The duty cycle D_1 of switch Q_1 is initially set at 0.50. MOSFET IRF540 was used for both switches Q_1 and Q_2. The total resistance of the MOSFETs' drain-to-source channel and the printed circuit board trace is approximately 0.15 Ω. Capacitors C_1 and C_2 are the two remaining values that will need to be determined from Eqs. 7.19-7.23.

The values and parameters that need to be determined are now a, c, C_1 and C_2. Eqs. 7.19-7.23 were programmed in Matlab using the Optimization Toolbox and Simulink was then used to measure voltages and currents throughout the converter. The Matlab code is included in Appendix. A.4.1. Table 7.2 lists the solutions obtained for D_2, C_1 and C_2. Table 7.2 also lists the maximum voltages across the switches V_{Q_1max} and V_{Q_2max}, the maximum current in the switches I_{Q_1max} and I_{Q_2max}, the input average DC current I_{In}, the primary coil's peak-to-peak current I_{Lp}, the output voltage across the load V_o and the overall DC-to-DC efficiency η. The solutions and measurements for three coupling coefficient values above and below the nominal value of 0.50 are included to show how the variation in the distance between the coils affects the converter. It can be seen that as the coils are further away from each other, or at loose coupling coefficients, the converter delivers more power to the load but at increased current stresses and reduced efficiencies. Efficiency is reduced due to the increasing currents in the coils which lead to higher ohmic losses. The converter delivers less power to the load as the coils are brought closer to each other or at tighter coupling coefficients. The duty cycle D_2 and phase ϕ remain relatively constant when the coupling coefficient varies. This is because the Class E rectifier's performance is mainly affected by the load [72, 122] which is kept constant at 10 Ω.

Table 7.3 lists the solutions and measurements for several load values above and below the nominal load. The distance between the coils is kept constant at a coupling coefficient of 0.50. The converter delivers more power to higher loads at increased current stress and reduced efficiencies. The output voltage is also reduced. At reduced loads, the converter delivers less power but at higher efficiencies. The duty cycle D_2 and phase ϕ vary accordingly since now the load does change. These variations will have to be considered and may increase the complexity of the driving circuitry for switch Q_2.

Table 7.2: Calculated parameters for a variable coupling coefficient and fixed load of 10 Ω

k	f(kHz)	D_1	D_2	ϕ	C_1(nF)	C_2(nF)	$V_{Q_1 max}$(V)	$V_{Q_2 max}$(V)	$I_{Q_1 max}$(A)	$I_{Q_2 max}$(A)	I_{In}(A)	I_{Lp}(A)	V_o(V)	η%
0.35	200	0.500	0.511	229.347	99.656	33.269	31.407	56.133	9.547	4.066	3.333	12.541	14.835	73.37
0.40	200	0.500	0.511	229.489	80.302	35.989	31.530	51.572	7.682	3.746	2.676	10.106	13.607	76.88
0.45	200	0.500	0.511	229.657	66.003	39.663	31.618	47.433	6.287	3.457	2.196	8.288	12.562	79.84
0.50	**200**	**0.500**	**0.511**	**229.864**	**55.230**	**44.773**	**31.683**	**43.736**	**5.223**	**3.202**	**1.820**	**6.905**	**11.571**	81.74
0.55	200	0.500	0.510	230.124	46.972	52.208	31.729	40.447	4.397	2.977	1.538	5.833	10.760	83.64
0.60	200	0.500	0.510	230.464	40.552	63.826	31.759	37.510	3.744	2.780	1.305	4.989	10.010	85.31
0.65	200	0.500	0.509	230.931	35.509	84.251	31.777	34.864	3.219	2.608	1.126	4.314	9.336	86.01

Table 7.3: Calculated parameters for a variable load and a fixed coupling coefficient of 0.5

R(Ω)	f(kHz)	D_1	D_2	ϕ	C_1(nF)	C_2(nF)	$V_{Q_1 max}$(V)	$V_{Q_2 max}$(V)	$I_{Q_1 max}$(A)	$I_{Q_2 max}$(A)	I_{In}(A)	I_{Lp}(A)	V_o(V)	η%
5	200	0.500	0.573	217.428	84.266	40.459	31.514	42.683	8.091	4.827	2.822	10.644	9.621	72.89
6	200	0.500	0.558	220.590	75.623	41.297	31.563	43.104	7.249	4.338	2.527	9.544	10.156	75.59
8	200	0.500	0.532	225.742	63.462	43.005	31.632	43.555	6.048	3.657	2.112	7.978	10.992	79.46
10	**200**	**0.500**	**0.511**	**229.864**	**55.230**	**44.773**	**31.683**	**43.736**	**5.223**	**3.202**	**1.820**	**6.905**	**11.571**	81.74
15	200	0.500	0.470	237.587	42.731	49.581	31.784	43.703	3.946	2.526	1.380	5.247	12.623	85.53
20	200	0.500	0.440	243.215	35.561	55.168	31.888	43.395	3.196	2.152	1.125	4.277	13.338	87.85
30	200	0.500	0.395	251.291	27.455	70.145	32.114	42.538	2.326	1.756	0.824	3.158	14.158	90.10
50	200	0.500	0.337	261.584	19.844	144.43	32.580	40.671	1.491	1.430	0.539	2.091	14.964	92.32

It is noted that solutions listed in Tables 7.2 and 7.3 are not unique, other solutions exist that satisfy the optimum switching conditions. However they were not considered since they are difficult to implement practically and can lead to poor efficiencies.

7.3.2 *Comparison with the Analytical Approach*

It is necessary to compare the presented state-space approach with the analytical approach [78, 109, 121, 125, 128–130, 135] in terms of accuracy and complexity. In this section, certain solutions will be obtained using the analytical approach to determine the level of agreement to those in Tables 7.2 and 7.3.

The analytical approach begins by representing the inductive link with an T-equivalent circuit [55] as shown in Fig. 7.5a. Next, the Class E rectifier part is replaced with an equivalent inductor L_{EQ} and equivalent resistor R_{EQ} as shown in Fig. 7.5b. Further details on determining the equivalent inductance and resistance of selected Class E rectifier configuration in this chapter can be found in [122]. Finally, the components in the output network of the Class E inverter can be represented by an equivalent inductor L_x and equivalent load resistance R_x as shown in Fig. 7.5c. Setting the duty cycle to D_1 to 0.50, the values of C_1 and C_2 can be determined using the design equations in [73, 89].

Table 7.4 compares between the solutions obtained using the two approaches for two load values of 10 Ω and 30 Ω. For the 10 Ω load case, the solutions for C_1, C_2 and D_2 in both approaches are relatively close to each other. However for the 30 Ω load case, the difference between the solutions of both approaches starts to increase. It can be assumed that the analytical approach is less accurate for the 30 Ω load case since the Q factor of the inverter is reduced. As a result, the current in coils of the inductive link is no longer sinusoidal, therefore the assumptions that the analytical approach is based on are not valid. The phase ϕ and output voltage V_o were not determined in the analytical approach since they involve tedious calculations.

PSPICE simulations were performed using the solutions in Table 7.4 for both approaches. Fig. 7.6 shows the voltage and current waveforms of Q_1 and Q_2 respectively. A difference can be observed in the waveforms due to mismatch in the solutions. It can be seen from the waveforms that the solutions obtained using the analytical approach do not completely satisfy the optimum switching conditions of the converter. The voltage across switch Q_1 in Figs. 7.6a and 7.6c is not zero when the switch is turned ON. This results in a large current spike to flow through switch Q_1 as can be seen in Figs. 7.6c and 7.6d. The analytical approach resulted in a DC output voltage

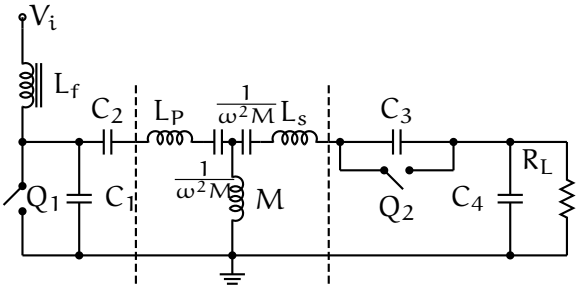

(a) Replacing the inductive link with a T-equivalent circuit

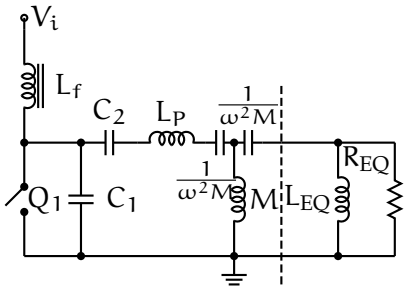

(b) Replacing the Class E rectifier with an equivalent impedance

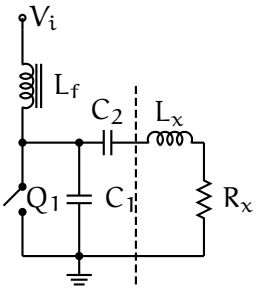

(c) Replacing the output network of the Class E inverter with an equivalent impedance

Fig. 7.5: Equivalent circuits of the Class E^2 converter for the analytical approach

Table 7.4: Calculated values and parameters comparing the analytical approach with the piecewise linear state-space approach

	$R_L = 10\,\Omega$, $k = 0.50$		$R_L = 30\,\Omega$, $k = 0.50$	
	Analytical	State-space	Analytical	State-space
C_1	58.088 nF	55.230 nF	29.666 nF	27.455 nF
C_2	45.195 nF	44.773 nF	76.667 nF	70.145 nF
D_2	0.515	0.511	0.404	0.395
ϕ	-	229.864°	-	251.291°
R_{EQ}	96.463 Ω	-	41.512 Ω	-
L_{EQ}	19.726 µH	-	15.504 µH	-
R_x	2.693 Ω	-	5.842 Ω	-
L_x	16.738 µH	-	14.825 µH	-
V_o	-	11.571 V	-	14.158 V

of 11.900 V and 14.093 V for a 10 Ω load and 30 Ω load respectively, whereas the state-space approach resulted in a DC output voltage of 11.571 V and 14.158 V for a 10 Ω load and 30 Ω load respectively.

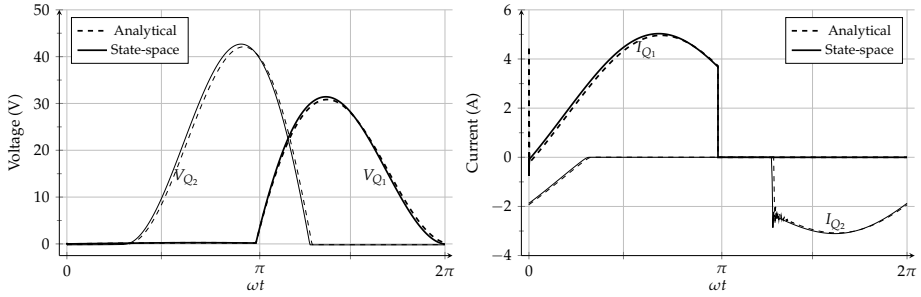

(a) Voltages for $R_L = 10\,\Omega$

(b) Currents for $R_L = 10\,\Omega$

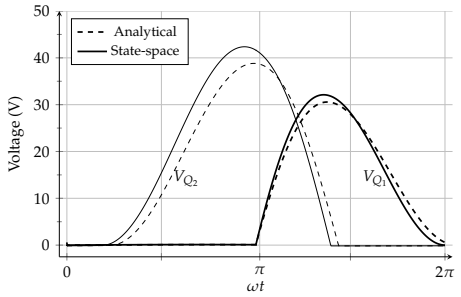

(c) Voltages for $R_L = 30\,\Omega$

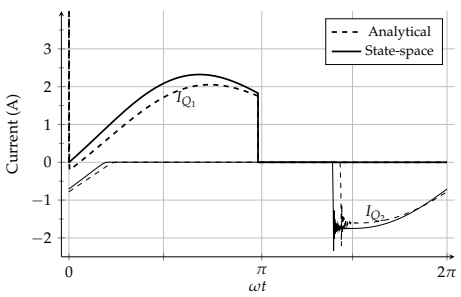

(d) Currents for $R_L = 30\,\Omega$

Fig. 7.6: Simulation results comparing the voltage and current waveforms of Q_1 and Q_2 for the analytical approach and the piecewise linear state-space modelling approach.

7.3.3 *Compensation for Load Variations and Coil Misalignments*

The Class E^2 converter prototype is to operate at a nominal load of $10\,\Omega$ at a coupling coefficient of 0.50. Variations can occur in the load and alignment of the coils while the converter is operating. Tables 7.2 and 7.3 list the solutions for different load and coupling coefficient values, however it is necessary to alter the values of capacitors C_1 and C_2 to compensate for any variations. Replacing capacitors may not be a practically feasible, therefore it is more efficient to keep the values of capacitors C_1 and C_2 constant for a specific nominal load and coupling coefficient. Other parameters such as the switching frequency, the duty cycles D_1 and D_2 and phase ϕ can be altered even when the converter is operating.

Table 7.5 lists the solutions for different values of loads and coupling coefficients when capacitors C_1 and C_2 are kept constant at 53.360 nF and 45.139 nF respectively. Altering the switching frequency will shift the operation of the Class E rectifier part of the converter from resonance, however efficient operation can still be maintained [135].

Table 7.5: Calculated parameters for a variable load and variable coupling coefficient

$R(\Omega)$	k	f(kHz)	D_1	D_2	ϕ	$V_{Q_1 max}$(V)	$V_{Q_2 max}$(V)	$I_{Q_1 max}$(A)	$I_{Q_2 max}$(A)	I_{In}(A)	I_{Lp}(A)	V_o(V)	η(%)
5	0.50	187.882	0.590	0.582	221.433	38.166	53.465	10.543	5.854	4.228	12.841	11.768	72.79
6	0.50	190.042	0.571	0.565	223.465	36.597	51.671	8.952	5.063	3.489	11.088	11.917	75.38
8	0.50	194.750	0.535	0.535	226.997	33.915	47.751	6.722	3.954	2.491	8.603	11.932	79.38
10	**0.50**	**200.000**	**0.500**	**0.511**	**229.864**	**31.683**	**43.736**	**5.223**	**3.202**	**1.820**	**6.905**	**11.571**	81.74
12	0.50	205.855	0.465	0.490	232.064	29.750	39.693	4.128	2.640	1.344	5.645	11.025	83.74
14	0.50	212.659	0.426	0.471	233.465	27.894	35.279	3.248	2.169	0.957	4.617	10.120	84.93
10	0.45	187.701	0.543	0.519	228.835	34.499	52.797	6.901	3.704	2.600	8.774	13.726	80.51
10	0.47	192.186	0.526	0.516	229.267	33.373	49.118	6.186	3.504	2.269	7.981	12.876	81.19
10	0.52	206.112	0.480	0.507	230.122	30.536	40.177	4.633	2.990	1.553	6.240	10.729	82.36
10	0.55	217.243	0.444	0.501	229.982	28.689	34.597	3.772	2.632	1.162	5.258	9.312	82.92

7.4 EXPERIMENTAL VERIFICATION

7.4.1 *Implementation and Set-up*

A Class E^2 converter was built based on the specifications and the design method presented in the previous sections. The complete circuit is shown in Fig. 7.7. The Class E inverter part is powered from a 9 V DC supply limited to 2.6 A. The switching signal of MOSFET Q_1 is supplied from a function generator via a MOSFET driver. An electronic load is connected to the output of the Class E rectifier to simulate various loading conditions. The coils of the inductive link are initially kept at a separation distance of 3 mm. A photograph of the experimental setup is shown in Fig. 7.8.

7.4.2 *Class E Rectifier Self-start and Driving circuit*

Driving MOSFET Q_2 of the rectifier requires additional circuitry to ensure that the switching signal is supplied at the correct instants. Referring to the time instant c in Fig. 8.5, MOSFET Q_2 switches ON once the voltage across it crosses zero volts. Therefore, the voltage across MOSFET Q_2 can used to trigger the switching signal using a comparator. On the other hand, the voltage across MOSFET Q_2 cannot be relied on as a trigger to turn it OFF. This is because the voltage has a near zero time derivative. Therefore a one-shot timer is used to drive MOSFET Q_2 with a time duration equal to or less than duty cycle D_2. The timer is triggered once the comparator detects a zero crossing in the voltage across MOSFET Q_2.

The Class E rectifier part is an isolated circuit. Power is not available immediately once the converter starts up, therefore the driving circuitry for MOSFET Q_2 will not be functional. However, the rectifier will still be able to start automatically due to the body diode of MOSFET Q_2. Once the output voltage rises to a sufficient level, the driving circuitry will then activate to allow for synchronous operation. A voltage regulator is connected to the output of the rectifier to supply power to the driving circuity.

7.4.3 *Results*

The Class E^2 converter prototype was operated at a nominal load 10 Ω, a coupling coefficient of 0.50 and a 200 kHz switching frequency. The duty cycle D_1 was set to 0.50 and the one-shot timer was set to provide a 2.56 µs pulse corresponding to a duty

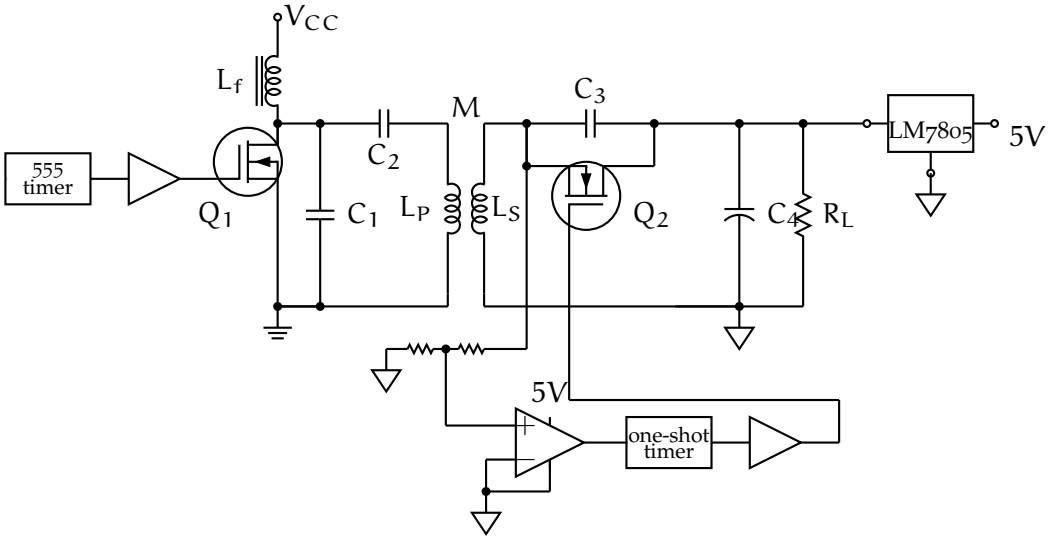

Fig. 7.7: Circuit of the experimental setup

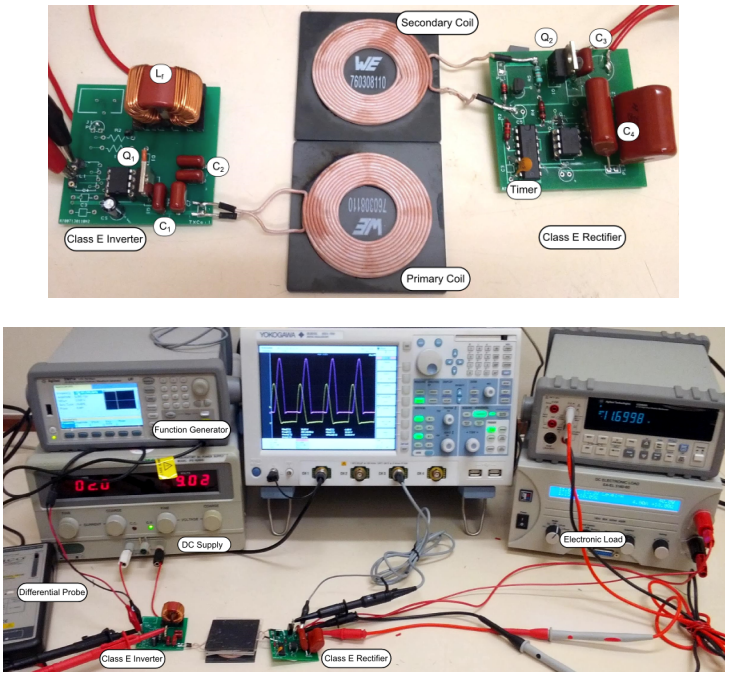

Fig. 7.8: Photograph of the Class E^2 converter and the experimental setup

cycle D_2 of 0.51. Fig. 7.9 shows the observed waveforms of the voltages across MOSFETs Q_1 and Q_2, the switching signals and the voltage across the primary coil. The waveforms of the piecewise linear state-space model are also plotted for comparison. It can be seen that the observed waveforms are in good agreement with the state-space model. Table 7.6 provides further comparison between several measured and calculated parameters. The errors between the measured and calculated parameters could be attributed to the tolerance of the capacitors' values and parasitic capacitance and inductance in the printed circuit board.

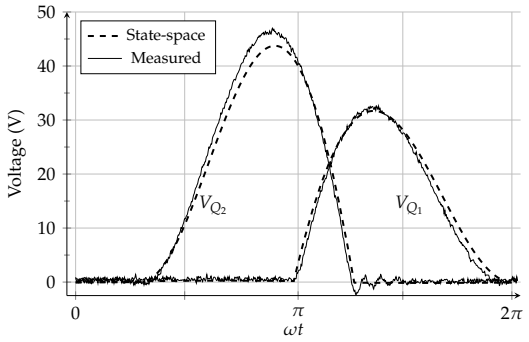

(a) Votages across MOSFETS Q_1 and Q_2

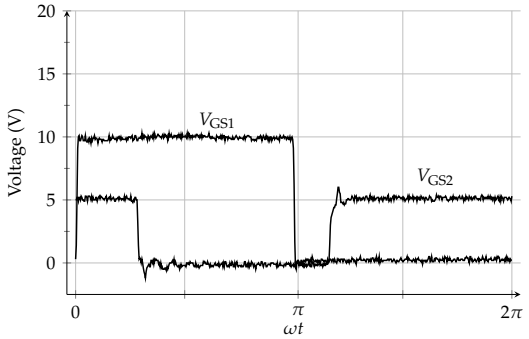

(b) Switching signals

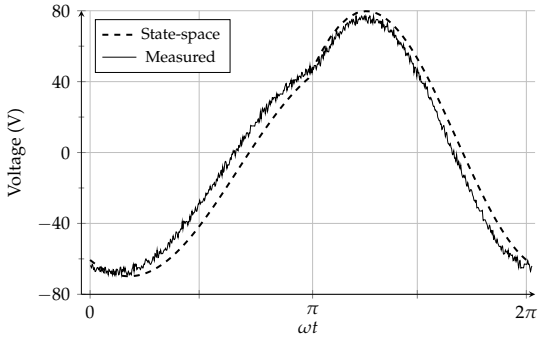

(c) Primary coil voltage

Fig. 7.9: Measured waveforms

Fig. 7.10 shows a loss breakdown analysis at nominal operating conditions. Power is mainly lost in the ESR of the inductive link coils, switching and conduction losses in MOSFETs Q_1 and Q_2 and other losses such as that of MOSFET drivers, the ESR of the capacitors and the timing and control circuitry of the rectifier. It can be seen that a significant amount of power is lost the ESR of the inductive link coils, whereas the power lost in the inverter and rectifier is low. Therefore, the overall efficiency can be improved by using coils with lower ESR.

Table 7.6: Calculated parameters for a variable load and variable coupling coefficient

Parameter	Measured	Calculated	Error
V_o(V)	11.53	11.571	-0.35 %
P_o(W)	13.294	13.389	-0.71 %
I_{IN}(A)	1.88	1.820	+3.30 %
η %	78.57	81.74	-3.88 %
$V_{Q_1 max}$(V)	32.6	31.683	+2.89 %
$V_{Q_2 max}$(V)	47.0	44.773	+4.97 %
$\phi°$	230	229.864	+0.06 %

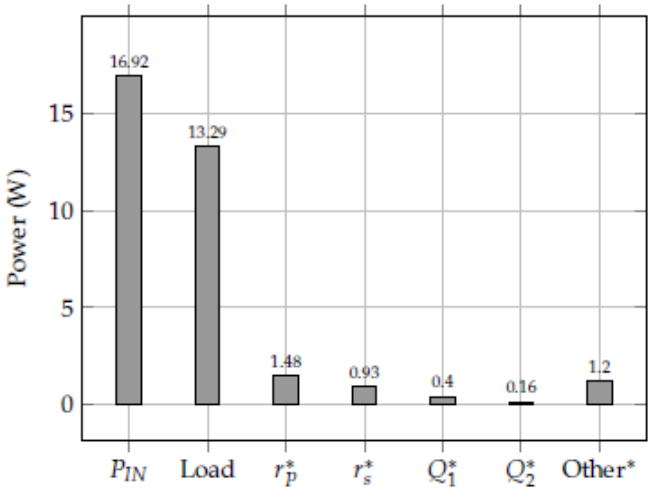

*Estimated Values

Fig. 7.10: Power distributions

7.4.4 *Load Variation*

The performance of the Class E^2 converter was investigated for variations in load and coil misalignment as discussed in the previous section. The load was varied from 8 Ω to 15 Ω and the coupling coefficient from 0.45 to 0.55. The duty cycles and switching frequencies were varied according to Table 7.5. Fig. 7.11 shows the measured output voltage, input power and efficiency for both load and coupling coefficient ranges. It can be seen that the measured parameters agree with the calculations in Table 7.5. The overall efficiency is reduced at higher loads and loose coupling coefficients, whereas lower loads and tighter coupling coefficients result in a higher overall efficiencies. The output voltage and output power are largest at loose coupling coefficients and higher loads and decrease as the coupling coefficient increases and the load decreases. The agreement between the measured parameters with the calculations in Table 7.5 confirm that the Class E^2 converter can adapt to variations in load and distance in inductive

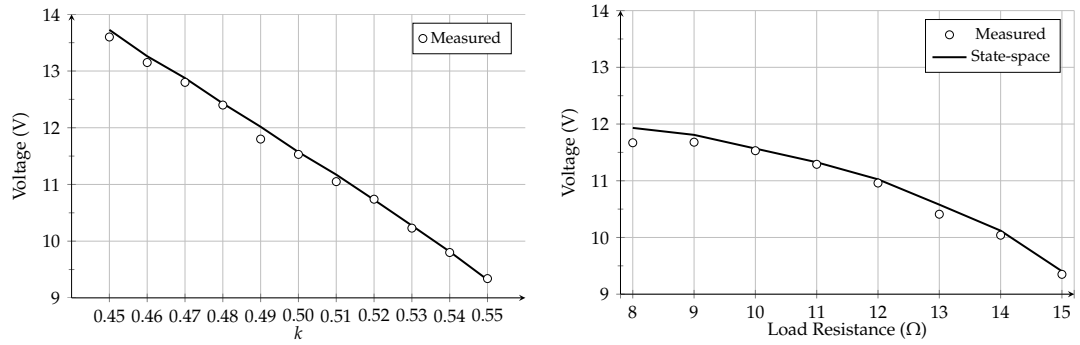

(a) Output voltage for a variable k

(b) Output voltage for a variable load

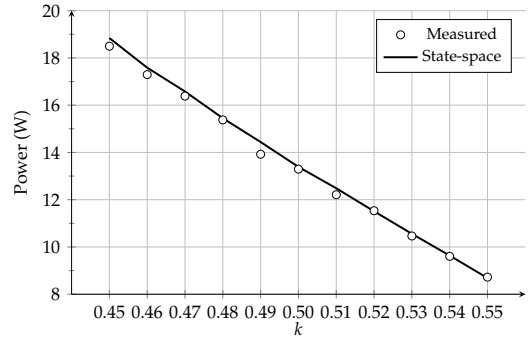

(c) Output power for a variable k

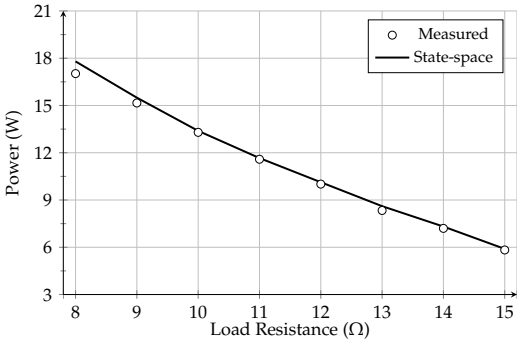

(d) Output power for a variable load

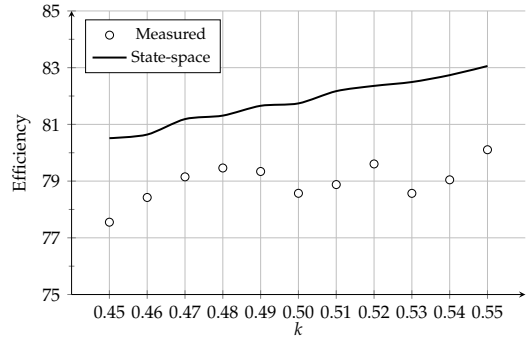

(e) Efficiency for a variable k

(f) Efficiency for a variable load

Fig. 7.11: Variation in coupling coefficient and load

links that may occur during operation. This is due to the result that the Class E inverter part of the converter can be tuned to achieve its optimum switching conditions by adjusting its duty cycle and switching frequency.

7.5 CONCLUSIONS

This chapter presented a Class E^2 converter to be used in IPT systems. The converter consists of a Class E ZVS and ZDVS inverter and a Class E ZVS low dv/dt rectifier. A 7th order piecewise linear state-space model has been used to model converter and the

inductive link including the ON resistance of the switches and the ESR of coils. The state-space model is used to calculate the values of the converter's components and parameters that will allow it to operate at optimum switching conditions. A compensation method is used to adapt for variations in the load and the distance between the coils by adjusting the switching frequency and the duty cycle of the switches.

The accuracy of the state-space model is compared to that of an analytical model. PSPICE simulations show the that calculations based on the state-space model satisfy the optimum switching conditions of the converter, whereas calculations derived from the analytical modelling approach do not completely satisfy the optimum switching conditions. Experimental results prove the accuracy of the state-space modelling approach and verify the compensation method for variations in load and distance between coils.

8

CONTROL AND VOLTAGE REGULATION IN DC/DC CONVERTERS

8.1 INTRODUCTION

The previous chapters focused on the design and optimization of Class E inverters and rectifiers. For the presented Class E inverters, it was assumed that their input voltage was constant. Whereas for Class E rectifiers, it was assumed that the load functions over a wide voltage range. Practically, the input voltage is not constant and DC loads can function only over narrow range of voltages. Therefore, input and output voltage regulation might be required. Referring to the overall diagram of an IPT system in Fig. 1.2, input voltage regulation of the Class E inverter can be achieved by powering it via a DC/DC converter. Whereas output voltage regulation of the Class E rectifier can be achieved by using a DC/DC converter connected between the load and the output of the Class E rectifier.

Using a DC/DC converter, especially at the input stage of the Class E inverter, not only results in a regulated voltage supply, but also allows it to be controlled and varied according to the operating conditions of the IPT system. Since variations in the distance between the coils of the inductive link are likely to occur, the input voltage to the Class E inverter may have to be adjusted in order to transfer a specific amount of power to the rectifier and the load. To regulate and control the output voltage of a DC/DC converter, a controller is required to continuously monitor the DC/DC converter's output voltage and/or current and modify the switching signal of the DC/DC converter's switches to counter for any variations and perturbations that may occur.

It was shown in Chapters four, five and six that Class E inverters and rectifiers are sensitive to load variations. Therefore the controller of the DC/DC converter should consider the dynamic behaviours and transient responses of the Class E inverter and the Class E rectifier. Although Class E inverters and rectifiers have been extensively

analysed, there appears to be little research on their dynamic behaviour and transient response. Consequently, deciding on which control method to implement may not be feasible. Several controllers might have to be individually implemented and tested in order to reach to a conclusion about which control methods can be suitable. Another issue that should be considered when choosing a certain controller, is the speed and bandwidth of the sensing and feedback circuit. Since Class E inverters and rectifiers can operate at frequencies exceeding 1 MHz, the choices of which feedback circuits and topologies that can be used efficiently and reliably are narrowed.

8.2 DESIGN REQUIREMENTS

Based on the previous introduction, the main aim of this chapter will be to introduce a controller for a synchronous buck DC/DC converter. The DC/DC converter can be used to provide a regulated and controlled voltage to a Class E inverter, or to regulate and control the output voltage of a Class E rectifier. Since the dynamic models of Class E inverters and rectifiers can be unknown or dependent on their operating conditions (as in the Class E inverter with finite DC-feed inductance), the controller must have the capability to operate independently of the dynamics of the DC/DC converter's load. In addition, the feedback network of the controller should be able to handle the high frequency operation of the Class E inverter and/or rectifier.

A certain method to create a controller that can function independently of the dynamics of the load is to set its control loop to operate at a specific frequency. In other words, the controller should reject all frequencies of disturbances and perturbations above a certain value. Therefore the loop gain of the controlled DC/DC converter will decline sharply at frequencies above a certain value. In this way, the dynamics of the load would not have any impact of the controller's operation. The controller that will be introduced in this chapter that implements the aforementioned control method, will be referred to as 'one-comparator counter-based controller'.

In the following sections, the one-comparator counter-based controller's principle of operation is described, the hardware components that form the controller are modelled. Mathematical analysis based on the describing function method will be performed and the equations that describe the amplitude and the frequency of the limit cycles as well as the transient response will be derived for several cases depending on the resolution of the counter, the pulse width modulation (PWM) generator and the clock frequency. The effect of resolution limitations of PWM generators and clock frequencies of digital counters, the values of passive components and the effect of the deadtime of MOSFET drivers on the limit cycles in the output voltage and the response time of the controller will be discussed. Simulation results will be presented

and the proposed controller's performance is assessed by comparing its performance with a linear analogue controller. Experimental results will be presented that show the performance and response of the prototype converter using the proposed controller under different loading conditions.

8.3 REVIEW OF CONTROL METHODS

Numerous control methods and techniques for DC/DC converters have been developed over the years and recently a trend towards digital-based control can be realised. Classical analog controllers that have been used for a few decades are now being replaced by digital controllers with enhanced performances. Due to the availability of design and simulation software, rapid prototyping tools and most importantly, the availability of powerful microprocessors and computers, new controllers that were not possible to implement previously are now being introduced. A literature survey conducted by Cortes [136] classified controllers for DC/DC converters into five groups; hysteresis controllers [137–141], linear controllers in their digital form such as voltage-mode [142] or current-mode controllers [143–146] and the classical PID controller [147–153], fuzzy-logic controllers [154–157], sliding-mode controllers [158–162], predictive controllers [163–169] and other advanced controllers [170, 171]. All of these controllers have been tested and demonstrated to provide precise control, excellent performance and robustness. However, the majority of these control techniques and methods are based on field programmable gate arrays (FPGAs) or require powerful microprocessors with a high computational capability in order to run smoothly and efficiently. This leads to an increase in the overall cost and greater system complexity as well as difficulties in implementation and manufacturing. Further design issues and limitations are highlighted in [172] and in [161] for sliding-mode controllers. As a result, the transition from analog-based to digital-based controllers in industrial and consumer applications for high power DC/DC converters has been slow and many manufacturers still use analog controllers for their simplicity, reliable performance and reduced implementation cost.

In digital based controllers, an analog-to-digital converter (ADC) is required to read the output voltage of a DC/DC converter and compare it with a reference voltage to generate an error signal. Obtaining a high performance digital controller requires a precision high sampling rate ADC and a processor or logic circuitry clocked at tens to hundreds of megahertz. For applications and loads that don't demand a high performance controller, using an ADC may not be the best design solution. In [173] and [174], a comparator is used in a digital controller for an ultra-low power buck converter instead of an ADC to provide the error signal. This drives an up/down digital counter representing the duty cycle of the PWM signal that controls the switches of the

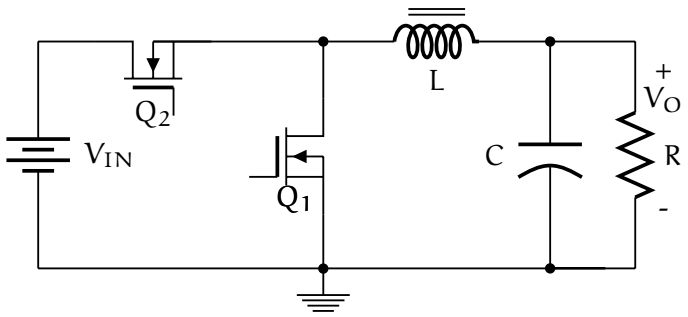

Fig. 8.1: Circuit diagram of a synchronous buck DC/DC Converter

buck converter. The output voltage of the converter will not settle at a steady voltage but instead enters a limit cycle about the desired level. Roh [175] further improved the controller by using a hysteresis or deadzone comparator to reduce the limit cycle in the output voltage. However, the controller was based on an ideal model of a buck converter and did not include the parasitic resistances of the converter's elements. The parasitic resistances should be considered and included in the DC/DC converter's model especially in high power converters as their influence on the converter's output and response is significant and cannot be ignored.

8.4 MODELLING AND ANALYSIS

8.4.1 *Large-signal Model of a Synchronous Buck DC/DC converter*

The circuit diagram of a synchronous buck DC/DC converter is shown in Fig. 8.1 and its small-signal low-frequency averaged model [176] obtained using the circuit-averaging method is shown in Fig. 8.2 [177]. The parasitic resistances are the equivalent series resistance of the inductor (r_L) and the equivalent series resistance of the capacitor (r_C). V_O is the output voltage of the converter, D is the duty cycle of the PWM driving signal to the MOSFETs and V_{IN} is the input voltage to the converter.

Assuming that MOSFETs Q_1 and Q_2 are identical, their ON resistances (r_{ON1} and r_{ON2}) are equal and the total resistance (r) in the inductor's branch is equal to

$$r = Dr_{ON1} + (1-D)r_{ON2} + r_L = r_{ON} + r_L. \tag{8.1}$$

The open loop control to output transfer function $G(s)$ including the parasitics and the resistance of the switches of the averaged model is:

$$G(s) = \frac{V_O(s)}{D(s)} = V_{IN}\frac{R(sCr_C+1)}{s^2LC(R+r_C)+s(C(r+r_C)+r_Cr)+L)+R+r}. \tag{8.2}$$

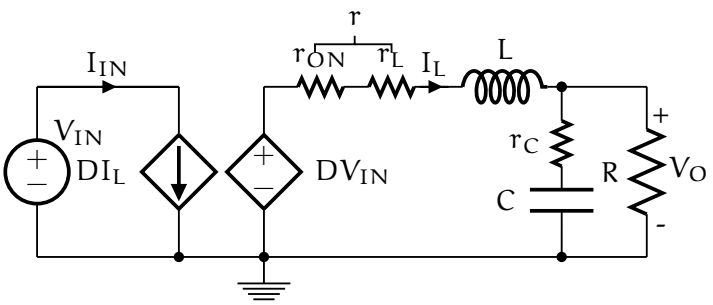

Fig. 8.2: Large-signal low-frequency model of a synchronous buck DC/DC Converter

The DC gain of $G(s)$ is:

$$G_{DC} = G(0) = V_{IN}\frac{R}{R+r} \tag{8.3}$$

and the angular undamped natural frequency is

$$\omega_n = \frac{1}{\sqrt{LC}}\sqrt{\frac{R+r}{R+r_C}} \tag{8.4}$$

and the damping factor is

$$\xi = \frac{C(r+r_C)+rr_C)+L}{2\sqrt{LC(R+r)(R+r_C)}} \tag{8.5}$$

The settling time calculated to 5% and the normalised peak overshoot are given by[178]

$$T_S \approx \begin{cases} \dfrac{3.2}{\xi\omega_n} & \text{if } \xi < 0.69 \\ \dfrac{4.5\xi}{\omega_n} & \text{if } \xi > 0.69 \end{cases} \tag{8.6}$$

$$M_{Peak} = e^{\left(\frac{-\pi\xi}{\sqrt{1-\xi^2}}\right)}. \tag{8.7}$$

8.4.2 *One-comparator Counter-based Control*

The block diagram of the proposed controller is shown in Fig. 8.3. The comparator will provide a positive output if the output voltage of the converter is below the reference voltage and a negative output if the output voltage is above the reference voltage. Depending on the output of the comparator, the counter will count up when the output of the comparator is positive, which will cause the duty cycle to increase leading the output voltage to rise towards the reference voltage. The counter will count down when the output of the comparator is negative causing the duty cycle to decrease,

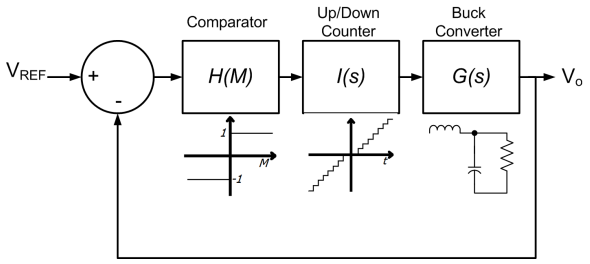

Fig. 8.3: Block diagram of the system

which leads the output voltage to decline to the reference voltage. For each count, the counter either increments or decrements the duty cycle by a minimum step and the clock of the counter sets the time interval between counts. Therefore the counter functions as an integrator and can be modelled as [173]

$$I(s) = \frac{k}{s} \tag{8.8}$$

where k is the gain of the integrator which is equivalent to the rise rate or "slew rate" of the counter and is equal to

$$k = \frac{\Delta D}{\Delta T_C} \tag{8.9}$$

and ΔD is the minimum change in duty cycle for an increment or decrement in the digital up/down counter or simply the resolution of the digital up/down counter and ΔT_C is the period of the digital counter's clock.

The proposed controller incorporates two nonlinear elements; a comparator and a counter. Consequently, the system is expected to support limit cycles and the output of the converter will oscillate around the reference voltage value. Therefore it is of interest to determine the stability of the limit cycles and their effect on the performance of the controller and the converter. A method used to analyse nonlinear systems is the describing function method [179]. It is an approximate method that can produce good results if the system under consideration is low-pass in nature [180]. Based on the resolution of the digital up/down counter ΔD, and the period of the digital counter's clock ΔT_C, three operating cases can be defined

- Case I

The counter has a constant rise rate, i.e. its output increases and decreases linearly with time. The counter can be said to have an infinite resolution and an infinite clock frequency. This case can be represented as

$$\Delta D \to dD \tag{8.10}$$

$$\Delta T_C \to dt. \tag{8.11}$$

The counter can be represented as a linear block and the only nonlinear element in this case is the comparator. The describing function of a comparator is obtained by observing the waveforms of its input and output signal. The output of the comparator is a square wave and since $I(s)$ and $G(s)$ act as low-pass filters, the output can be approximated by the its first Fourier coefficient at the fundamental frequency. The describing function for a comparator $H_C(M)$ for a sinusoidal input signal is [179]

$$H_C(M) = \frac{4}{\pi M} \qquad |M| > 0 \tag{8.12}$$

where M is the amplitude of the sinusoidal input signal to the comparator.

The limit cycle's frequency and amplitude can be determined by examining the characteristic equation $1 + H_C(M)I(j\omega)G(j\omega) = 0$, thus

$$-j\omega^3 - \omega^2 \frac{C(R(r+r_C)+rr_C)+L}{LC(R+rc)} + j\omega \frac{R+r+H_C k V_{IN} R C r_C}{LC(R+r_C)} + \frac{H_C k V_{IN} R}{LC(R+r_C)} = 0 \tag{8.13}$$

which can be written as

$$-a_3 j\omega^3 - a_2\omega^2 + a_1 j\omega + a_0 = 0. \tag{8.14}$$

The frequency f of the limit cycle is determined by setting the imaginary terms in (8.14) to zero

$$f = \frac{\sqrt{a_1}}{2\pi} = \frac{1}{2\pi\sqrt{LC}} \sqrt{\frac{R+r+\dfrac{4kV_{IN}RCr_C}{\pi M}}{R+r_C}}. \tag{8.15}$$

Equation (8.15) shows that the frequency is not only a function of the capacitance, inductance and the parasitic resistances of the converter but also a function of the input voltage, the output load and the amplitude of the output voltage oscillation M. The maximum value of M is obtained by substituting (8.15) in (8.14) and solving for M

$$M = \frac{4kRV_{IN}(1-a_2Cr_C)}{a_2\pi(R+r)}. \tag{8.16}$$

- Case II

In this case the counter has finite resolution and clock frequency is limited. Therefore the counter's output will appear as steps with a duration equal to the clock period. It is assumed that the counter has a very high resolution and that clock period is much smaller than the settling time of the DC/DC converter. The counter in this case can still be modelled as an integrator according to (8.8), however it is now followed by a quantizer block with a quantization interval equal to the resolution of the PWM

generator Δ_P. The resolution of the PWM generator Δ_P is generally equal or smaller than ΔD, therefore in this case

$$\Delta T_C \ll T_S \tag{8.17}$$

$$\Delta D \geqslant \Delta_P. \tag{8.18}$$

The comparator and quantizer constitute a system with two nonlinearities separated by a first order linear block as shown in Fig. 8.4. Due to the integrator, the describing functions to be derived are expected to not only be a function of the amplitude of their input signals, but also of their frequency.

Analysis of the system in this case may not be feasible due to the increased complexity of the describing function. However, the system can be solved and the describing function can be simplified for a particular operating mode of the controller. Consider the operation of the controller at a steady state. For the output to be bounded, the output of the comparator will continuously be switched between 1 and -1. Therefore the number of states that the counter and the PWM generator increments can be assumed to be equal to the number of states that are decremented, i.e

$$m_H \Delta D_{H_C=+1} = m_L \Delta D_{H_C=-1} = m\Delta D \tag{8.19}$$

where m_H and m_L are the number of states the counter is incremented and decremented when the comparator's output is $+1$ and -1 respectively. The number of states that the PWM generator increments or decrements are proportional to the number of states of the counter:

$$m\Delta D = n\Delta_P. \tag{8.20}$$

Therefore the describing function of the quantizer H_Q is

$$H_Q(N) = \begin{cases} \frac{\Delta_P}{2}\frac{4}{\pi N} & |N| \leqslant \frac{\Delta_P}{2} \\ \frac{\Delta_P}{2}\frac{4}{\pi N}\left(1+\sqrt{1-\left(\frac{\Delta_P}{N}\right)^2}\right) & \frac{\Delta_P}{2} \leqslant |N| \leqslant 2\frac{\Delta_P}{2} \\ \vdots & \vdots \\ \frac{\Delta_P}{2}\frac{4}{\pi N}\left(1+n\sqrt{1-\left(\frac{\Delta_P}{N}\right)^2}\right) & (n-1)\frac{\Delta_P}{2} \leqslant |N| \leqslant n\frac{\Delta_P}{2} \end{cases} \tag{8.21}$$

where N is the amplitude of the input signal to the quantizer.

The waveforms of the outputs of the comparator, the integrator and the quantizer are shown in Fig. 8.5. The output of the comparator will be a square wave that switches between the values $+1$ and -1 according to the polarity of M. Since the input signal to the integrator is a square wave, then its output will be a triangular wave with an

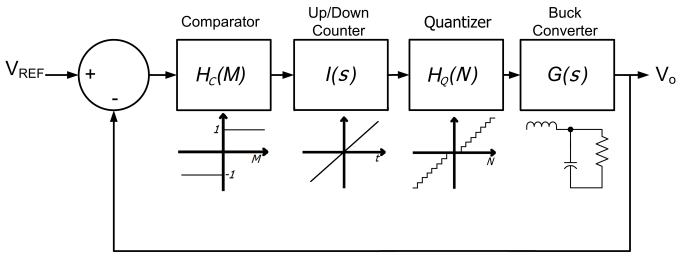

Fig. 8.4: Block diagram of the system including a quantizer

amplitude proportional to k/ω. Therefore, by taking the first Fourier coefficients of the integrator's output and input signals, the describing function of the integrator H_I is

$$H_I(j\omega) = \frac{8k/j\omega\pi^2}{4/\pi} = \frac{2}{\pi}\frac{k}{j\omega} \tag{8.22}$$

and N is given by

$$N = \frac{k}{\omega}\frac{8}{\pi^2}. \tag{8.23}$$

If a small value of k is chosen such that (8.23) is bounded between $-\Delta_P/2$ and $\Delta_P/2$, then substituting (8.23) in (8.21) results in

$$H_Q = \frac{\Delta_P \pi\omega}{4k}. \tag{8.24}$$

Consequently the overall describing function of Fig. 8.4 is given as

$$H_O(M, N, j\omega) = H_C(M)H_I(j\omega)H_Q(N). \tag{8.25}$$

Substituting (8.12), (8.22) and (8.24) in (8.25), the overall describing function at steady-state is

$$H_O(M) = \frac{2\Delta_P}{j\pi M}. \tag{8.26}$$

Equation (8.26) shows that the overall describing function is simply a relay with a phase shift of -90°. The amplitude and the frequency of the limit cycle can now be found by solving the characteristic equation $1 + H_O(M)G(j\omega) = 0$, thus

$$-j\omega^2 - \omega\frac{C(R(r+r_C)+rr_C)+L}{LC(R+r_C)} + j\frac{R+r}{LC(R+r_C)} + j\omega\frac{|H_O|VRCr_C}{LC(R+r_C)} + \frac{|H_O|VR}{LC(R+r_C)} = 0. \tag{8.27}$$

By setting the real and imaginary parts equal to zero, the amplitude and the frequency of the limit cycle are

$$f = \frac{\Delta_P V_{IN} R}{\pi^2 M(C(R(r+r_C)+rr_C)+L)} \tag{8.28}$$

$$M = \frac{2\Delta_P V_{IN} R}{\pi\sqrt{\dfrac{(C(R(r+r_C)+rr_C)+L)^2(R+r)}{LC(R+r_C) - Cr_C(C(R(r+r_C)+rr_C)+L)}}}. \tag{8.29}$$

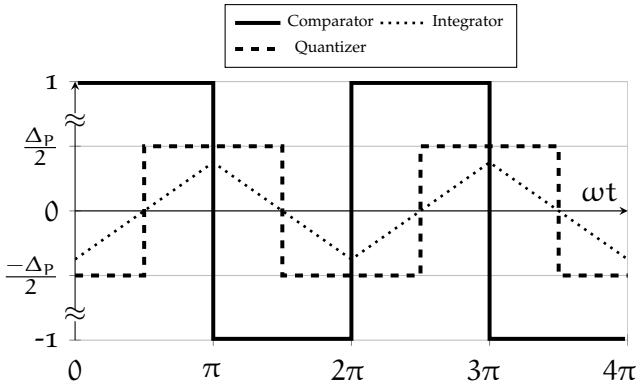

Fig. 8.5: The output waveforms of the comparator, integrator and quantizer blocks

- Case III

This is similar to Case II, however the clock is equal to or larger than half the settling time of the converter and the resolution of the counter is equal to the resolution of the PWM generator, i.e

$$\Delta T_C \geqslant \frac{T_S}{2} \tag{8.30}$$

$$\Delta D = \Delta_P. \tag{8.31}$$

Since the output voltage of the converter reaches a steady value before the duty cycle is changed, this case resembles the step response of the converter to a sequence of positive and negative step changes in the duty cycle of the PWM signal. Therefore, the output of the converter is expected to alternate between two consecutive states of the counter. Though the limit cycle may not be sinusoidal, the peak-to-peak voltage of the limit cycle can be calculated as

$$M_{PP} = \Delta_P(G_{DC} + V_{IN}M_{Peak}) = \Delta_P V_{IN}\left(\frac{R}{R+r} + 2M_{Peak}\right) \tag{8.32}$$

and the period is equal to

$$T_O = 2T_C. \tag{8.33}$$

Equations (8.16), (8.29) and (8.32) show that the amplitude of the limit cycles is a function of the input voltage V_{IN}. The input voltage affects the amplitude through the resolution of the up/down counter ΔD for Case I as well as the PWM generator for Case II and Case III. Since the up/down counter that represents the duty cycle of the PWM signal needs to allow the converter to generate an output voltage that is proportional to the input voltage, then increasing the input voltage would mean that the voltage gap or window between two consecutive finite states of the up/down counter would increase. This eventually leads the output voltage to swing at higher voltages and therefore increasing the amplitude of the limit cycle. This is analogous

to the quantization error in ADCs where the voltage error due to the least significant bit (LSB) is proportionally related to the voltage difference between the two reference voltages of the ADC. If the voltage difference is increased, then a higher amplitude signal is required to switch between the finite states of the ADC. The output capacitor of the converter also affects the amplitude of the limit cycle. Since the frequency of the limit cycle is generally much lower than the switching frequency, a large capacitor may be required to further dampen the limit cycles and reduce their amplitudes.

The gain k also affects the amplitude of the limit cycle, reducing the gain would reduce its amplitude. According to (8.9), increasing the resolution of the up/down counter (lowering ΔD) would allow more output voltage levels to be achieved for a given input voltage and thus the output voltage would swing between smaller voltage windows. Decreasing the counter's clock frequency (increasing ΔT_C) or slowing down the control loop might initially seem to contradict the common practice or belief that increasing the sampling rate of a controller will improve its accuracy and performance. A higher clock frequency will cause the counter to count faster increasing the number of states that the duty cycle is incremented and therefore increasing the output voltage of the converter. The only benefit of increasing the clock frequency is the improvement of the controller's response time to any sudden changes in the load current or in the input voltage. Therefore a tradeoff has to be made between the amplitude of the limit cycles and the response time of the controller.

8.4.3 *Transient Analysis*

In order to investigate the performance of the controller during a change in the load current, the output impedance of the synchronous buck converter has to be derived. By setting V_{IN} and D in Fig. 8.2 to zero and applying a voltage source to the output of the converter as shown in Fig. 8.6, the output impedance is equal to

$$Z_O(s) = \frac{V_O(s)}{I_O(s)} = \frac{R_{NL}(sL + r)(sCr_C + 1)}{s^2LC(R_{NL} + r_C) + s(C(R_{NL}r + rr_C) + L) + R_{NL} + r} \tag{8.34}$$

where R_{NL} is the minimum load value that is connected to the converter. For a step change in the output current at $t = 0$, the transient component of the output voltage of the converter is given by

$$v_o(s) = -I_O(s)Z_O(s) = \frac{-\Delta I}{s} Z_O(s). \tag{8.35}$$

Since MOSFETS Q_1 and Q_2 a driven in a complementary manner, a certain deadtime is required practically to avoid possible cross-conduction between the two MOSFETs. The deadtime (T_{DT}) causes a reduction in the output voltage of the converter equal to

$$\Delta V_O = V_{DT} = T_{DT} f_S V_{IN}. \tag{8.36}$$

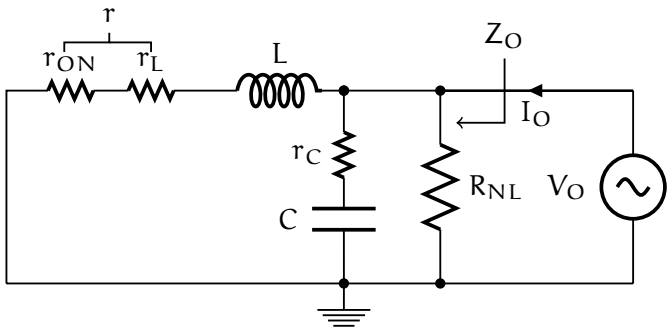

Fig. 8.6: Calculating the output impedance of a synchronous buck DC/DC converter

Synchronous buck converters always operate in continuous conduction mode (CCM). However at light loads or standby modes efficiency is reduced since MOSFET Q_1 conducts, therefore power supplied by the source will be mainly dissipated as conduction losses. To avoid these losses, synchronous buck converters are often operated in discontinuous conduction mode (DCM) by disabling MOSFET Q_1 if the output current is low enough to cause the inductor's current to become zero or negative before MOSFET Q_1 switches ON. Consequently the output of the synchronous buck converter with deadtime control can be written as

$$V_O(t) = V_O(0^-) + v_o(t) - V_{DT}. \tag{8.37}$$

During a step change in the output current, the output voltage of the converter will drop below the reference voltage. Consequently the comparator's output will remain positive (+1) causing the counter and the duty cycle to increment continuously until the output voltage reaches the reference value. For Cases II and III, this period can be considered as a finite sequence of step increments in the duty cycle, therefore the output voltage of the converter is equal to the sum of the step responses due to the increments in the duty cycle. Equation (8.35) becomes

$$v_o(s) = \frac{-\Delta I}{s} Z_O(s) + \sum_{n=0}^{P} \frac{\Delta_P}{s} G_{LD}(s) e^{-P\Delta T_C s} \tag{8.38}$$

where G_{LD} is the control to output transfer function for a loaded converter, i.e

$$R = R_{LD} = \frac{V_O(0^-) - V_{DT} + \lim\limits_{s\to 0} s(I_O(s)Z_O(s))}{\lim\limits_{s\to 0} -sI_O(s)} \tag{8.39}$$

and P is the number of states that the counter has to be incremented in order for the output voltage to reach V_{Ref}

$$P = \frac{V_{DT} + \lim\limits_{s\to 0} s(I_O(s)Z_O(s))}{\Delta_P V_{IN}}. \tag{8.40}$$

Table 8.1: Synchronous buck DC/DC converter operating values and calculated parameters

Parameter	Value	Parameter	Value
L	100μH	r_L	0.165Ω
C	2200μF	r_C	0.022Ω
R_{NL}/R_{LD}	1kΩ/4Ω	r_{ON}	0.024Ω
I_O	3A	f_S	50 kHz
V_{IN}	20V	V_{Ref}	12V
V_{DT}	1V	ξ	0.50
T_S	30.0ms	M_{Peak}	16.29%

Therefore, the total response at $t = 0$ is

$$V_O(t) = V_O(0^-) - V_{DT} + \mathscr{L}^{-1}\left\{\frac{-I}{s}Z_O(s)\right\} + \sum_{n=0}^{P}\mathscr{L}^{-1}\left\{\frac{\Delta_P}{s}G_{LD}(s)e^{-P\Delta T_C s}\right\}. \tag{8.41}$$

8.5 IMPLEMENTATION AND PERFORMANCE ASSESSMENT

A simulation model based on the block diagrams shown in Fig. 8.3 and Fig. 8.4 was constructed in MATLAB/Simulink for a synchronous buck DC/DC converter with parameters shown in Table 8.1. The simulation model is shown in Fig. 8.7. The three cases of the proposed controller described in Section 8.4.2 were simulated with parameters shown in Table 8.2. Fig. 8.8 shows the simulated response of the output voltage of the converter to a step increment and decrement in the PWM generator according to the transfer function in Eq. 8.2. The simulated response is verified by experimental results. Fig. 8.9 shows the output voltage at a load current of 3A for the three cases. Case I represents an ideal operation of the controller where the resolution of the counter and the PWM generator are infinite and the clock frequency is several orders of magnitude higher than the switching frequency. For Case II the counter and the PWM generator are assumed to have a resolution of 12 bits and 8 bits respectively and the clock frequency is 2^{-14}Hz creating an integrator with a gain of 4. For Case III the resolution for both the counter and the PWM generator is 8 bits and the clock period is two thirds of the loaded settling time of the converter (2^{-9})ms, therefore the gain of the integrator is 2.

Table 8.2: Controller parameters

Parameter	Case I	Case II	Case III
Δ_P	~ 0	$\frac{1}{2^8}$	$\frac{1}{2^8}$
ΔD	~ 0	$\frac{1}{2^{12}}$	$\frac{1}{2^8}$
ΔT_C	~ 0	$\frac{1}{2^{14}}$ s	$\frac{1}{2^9}$ s
k	2	4	2

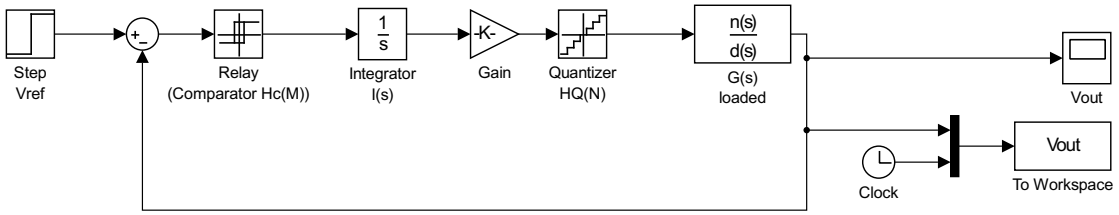

Fig. 8.7: Simulink Model of the proposed controller

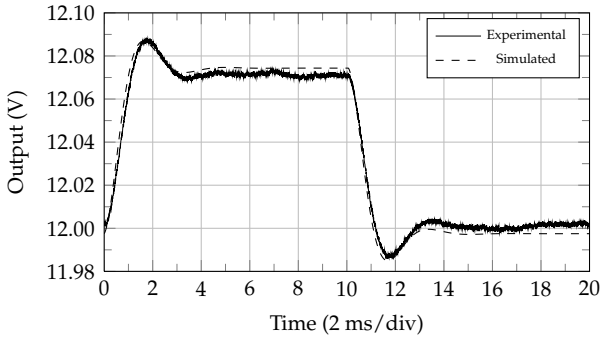

Fig. 8.8: Step response of the converter's output voltage due to an increment and decrement in the PWM generator

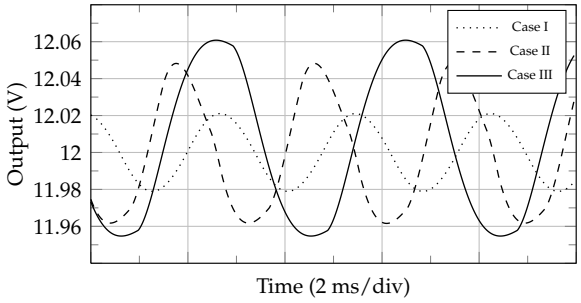

Fig. 8.9: Simulated output voltages for Cases I, II and III

It can be noticed that the amplitude of the limit cycles in Case II and III is larger than that of Case I due to the nonlinearity and the quantization effect of the PWM generator. In addition, the output voltage waveforms contain more harmonics. The

Table 8.3: Comparison between the simulated and calculated limit cycle magnitudes and frequencies

Case	M (mV)			f (Hz)		
	Calc.	**Sim.**	**Err.**	**Calc.**	**Sim.**	**Err.**
I	21.20	21.05	0.71%	361.01	358.72	−0.63%
II	46.34	43.23	−6.71%	360.94	351.07	−2.73%
III	102.4*	106.06*	3.45%	256	256.2	0.08%

*Peak to peak

amplitude of the limit cycles of Case II is lower than of Case III due to the increased resolution of the counter, the frequency of the limit cycles is higher since the counter is operating at a higher clock speed. Table 8.3 compares the amplitude and frequency of the simulated limit cycles to that of the calculated using the describing function method. The calculated limit cycle amplitudes and frequencies are not expected to match exactly the simulations due to the errors that result from linearisation by the describing functions. The error is larger in Case II compared to Case I since the comparator and the quantizer are linearised by their describing functions, whereas the only linearised element in Case I is the comparator.

The simulated transient response of the converter and the controller is shown in Fig. 8.10 for Cases II and III. The output current of the converter is initially close to zero Amperes. A step change of 3A occurs at $t = 0$ in the load's current. The output voltage of the converter begins to decrease below V_{Ref} and then the controller increments the duty cycle 19 times according to Eq. 8.40. The effect of the deadtime of the MOSFET driver is modelled as a constant voltage drop. The controller's response time for Case II is twice as fast of Case III due to the increase in the gain of the integrator by a factor of 2. For comparison, the response of a third-order integral-double-lead controller, also known as a Type III compensation controller is shown. The Type III compensation controller was designed to ensure a stable output with a reasonable response time while taking into account practical considerations such as the compensator's components values and the response time of the MOSFET driver. The output voltage of the converter using the Type III compensation controller results in a lower voltage drop due to a step change in the load current compared to the proposed controller. However the Type III compensator requires a high bandwidth error amplifier and six additional components and is difficult to design, whereas the proposed controller consists of only a comparator and a counter. Figs. 8.11 and 8.12 shows the Simulink simulation model in for the transient response and the Type III compensation controller respectively.

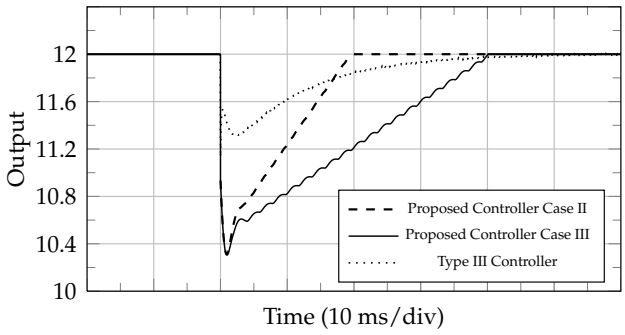

Fig. 8.10: Simulated transient response for a step change in load current from 0 to 3A at t = 0

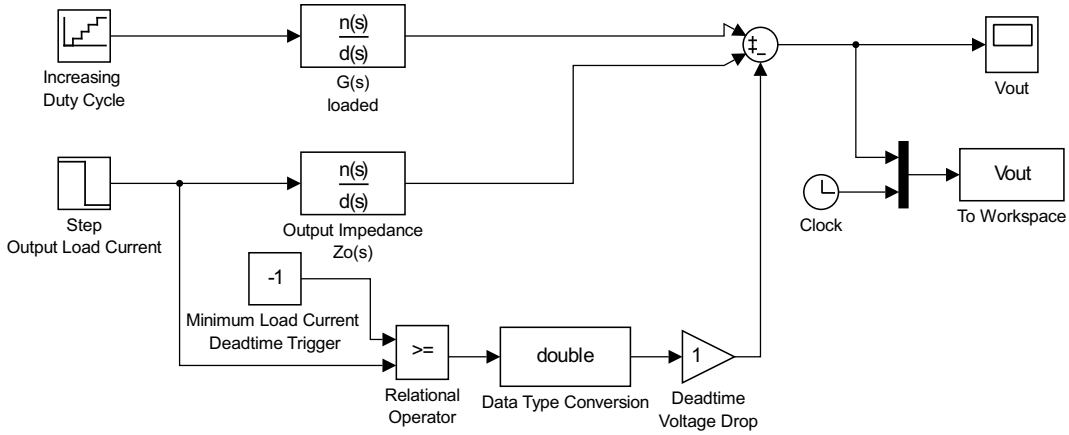

Fig. 8.11: Simulink Model of the transient response

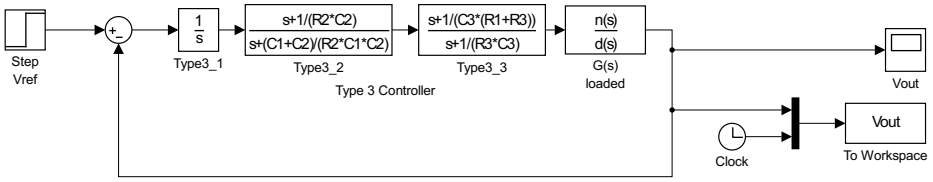

Fig. 8.12: Simulink Model of the type 3 controller

8.6 RESULTS AND DISCUSSION

The proposed controller, set to operate in Cases II and III, was applied to the prototyped synchronous buck DC/DC converter with the operating conditions shown in Tables 8.1 and 8.2. The implemented system block diagram is shown in Fig. 8.13 and picture of the system is shown in Fig. 8.14. The counter is based on 74LS191 4 bit up/down counters. For Case II, three counters were cascaded producing a 12 bit up-/down counter, whereas for Case III two counters were cascaded producing a 8 bit up/down counter. An 8 bit digital-to-analog converter TLC7524 which represents the PWM modulator in Fig. 8.4 is used to convert the up/down counter's output to a voltage signal. The voltage signal is compared against a sawtooth signal and a PWM

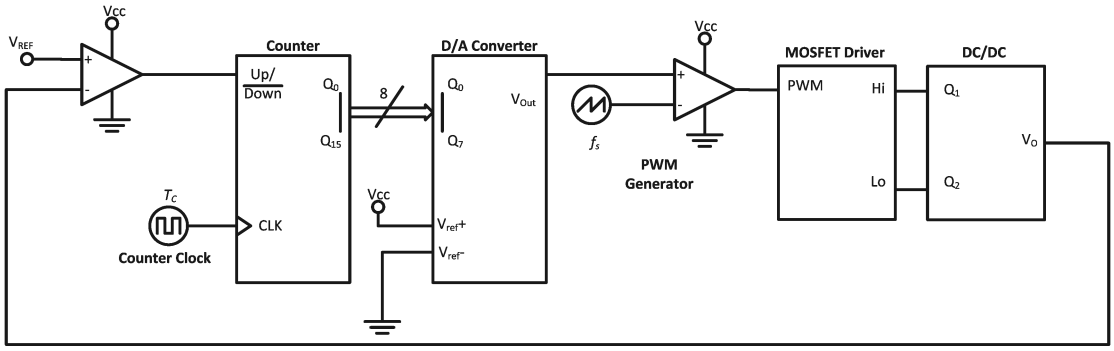

Fig. 8.13: Implemented system architecture

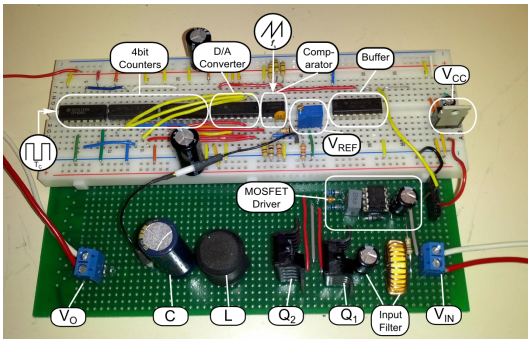

Fig. 8.14: Picture of the implemented synchronous buck DC/DC converter and the proposed controller

signal is generated. A constant current electronic load was connected to the output of the DC/DC converter to simulate different loading conditions.

Figs. 8.15 and 8.16 show the DC/DC converter's output voltage waveforms and the comparator's output at a load current of 3A for Cases II and III respectively. The observed limit cycles in the output voltages confirm the description of the controller's principle of operation. The comparator's output is high if the output voltage is below the reference value setting the counter to count upwards and the duty cycle is increased. As the output voltage exceeds the reference value, the comparator's output is low setting the counter to count downwards reducing the duty cycle untill the output voltage is below the reference value and the system enters a limit cycle state. The observed amplitudes and frequencies of the limit cycles for Cases II and III are compared to the calculated values in Table 8.4.

The observed transient response of the controller for Cases II and III is shown in Figs. 8.17 and 8.18 respectively for a step change in the load current from 0A to 3A. For both cases the output voltage decreases rapidly due to the load current in addition to the voltage drop due to the deadtime of the MOSFET driver. During the transition period the system exits the limit cycle state and the comparator's output remains high

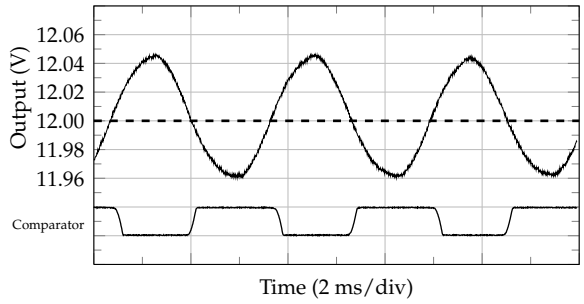

Fig. 8.15: Output voltage of the converter and the comparator's state of the controller operating in Case II

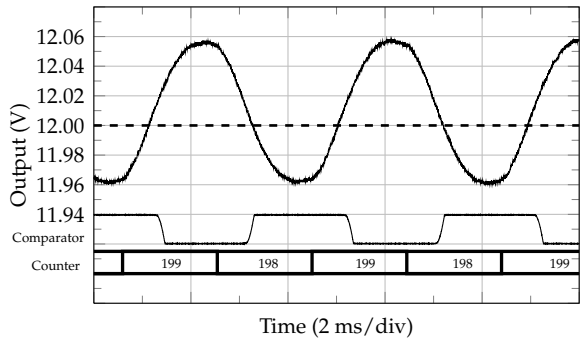

Fig. 8.16: Output voltage of the converter and the comparator's state of the controller operating in Case III

Table 8.4: Comparison between the measured and calculated limit cycle magnitudes and frequencies

Case	M **(mV)**			f **(Hz)**		
	Calc.	**Exp.**	**Err.**	**Calc.**	**Exp.**	**Err.**
II	46.34	42.50	−8.29%	360.94	312.5	13.42%
III	102.4*	96.00*	−6.25%	256	256	0.00%

*Peak to peak

setting the counter to count upwards. The duty cycle is continuously incremented until the output voltage reaches the reference value of 12V and the system returns to its limit cycle state. For Case III the duty cycle is incremented 18 times. As predicted, the response time for the controller operating in Case II is faster than that of Case III due to the increased resolution of the counter and the higher clock speed of the counter. The observed steady-state and transient responses are in good agreement with simulated responses.

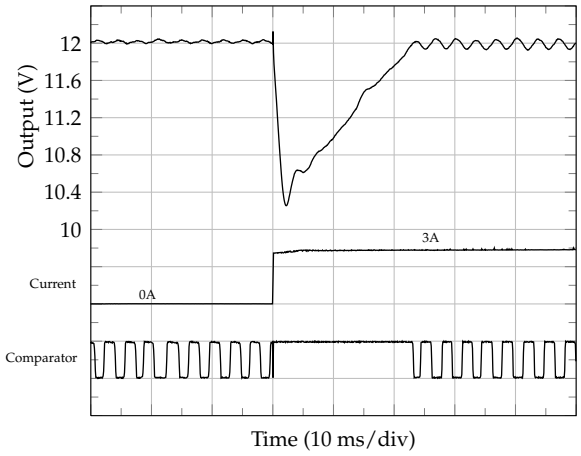

Fig. 8.17: Observed transient response for a step change in load current from 0 to 3A for Case II

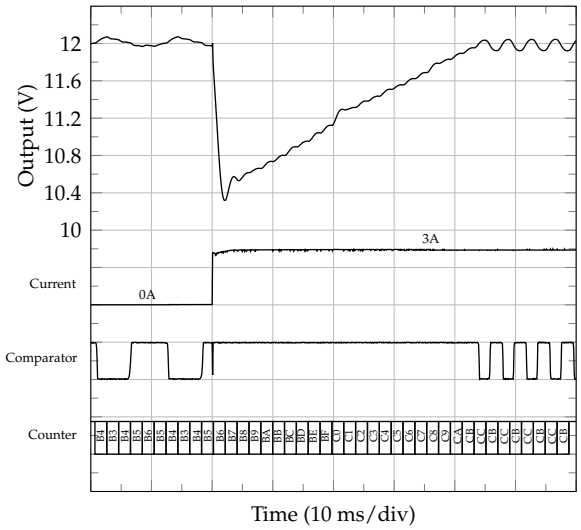

Fig. 8.18: Observed transient response for a step change in load current from 0 to 3A for Case III

8.7 CONCLUSIONS

A digital controller based on a single comparator and a digital counter is proposed for synchronous buck DC/DC converters. The controller functions independently of the dynamics of the load. The controller features a simple design and low component count which allows it to be easily implemented and manufactured as well as reducing the overall cost of DC/DC converters. Not including an ADC eliminates the need to use fast processors and makes the controller suitable for a wide range of switching frequencies since the control loop is now no longer limited by the ADC's sampling rate. Simulations constructed in MATLAB Simulink and experimental results verify the converter's model and the derived limit cycle frequency and amplitude equations. It was shown that the limit cycles introduced by the proposed control scheme are

not deleterious. Further experimental results based on a synchronous buck DC/DC converter prototype show the controller's response capability for large step changes in the output load which indicate the suitability of this controller for applications with variable power demands and load transitions.

9

CONCLUSIONS AND FUTURE WORK

The final chapter concludes this thesis. It begins by summarising the work done in this research project and outlines the outcomes and findings. A discussion on how the aims and objectives are met is presented. An overall conclusion is given and the chapter ends with suggestions and recommendations for future work.

9.1 REVIEW AND CONCLUSIONS

Wireless power transfer via magnetic induction, or IPT technology has come a long way since it was conceptualized two decades ago. It has become more efficient, more applicable to today's applications and smarter. The work presented in this thesis was directed towards pushing IPT technology to the next level. The work has presented solutions to several problems and issues that have not been addressed in previous work.

9.1.1 *Inductive Links*

The principle of operation of inductive links from a circuit point of view. It was shown that by operating the inductive link at its resonant frequency, its reflected impedance is maximised. This results in a more efficient operation of the primary coil driver since it can operate at reduced current stresses. The choice of using a parallel resonant secondary coil configuration or a series resonant coil configuration depends on the load value and the power transfer distance. A parallel resonant secondary coil configuration is used if the load resistance is much larger than the impedance of the secondary coil and for large transfer distances. Whereas a series resonant secondary coil configuration is used if the load resistance is much smaller the impedance of the coil and for shorter transfer distances. It was also shown how the reflected impedance

of the secondary coil circuitry of the inductive link can be represented as a sum of several reflected resistances and reactances. Each reflected resistance and reactance corresponds to a certain element or parameter of the secondary coil circuitry. This can lead to a better understanding of how the power received in the secondary coil is distributed amongst its elements. A design example was given in Chapter 3 for an inductive link with a parallel resonant secondary configuration.

9.1.2 *Modelling and Analysis of Class E DC/AC Inverters in Inductive Links*

According to the first and second objectives, Chapter 4 presented the different configurations of Class D and Class E DC/AC inverters that are commonly used as primary coil drivers. Class D inverters can operate efficiently over a wider load range and have lower voltage and current stresses. Certain configurations of the Class D inverter, such as the full-bridge Class D ZVS inverter, can operate at power levels that can reach up to 20 kW. Class E inverters can operate efficiently over a lower load range and have higher voltage and current stresses. However, they are simpler to construct and have a high power-output capability. Therefore, Class E inverters are more compact and have a higher power density than Class D inverters. Although both Class D and Class E inverters have a theoretical efficiency of 100 %, practical efficiencies are less since it can be difficult to ensure that they operate at their optimum switching conditions, especially at switching frequencies above 500 kHz.

An investigation of the performance of a Class E ZVS and ZVDS DC/AC inverter as a primary coil driver was performed in Chapter 5. A detailed analysis was presented which was initially based on an analytical analysis approach and then on a more detailed state-space representation approach. It was shown that the Class E inverter would operate at optimum switching conditions for a specific coupling coefficient value and a specific load value. An increase in either the distance (or coupling coefficient) of the inductive link or the load would lead the Class E inverter to operate in sub-optimum switching conditions. The operation in sub-optimum switching conditions can degrade the efficiency of the inverter since voltage and current stresses are increased. Whereas a decrease in the distance (or coupling coefficient) or the load would lead the Class E inverter to operate in non-optimum switching conditions. Operating in non-optimum switching condition is highly unrecommended since permanent damage may occur in the switching element.

9.1.3 *Electronic Tuning Methods for Class E DC/AC Inverters*

Based on the preformed investigation of Class E inverters in inductive links, several novel tuning methods were presented in Chapter 5. The tuning methods will allow the Class E inverter to be tuned to operate at optimum switching conditions as variations in the distance between the coils or the load that might occur during operation. A tuning method was suggested for each configuration of the Class E inverter. Each tuning method requires two values or parameters to be controlled. For the Class E inverter with infinite DC-feed inductance, the switching frequency and the value of the switch's shunt capacitor were controlled. Whereas for the Class E inverter with finite DC-feed inductance, the values of the DC-feed inductance and switching frequency were controlled in one method, and the DC-feed inductance and the duty cycle of the switching signal were controlled in another method. A novel use of saturable reactors (magnetic amplifiers) was shown to provide electronic control of all the tuning methods. All of the tuning methods were experimentally implemented and successfully validated. Therefore the third objective of this research was successfully met.

9.1.4 *Class D and Class E Rectifiers*

According to the second objective, Chapter 6 discussed a unaddressed topic about the classes and configurations of rectifiers that can be used in inductive links. It was shown that in all recent publications regarding IPT systems, traditional rectifiers, such as half-wave and bridge rectifiers, have been the only rectifiers used. It was also shown how the traditional rectifiers may not be suitable in resonant inductive links since their input currents contains a large number of harmonics. These harmonics will prevent resonance operation and will lead the primary coil driver to operate at non-optimum switching conditions. Therefore, Class D and Class E rectifiers were suggested as alternatives to the traditional rectifiers. Class D and Class E rectifiers are the dual of Class D and Class E inverters respectively, therefore their compatibility to be used along with either a Class D or Class E primary coil driver and a resonant inductive link is ensured.

Class D rectifiers were discussed, their principle of operation was described and a detailed analysis was presented. Class E rectifiers were modelled and mathematically analysed in great detail. Both Class D and Class E rectifiers can have a near sinusoidal input current with minimum harmonic content. A half-wave Class D voltage-switching rectifier was implemented. A Class E ZVS low dv/dt rectifier was also implemented to highlight the advantages of Class E rectifiers and an impressive ef-

ficiency of 94 % was achieved at a frequency of 800 kHz. Both Class D and Class E rectifiers were used for the first time in this research.

9.1.5 *Class E^2 DC/DC Converters*

Referring to the second objective of this research, a Class E^2 DC/DC converter was introduced for IPT systems in Chapter 7. The converter consists of a Class E ZVS and ZDVS inverter and a Class E ZVS low dv/dt rectifier separated by an inductive link. The benefit of using a Class E^2 converter is that it simplifies the modelling and analysis of the entire IPT system since the IPT system can be now represented as a single circuit. This leads to a better understanding on how all of the elements and parameters of the IPT system interact with each other. A seventh order piece-wise linear state-space representation was used to analyse the system and to calculate the parameters and values of the converter. The accuracy of the analysis was compared to a common analytical analysis method and PSPICE simulation results verified the improved accuracy. In addition, certain parameters, such as the phase difference between the two switching elements, were calculated for the first time since the Class E^2 DC/DC converter was introduced in 1989.

9.1.6 *Control for DC/DC Converters in IPT Systems*

As mentioned in fourth and final objective, a new controller referred to as 'one-comparator counter-based controller' was introduced in Chapter 8. The controller's purpose is to regulate the output voltage of a synchronous buck DC/DC converter. A DC/DC converter may be required to provide a regulated and controllable input voltage to the primary coil driver. Another DC/DC converter may be required at the output of the rectifier to provide a regulated and controllable voltage to the load. The dynamics of the primary coil driver and the rectifier may be unknown, therefore the proposed controller functions regardless of the DC/DC converter's load dynamics. This was achieved by maximising the gain of the control loop for a single frequency and minimising all other frequencies.

9.2 FUTURE WORK

The research and development in IPT technology has brought several new applications and products to the market such as wireless charging for mobile phones and vehicles.

Several standards have been introduced for wireless charging such as the Wireless Power Consortium and the Alliance for Wireless Power. The current research and development is starting to move towards the next generation of IPT technology; pushing the technology into areas that haven't been investigated and researched before. Tomorrow's applications will demand for higher power levels, improved efficiencies and the freedom of mobility without being constrained to a specific charging area. The following topics are suggested for future work

A. Bidirectional IPT

It has been assumed that an IPT system consists of a transmitter located in a base station and receiver on board a certain object containing the load. Power has been always transferred in one direction; from the source to the load. Several questions can be raised here about this mode of operation, what if the load had certain stored energy that is not in demand? Will it be possible to return that energy to the source? Or what if the load was able to send this energy to another system that is demanding energy? In order to transfer energy between several sources and load, a bidirectional IPT may be required. Bidirectionality is an emerging concept in IPT systems and further investigation is required to determine whether bidirectionality could be achieved by using two back-to-back unidirectional IPT systems or a designing a new topology that could implement bi-directionality.

B. Increasing the power delivering capability

The transmitted power levels achieved this research were are up to 20 W. More power is required to be transmitted to power higher loads such as motors. This can be achieved by scaling up the transmitter, i.e. increasing the input voltage and using larger coils with a larger wire diameter to allow more current to flow or using multiple transmitters. Moreover, other configurations of the Class E DC/AC inverter could be implemented, such as the push-pull configuration.

C. Automatic tuning

The tuning methods that were presented in Chapter 5 were implemented manually, future work should include designing controllers to achieve automatic tuning. Moreover, improving the modelling of the Class E inverter can be further improved by including the saturable reactor instead of a single inductor representation.

E. Further research in Class E rectifiers and resonant rectifiers

Although Chapter 6 presented a simple voltage-driven Class E ZVS low dv/dt rectifier that is compatible with resonant inductive links and resonant primary coil drivers, there are other configurations of the Class E rectifier that might have improved features for specific applications. Since the use rectifiers in IPT haven't been discussed before, further research and investigation into this area is required to emphasis on the importance of the rectifier in IPT systems.

REFERENCES

[1] J. P. Barrett. *Electricity at the Columbian Exposition*. R. R. Donnelley, 1894.

[2] N. Tesla. *The Wireless Tesla*. Wilder Publications, 2007.

[3] W. C. Brown. A survey of the elements of power transmission by microwave beam. In *IRE International Conference*, pages 93 – 105, Sept. 1961.

[4] A. Fisher. Beam-power plane. *Popular Science*, pages 62–65, Jan 1988.

[5] W. C. Brown. The solar power satellite as a source of base load electrical power. *IEEE Transactions on Power Apparatus and Systems*, Vol. 1(6):41 – 42, Jun. 1981.

[6] H. Suzuki, T. Fujita, and M. Mori. Technology demonstration and elemental technology development of space solar power systems. In *59th International Astronautical Congress*, 2008.

[7] F. Steinsiek, K. H. Weber, W. P. Foth, H. J. Foth, and C. Schafer. Wireless power transmission experiment using an airship as relay system and a moveable rover as ground target for later planetary exploration missions. In *8th ESA Workshop on Advanced Space Technologies for Robotics and Automation ASTRA*, Nov. 2004.

[8] NASA. Nasa research team successfully flies first laser-powered aircraft (2003). http://www.nasa.gov/vision/earth/improvingflight/laser_plane.html, Accessed on 10 October 2011 .

[9] L. Summerer and O. Purcell. Concepts for wireless energy transmission via laser. European Space Agency, 2008.

[10] E. J. Conway. Solar pumped laser technology options for space power transmission. In *21st Intersociety Energy Conversion Engineering Conference*, pages 1862 – 1868., San Diego, CA, Aug. 1986.

[11] M. Weksler and J. Shwartz. Solar-pumped solid-state lasers. *IEEE Journal of Quantum Electronics*, 24(6):1222 – 1228, Jun. 1988.

[12] R. Dickinson and J. Grey. Lasers for wireless power transmission. Technical report, Jet Propulsion Lab, NASA, Jan. 1999.

[13] W. C. Brown. The history of power transmission by radio waves. *IEEE Transactions on Microwave Theory and Techniques*, 32(9):1230 – 1242, Sept. 1984.

[14] R. M. Dickinson. Evaluation of a microwave high-power reception-conversion array for wirelesspower transmission. Tech. memo, Jet Propulsion Lab, NASA, Sept. 1975.

[15] H. Matsumoto. Research on solar power satellites and microwave power transmission in japan. *IEEE Microwave Magazine*, 3(4):36 – 45, Dec. 2002.

[16] J. J. Schlesak, A. Alden, and T. Ohno. A microwave powered high altitude platform. In *Microwave Symposium Digest, 1988., IEEE MTT-S International*, pages 283 – 286, May 1988.

[17] L. J. Chen, W. I. S. Tong, B. Meyer, A. Abdolkhani, and A. P. Hu. A contactless charging platform for swarm robots. In *IEEE 37th Annual Conference on Industrial Electronics Society IECON*, pages 4088 – 4093, Nov. 2011.

[18] S. Y. R. Hui and W. C. Ho. A new generation of universal contactless battery charging platform for portable consumer electronic equipment. In *IEEE 35th Annual Power Electronics Specialists Conference PESC*, volume 1, pages 638 – 644, Jun. 2004.

[19] X. Liu and S. Y. R. Hui. Equivalent circuit modeling of a multilayer planar winding array structure for use in a universal contactless battery charging platform. *IEEE Transactions on Power Electronics*, 22(1):21 – 29, Jan. 2007.

[20] C. H. Hu, C. M. Chen, Y. S. Shiao, T. J. Chan, and T. R. Chen. Development of a universal contactless charger for handheld devices. In *IEEE International Symposium on Industrial Electronics*, pages 99 – 104, Jul. 2008.

[21] H. Y. Shen, J. Y. Lee, and T. W. Chang. Study of contactless inductive charging platform with core array structure for portable products. In *IEEEInternational Conference on Consumer Electronics, Communications and Networks CECNet*, pages 756 – 759, Apr. 2011.

[22] Wireless power consortium. www.wirelesspowerconsortium.com, Accessed Jan 2014.

[23] Alliance for wireless power. http://www.rezence.com, Accessed Jan 2014.

[24] *bqTESLA Wireless Power Transmitter Manager EVM User's Guide*. Texas Instruments, Jun. 2011.

[25] *bq5101x Integerated Wireless Power Supply Receiver datasheet*. Texas Instruments, Apr. 2012.

[26] E. B. Tarrson. Electric toothbrush which is rechargeable with or without a recharging stand. US Patent 3379952, Apr. 1968.

[27] S. Inakagata. Induction charger. Japanese Patent 6054454, Feb. 1994.

[28] *WM7200 Inductive Charger Owner's Manual*. GM Advanced Technology Vehicles, 1998.

[29] K. W. Klontz, D. M. Divan, D. W. Novotny, and R. D. Lorenz. Contactless battery charging system. US Patent 5341083, Aug. 1994.

[30] D. W. Baarman. Portable inductive power station. US Patent 7462951, Dec. 2008.

[31] Y. Hori. Future vehicle society based on electric motor, capacitor and wireless power supply. In *International Power Electronics Conference (IPEC)*, pages 2930 – 2934, Jun. 2010.

[32] J. Huh, S.W. Lee, W.Y. Lee, G.H. Cho, and C.T. Rim. Narrow-width inductive power transfer system for online electrical vehicles. *IEEE Transactions on Power Electronics*, 26(12):3666–3679, Dec. 2011.

[33] A. Gilchrist, H. Wu, and K. Sealy. Novel system for wireless in-motion EV charging and disabled vehicle removal. In *IEEE International Electric Vehicle Conference (IEVC)*, pages 1 – 4, Mar. 2012.

[34] Y. J. Jang, Y. D. Ko, and S. Jeong. Optimal design of the wireless charging electric vehicle. In *IEEE International Electric Vehicle Conference (IEVC)*, pages 1 – 5, Mar. 2012.

[35] S. Mohrehkesh and T. Nadeem. Toward a wireless charging for battery electric vehicles at traffic intersections. In *IEEE 14th International Conference on Intelligent Transportation Systems (ITSC)*, pages 113 – 118, Oct. 2011.

[36] T. McGinnis, C.P. Henze, and K. Conroy. Inductive power system for autonomous underwater vehicles. In *OCEANS 2007*, pages 1 – 5, Oct. 2007.

[37] K. W. Klontz, D. M. Divan, D. W. Novotnym, and R. D. Lorenz. Submersible contactless power delivery system. US Patent 5301096, Apr. 1994.

[38] V. Chawla and D. S. Ha. An overview of passive RFID. *IEEE Communications Magazine*, 45(9):11 – 17, Sept. 2007.

[39] P. Sorrells. Passive RFID basics. Application note, Microchip Technology Inc., 2002.

[40] M. Soma, Douglas C. Galbraith, and R. L. White. Radio-frequency coils in implantable devices: Misalignment analysis and design procedure. *IEEE Transactions on Biomedical Engineering*, BME-34(4):276 – 282, Apr. 1987.

[41] Reid R. Harrison. Designing efficient inductive power links for implantable devices. In *IEEE Int. Symp. on Circuits and Systems (ISCAS)*, pages 2080 – 2083, May 2007.

[42] Kanber Mithat Silay, Catherine Dehollain, and Michel Declercq. Inductive power link for a wireless cortical implant with two-body packaging. *IEEE Sensors J.*, 11 (11):2825 – 2833, Nov. 2011.

[43] R. Carta and R. Puers. Wireless power and data transmission for robotic capsule endoscopes. In *IEEE 18th Symposium on Communications and Vehicular Technology in the Benelux (SCVT)*, pages 1 – 6, Nov. 2011.

[44] G. Yan, D. Ye, P. Zan, K. Wang, and G. Ma. Micro-robot for endoscope based on wireless power transfer. In *Mechatronics and Automation, 2007. ICMA 2007. International Conference on*, pages 3577 – 3581, Aug. 2007.

[45] G. A. Covic and J. T. Boys. Inductive power transfer. *Proc. IEEE*, 101(6):1276–1289, Jun. 2013.

[46] G.A. Covic and J.T. Boys. Modern trends in inductive power transfer for transportation applications. *IEEE Journal of Emerging and Selected Topics in Power Electronics*, 1(1):28–41, Jul. 2013.

[47] J. Garnica, R.A. Chinga, and Jenshan Lin. Wireless power transmission: From far field to near field. *Proceedings of the IEEE*, 101(6):1321–1331, Jul. 2013.

[48] André Kurs, Aristeidis Karalis, Robert Moffatt, J. D. Joannopoulos, Peter Fisher, and Marin Soljacic. Wireless power transfer via strongly coupled magnetic resonances. *Science*, 317(5834):83 – 86, 2007.

[49] Seung-Hwan Lee and R.D. Lorenz. Development and validation of model for 95%-efficiency 220-W wireless power transfer over a 30-cm air gap. *IEEE Transactions on Industry Applications*, 47(6):2495–2504, 2011.

[50] Seung-Hwan Lee and R.D. Lorenz. A design methodology for multi-kw, large air-gap, mhz frequency, wireless power transfer systems. In *IEEE Energy Conversion Congr. and Expo. (ECCE)*, pages 3503 – 3510, Sept. 2011.

[51] Zhen Ning Low, Raul Andres Chinga, Ryan Tseng, and Jenshan Lin. Design and test of a high-power high-efficiency loosely coupled planar wireless power transfer system. *IEEE Transactions on Industrial Electronics*, 56(5):1801 – 1812, May 2009.

[52] J. J. Casanova, Z. N. Low, J. Lin, and R. Tseng. Transmitting coil achieving uniform magnetic field distribution for planar wireless power transfer system. In *IEEE Radio and Wireless Symposium RWS*, pages 530 – 533, Jan. 2009.

[53] Joaquin J. Casanova, Zhen Ning Low, and Jenshan Lin. Design and optimization of a Class-E amplifier for a loosely coupled planar wireless power system. *IEEE Transactions on Circuits and Systems II: Express Briefs*, 56(11):830 – 834, Nov. 2009.

[54] K. Kadota. Designing wireless power supply systems. *ANSYS Advantage*, Volume V(Issue 3):38 – 40, 2011.

[55] C. Alexander and M. Sadiku. *Fundamentals of Electric Circuits*. McGraw-Hill, 2nd edition, 2003.

[56] M.N.O. Sadiku. *Elements of Electromagnetics*. Oxford University Press, Incorporated, 2010.

[57] K. Van Schuylenbergh and R. Puers. The concepts of inductive powering. In Koenraad Schuylenbergh and Robert Puers, editors, *Inductive Powering*, Analog Circuits and Signal Processing, pages 41–76. Springer Netherlands, 2009.

[58] Marian K. Kazimierczuk. *RF Power Amplifiers*. John Wiley & Sons, Chichester, UK, 2008.

[59] N. Mohan, T. M. Undeland, and W. P. Robbins. *Power Electronics, Converters, Applications and Design*. John Wiley & Sons, New York, 3rd edition, 2002.

[60] Michael de Rooij and Johan Strydom. Low power wireless energy converters. White Paper: WP014, 2013.

[61] W. Zhang, S.-C. Wong, C. K. Tse, and Q. Chen. Design for efficiency optimization and voltage controllability of series-series compensated inductive power transfer systems. *IEEE Transactions on Power Electronics*, 29(1):191–200, Jan. 2014.

[62] Hao Hao, G.A. Covic, and J.T. Boys. A parallel topology for inductive power transfer power supplies. *IEEE Transactions on Power Electronics*, 29(3):1140–1151, Mar 2014.

[63] M. Budhia, G.A. Covic, and J.T. Boys. Design and optimization of circular magnetic structures for lumped inductive power transfer systems. *IEEE Transactions on Power Electronics*, 26(11):3096–3108, Nov. 2011.

[64] J.L. Villa, J. Sallan, J.F. Sanz Osorio, and A. Llombart. High-misalignment tolerant compensation topology for ICPT systems. *IEEE Transactions on Industrial Electronics*, 59(2):945–951, Feb. 2012.

[65] Jaegue Shin, Seungyong Shin, Yangsu Kim, Seungyoung Ahn, Seokhwan Lee, Guho Jung, Seong-Jeub Jeon, and Dong-Ho Cho. Design and implementation of shaped magnetic-resonance-based wireless power transfer system for roadway-powered moving electric vehicles. *IEEE Transactions on Industrial Electronics*, 61 (3):1179–1192, Mar. 2014.

[66] Dukju Ahn and Songcheol Hong. A transmitter or a receiver consisting of two strongly coupled resonators for enhanced resonant coupling in wireless power transfer. *IEEE Transactions on Industrial Electronics*, 61(3):1193–1203, Mar 2014.

[67] Erin M. Thomas, Jason D. Heebl, Carl Pfeiffer, and Anthony Grbic. A power link study of wireless non-radiative power transfer systems using resonant shielded loops. *IEEE Transactions on Circuits and Systems I, Reg. Papers*, 59(9):2125 – 2136, Sept. 2012.

[68] Marian K. Kazimierczuk and Dariusz Czarkowski. *Resonant Power Converters*. John Wiley & Sons, New Jersey, USA, 2nd edition edition, 2011.

[69] M.K. Kazimierczuk and A. Abdulkarim. Current-source parallel-resonant DC/DC converter. *IEEE Transactions on Industrial Electronics*, 42(2):199–208, Apr. 1995.

[70] Andrei Grebennikov and Nathan O. Sokal. *Switchedmode RF Power Amplifiers*. Newnes, Oxford, UK, 2007.

[71] Nathan O. Sokal and Alan D. Sokal. Class E-a new class of high-efficiency tuned single-ended switching power amplifiers. *IEEE J. Solid-State Circuits*, 10(3):168 – 176, Jun. 1975.

[72] Samer Aldhaher, Patrick C. K. Luk, and James F. Whidborne. High input voltage high frequency Class E rectifiers for inductive links. *IEEE Transactions on Power Electronics*, to be published, 2014.

[73] Samer Aldhaher, Patrick C. K. Luk, and James F. Whidborne. Wireless power transfer using Class E inverter with saturable DC-feed inductor. In *Proc. IEEE Energy Convers. Congr. Expo.*, pages 1902–1909, Sep. 2013.

[74] Samer Aldhaher, Patrick C. K. Luk, and James F. Whidborne. Tuning Class inverters applied in inductive links using saturable reactors. *IEEE Transactions on Power Electronics*, to be published, 2013.

[75] Manuel Pinuela, David C. Yates, Stepan Lucyszyn, and Paul D. Mitcheson. Maximizing DC-to-load efficiency for inductive power transfer. *IEEE Transactions on Power Electronics*, 28(5):2437 – 2447, May 2013.

[76] Linhui Chen, Shuo Liu, Yong Chun Zhou, and Tie Jun Cui. An optimizable circuit structure for high-efficiency wireless power transfer. *IEEE Transactions on Industrial Electronics*, 60(1):339 – 349, Jan. 2013.

[77] Gurhan Alper Kendir, Wentai Liu, Guoxing Wang, Mohanasankar Sivaprakasam, Rizwan Bashirullah, Mark S. Humayun, and James D. Weiland. An optimal design methodology for inductive power link with class-E amplifier. *IEEE Transactions on Circuits and Systems I, Reg. Papers*, 52(5):857 – 866, May 2005.

[78] M. K. Kazimierczuk and J. Jozwik. Resonant DC/DC converter with Class E inverter and Class E rectifier. *IEEE Transactions on Industrial Electronics*, 36(4): 468–478, Nov. 1989.

[79] F.H. Raab. Idealized operation of the Class E tuned power amplifier. *IEEE Transactions on Circuits and Systems*, 24(12):725–735, Dec. 1977.

[80] G.H. Smith and R.E. Zulinski. An exact analysis of Class E amplifiers with finite DC-feed inductance at any output Q. *IEEE Transactions on Circuits and Systems*, 37(4):530–534, Apr. 1990.

[81] C.P. Avratoglou and N.C. Voulgaris. A Class E tuned amplifier configuration with finite DC-feed inductance and no capacitance in parallel with switch. *IEEE Transactions on Circuits and Systems*, 35(4):416–422, Apr. 1988.

[82] R.E. Zulinski and John W. Steadman. Class E power amplifiers and frequency multipliers with finite DC-feed inductance. *IEEE Transactions on Circuits and Systems*, 34(9):1074–1087, Sep. 1987.

[83] M. Acar, A.J. Annema, and B. Nauta. Analytical design equations for Class-E power amplifiers. *IEEE Transactions on Circuits and Systems-I:Regular Papers*, 54 (12):2706 – 2717, 2007.

[84] M.K. Kazimierczuk and K. Puczko. Exact analysis of Class E tuned power amplifier at any Q and switch duty cycle. *IEEE Transactions on Circuits and Systems*, 34(2):149–159, Feb. 1987.

[85] R. Redl, Bela Molnar, and N.O. Sokal. Class E resonant regulated DC/DC power converters: Analysis of operations, and experimental results at 1.5 MHz. *IEEE Transactions on Power Electronics*, PE-1(2):111–120, Apr. 1986.

[86] M. K. Kazimierczuk. Class E tuned power amplifier with shunt inductor. *IEEE Journal of Solid-State Circuits*, 16(1):2–7, Feb. 1981.

[87] Frederick H. Raab. Effects of circuit variations on the class E tuned power amplifier. *IEEE J. Solid-State Circuits*, 13(2):239 – 247, Apr. 1978.

[88] Marian K. Kazimierczuk and Xung T. Bui. Class-E amplifier with an inductive impedance inverter. *IEEE Transactions on Industrial Electronics*, 37(2):160 – 166, Apr. 1990.

[89] Marian K. Kazimierczuk and Xung T. Bui. Class E DC/DC converters with an inductive impedance inverter. *IEEE Transactions on Power Electronics*, 4(1):124 – 135, Jan. 1989.

[90] K. Thomas, S. Hinchliffe, and L. Hobson. Class E switching-mode power amplifier for high-frequency electric process heating applications. *Electron. Lett.*, 23(2): 80 – 82, 1987.

[91] Yehui Han, Olivia Leitermann, David A. Jackson, Juan M. Rivas, and David J. Perreault. Resistance compression networks for radio-frequency power conversion. *IEEE Transactions on Power Electronics*, 22(1):41 – 53, Jan. 2007.

[92] D. Collins, S. Hinchliffe, and L. Hobson. Optimised class-E amplifier with load variation. *Electron. Lett.*, 23(18):973 – 974, 1987.

[93] Miroslav Vasic, Oscar Garcia, Jesus A. Oliver, Pedro Alou, Daniel Diaz, Roberto Prieto, and Jose A. Cobos. Envelope amplifier based on switching capacitors for high-efficiency RF amplifiers. *IEEE Transactions on Power Electronics*, 27(3):1359 – 1368, Mar. 2012.

[94] R.E. Zulinski and K.J. Grady. Load-independent class E power inverters. i. theoretical development. *IEEE Transactions on Circuits and Systems I, Reg. Papers*, 37 (8):1010 – 1018, Aug. 1990.

[95] L. Roslaniec and D.J. Perreault. Design of variable-resistance class E inverters for load modulation. In *IEEE Energy Conversion Congress and Expo.*, pages 3226 – 3232, Sept. 2012.

[96] Yen-Fang Li. Auto-tuning controller design of class E inverter with resonant components varying. In *IEEE Int. Symp. on Industrial Electronics*, pages 217 – 221, May 2012.

[97] Robert C. N. Pilawa-Podgurski, Anthony D. Sagneri, Juan M. Rivas, David I. Anderson, and David J. Perreault. Very-high-frequency resonant boost converters. *IEEE Transactions on Power Electronics*, 24(6):1654 – 1665, Jun. 2009.

[98] Magnetic amplifiers: A rising star in naval electronics. Electronics Design and Development Division, Bureau of Ships, U. S. Navy, 1951.

[99] C.W.T. McLyman. *Designing magnetic components for high frequency DC-DC converters*. KG Magnetics, 1993.

[100] C.W.T. McLyman. *Magnetic Core Selection for Transformers and Inductors*. Marcel Dekker Inc., 2nd edition edition, 1997.

[101] Zachary Battles and Lloyd N. Trefethen. An extension of Matlab to continuous functions and operators. *SIAM J. Sci. Comp.*, 2004.

[102] L. N. Trefethen et al. *Chebfun Version 4.2*. The Chebfun Development Team, 2011. http://www.maths.ox.ac.uk/chebfun/.

[103] Magnetics Inc., MPP550 C055202A2 datasheet, .

[104] MPP Material Curves, Magnetic Inc. [Online]. Available: http://www.mag-inc.com/products/powder-cores/mpp-cores/mpp-material-curves, .

[105] S. Raju, R. Wu, M. Chan, and C. P. Yue. Modeling of mutual coupling between planar inductors in wireless power applications. *IEEE Transactions on Power Electronics*, 29(1):481–490, Jan 2014.

[106] A. P. Sample, B. H. Waters, S. T. Wisdom, and J. R. Smith. Enabling seamless wireless power delivery in dynamic environments. *Proc. IEEE*, 101(6):1343–1358, Apr. 2013.

[107] W.X. Zhong, X. Liu, and S. Y. R. Hui. A novel single-layer winding array and receiver coil structure for contactless battery charging systems with free-positioning and localized charging features. *IEEE Transactions on Industrial Electronics*, 58(9):4136–4144, Sept. 2011.

[108] B. L. Cannon, J. F. Hoburg, D. D. Stancil, and S. C. Goldstein. Magnetic resonant coupling as a potential means for wireless power transfer to multiple small receivers. *IEEE Transactions on Power Electronics*, 24(7):1819–1825, Jul. 2009.

[109] M. K. Kazimierczuk and J. J. Jozwik. Class-E zero-voltage-switching and zero-current-switching rectifiers. *IEEE Transactions on Circuits and Systems*, 37(3):436–444, Mar. 1990.

[110] M. Rashid. *Power Electronics Handbook*. Butterworth-Heinemann, third edition edition, 2011.

[111] A. Reatti and M.K. Kazimierczuk. Comparison of the efficiencies of Class D and Class E rectifiers. In *Proceedings of the 36th Midwest Symposium on Circuits and Systems*, pages 871–874 vol.2, Aug. 1993.

[112] M.K. Kazimierczuk. Class D current-driven rectifiers for resonant DC/DC converter applications. *IEEE Transactions on Industrial Electronics*, 38(5):344–354, Oct. 1991.

[113] M. Mikotajewski. Class D synchronous rectifiers. *IEEE Transactions on Circuits and Systems*, 38(7):694–697, Jul. 1991.

[114] K. Fukui and H. Koizumi. Class-E rectifier with controlled shunt capacitor. *IEEE Transactions on Power Electronics*, 27(8):3704–3713, Jan. 2012.

[115] J.A. Garcia, R. Marante, and M. de las Nieves Ruiz Lavin. GaN HEMT Class E^2 resonant topologies for UHF DC/DC power conversion. *IEEE Transactions on Microwave Theory and Techniques*, 60(12):4220–4229, Dec. 2012.

[116] J.M. Rivas, O. Leitermann, Yehui Han, and D.J. Perreault. A very high frequency DC-DC converter based on a Class Φ_2 resonant inverter. *IEEE Transactions on Power Electronics*, 26(10):2980–2992, Oct. 2011.

[117] J. J. Jozwik and M. K. Kazimierczuk. Analysis and design of Class E^2 DC/DC converter. *IEEE Transactions on Industrial Electronics*, 37(2):173–183, Apr. 1990.

[118] M. K. Kazimierczuk and J. J. Jozwik. Resonant DC/DC converter with class-E inverter and class-E rectifier. *IEEE Transactions on Industrial Electronics*, 36(4): 468–478, Nov. 1989.

[119] S. H. Abdelhalem, P. S. Gudem, and L. E. Larson. An RF-DC converter with wide-dynamic-range input matching for power recovery applications. *IEEE Transactions on Circuits and Systems II: Express Briefs*, 60(6):336–340, Apr. 2013.

[120] W.C. Bowman, F.M. Magalhaes, W.B. Suiter, and N.G. Ziesse. Resonant rectifier circuit, Aug. 1987. US Patent 4,685,041.

[121] S. Birca-Galateanu and A. Ivascu. Class E low dv/dt and low di/dt rectifiers: energy transfer, comparison, compact relationships. *IEEE Transactions on Circuits and Systems I: Fundamental Theory and Applications*, 48(9):1065–1074, Sep. 2001.

[122] A. Ivascu, M. K. Kazimierczuk, and S. Birca-Galateanu. Class E resonant low dv/dt rectifier. *IEEE Transactions on Circuits and Systems I: Fundamental Theory and Applications*, 39(8):604–613, Aug. 1992.

[123] S. Jalbrzykowski, A. Bogdan, and T. Citko. A dual full-bridge resonant Class E bidirectional DC/DC converter. *IEEE Transactions on Industrial Electronics*, 58(9): 3879–3883, Aug. 2011.

[124] H. Hase, H. Sekiya, Jianming Lu, and T. Yahagi. Resonant DC/DC converter with Class E oscillator. *IEEE Transactions on Circuits and Systems I: Regular Papers*, 53(9):2025–2035, Sep. 2006.

[125] I. Boonyaroonate and S. Mori. Analysis and design of Class E isolated DC/DC converter using Class E low dv/dt PWM synchronous rectifier. *IEEE Transactions on Power Electronics*, 16(4):514–521, Jun. 2001.

[126] Yan-Fei Liu and P.C. Sen. New Class E DC/DC converter topologies with constant switching frequency. *Industry Applications, IEEE Transactions on*, 32(4):961–969, Jul. 1996.

[127] W.J. Gu and K. Harada. A circuit model for the Class E resonant DC/DC converter regulated at a fixed switching frequency. *IEEE Transactions on Power Electronics*, 7(1):99–110, Aug 1992.

[128] J. J. Jozwik and M. K. Kazimierczuk. Analysis and design of Class E^2 DC/DC converter. *IEEE Trans. Ind. Electron*, 37(2):173–183, Aug. 1990.

[129] M. K. Kazimierczuk and X.T. Bui. Class E DC/DC converters with an inductive impedance inverter. *IEEE Trans. Power Electron.*, 4(1):124–135, Jan. 1989.

[130] M. K. Kazimierczuk and X.T. Bui. Class E DC/DC converters with a capacitive impedance inverter. *IEEE Transactions on Industrial Electronics*, 36(3):425–433, 1989.

[131] M. K. Kazimierczuk and J. Jozwik. DC/DC converter with Class E zero-voltage-switching inverter and class E zero-current-switching rectifier. *IEEE Transactions on Circuits and Systems*, 36(11):1485–1488, Nov. 1989.

[132] R. Redl, Bela Molnar, and N.O. Sokal. Small-signal dynamic analysis of regulated Class E DC/DC converters. *IEEE Transactions on Power Electronics*, PE-1(2): 121–128, Apr. 1986.

[133] [Online]. Available: http://www.wirelesspowerconsortium.com.

[134] Würth Elektronik, WE-WPCC Wireless Power Charging Coil 760308110 datasheet.

[135] S. Birca-Galateanu and J.-L. Cocquerelle. Class E half-wave low dv/dt rectifier operating in a range of frequencies around resonance. *IEEE Transactions on Circuits and Systems I: Fundamental Theory and Applications*, 42(2):83–94, Feb. 1995.

[136] Patricio Cortés, Marian P. Kazmierkowski, Ralph M. Kennel, Daniel E. Quevedo, and José Rodríguez. Predictive control in power electronics and drives. *IEEE Transactions on Industrial Electronics*, 55(12):4312–4324, Dec. 2008.

[137] Axel Schild, Jan Lunzez, Jörg Krupar, and Wolfgang Schwarz. Design of generalized hysteresis controllers for DC/DC switching power converters. *IEEE Transactions on Power Electronics*, 24(1):138–146, Jan. 2009.

[138] Jonathan W. Kimball, Philip T. Krein, and Yongxiang Chen. Hysteresis and delta modulation control of converters using sensorless current mode. *IEEE Transactions on Power Electronics*, 21(4):1154–1158, Jul. 2006.

[139] Santa Concepción Huerta, Pedro Alou, Jesús Á. Oliver, Oscar García, José A. Cobos, and Ahmed M. Abou-Alfotouh. Nonlinear control for DC/DC converters based on hysteresis of the current with a frequency loop to operate at constant frequency. *IEEE Transactions on Industrial Electronics*, 58(3):1036–1043, Mar. 2011.

[140] Han-Hsiang Huang, Chi-Lin Chen, and Ke-Horng Chen. Adaptive window control AWC technique for hysteresis DC/DC buck converters with improved light and heavy load performance. *IEEE Transactions on Power Electronics*, 24(6):1607–1617, Jun. 2009.

[141] Feng Su, Wing-Hung Ki, and Chi-Ying Tsui. Ultra fast fixed-frequency hysteretic buck converter with maximum charging current control and adaptive delay compensation for DVS applications. *IEEE J. Solid-State Circuits*, 43(4):815–822, Apr. 2008.

[142] Enric Vidal-Idiarte, Carlos E. Carrejo, Javier Calvente, and Luis Martínez-Salamero. Two-loop digital sliding mode control of DC/DC power converters based on predictive interpolation. *IEEE Transactions on Industrial Electronics*, 58 (6):2491–2501, Jun. 2011.

[143] H. Peng and D. Maksimovic. A digital current mode control technique for DC/DC converters. In *Proc. IEEE 20th Ann. Applied Power Electronics Conf. and Expo.*, volume 2, pages 885–891, Mar. 2005.

[144] Souvik Chattopadhyay and Somshubhra Das. A digital current-mode control technique for DC/DC converters. *IEEE Transactions on Power Electronics*, 21(6): 1718–1726, Nov. 2006.

[145] Takahiko Iida. Emulated current mode control system for DC/DC boost converter using FPGA. In *Proc. IEEE 35th Ann. Conf. Industrial Electronics*, pages 432–436, Nov. 2009.

[146] Ying Qiu, Xiyou Chen, and Helen Liu. Digital average current-mode control using current estimation and capacitor charge balance principle for DC/DC converters operating in DCM. *35th Ann. Conf.*, 25(6):1537–1545, Jun. 2010.

[147] Liping Guo, John Y. Hung, and R. M. Nelms. Evaluation of DSP-based PID and fuzzy controllers for DC/DC converters. *IEEE Transactions on Industrial Electronics*, 56(6):2237–2248, Jun. 2009.

[148] Aleksandar Prodic and Dragan Maksimovic. Design of a digital PID regulator based on look-up tables for control of high-frequency DC/DC converters. In *Proc. IEEE Computers in Power Electronics*, pages 18–22, Jun. 2002.

[149] Liping Guo. Implementation of digital PID controllers for DC/DC converters using digital signal processors. In *Proc. IEEE Int. Conf. Electro/Information Technology*, pages 306–311, May. 2007.

[150] Chan Ho Kang, Kyung Man Kim, Kyung Ho Lee, and Hee Jun Kim. Development of a 1.5kW digital controlled DC/DC converter for mild hybrids. In *Proc. IEEE 33rd Int. Telecommunications Energy Conf.*, pages 1–5, Oct. 2011.

[151] Yanxia Gao, Shuibao Guo, Yanping Xu, Shi Xuefang Lin, and B. Allard. FPGA-based DPWM for digitally controlled high-frequency DC/DC SMPS. In *Proc. IEEE 3rd Int. Conf. Power Electronics Systems and Applications*, pages 1–7, May. 2009.

[152] Shuibao Guo, Xuefang Lin-Shi, B. Allard, Bo Li, Yanxia Gao, and Yi Ruan. High-resolution digital PWM controller for high-frequency low-power SMPS. In *Proc. IEEE 13th European Conf. Power Electronics and Applications*, pages 1–9, Sep. 2009.

[153] VaraPrasad Arikatla and Jaber A. Abu-Qahouq. An adaptive digital PID controller scheme for power converters. In *IEEE Energy Conversion Congress and Expo.*, pages 223–227, Sep. 2010.

[154] Ahmed Rubaa, Abdul R. Ofoli, Legand Burge, and Moses Garuba. Hardware implementation of an adaptive network-based fuzzy controller for DC/DC converters. *IEEE Transactions on Industry Applications*, 41(6):1557–1565, Nov. 2005.

[155] Alexander G. Perry, Guang Feng, Yan Fei Liu, and Paresh C. Sen. A design method for PI-like fuzzy logic controllers for DC/DC converter. *IEEE Transactions on Industrial Electronics*, 54(5):2688–2696, Oct. 2007.

[156] Tarun Gupta, R. R. Boudreaux, R. M. Nelms, and John Y. Hung. Implementation of a fuzzy controller for DC/DC converters using an inexpensive 8-b microcontroller. *IEEE Transactions on Industrial Electronics*, 44(5):661–669, Oct. 1997.

[157] C.-F. Hsu, I.-F. Chung, C.-M. Lin, and C.-Y. Hsu. Self-regulating fuzzy control for forward DC/DC converters using an 8-bit microcontroller. *IET Power Electron.*, 2 (1):1–12, Jan. 2009.

[158] Shuibao Guo, Xuefang Lin-Shi, Bruno Allard, Bo Li, Yanxia Gao, and Yi Ruan. A fpga-prototype of a sliding-mode-controller IC for high-switching-frequency DC/DC converters. In *Proc. IEEE 35th Ann. Conf. Industrial Electronics*, pages 2895–2900, Nov. 2009.

[159] Y. He and F.L. Luo. Sliding-mode control for DC/DC converters with constant switching frequency. *IEE Proc. Control Theory and Applications*, 153(1):37–45, Jan. 2006.

[160] Rong-Jong Wai and Li-Chung Shih. Design of voltage tracking control for DC/DC boost converter via total sliding-mode technique. *IEEE Transactions on Industrial Electronics*, 58(6):2502–2511, Jun. 2011.

[161] Siew-Chong Tan, Y. M. Lai, and Chi K. Tse. General design issues of sliding-mode controllers in DC/DC converters. *IEEE Transactions on Industrial Electronics*, 55(3):1160–1174, Mar. 2008.

[162] Enric Vidal-Idiarte, Carlos E. Carrejo, Javier Calvente, and Luis Martínez-Salamero. Two-loop digital sliding mode control of DC/DC power converters based on predictive interpolation. *IEEE Transactions on Industrial Electronics*, 58 (6):2491–2501, Jun. 2011.

[163] Suyong Chae, Byungchul Hyun, Pankaj Agarwal, Woosup Kim, and Bohyung Cho. Digital predictive feed-forward controller for a DC/DC converter in plasma display panel. *IEEE Transactions on Power Electronics*, 23(2):627–634, Mar. 2008.

[164] G. Zhou, J. Xu, and Y. Jin. Improved digital peak current predictive control for switching DC/DC converters. *IET Power Electron.*, 4(2):227–234, Feb. 2011.

[165] Jianping Xu, Guohua Zhou, and Mingzhi He. Improved digital peak voltage predictive control for switching DC/DC converters. *IEEE Transactions on Industrial Electronics*, 56(8):3222–3229, Aug. 2009.

[166] Woonki Na, Taesik Park, Taehyung Kim, and Sangshin Kwak. Light fuel-cell hybrid electric vehicles based on predictive controllers. *IEEE Transactions on Vehicular Technology*, 60(1):89–97, Jan. 2011.

[167] C.E. Carrejo, E. Vidal-Idiarte, R. Giral, and L. Martinez-Salamero. Predictive digital interpolation current control for DC/DC power converters. *IET Power Electron.*, 2(5):545–554, Sep. 2009.

[168] Stéphane Bibian and Hua Jin. High performance predictive dead-beat digital controller for dc power supplies. *IEEE Transactions on Power Electronics*, 17(3): 420–427, May 2002.

[169] Tobias Geyer, Georgios Papafotiou, and Manfred Morari. Hybrid model predictive control of the step-down DC/DC converter. *IEEE Transactions on Control Systems Technology*, 16(6):1112–1124, Nov. 2008.

[170] Sébastien Mariéthoz, Stefan Almér, Mihai Bâja, Andrea Giovanni Beccuti, Diego Patino, Andreas Wernrud, Jean Buisson, Hervé Cormerais, Tobias Geyer, Hisaya Fujioka, Ulf T. Jönsson, Chung-Yao Kao, Manfred Morari, Georgios Papafotiou, Anders Rantzer, and Pierre Riedinger. Comparison of hybrid control techniques for buck and boost DC/DC converters. *IEEE Transactions on Control Systems Technology*, 18(5):1126–1145, Sep. 2010.

[171] Andreas Kugi and Kurt Schlacher. Nonlinear H_∞ controller design for a DC-to-DC power converter. *IEEE Transactions on Control Systems Technology*, 7(2): 230–237, Mar. 1999.

[172] Yan-Fei Liu, E. Meyer, and Xiaodong Liu. Recent developments in digital control strategies for dc/dc switching power converters. *35th Ann. Conf.*, 24(11):2567–2577, Nov. 2009.

[173] Abram P. Dancy and Anantha P. Chandrakasan. Ultra low power control circuits for PWM converters. In *28th Ann. Power Electronics Specialists Conf.*, volume 1, pages 21–27, Jun. 1997.

[174] K.I. Hwu and Y.T. Yau. Improvement of one-comparator counter-based PFM control for DC/DC converter. In *IEEE Int. Symp. on Industrial Electronics*, pages 1604 – 1607, Jul. 2009.

[175] J. Roh, S. D. Lee, and S. Park. Digital PWM controller for DC/DC converters with minimum analogue circuits. *Electron. Lett.*, 39(19):1402–1403, Sep. 2003.

[176] Marian K. Kazimierczuk. *Pulse-width Modulated DC/DC Power Converters*. John Wiley, West Sussex, United Kingdom, 2008.

[177] R. D. Middlebrook and Slobodan Ćuk. A general unified approach to modelling switching-converter power stages. *Int. J. Electron.*, 42(6):521–550, 1977.

[178] Benjamin C. Kuo and Farid Golnaraghi. *Automatic Control Systems*. John Wiley, NJ, USA, 8th edition, 2002.

[179] H. K. Khalil. *Nonlinear Systems*. Prentice Hall, 3rd edition, 2001, pp. 280-296.

[180] Shlomo Engelberg. Limitations of the describing function for limit cycle prediction. *IEEE Transactions on Automatic Control*, 47(11):1887–1890, Nov. 2002.

A

MATLAB CODES

A.1 MATLAB CODES FOR CHAPTER 4

A.1.1 *Class E with Finite DC-Feed Inductance*

```
%%define domains%%
qdomain = [0.5 2];                          %q domain
pdomain = [0.01 25];                        %p domain
phidomain = [0 2*pi];                       %phi domain
wtdomain=[pi 2*pi];                         %time OFF domain
wt2domain=[0 pi];                           %time ON domain
V2= [phidomain  pdomain];
%%%%%%%%%%%%%%%%%%
%%define chebfuns
phi=chebfun2(@(phi,p) phi, V2);
p=chebfun2(@(phi,p) p, V2);
wt=chebfun('wt', wtdomain);
wt2=chebfun('wt2', wt2domain);
%initialise loop varaibles
ni=40;                                      %number of data points
q=qdomain(1):diff(qdomain)/ni:qdomain(2);
r1=zeros(ni,2);                             %all solved values
p_s=zeros(ni,1);                            %solved p values
phi_s=zeros(ni,1);                          %solved phi values
VDSmax=zeros(ni,1);                         %calculated VDSmax values
IDSmax=zeros(ni,1);                         %calculated IDSmax values
Po=zeros(ni,1);                             %calculated power values
cp=zeros(ni,1);                             %calculated cp values

%%%loop begins
for i=1:ni+1
    A=(q(i)*cos(q(i)*pi).*cos(phi)+(2*q(i)^2-1)*sin(q(i)*pi).*sin(phi))/(q(i)^2-1)...
        + pi*sin(q(i)*pi)./p + cos(q(i)*pi)./(q(i)*p); %A
    B=(-q(i)*sin(q(i)*pi).*cos(phi)+(2*q(i)^2-1)*cos(q(i)*pi).*sin(phi))/(q(i)^2-1)...
        + pi*cos(q(i)*pi)./p -sin(q(i)*pi)./(q(i)*p); %B
    eq43=1-q(i).*A.*p*cos(2*pi*q(i)) +q(i).*B.*p*sin(2*pi*q(i)) - ...
        q(i)^2.*p.*cos(phi)/(q(i)^2-1);
```

```
        eq44=q(i)^2.*A*sin(2*pi*q(i)) + q(i)^2.*B*cos(2*pi*q(i)) + ...
            q(i)^2.*sin(phi)/(q(i)^2-1);
        r1(i,:) = roots(eq43,eq44);
        phi_s(i)=r1(i,1) ;
        p_s(i)=r1(i,2) ;

        %%%%%
        A_s=(q(i)*cos(q(i)*pi)*cos(phi_s(i))+(2*q(i)^2-1)*sin(q(i)*pi)...
            *sin(phi_s(i)))/(q(i)^2-1)+ pi*sin(q(i)*pi)/p_s(i)...
            + cos(q(i)*pi)/(q(i)*p_s(i));%substitue solved values of p and phi
        B_s=(-q(i)*sin(q(i)*pi)*cos(phi_s(i))+(2*q(i)^2-1)...
            *cos(q(i)*pi)*sin(phi_s(i)))/(q(i)^2-1)+pi*cos(q(i)*pi)/p_s(i)...
            -sin(q(i)*pi)/(q(i)*p_s(i));%substitue solved values of p and phi

        Vds=1 - A_s*q(i)*p_s(i)*cos(q(i)*wt) + B_s*q(i)*p_s(i)*sin(q(i)*wt) ...
            - q(i)^2*p_s(i)*cos(wt+phi_s(i))/(q(i)^2-1); %calculated VDS(wt)
        VDSmax(i)=max(Vds);                              %calculated VDSmax

        k= (pi^2/(2*p_s(i)) - 2*cos(phi_s(i)) + pi*sin(phi_s(i)))/(2*pi);
        Ids= (wt2/p_s(i) -sin(wt2+phi_s(i)) +sin(phi_s(i)))/k;
        IDSmax(i)=max(Ids);

        Po(i)= 0.5*((pi^2/(2*p_s(i))-2*cos(phi_s(i))+pi*sin(phi_s(i)))/pi)^2;
        cp(i)=1/(VDSmax(i)*IDSmax(i));
    end
```

A.1.2 *Class E at Any Q and D*

```
    function [XC1 ,XC2, VDS, IDS,tON, tOFF, VDSmax, IDSmax, Po, Iin, ...
        cp]=ClassESSnorm(Q, D)

    XLf=1e4;                        %assume Lf is very large
    ron=1e-4;                       %assume rON is very small
    %%%%%
    %solve for C1 and C2 for a given Q and D
    [XC1, XC2]=fsolve(@fun,[5.2,18.8]);
    %%%%%%
    %simulate system
    %%%%%%
    C=eye(4);                       %define C matrix
    sysON=ss(Aon, B, C, 0);         %construct state-space for the ON interval
    sysOFF=ss(Aoff, B, C, 0);       %construct state-space for the OFF interval
    tON=0:pi/100:2*pi*D;            %define ON interval
    tOFF=0:pi/100:2*pi*(1-D);       %define OFF interval
    [xON]=initial(sysON, xinitON, tON) + step(sysON, tON); ...
                                    %state variable for the ON interval
    [xOFF]=initial(sysOFF, xinitOFF, tOFF) + step(sysOFF, tOFF);...
                                    %state variable for the OFF interval
    %%%%%%%
    %denote voltages and currents from state space variables
    VDS=xOFF(:,1);                  %VDS(wt)
    VDSmax=max(VDS);                %VDS max
    Iin=(trapz(tON,xON(:,3))+trapz(tOFF,xOFF(:,3)))/(2*pi); %DC input current
```

```
IDS=xON(:,3)—xON(:,4);          %IDS(wt)
IDSmax=max(IDS)/Iin;            %IDS max
Po=mean(0.5* xON(:,4).*xON(:,4)) + mean(0.5*xOFF(:,4).*xOFF(:,4));...
                                %Output power
cp= 1/(IDSmax*VDSmax);          %cp
function F=fun(x)               %this function solves for C1 and C2 for a given ...
    Q and D
XC1=x(1); XC2=x(2);
%set matrices
Aon=[—XC1/ron, 0, XC1, —XC1 ; 0, 0, 0, XC2 ; —1/XLf, 0, 0, 0 ; 1/Q, —1/Q, 0, —1/Q];
Aoff=Aon; Aoff(1,1)=0; %assuming Roff=inf
B=[0;0;1/XLf;0];
x1=[—expm(Aon*2*pi*D), eye(4) ; eye(4), —expm(Aoff*2*pi*(1—D))];          %temp
x2=[Aon\(expm(Aon*2*pi*D)—eye(4)) ; Aoff\(expm(Aoff*2*pi*(1—D))—eye(4))]; %temp
xinit=x1\(x2*B); %calculate initial conditions
xinitON=xinit(1:4);
xinitOFF=xinit(5:8);
F=[xinit(1);xinit(3)—xinit(4)]; %Define optimum switching conditions
end %fun
end %ClassESSnorm
```

A.1.3 *Sub-optimum Class E*

```
function [D,VDSmax, IDSmax, Po, Iin, cp, tON, tOFF, VDS, ...
    IDS]=ClassESSsub(s,Q,XC1, XC2)

XLf=1e4;                        %assume Lf is very large
ron=1e—4;                       %assume rON is very small
%%%%%
%solve for D for a given Q, C1 and C2
options=optimset('MaxFunEvals',2000, 'MaxIter',2000, 'TolX',1e—9, ...
    'TolFun',1e—9, 'Display','iter');
D=fsolve(@fun,0.625, options);
%%%%%%
sysON=ss(Aon, B, eye(4), 0);        %construct state—space for the ON interval
sysOFF=ss(Aoff, B, eye(4), 0);      %construct state—space for the OFF interval
tON=0:pi/100:2*pi*D;                %define ON interval
tOFF=0:pi/100:2*pi*(1—D);           %define OFF interval
[xON]=initial(sysON, xinitON, tON) + step(sysON, tON);...
                                    %state variable for the ON interval
[xOFF]=initial(sysOFF, xinitOFF, tOFF) + step(sysOFF, tOFF);...
                                    %state variable for the OFF interval
%%%%%%%
VDS=xOFF(:,1);                      %VDS(wt)
VDSmax=max(VDS);                    %VDS max
Iin=(trapz(tON,xON(:,3))+trapz(tOFF,xOFF(:,3))) / (2*pi);%DC input current
IDS=xON(:,3)—xON(:,4);              %IDS(wt)
IDSmax=max(IDS)/Iin;                %IDS max

Po=mean(0.5* xON(:,4).*xON(:,4)) + mean(0.5*xOFF(:,4).*xOFF(:,4));...
                                    %Output power
cp= 1/(IDSmax*VDSmax);              %cp
```

```
function F=fun(x)                    %this functions solves for D for a given ...
    Q,C1,C2
D=x(1);
%set matrices
Aon=[-XC1/ron, 0, XC1, -XC1 ; 0, 0, 0, XC2 ; -1/XLf, 0, 0, 0 ; 1/Q, -1/Q, 0, -s/Q];
Aoff=Aon; Aoff(1,1)=0; %assuming Roff=inf
B=[0;0;1/XLf;0];
x1=[-expm(Aon*2*pi*D), eye(4) ; eye(4), -expm(Aoff*2*pi*(1-D))];            %temp
x2=[Aon\(expm(Aon*2*pi*D)-eye(4)) ; Aoff\(expm(Aoff*2*pi*(1-D))-eye(4))];   %temp
xinit=x1\(x2*B); %calculate initial conditions
xinitON=xinit(1:4);
xinitOFF=xinit(5:8);
F=xinit(1); %Define sub-optimum switching condition
end %fun
end %ClassESS
```

A.2 MATLAB CODES FOR CHAPTER 5

A.2.1 *Design Example*

```
function [C1 ,C2]=ClassESS(ron, q, Lp, R, V, D, f, Ls, Cs, rp, rs, k, rf)
w=2*pi*f;

M=k*sqrt(Lp*Ls);                %calculate mutual inductance M
XCs=1/(w*Cs);                   %calculate inductance of Cs
XL1=w*Lp; XL2=w*Ls; XM=w*M;     %calculate inductances of inductors

[F]=fsolve(@fun,[50,20]);       %solve for C1 and C2 with an initial guess
C1=inv(F(1)*w); C2=inv(F(2)*w); %solved values of C1 and C2

function F=fun(x)
XC1=x(1); XC2=x(2);
XLf=XC1/(q^2);
%set matrices
a=XL1*XL2-XM^2;
Aon=[-XC1/ron, 0, 0, XC1, -XC1, 0 ; 0, 0, 0, 0, XC2, 0; 0, 0, -XCs/R, 0, 0, XCs;...
    -1/XLf, 0, 0, -rf/XLf, 0, 0; XL2/a, -XL2/a, -XM/a, 0, -XL2*rp/a, -XM*rs/a;...
    XM/a, -XM/a, -XL1/a, 0, -XM*rp/a, -XL1*rs/a];
Aoff=Aon; Aoff(1,1)=0;          %assuming Roff=inf
B=[0;0;0;V/XLf;0;0];

x1=[-expm(Aon*2*pi*D), eye(6) ; eye(6), -expm(Aoff*2*pi*(1-D))];
x2=[Aon\(expm(Aon*2*pi*D)-eye(6)) ; Aoff\(expm(Aoff*2*pi*(1-D))-eye(6))];
xinit=x1\(x2*B);                %calculate initial conditions

xinitON=xinit(1:6);
xinitOFF=xinit(7:12);

F=[xinit(1);xinit(4)-xinit(5)]; %Define optimum switching conditions
end %fun
end %ClassESS
```

A.2.2 *Frequency and* L_f *Tuning*

```
%%set parameters%%%
micro=1e6;
Lp=5.76e-6*micro; Ls=6.69e-6*micro;          %microHenries
Cs=5.918e-9*micro;                           %microFarads
R=47;
rp=0.17; rs=0.28; rc=0.25;
C1=22e-9*micro; C2=7.9e-9*micro;
%%%%%%%%%%%%%%%%%%%

%%define domains%%
qdomain = [0.5 2];                           % q domain
pdomain = [0.01 25];                         % p domain
phidomain = [0 2*pi];                        % phi domain
kdomain=[0.1 0.4];                           %coupling coefficient domain
wdomain=[2*pi*5e5/micro 2*pi*1e6/micro];     %switching frequency domain
wtdomain=[pi 2*pi];                          %time domain
V1=[wdomain kdomain];
V2= [phidomain  pdomain];
%%%%%%%%%%%%%%%%%%%

%%define chebfuns
w=chebfun2(@(w,k) w, V1);
k=chebfun2(@(w,k) k, V1);
phi=chebfun2(@(phi,p) phi, V2);
p=chebfun2(@(phi,p) p, V2);
wt=chebfun('wt', wtdomain);

%initialise loop varaibles
ni=40; %number of data points
q=qdomain(1):diff(qdomain)/ni:qdomain(2);
r1=zeros(ni,2);
r2=zeros(ni,2);
p_s=zeros(ni,1);
phi_s=zeros(ni,1);
w_s=zeros(ni,1);
k_s=zeros(ni,1);


    M=k*(sqrt(Lp*Ls));
    z_ref = ((1.*M.*w).^2)./(1i.*w*Ls+rs+R.*(rc-1i./(Cs.*w))./(R+rc-1i./(Cs.*w)));
    Rt = rp + real(z_ref);
    Xb = w*Lp + imag(z_ref) - 1./(w*C2);
%%%loop begins
for i=1:ni
%%%%%%%%%%%%%%%%%%
% this section of the loop solves equations 43 and 44 for p and phi as a
% function of q
    A=(q(i)*cos(q(i)*pi).*cos(phi)+(2*q(i)^2-1)*sin(q(i)*pi).*sin(phi))/(q(i)^2-1)...
        + pi*sin(q(i)*pi)./p + cos(q(i)*pi)./(q(i)*p);
    B=(-q(i)*sin(q(i)*pi).*cos(phi)+(2*q(i)^2-1)*cos(q(i)*pi).*sin(phi))/(q(i)^2-1)...
        + pi*cos(q(i)*pi)./p -sin(q(i)*pi)./(q(i)*p);
    eq43=1-q(i).*A.*p*cos(2*pi*q(i)) +q(i).*B.*p*sin(2*pi*q(i)) - ...
        q(i)^2.*p.*cos(phi)/(q(i)^2-1);
```

```
        eq44=q(i)^2.*A*sin(2*pi*q(i)) + q(i)^2.*B*cos(2*pi*q(i)) + ...
            q(i)^2.*sin(phi)/(q(i)^2-1);
        r1(i,:) = roots(eq43,eq44);
        phi_s(i)=r1(i,1) ;                          %solved values of phi
        p_s(i)=r1(i,2) ;                            %solved values of p
        %%%%
    %%%%%%%%%%%%%%%%%%%%%%
    %the solved values of p and phi and q are used to solve for the frequency w
    %and k using equations 2, 34, 41, 42, 46, 47 and 48
       A_s=(q(i)*cos(q(i)*pi)*cos(phi_s(i))+(2*q(i)^2-1)*sin(q(i)*pi)...
            *sin(phi_s(i)))/(q(i)^2-1)+ pi*sin(q(i)*pi)/p_s(i)...
            + cos(q(i)*pi)/(q(i)*p_s(i));%substitue solved values of p and phi
        B_s=(-q(i)*sin(q(i)*pi)*cos(phi_s(i))+(2*q(i)^2-1)...
            *cos(q(i)*pi)*sin(phi_s(i)))/(q(i)^2-1)+pi*cos(q(i)*pi)/p_s(i)...
            -sin(q(i)*pi)/(q(i)*p_s(i));%substitue solved values of p and phi

        Vds=1 - A_s*q(i)*p_s(i)*cos(q(i)*wt) + B_s*q(i)*p_s(i)*sin(q(i)*wt) ...
            - q(i)^2*p_s(i)*cos(wt+phi_s(i))/(q(i)^2-1); %calculated VDS(wt)
    %
    %     M=k*(sqrt(Lp*Ls));
    %     z_ref = ...
         ((1.*M.*w).^2)./(1i.*w*Ls+rs+R.*(rc-1i./(Cs.*w))./(R+rc-1i./(Cs.*w)));
    %     Rt = rp + real(z_ref);
    %     Xb = w*Lp + imag(z_ref) - 1./(w*C2);

        vm=sum(Vds.*sin(wt+phi_s(i)))/pi;
        vxm=sum(Vds.*cos(wt+phi_s(i)))/pi;

        eq48=Rt*vxm/vm - Xb;
        eq41=p_s(i)/(0.5*pi/p_s(i) - 2*cos(phi_s(i))/pi + sin(phi_s(i))) - ...
            1./(q(i)^2.*w.*Rt.*C1);

        r2(i,:)=roots(eq48,eq41);
        w_s(i)=r2(i,1);                             %solved values of w
        k_s(i)=r2(i,2);                             %solved values of k
    end%for

    %plot results
    figure
    plot(k_s,w_s/(2*pi))
    ylabel('frequency (kHz)'), xlabel('k')
    axis([0.15 0.4 0.6 0.9])
    grid

    q=q(1:40)';
    Lf=1./(q.^2.*w_s.^2*C1);
    M_s=k_s.*(sqrt(Lp*Ls));
    z_ref_s = ...
         ((1.*M_s.*w_s).^2)./(1i.*w_s*Ls+rs+R.*(rc-1i./(Cs.*w_s))./(R+rc-1i./(Cs.*w_s)));
    Rt_s=real(z_ref_s);
    XLs=w_s*Ls;
    XCs=1./(Cs.*w_s);
    a=R*(rs+rc) + rs*rc+XLs.*XCs;
    b=R.*(XLs-XCs)+XLs*rc-XCs*rs;
    XM=M_s.*w_s;
    R_ref=XM.^2.*XCs.^2*R./(a.^2+b.^2);
    r_ref=XM.^2.*(R^2*(rs+rc)+2*R*rs*rc+R*rc^2+rs*rc^2+XCs.^2*rs)./(a.^2+b.^2);
```

A.2.3 *Duty Cycle and L_f Tuning*

```
function [Lf ,D]=ClassESSDLfTuning(ron, Lp, R, V, f, Ls, Cs, rp, rs, k, rf)
w=2*pi*f;
M=k*sqrt(Lp*Ls);                %calculate mutual inductance M
XCs=1/(w*Cs);                   %calculate inductance of Cs
XL1=w*Lp; XL2=w*Ls; XM=w*M;     %calculate inductances of inductors
[F]=fsolve(@fun,[5,0.5]);       %solve for XLf and D with an initial guess
Lf=F(1)/w; D=F(2);              %solved values of Lf and D

function F=fun(x)
XLf=x(1); D=x(2);

%set matrices
a=XL1*XL2-XM^2;
Aon=[-XC1/ron, 0, 0, XC1, -XC1, 0 ; 0, 0, 0, 0, XC2, 0; 0, 0, -XCs/R, 0, 0, XCs;...
    -1/XLf, 0, 0, -rf/XLf, 0, 0; XL2/a, -XL2/a, -XM/a, 0, -XL2*rp/a, -XM*rs/a;...
    XM/a, -XM/a, -XL1/a, 0, -XM*rp/a, -XL1*rs/a];
Aoff=Aon; Aoff(1,1)=0;          %assuming Roff=inf
B=[0;0;0;V/XLf;0;0];

x1=[-expm(Aon*2*pi*D), eye(6) ; eye(6), -expm(Aoff*2*pi*(1-D))];
x2=[Aon\(expm(Aon*2*pi*D)-eye(6)) ; Aoff\(expm(Aoff*2*pi*(1-D))-eye(6))];
xinit=x1\(x2*B);                %calculate initial conditions

xinitON=xinit(1:6);
xinitOFF=xinit(7:12);

F=[xinit(1);xinit(4)-xinit(5)]; %Define optimum switching conditions
end %fun
end %ClassESS
```

A.3 MATLAB CODES FOR CHAPTER 6

A.3.1 *Class E Rectifier Duty Cycle, Phase and Output Voltage*

```
function [Vo, phi, D, xinitON, xinitOFF]=ClassErectSS(Vm,ron, rL,L,Co,R)

w=2*pi*f;                               %calculate frequency
C=1/(w^2*L);                            %calculate value of resonant capacitor C

[F]=fsolve(@fun,[0.5,-1.2]);            %solve for D and phi with an initial guess
D=F(1); phi=F(2);                       %solved values of duty cycle and phi
Vo=(xinitOFF(3)+xinitON(3))/2;          %calculate output voltage
function F=fun(x)
D=x(1); phi=x(2);
%set Matrices
Aon=[-rL/(w*L), -1/(w*L), -1/(w*L) ; 1/(w*C), -1/(w*C*ron), 0 ;...
```

```
    1/(w*Co), 0, -1/(w*Co*R) ];
Aoff=[-rL/(w*L), -1/(w*L), -1/(w*L) ; 1/(w*C), 0, 0 ;...
    1/(w*Co), 0, -1/(w*R*Co)];
B1=[ Vm/(w*L) ;0 ;0 ];
B2=[0; Vf/(w*C*ron);0];
Bon=[B1,B2];
Boff=B1;

kon= Aon\(expm(Aon*2*pi*D)-eye(3))*B2  + (Aon*Aon+eye(3))\...
    (expm(Aon*2*pi*D)*(eye(3)*cos(phi+2*pi*(1-D)) + Aon*sin(phi+2*pi*(1-D)))...
    -cos(2*pi*D+phi+2*pi*(1-D))*eye(3) - Aon*sin(2*pi*D+phi+2*pi*(1-D)))*B1;

koff=(Aoff*Aoff+eye(3))\(expm(Aoff*2*pi*(1-D))*(eye(3)*cos(phi) + Aoff*sin(phi))...
    - cos(2*pi*(1-D)+phi)*eye(3) - Aoff*sin(2*pi*(1-D)+phi))*B1;

x1=[ -expm(Aon*2*pi*D) , eye(3) ; eye(3), -expm(Aoff*2*pi*(1-D))];
x2=[ kon ; koff ];

xinit= x1\x2;                          %calculate initial conditions
xinitON=xinit(1:3); xinitOFF=xinit(4:6);
F=[xinit(2)-Vf ;xinit(5)-Vf];          %define optimum switching conditions

end %fun
end %ClassESS
```

A.3.2 *Class E Rectifier Input RMS Current and PF*

```
function [Xrmsn, PF]=ClassErectnormRMS(Aon, Aoff, Bon, Boff, xinitON, xinitOFF, ...
    D, phi,R,Vm,rL, Vf, ron)

%define time domain function for the ON state
Xon=@(wt) [(Aon*Aon+eye(3))\(expm(Aon*wt)*(eye(3)*cos(phi+2*pi*(1-D)) + ...
    Aon*sin(phi+2*pi*(1-D)))...
    -cos(wt+phi+2*pi*(1-D))*eye(3) - Aon*sin(wt+phi+2*pi*(1-D)))...
    , Aon\(expm(Aon*wt)-eye(3))]*Bon + expm(Aon*wt)*xinitON ;
X2on=@(wt) Xon(wt).*Xon(wt);                    %squared

%define time domain function for the OFF state
Xoff=@(wt) (Aoff*Aoff+eye(3))\(expm(Aoff*wt)*(eye(3)*cos(phi) + Aoff*sin(phi)) ...
    - cos(wt+phi)*eye(3) - Aoff*sin(wt+phi))*Boff + expm(Aoff*wt)*xinitOFF;
X2off=@(wt) Xoff(wt).*Xoff(wt);                 %squared

Xrmsn=sqrt( 1/(2*pi) *( integral(X2on,0,2*pi*D, 'ArrayValued',true) + ...
    integral(X2off,0,2*pi*(1-D),'ArrayValued',true)));  %calculate normalised ...
        input RMS current

PF=acos( sqrt(2)*(Xrms(3)^2/R + Xrms(1)^2*rL + Vf*Xrms(3)/R ...
    +(Xrms(3)/R)^2*ron )/(Vm*Xrms(1))  );       %calculate power factor
end
```

A.3.3 *Class E Rectifier THD*

```
function [THD]=ClassErectTHD(Aon, Aoff, Bon, Boff, xinitON, xinitOFF, D, phi)

k=5;                                    %number of harmonics to calculate
%initialise matrices
an=zeros(3,k);                          %An fourier series coefficient
bn=zeros(3,k);                          %Bn fourier series coefficient
cn=zeros(3,k);                          %Cn fourier series coefficient
Pin=0;                                  %input power
%set time domain funtion for the ON state
Xon=@(wt) [(Aon*Aon+eye(3))\(expm(Aon*wt)*(eye(3)*cos(phi+2*pi*(1-D)) + ...
    Aon*sin(phi+2*pi*(1-D)))-cos(wt+phi+2*pi*(1-D))*eye(3) - ...
    Aon*sin(wt+phi+2*pi*(1-D)))...
    , Aon\(expm(Aon*wt)-eye(3))]*Bon + expm(Aon*wt)*xinitON ;
%set time domain funtion for the OFF state
Xoff=@(wt) (Aoff*Aoff+eye(3))\(expm(Aoff*wt)*(eye(3)*cos(phi) + Aoff*sin(phi)) ...
    - cos(wt+phi)*eye(3) - Aoff*sin(wt+phi))*Boff + expm(Aoff*wt)*xinitOFF;

for n=1:1:k
    %define fourier series integral functions
    Xaon=@(wt) Xon(wt).*cos(n*(wt+phi+2*pi*(1-D)));
    Xbon=@(wt) Xon(wt).*sin(n*(wt+phi+2*pi*(1-D)));

    Xaoff=@(wt) Xoff(wt).*cos(n*(wt+phi));
    Xboff=@(wt) Xoff(wt).*sin(n*(wt+phi));

    an(:,n)=(integral(Xaon,0, 2*pi*D, ...
        'ArrayValued',true)+integral(Xaoff,0,2*pi*(1-D), 'ArrayValued',true))/pi;
    bn(:,n)=(integral(Xbon,0, 2*pi*D, ...
        'ArrayValued',true)+integral(Xboff,0,2*pi*(1-D), 'ArrayValued',true))/pi;
    cn(:,n)=sqrt(an(:,n).^2+bn(:,n).^2);
    %Pin=Pin+cn(:,n).*cos(psi(:,n));
    Pin=Pin+cn(:,n).^2;
end
THD= sqrt(Pin-cn(:,1).^2)./cn(:,1);     %calculate THD
end
```

A.4 MATLAB CODES FOR CHAPTER 7

A.4.1 *Class E^2 DC/DC Converter*

```
function [C1, C2, D2, phi, a, c]=ClassEDCDC1(ron1, ron2,rp, rs, Lf,  Lp, Ls, k, ...
    C3, C4, R,  V, f)

[F]=fsolve(@fun2,[0.06, 0.06, 0.147, 0.63]);            %solve for wC1, wC2, a ...
    and c
wC1=F(1); wC2=F(2); a=F(3); c=F(4);
```

```
5
C1=wC1/w;                                                   %calculate C1
C2=wC2/w;                                                   %calculate C2
D2=1-c+a;                                                   %calculate D2
phi=360*c;                                                  %calculate Phi
10


function F=fun2(x)
wC1=x(1); wC2=x(2); a=x(3); c=x(4);
b=0.5;                                                      %assume D1=0.5
15 w=2*pi*f;
M=k*sqrt(Lp*Ls);
alpha=w^2*(Lp*Ls-M^2);
%set matrices
A=[ -1/(wC1*ron1), 0, 0, 0, 1/(wC1), -1/(wC1), 0;...       %x1dot
20     0, 0, 0, 0, 0, 1/(wC2), 0;...                        %x2dot
       0, 0, -1/(w*C3*ron2), 0, 0,0,  1/(w*C3);...          %x3dot
       0, 0, 0, -1/(w*C4*R), 0, 0, 1/(w*C4);...             %x4dot
       -1/(w*Lf), 0, 0, 0, 0, 0, 0;...                      %x5dot
       w*Ls/alpha, -w*Ls/alpha, -w*M/alpha, -w*M/alpha, 0, -w*Ls*rp/alpha, ...
           -w*M*rs/alpha;...   %x6dot
25     w*M/alpha, -w*M/alpha, -w*Lp/alpha, -w*Lp/alpha, 0, -w*M*rp/alpha, ...
           -w*Lp*rs/alpha];

B=[0; 0; 0; 0; V/(w*Lf); 0; 0];

AONON=A;
30 AONOFF=A; AONOFF(3,3)=0;
AOFFOFF=A; AOFFOFF(1,1)=0; AOFFOFF(3,3)=0;
AOFFON=A; AOFFON(1,1)=0;

kONON=AONON\((expm(AONON*2*pi*a)-eye(7))*B);
35 kONOFF=AONOFF\((expm(AONOFF*2*pi*(b-a))-eye(7))*B);
kOFFOFF=AOFFOFF\((expm(AOFFOFF*2*pi*(c-b))-eye(7))*B);
kOFFON=AOFFON\((expm(AOFFON*2*pi*(1-c))-eye(7))*B);

x1=[-expm(AONON*2*pi*a), eye(7), zeros(7), zeros(7);...
40     zeros(7), -expm(AONOFF*2*pi*(b-a)), eye(7), zeros(7);...
       zeros(7), zeros(7), -expm(AOFFOFF*2*pi*(c-b)), eye(7);...
       eye(7), zeros(7), zeros(7), -expm(AOFFON*2*pi*(1-c))];

x2=[kONON; kONOFF; kOFFOFF;kOFFON];
45 xinit=pinv(x1)*x2;
xinitONON=xinit(1:7);                              %set optimum switching conditions
xinitONOFF=xinit(8:14);
xinitOFFOFF=xinit(15:21);
xinitOFFON=xinit(22:28);
50

F=[xinitONON(1) ; xinitONON(5)-xinitONON(6) ; xinitONOFF(3) ; xinitOFFON(3)];
end

end
```

B

DATASHEETS

STP40NF10

N-channel 100 V, 0.025 Ω, 50 A TO-220 low gate charge STripFET™ II Power MOSFET

Features

Order code	V_{DSS}	$R_{DS(on)}$ max.	I_D
STP40NF10	100 V	< 0.028 Ω	50 A

- Exceptional dv/dt capability
- Low gate charge
- 100% avalanche tested

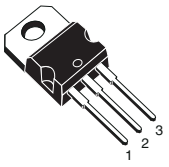

TO-220

Application

Switching applications

Description

This N-channel 100 V Power MOSFET is the latest development of STMicroelectronics unique "single feature size" strip-based process. The resulting transistor shows extremely high packing density for low on-resistance, rugged avalanche characteristics and less critical alignment steps allowing remarkable manufacturing reproducibility.

Figure 1. Internal schematic diagram

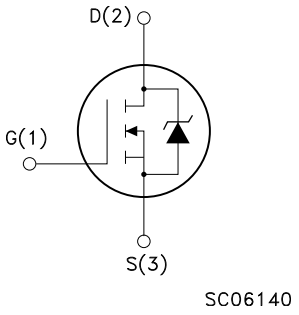

Table 1. Device summary

Order code	Marking	Package	Packaging
STP40NF10	P40NF10@	TO-220	Tube

1 Electrical ratings

Table 2. Absolute maximum ratings

Symbol	Parameter	Value	Unit
V_{DS}	Drain-source voltage (V_{GS} = 0)	100	V
V_{GS}	Gate- source voltage	±20	V
I_D (1)	Drain current (continuous) at T_C = 25 °C	50	A
I_D	Drain current (continuous) at T_C = 100 °C	35	A
I_{DM} (2)	Drain current (pulsed)	200	A
P_{TOT}	Total dissipation at T_C = 25 °C	150	W
	Derating factor	1	W/°C
dv/dt(3)	Peak diode recovery voltage slope	27	V/ns
E_{AS} (4)	Single pulse avalanche energy	385	mJ
T_{stg}	Storage temperature	- 55 to 175	°C
T_j	Max. operating junction temperature		

1. Limited by wire bonding
2. Pulse width limited by safe operating area
3. $I_{SD} \leq 50$ A, di/dt ≤600 A/µs, $V_{DD} \leq V_{(BR)DSS}$, $T_j \leq T_{JMAX.}$
4. Starting T_j= 25 °C, I_D= 50 A, V_{DD}=25 V

Table 3. Thermal data

Symbol	Parameter	Value	Unit
$R_{thj\text{-}case}$	Thermal resistance junction-case max	1	°C/W
$R_{thj\text{-}a}$	Thermal resistance junction-ambient max	62.5	°C/W
T_l	Maximum lead temperature for soldering purpose	300	°C

Power MOSFET

PRODUCT SUMMARY		
V_{DS} (V)	100	
$R_{DS(on)}$ (Ω)	V_{GS} = 10 V	0.077
Q_g (Max.) (nC)	72	
Q_{gs} (nC)	11	
Q_{gd} (nC)	32	
Configuration	Single	

TO-220AB

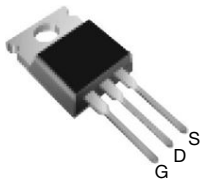

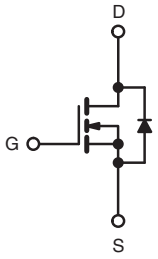

N-Channel MOSFET

FEATURES

- Dynamic dV/dt Rating
- Repetitive Avalanche Rated
- 175 °C Operating Temperature
- Fast Switching
- Ease of Paralleling
- Simple Drive Requirements
- Compliant to RoHS Directive 2002/95/EC

Available
RoHS* COMPLIANT

DESCRIPTION

Third generation Power MOSFETs from Vishay provide the designer with the best combination of fast switching, ruggedized device design, low on-resistance and cost-effectiveness.

The TO-220AB package is universally preferred for all commercial-industrial applications at power dissipation levels to approximately 50 W. The low thermal resistance and low package cost of the TO-220AB contribute to its wide acceptance throughout the industry.

ORDERING INFORMATION	
Package	TO-220AB
Lead (Pb)-free	IRF540PbF
	SiHF540-E3
SnPb	IRF540
	SiHF540

ABSOLUTE MAXIMUM RATINGS (T_C = 25 °C, unless otherwise noted)

PARAMETER			SYMBOL	LIMIT	UNIT
Drain-Source Voltage			V_{DS}	100	V
Gate-Source Voltage			V_{GS}	± 20	
Continuous Drain Current	V_{GS} at 10 V	T_C = 25 °C	I_D	28	A
		T_C = 100 °C		20	
Pulsed Drain Current[a]			I_{DM}	110	
Linear Derating Factor				1.0	W/°C
Single Pulse Avalanche Energy[b]			E_{AS}	230	mJ
Repetitive Avalanche Current[a]			I_{AR}	28	A
Repetitive Avalanche Energy[a]			E_{AR}	15	mJ
Maximum Power Dissipation	T_C = 25 °C		P_D	150	W
Peak Diode Recovery dV/dt[c]			dV/dt	5.5	V/ns
Operating Junction and Storage Temperature Range			T_J, T_{stg}	- 55 to + 175	°C
Soldering Recommendations (Peak Temperature)	for 10 s			300[d]	
Mounting Torque	6-32 or M3 screw			10	lbf · in
				1.1	N · m

Notes

a. Repetitive rating; pulse width limited by maximum junction temperature (see fig. 11).
b. V_{DD} = 25 V, starting T_J = 25 °C, L = 440 µH, R_g = 25 Ω, I_{AS} = 28 A (see fig. 12).
c. I_{SD} ≤ 28 A, dI/dt ≤ 170 A/µs, V_{DD} ≤ V_{DS}, T_J ≤ 175 °C.
d. 1.6 mm from case.

* Pb containing terminations are not RoHS compliant, exemptions may apply

THERMAL RESISTANCE RATINGS				
PARAMETER	**SYMBOL**	**TYP.**	**MAX.**	**UNIT**
Maximum Junction-to-Ambient	R_{thJA}	-	62	°C/W
Case-to-Sink, Flat, Greased Surface	R_{thCS}	0.50	-	
Maximum Junction-to-Case (Drain)	R_{thJC}	-	1.0	

SPECIFICATIONS (T_J = 25 °C, unless otherwise noted)							
PARAMETER	**SYMBOL**	**TEST CONDITIONS**		**MIN.**	**TYP.**	**MAX.**	**UNIT**
Static							
Drain-Source Breakdown Voltage	V_{DS}	V_{GS} = 0 V, I_D = 250 µA		100	-	-	V
V_{DS} Temperature Coefficient	$\Delta V_{DS}/T_J$	Reference to 25 °C, I_D = 1 mA		-	0.13	-	V/°C
Gate-Source Threshold Voltage	$V_{GS(th)}$	V_{DS} = V_{GS}, I_D = 250 µA		2.0	-	4.0	V
Gate-Source Leakage	I_{GSS}	V_{GS} = ± 20 V		-	-	± 100	nA
Zero Gate Voltage Drain Current	I_{DSS}	V_{DS} = 100 V, V_{GS} = 0 V		-	-	25	µA
		V_{DS} = 80 V, V_{GS} = 0 V, T_J = 150 °C		-	-	250	
Drain-Source On-State Resistance	$R_{DS(on)}$	V_{GS} = 10 V	I_D = 17 A[b]	-	-	0.077	Ω
Forward Transconductance	g_{fs}	V_{DS} = 50 V, I_D = 17 A[b]		8.7	-	-	S
Dynamic							
Input Capacitance	C_{iss}	V_{GS} = 0 V,		-	1700	-	pF
Output Capacitance	C_{oss}	V_{DS} = 25 V,		-	560	-	
Reverse Transfer Capacitance	C_{rss}	f = 1.0 MHz, see fig. 5		-	120	-	
Total Gate Charge	Q_g	V_{GS} = 10 V	I_D = 17 A, V_{DS} = 80 V, see fig. 6 and 13[b]	-	-	72	nC
Gate-Source Charge	Q_{gs}			-	-	11	
Gate-Drain Charge	Q_{gd}			-	-	32	
Turn-On Delay Time	$t_{d(on)}$	V_{DD} = 50 V, I_D = 17 A R_g = 9.1 Ω, R_D = 2.9 Ω, see fig. 10[b]		-	11	-	ns
Rise Time	t_r			-	44	-	
Turn-Off Delay Time	$t_{d(off)}$			-	53	-	
Fall Time	t_f			-	43	-	
Internal Drain Inductance	L_D	Between lead, 6 mm (0.25") from package and center of die contact 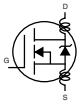		-	4.5	-	nH
Internal Source Inductance	L_S			-	7.5	-	
Drain-Source Body Diode Characteristics							
Continuous Source-Drain Diode Current	I_S	MOSFET symbol showing the integral reverse p - n junction diode 		-	-	28	A
Pulsed Diode Forward Current[a]	I_{SM}			-	-	110	
Body Diode Voltage	V_{SD}	T_J = 25 °C, I_S = 28 A, V_{GS} = 0 V[b]		-	-	2.5	V
Body Diode Reverse Recovery Time	t_{rr}	T_J = 25 °C, I_F = 17 A, dI/dt = 100 A/µs[b]		-	180	360	ns
Body Diode Reverse Recovery Charge	Q_{rr}			-	1.3	2.8	µC
Forward Turn-On Time	t_{on}	Intrinsic turn-on time is negligible (turn-on is dominated by L_S and L_D)					

Notes

a. Repetitive rating; pulse width limited by maximum junction temperature (see fig. 11).

b. Pulse width ≤ 300 µs; duty cycle ≤ 2 %.

FAIRCHILD SEMICONDUCTOR®

SB320 - SB3100

Features

- 3.0 ampere operation at T_A = 75°C with no thermal runaway.
- For use in low voltage, high frequency inverters free wheeling, and polarity protection applications.

DO-201AD
COLOR BAND DENOTES CATHODE

Schottky Rectifiers

Absolute Maximum Ratings* T_A = 25°C unless otherwise noted

Symbol	Parameter	Value							Units
		320	330	340	350	360	380	3100	
V_{RRM}	Maximum Repetitive Reverse Voltage	20	30	40	50	60	80	100	V
$I_{F(AV)}$	Average Rectified Forward Current .375 " lead length @ T_A = 75°C	3.0							A
I_{FSM}	Non-repetitive Peak Forward Surge Current 8.3 ms Single Half-Sine-Wave	80							A
T_{stg}	Storage Temperature Range	-65 to +125							°C
T_J	Operating Junction Temperature	-65 to +125							°C

*These ratings are limiting values above which the serviceability of any semiconductor device may be impaired.

Thermal Characteristics

Symbol	Parameter	Value	Units
P_D	Power Dissipation	3.6	W
$R_{\theta JA}$	Thermal Resistance, Junction to Ambient	40	°C/W

Electrical Characteristics T_A = 25°C unless otherwise noted

Symbol	Parameter	Device							Units
		320	330	340	350	360	380	3100	
V_F	Forward Voltage @ 3.0 A	500			740		850		mV
I_R	Reverse Current @ rated V_R T_A = 25°C	0.5							mA
	T_A = 100°C	20			10		10		mA
I_{rr}	Maximum Full Load Reverse Current, Full Cycle T_A = 100°C	30							mA
C_T	Total Capacitance V_R = 4.0 V, f = 1.0 MHz	180							pF

Typical Characteristics

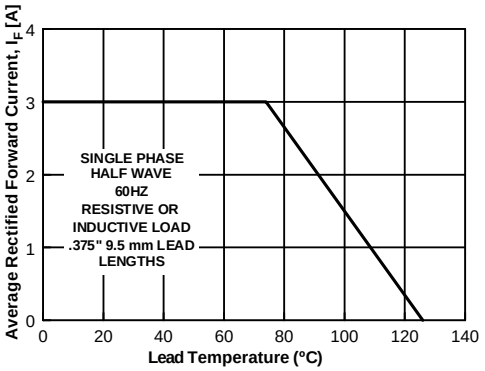

Figure 1. Forward Current Derating Curve

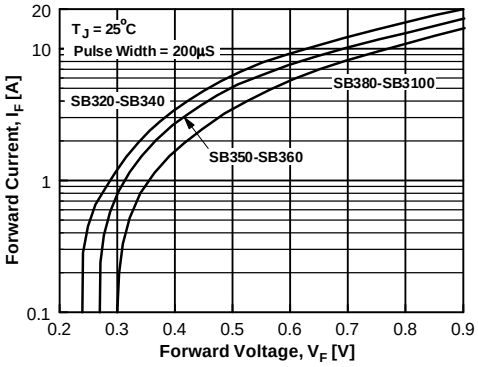

Figure 2. Forward Voltage Characteristics

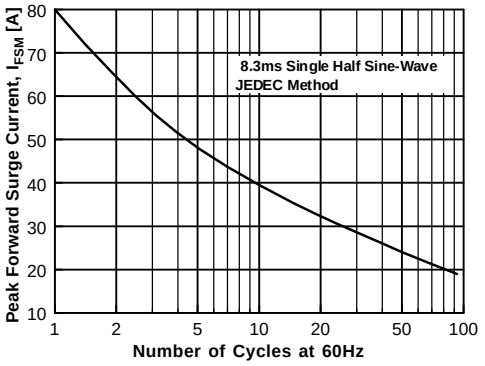

Figure 3. Non-Repetitive Surge Current

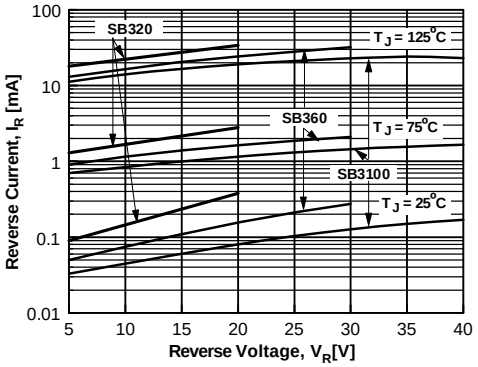

Figure 4. Reverse Current vs Reverse Voltage

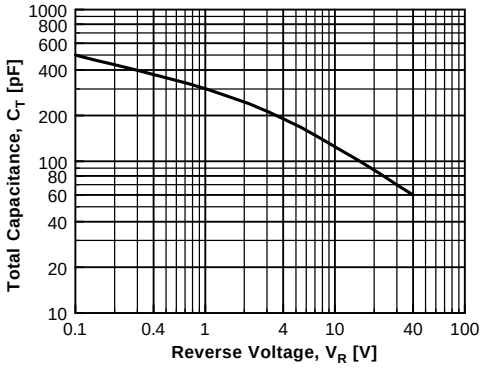

Figure 5. Total Capacitance

TC1412/TC1412N

2A High-Speed MOSFET Drivers

Features

- Latch-Up Protected: Will Withstand 500 mA Reverse Current
- Input Will Withstand Negative Inputs Up to 5V
- ESD Protected: 4 kV
- High Peak Output Current: 2A
- Wide Input Supply Voltage Operating Range:
  - 4.5V to 16V
- High Capacitive Load Drive Capability:
  - 1000 pF in 18 nsec
- Short Delay Time: 35 nsec Typ.
- Matched Delay Times
- Low Supply Current:
  - With Logic '1' Input: 500 µA
  - With Logic '0' Input: 100 µA
- Low Output Impedance: 4Ω
- Available in Space-Saving 8-pin MSOP Package
- Pinout Same as TC1410/TC1411/TC1413

Applications

- Switch Mode Power Supplies
- Pulse Transformer Drive
- Line Drivers
- Relay Driver

Package Type

8-Pin MSOP/PDIP/SOIC

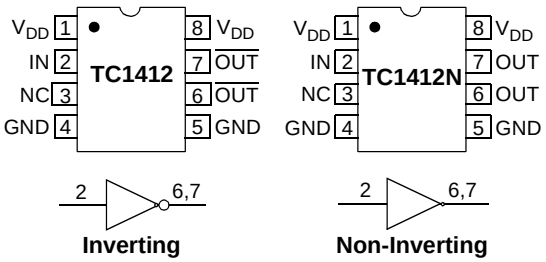

NC = No Internal Connection

NOTE: Duplicate pins must be connected together for proper operation.

General Description

The TC1412/TC1412N are 2A CMOS buffers/drivers. They will not latch-up under any conditions within their power and voltage ratings. They are not subject to damage when up to 5V of noise spiking of either polarity occurs on the ground pin. They can accept, without damage or logic upset, up to 500 mA of current of either polarity being forced back into their output. All terminals are fully protected against up to 4 kV of electrostatic discharge.

As MOSFET drivers, the TC1412/TC1412N can easily charge a 1000 pF gate capacitance in 18 nsec with matched rise and fall times, and provide low enough impedance in both the ON and the OFF states to ensure the MOSFET's intended state will not be affected, even by large transients. The leading and trailing edge propagation delay times are also matched to allow driving short-duration inputs with greater accuracy.

General Purpose, Pulse and DC Transient Suppression

PHE450 Series Double Metallized Polypropylene Film

The Capacitance Company
KEMET CHARGED.

Overview

The PHE450 Series is a polypropylene dielectric with double metallized polyester film as electrodes. The capacitor is encapsulated in self-extinguishing resin in a box of material meeting the requirements of UL 94 V–0.

Applications

Typical applications include high frequency applications with high current stress such as deflection circuits in televisions and protection circuits in switched mode power supply (SMPS) and electronic ballasts.

Benefits

- Rated voltage: 250 – 3,000 VDC
- Rated voltage: 180 – 1,000 VAC
- Capacitance range: 0.00033 – 10 µF
- Lead spacing: 7.5 – 37.5 mm
- Capacitance tolerance: ±5%, other tolerances on request
- Climatic category: 55/105/56, IEC 60068–1
- Tape and reel packaging in accordance with IEC 60286–2
- RoHS Compliant and lead-free terminations
- Category temperature range of -55˚C to +105˚C

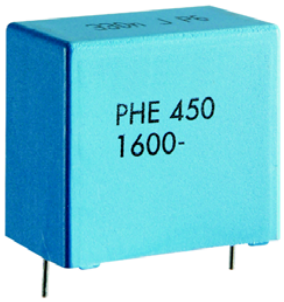

Legacy Part Number System

PHE450	P	B	5180	J	B04	R06
Series	Rated Voltage (VDC)	Lead Spacing (mm)	Capacitance Code (pF)	Capacitance Tolerance	Optional Box Code	Lead and Packaging Code
Metallized Polypropylene	H = 250 K = 400 M = 630 P = 1000 R = 1600 S = 2000 T = 2500 X = 3000	K = 7.5 A = 10.0 B = 15.0 D = 22.5 F = 27.5 R = 37.5	Digits 2 – 4 indicate the first three digits of the capacitance value. First digit indicates the number of zeros to be added.	J = ±5% On request: F = ±1% G = ±2% H = ±2.5% K = ±10% M = ±20%	See Dimension Table	See Ordering Options Table

New KEMET Part Number System

F	450	B	D	183	J	1K0	C
Capacitor Class	Series	Lead Spacing (mm)	Size Code	Capacitance Code (pF)	Capacitance Tolerance	Rated Voltage (VDC)	Lead and Packaging Code
F = Film	Metallized Polypropylene	K = 7.5 A = 10.0 B = 15.0 D = 22.5 F = 27.5 R = 37.5	See Dimension Table	First two digits indicate the two most significant digits of the capacitance value in picofarads. The third digit is the number of following zeros.	J = ±5% On request: F = ±1% G = ±2% H = ±2.5% K = ±10% M = ±20%	250 = 250 400 = 400 630 = 630 1K0 = 1000 1K6 = 1600 2K0 = 2000 2K5 = 2500 3K0 = 3000	See Ordering Options Table

Performance Characteristics

Sections	1	1	1	2	1	2	2	2	3	3
Voltage Range (VDC)	250	400	630	630	1000	1000	1600	2000	2500	3000
Voltage Range (VAC)	180	250	300	400	375	600	650	700	900	1000
Capacitance Range (µF)	0.00033 – 0.033	0.00033 – 5.6	0.00033 – 0.039	0.01 – 3.3	0.00033 – 0.018	0.0039 – 2.2	0.0027 – 1	0.001 – 0.68	0.0010 – 0.33	0.001 – 0.033

Capacitance Values	In accordance with IEC E12 series
Capacitance Tolerance	±5%, other tolerances on request
Category Temperature Range	-55°C to +105°C
Rated Temperature	+85°C
Voltage Derating	The rated voltage is decreased with 1.3%/°C between +85°C and +105°C
Climatic Category	IEC 60068–1, 55/105/56/B
Passive Flammability	Category B according to IEC 60065
Maximum Pulse Steepness	dV/dt according to Table 1. For peak to peak voltages lower than rated voltage ($V_{PP} < V_R$), the specified dV/dt can be multiplied by the factor V_R/V_{PP}.
Self-Inductance	Approximately 6 nH/cm for the total length of capacitor winding and the leads

Dissipation Factor tanδ

Maximum Values at +23°C			
	C ≤ 0.1 µF	0.1 µF < C ≤ 1.0 µF	C > 1.0 µF
1 kHz	0.0003	0.0003	0.0003
10 kHz	0.0004	0.0006	–
100 kHz	0.0015	–	–

Insulation Resistance

Measured at +23°C, 100 VDC 60 seconds for V_R < 500 VDC and at 500 VDC for V_R ≥ 500 VDC

Minimum Values Between Terminals	
C ≤ 0.33 µF	≥ 100 000 MΩ
C > 0.33 µF	≥ 30 000 MΩ • µF
Minimum Values Between Terminals and Case	
	≥ 100 000 MΩ

Derating of V_{rms} vs. Frequency, +85ºC Ambient Temperature and 10ºC Internal Heating, Typical Values

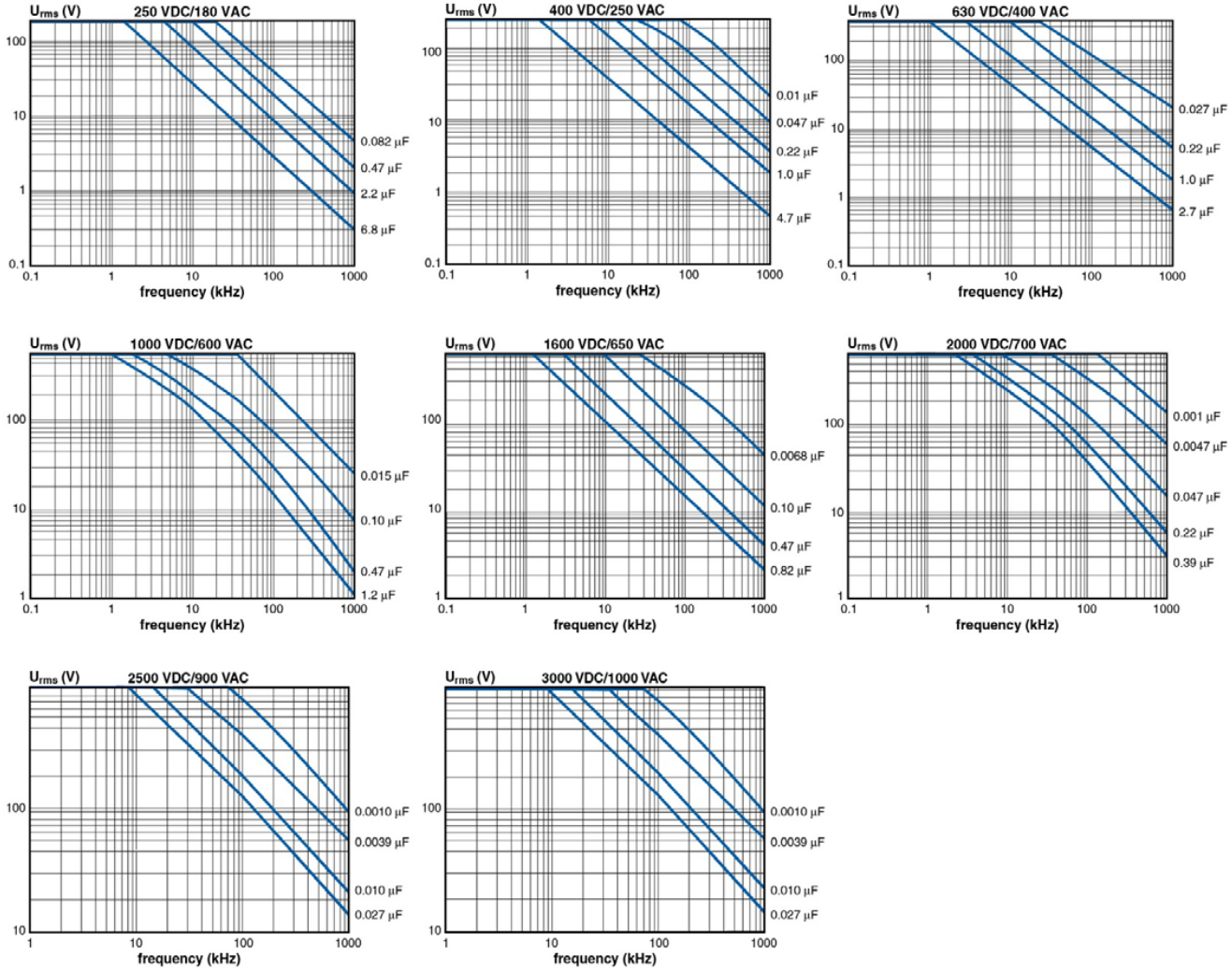

3C90 SPECIFICATIONS

A low frequency power material for use in power and general purpose transformers at frequencies up to 0.2 MHz.

	CONDITIONS	VALUE	UNIT
μ_i	25 °C; ≤10 kHz; 0.25 mT	2300 ±20%	
μ_a	100 °C; 25 kHz; 200 mT	5500 ±25%	
B	25 °C; 10 kHz; 1200 A/m	≈ 470	mT
	100 °C; 10 kHz; 1200 A/m	≈ 380	mT
P_V	100 °C; 25 kHz; 200 mT	≤ 80	kW/m^3
	100 °C; 100 kHz; 100 mT	≤ 80	
	100 °C; 100 kHz; 200 mT	≈ 450	
ρ	DC, 25 °C	≈ 5	Ωm
T_C		≥ 220	°C
density		≈ 4800	kg/m^3

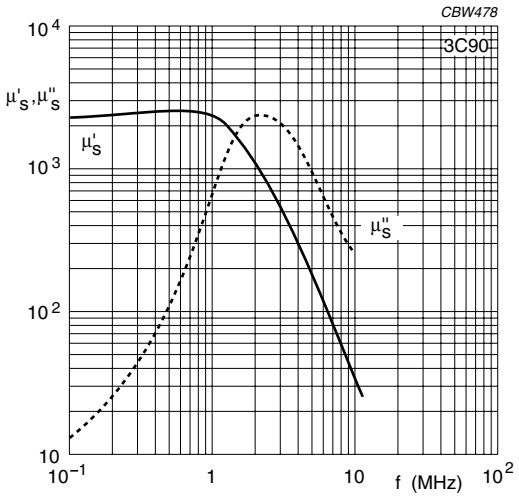

Fig.1 Complex permeability as a function of frequency.

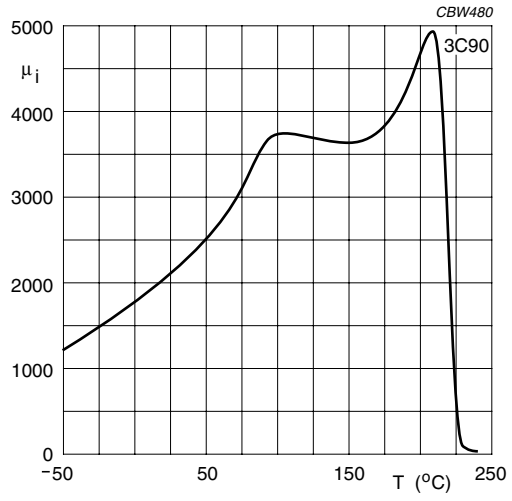

Fig.2 Initial permeability as a function of temperature.

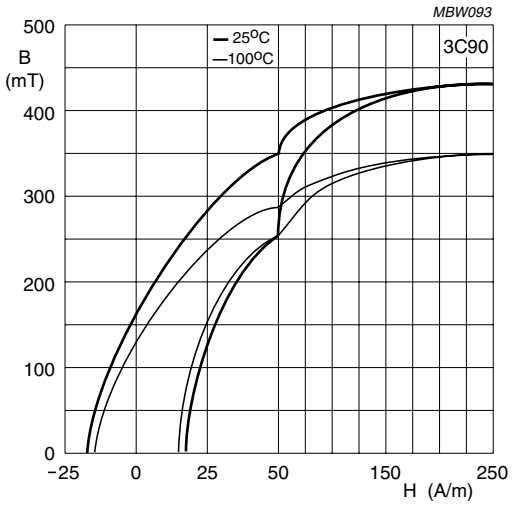

Fig.3 Typical B-H loops.

C055202A2

110 Delta Drive
Pittsburgh, PA 15238
Phone: 412/696-1333
Fax: 412/696-0333
Email:magnetics@spang.com

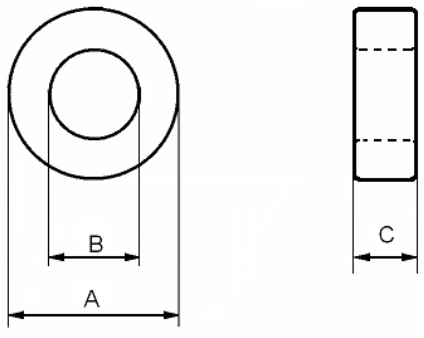

Permeability (μ)	A_L (nH/T^2)	Nominal DC Resistance (Ohms/mH)	B/NI Gauss per Amp. Turn
550	320 ± 8%	0.025	136 (<50 gauss)

Dimensions (mm)		
	Uncoated	Coated
O.D. (A)	20.3 nom	21.08 max
I.D. (B)	12.7 nom	12.06 min
Ht. (C)	6.35 nom	7.11 max

Markings		
XXXXXX	55202A2	X
Lot Number	Part Number	Inductance Grade

Physical Characteristics					
W_A (mm^2) Window Area	A_e (mm^2) Cross Section	L_e (mm) Path Length	V_e (mm^3) Volume	Weight (grams)	Box Quantity (pieces)
114	22.1	50.9	1,120	9.8	1,600

Winding Turn Length (mm)	
Winding Factor	Length/Turn
100% (Unity)	36.7
60%	31.5
40%	26.4
20%	24.1
0%	23.3

Wound Coil Dimensions (mm)	
Maximum O.D. (u.w.f.)*	29.2
Maximum HT. (u.w.f.)*	17.4

*u.w.f. – unity winding factor

Surface Area (mm^2)	
Unwound Core	1,210
40% Winding Factor	1,890

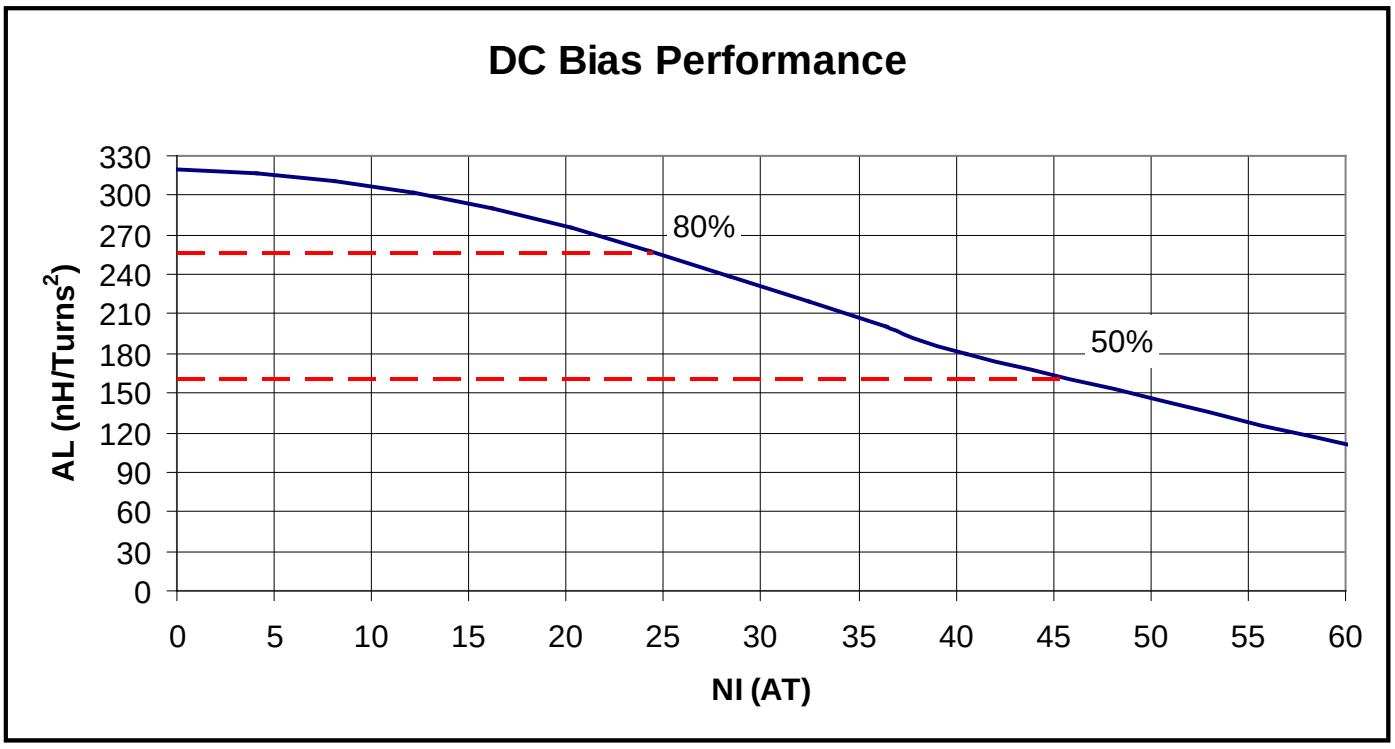

Revision date 5/28/2009

C

SELECTED PUBLICATIONS

This article has been accepted for publication in a future issue of this journal, but has not been fully edited. Content may change prior to final publication. Citation information: DOI 10.1109/TPEL.2014.2297993, IEEE Transactions on Power Electronics

Electronic Tuning of Misaligned Coils In Wireless Power Transfer Systems

Samer Aldhaher, Patrick C. K. Luk, *Senior Member, IEEE* James F. Whidborne, *Senior Member, IEEE*
School of Engineering, Cranfield University, Bedford, UK
p.c.k.luk@cranfield.ac.uk

***Abstract*—The misalignment and displacement of inductively coupled coils in a wireless power transfer system (WPT) can degrade the power efficiency and limit the amount of power that can be transferred. Coil misalignment leads the primary coil driver to operate in an untuned state which causes non-optimum switching operation and results in an increase in switching losses. This paper presents a novel method to electronically tune a Class E inverter used as a primary coil driver in an inductive WPT system to minimize the detrimental effects of misalignment between the inductively coupled coils which may occur during operation. The tuning method uses current controlled inductors (saturable reactors) and a variable switching frequency to achieve optimum switching conditions regardless of the misalignment. Mathematical analysis is performed on a Class E inverter based on an improved model of a resonant inductive link. Experimental results are presented to confirm the analysis approach and the suitability of the proposed tuning method.**

***Index Terms*—Inductive power transmission, Coupling circuits, Resonant inverters, Tunable circuits and devices**

I. Introduction

Research in wireless power transfer (WPT) technologies based on magnetic induction is gaining momentum recently due to the increasing reliance on battery-powered applications ranging from electric vehicles to mobile devices and medical implants [1]–[6]. However, the issues of coil misalignment and displacement, highlighted in wireless charging of electric vehicles, appear to be not adequately addressed. Improper parking of the vehicle will result in the wireless charging platform operating at a degraded performance of lower efficiency, reduced power transfer and longer charging time. A possible solution is to include additional coils either in the transmitter or in the vehicle so that the effect of misalignment is reduced over a certain range [2], [7]–[9]. The main disadvantages of this solution are larger required surface area, higher cost and weight of the overall system. An alternative solution that addresses these shortcomings is to retune the transmitter in order to operate at optimum switching conditions when the coils are in a misaligned state [5], [10]–[15]. This paper further explores and investigates the viability and practicality of the tuning solution presented in [10], [11] by using saturable reactors to tune a Class E DC/AC inverter designed to drive an inductive link at 800 kHz.

This paper is organised as follows. Section II derives analytical expressions of the reflected impedances of a resonant inductive link while considering the equivalent series resistance (ESR) of the resonant elements. Section III analyses the Class E inverter including the reflected impedances of the inductive link. A numerical solution is presented to calculate the values of the Class E inverter's parameters to be controlled as the coupling coefficient of the inductive link varies. Section IV discusses the use of saturable reactors as tuning elements and the key design aspects. Section V describes an implemented WPT system, the principle of operation of the electronic tuning method is discussed and extensive results based on experimental measurements are presented. Finally, Section VI includes the conclusion and future work.

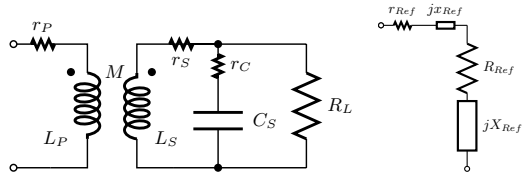

(a) circuit representation (b) equivalent circuit

Fig. 1. Resonant inductive link circuit model

II. Inductive Link Model

Fig. 1a shows a typical inductively coupled circuit, which consists of a primary coil represented by inductance L_P and its ESR r_P, and a secondary coil represented by an inductance L_S and its ESR r_S. The ESR of the primary and the secondary coils includes the ohmic resistance, the skin effect and the proximity effect. A capacitor C_S is connected in parallel with the secondary coil to allow for resonant operation. Resistance r_C represents the ESR of the capacitor which includes its dielectric losses. The load represented by a resistance R_L is connected in parallel with the secondary coil. Inductance M represents the mutual inductance between the primary and secondary coils and is equal to

$$M = k\sqrt{L_P L_S} \tag{1}$$

where k is the coupling coefficient between the primary and secondary coils.

The reflected impedance of the secondary coil seen by a voltage source connected to the primary coil is

This article has been accepted for publication in a future issue of this journal, but has not been fully edited. Content may change prior to final publication. Citation information: DOI 10.1109/TIA.2014.2300200, IEEE Transactions on Industry Applications

Wireless Power Transfer Using Class E Inverter with Saturable DC-Feed Inductor

Samer Aldhaher, Patrick C. K. Luk *Senior Member, IEEE*, Akram Bati
School of Engineering, Cranfield University, Bedford, UK
p.c.k.luk@cranfield.ac.uk

***Abstract*—Resonant converters used as coil drivers in inductive links generally operate efficiently at optimum switching conditions for constant load values and ranges. Changes in load and range can shift the operation of the coil driver to a non-optimum switching state which results in higher switching losses and reduced output power levels. This paper presents a method to adapt to variations in range for a Class E inverter used as a coil driver in a wireless power transfer (WPT) system based on inductive coupling. It is shown that by controlling the duty cycle of the inverter's switch and the value of its DC-feed inductance, the Class E inverter can be tuned to operate at optimum switching conditions as the distance between the coils of the WPT system changes. Mathematical analysis is presented based on a linear piecewise state-space representation of the inverter and the inductive link. Extensive experimental results are presented to verify the performed analysis and validity of the proposed tuning procedure.**

***Index Terms*—Inductive power transmission, Coupling circuits, Resonant inverters, Tunable circuits and devices**

I. Introduction

The weak coupling of the coils in an inductive link requires a strong magnetic field to be created to deliver high power levels at large ranges. To achieve this, it requires the use of coil drivers that can generate large currents at frequencies often in the kilohertz and megahertz ranges. The Class E inverter is a suitable type of DC/AC inverters to meet such a requirement. Invented by the Sokals [1] in 1975, it has been studied extensively and its analysis is well documented in literature [2]–[10]. The Class E inverter is simple to construct, and consists of a single switching element and has a large power handling capability compared to other inverters. It can achieve a theoretical 100% power efficiency by zero-voltage switching (ZVS) and zero-voltage derivative switching (ZVDS). It is considered as a resonant converter and operates at optimum switching conditions for a fixed value of load and switching frequency. Due to this operating constraint, the use of the Class E inverter as the coil driver in an inductive link means that the wireless power transfer (WPT) system can only operate efficiently for fixed values of load, range and resonant frequency. As a result, novel WPT applications where mobility and dynamic range are required, cannot benefit from the features of the Class E inverter.

The effect of displacement and misalignment of the coils in a WPT system on the performance of Class E inverters are investigated in [11], [12]. It is shown that the displacement of the coils from their optimum position shifts the operation of the Class E inverter to a non-optimum switching condition. As a result, the overall efficiency of the WPT system is degraded and the power delivered to the load is reduced. In addition, large voltages and current spikes can develop in the Class E inverter and may result in permanent damage to the inverter's switching element. Therefore, the Class E inverter will have to be tuned to operate at optimum switching conditions as the displacements in the coils occur. A tuning method has been presented in [12] to allow the Class E inverter to operate optimally by replacing a capacitor and adjusting the switching frequency. This tuning method may not be a practical solution since the inverter has to be powered off before physical replacements and adjustments can be then performed. In [13], adaptive frequency tuning is used at the primary coil driver and an adaptive impedance matching circuit is included at the secondary coil side. The received power is regulated as the range of the coils changes. Although this solution allows for maximum power efficiency to be achieved over a certain coil separation range, it requires complex circuitry and powerful signal processing microcontrollers and does not necessary allow the coil driver to operate at its optimum conditions. In this paper, we extend on our previous work presented in [11] in order to achieve optimum switching conditions of the coil driver by using duty cycle control and saturable reactors.

This paper is organised as follows. Section II provides a brief review on the operation of inductive links. Section III analyses the Class E inverter including the inductive link using a piecewise linear state-space representation. Section IV presents the tuning method of the Class E inverter and discusses how the values of the duty cycle of the switching signal and DC-feed inductance are calculated to achieve optimum switching conditions. Section V presents extensive experimental results to verify the analysis of the Class E inverter and to confirm the successful operation of the tuning method. Finally, Section VII includes the conclusion and future work.

II. Resonant Inductive Links Review

This section provides a brief review of inductive links, further details can be found in [12], [14]–[23]. An inductive link consists of a primary coil driven by a power current signal at a certain frequency and a secondary coil tuned to that frequency. The secondary coil, to which the load is connected to, can be tuned by using an external capacitor. The secondary coil can also be designed with a self-resonant frequency that is equal to the frequency of the power current signal of the primary coil. Both coils are separated by a certain

This article has been accepted for publication in a future issue of this journal, but has not been fully edited. Content may change prior to final publication. Citation information: DOI 10.1109/TPEL.2014.2316170, IEEE Transactions on Power Electronics

High Input Voltage High Frequency Class E Rectifiers for Resonant Inductive Links

Samer Aldhaher, Patrick C. K. Luk, *Senior Member, IEEE*, Khalil El Khamlichi Drissi, James F. Whidborne, *Senior Member, IEEE*

***Abstract*—The operation of traditional rectifiers such as half-wave and bridge rectifiers in wireless power transfer applications may be inefficient and can reduce the amount of power that is delivered to a load. An alternative is to use Class E resonant rectifiers which are known to operate efficiently at high resonant frequencies and at large input voltages. Class E rectifiers have a near sinusoidal input current which leads to an improved overall system performance and increased efficiency, especially that of the transmitting coil driver. This paper is the first to investigate the use of Class E resonant rectifiers in wireless power transfer systems based on resonant inductive coupling. A piecewise linear state-space representation is used to model the Class E rectifier including the rectifying diode's forward voltage drop, its ON resistance and the equivalent series resistance of the resonant inductor. Power quality parameters, such as power factor and total harmonic distortion, are calculated for different loading conditions. Extensive experimental results based on a $10\,\mathrm{W}$ prototype are presented to confirm the performed analysis and the efficient operation of the rectifier. An impressive operating efficiency of $94.43\,\%$ has been achieved at a resonant frequency of $800\,\mathrm{kHz}$.**

***Index Terms*—Inductive power transmission, AC-DC power converters, high frequency rectifiers.**

I. Introduction

Whilst most of recent published work in inductive power transfer (IPT) technology focuses on the design and optimization issues of the resonant inductive coils [1]–[8] and the transmitting coil driver [9]–[13], there has been little research in high frequency, high efficiency rectifiers for IPT applications and their impact on the overall performance of an IPT system. In previous papers, the load connected to the secondary coil of the inductive link has either been an AC load in the form of a resistor [1], [2], [8]–[14], or a DC load connected through an AC/DC rectifier. Since DC loads are more common than AC loads, more research into rectifiers that are suitable for IPT systems is required.

The majority of AC/DC rectifiers that have been used in recent publications about IPT systems are either traditional half-wave rectifiers [15] or bridge rectifiers [3], [7], [16], [17]. The main losses that occur in the rectifiers are due to the forward voltage drop of the rectifying elements and their switching losses. Synchronous rectifiers based on a bridge configuration can improve the overall efficiency in IPT systems. However timing and control of the four switches may be difficult especially at high resonant frequencies [18]. In addition, traditional half-wave rectifiers and bridge rectifiers have a non-sinusoidal input current and can cause a non-sinusoidal current to flow out of the secondary resonant circuit of the inductive link. This affects the performance and efficiency of the primary coil driver since most primary coil drivers operate at resonance and generate a sinusoidal driving current.

Class E rectifiers are resonant switching circuits that can operate efficiently at frequencies exceeding $500\,\mathrm{kHz}$. Efficient operation is achieved due to the zero-voltage switching (ZVS), low voltage-slope (dv/dt) switching, zero-current switching (ZCS) and low current-slope (di/dt) switching of the rectifying element. The principle of operation of Class E rectifiers and the different configurations that have been researched are summarised in [19], [20] and the references therein. Class E rectifiers have a near sinusoidal input current with low harmonic distortion which makes them compatible with resonant inverters, such as Class D and Class E, that are used as primary coil drivers in IPT systems. Class E rectifiers have been used to form resonant DC-DC converters [21]–[26] and in power harvesting and power recovery applications [27]. Nonetheless, there appears no report in literature on the use of Class E rectifiers for IPT systems.

This paper is the first to propose and implement a Class E rectifier for IPT. Here, a Class E half-wave ZVS, low dv/dt resonant switching rectifier is developed for IPT systems with a parallel resonant secondary coil to improve their performance and increase their overall efficiency. Based on the well established Class E rectifier configuration in [28], this paper extends the work by introducing a novel analysis based on state-space modelling to provide a more accurate mathematical representation of the rectifier. The state-space model takes into consideration the diode forward voltage drop, its ON resistance and the equivalent series resistance (ESR) of the resonant inductor, all of which have been omitted in the analysis of Class E rectifiers in previous work.

This paper is organised as follows. Section II introduces the Class E rectifier and presents a piecewise linear state-space model, parameters such as duty cycle and output voltage are numerically evaluated. Section III discusses the performance of the Class E rectifier by evaluating several parameters which haven't been evaluated before for Class E rectifiers such as the power factor, the normalised input root mean square (RMS) current and its total harmonic distortion (THD). Section IV presents extensive experimental results about the operation and the performance of a Class E rectifier used in an IPT system. Section V gives the conclusion and suggests future work.

Manuscript received Aug. 2013; revised Feb. 2014; accepted Apr. 2014.

S. Aldhaher, P. C. K. Luk and J. F. Whidborne are with the School of Engineering, Cranfield University, Bedford, MK43 0AL, UK. E-mail: p.c.k.luk@cranfield.ac.uk.

Tuning Class E Inverters Applied in Inductive Links Using Saturable Reactors

Samer Aldhaher, Patrick Chi-Kwong Luk, *Senior Member, IEEE*, and James F. Whidborne, *Senior Member, IEEE*

***Abstract*—This paper investigates the performance of Class E inverters used in wireless power transfer applications based on resonant inductive coupling. The variations in the load and the distance between the coils cause Class E inverters to operate under nonoptimal switching conditions, which result in inefficient operation and can lead to permanent damage to its switching transistor. Therefore, a novel approach to tune Class E inverters electronically is proposed. The tuning method relies on saturable reactors to ensure that the inverter operates under optimal switching conditions regardless of variations in the load and the distance between the coils. In addition, a more accurate model of inductive links is presented in order to provide a better understanding of the major power losses in resonant inductive links. Experimental results are presented to confirm the improved accuracy of the inductive link model and the validity of the tuning method.**

***Index Terms*—Coupling circuits, inductive power transmission, resonant inverters, tunable circuits and devices.**

I. Introduction

WIRELESS power transfer (WPT) based on resonant inductive links has received a lot of attention recently to provide power to a wide variety of applications such as portable handheld devices, medical implants [1], [2], lighting [3], and charging of electric vehicles [4], [5]. Increasing the range and power transfer capability of WPT systems requires higher resonant frequencies and more powerful primary coil drivers. The Class E inverter, first introduced by Sokal and Sokal in 1975 [6], is an example of such a design that can match the requirements of WPT systems by having the ability to deliver large power levels at higher switching frequencies. Class E inverters feature simplicity, low component count, and can be constructed using a single-switching transistor, and therefore, require less complicated gate driving circuitry and timing control. Hence, the Class E inverter is suited to be used as the primary coil driver in resonant inductive links [7]–[15].

In general, Class E inverters are sensitive to variations in the load impedance [16]. Small deviations from the optimum load value would cause the inverter to operate under nonoptimal and inefficient switching conditions, whereas large deviations could cause permanent damage to its switch. In resonant inductive links, the variations in the load or in the distance between the primary and secondary coils cause the reflected impedance seen by the primary coil driver to vary significantly. This limits the operation of Class E inverters in resonant inductive links to a narrow range of load and distance values. A significant benefit for a WPT system would be the ability to maintain optimum power transfer and efficiency of the primary coil driver over a useful load and distance ranges. This would increase the scope of WPT applications and allow novel applications such as dynamic grid-to-vehicle charging and vehicle-to-vehicle charging to be implemented. To achieve this, the Class E inverter would need to be tuned as the load and distance vary.

Tuning methods based on impedance transformation [17]–[20], impedance network switching [21], [22], and phase control and load modulation [23]–[26] have been proposed. These methods allow the Class E inverter to operate under optimal switching conditions, achieving zero-voltage switching (ZVS) and zero-voltage derivative switching (ZVDS) regardless of the load value. However, these methods may not be applicable to resonant inductive links due to the complexity of the load and the reflected impedances. Furthermore, including additional components in series with the primary coil is undesirable since this increases the equivalent series resistances (ESR), and hence, an increase in ohmic power losses. It should be noted that in recent publications in high power resonant inductive links [1], [27]–[30], only the ESR of the coils is included in the modeling of the inductive link, whereas the ESR of the resonant capacitors is ignored.

This paper investigates the effect of changing the load value and the distance between the coupled coils in resonant inductive links, as well as the effect of these changes on the performance of Class E inverters based on an improved circuit representation of the inductive link. A novel method is proposed to electronically tune the Class E inverter by using a saturable reactor to ensure that the inverter operates under optimum switching conditions for any load and distance values, while maintaining a relatively constant power transfer and efficiency over a certain load and distance ranges.

This paper is organized as follows. Section II provides a brief review of the theory behind resonant inductive links, discusses the operation in near resonance, and the factors that affect the value of the reflected impedance. Section III shows the effect of the load and the mutual inductance between the coils on the performance of Class E inverters and describes the proposed tuning method. Section IV-A describes the experimental setup and the validation process of the proposed method. Section IV-B includes the experimental results and discussion. Finally, Section V provides the conclusions and future work.

Manuscript received February 27, 2013; revised May 14, 2013; accepted June 17, 2013. Date of current version January 29, 2014. Recommended for publication by Associate Editor U. K. Madawala.

The authors are with the School of Engineering, Cranfield University, Bedford, MK43 0AL U.K. (e-mail: s.aldhaher@cranfield.ac.uk; p.c.k.luk@cranfield.ac.uk; j.f.whidborne@cranfield.ac.uk).

Color versions of one or more of the figures in this paper are available online at http://ieeexplore.ieee.org.

Digital Object Identifier 10.1109/TPEL.2013.2272764

A One-comparator Counter-based Controller for Synchronous DC/DC Converters

Samer Aldhaher, James F. Whidborne, *Senior Member, IEEE,* Patrick C. K. Luk, *Senior Member, IEEE*

***Abstract*—A low complexity, low component-count digital controller consisting of a single comparator and a digital counter is proposed for the purpose of providing control and voltage regulation for synchronous buck DC/DC converters used in voltage ripple insensitive applications. The system is modelled and analysed based on an averaged-circuit representation of the buck converter including the parasitic resistances of its passive and active components. The existence of limit cycles is investigated by using a describing function to represent the comparator and the PWM generator. Simulation results are presented and are verified with experimental results for a 36W prototype. The validity of the predicted performance of the proposed controller for higher loading conditions is thus confirmed.**

I. Introduction

Numerous control methods and techniques for DC/DC converters have been developed over the years and recently a trend towards digital-based control can be realised. Classical analog controllers that have been used for a few decades are now being replaced by digital controllers with enhanced performances. Due to the availability of design and simulation software, rapid prototyping tools and most importantly, the availability of powerful microprocessors and computers, new controllers that were not possible to implement previously are now being introduced. A literature survey conducted by Cortes [1] classified controllers for DC/DC converters into five groups; hysteresis controllers [2–7], linear controllers in their digital form such as voltage-mode [8–10] or current-mode controllers [9, 11–14] and the classical PID controller [15–23], fuzzy-logic controllers [24–27], sliding-mode controllers [28–32], predictive controllers [33–39] and other advanced controllers [40–44]. All of these controllers have been tested and demonstrated to provide precise control, excellent performance and robustness. However, the majority of these control techniques and methods are based on field programmable gate arrays (FPGAs) or require powerful microprocessors with a high computational capability in order to run smoothly and efficiently. This leads to an increase in the overall cost and greater system complexity as well as difficulties in implementation and manufacturing. Further design issues and limitations are highlighted in [45] and in [31] for sliding-mode controllers. As a result, the transition from analog-based to digital-based controllers for DC/DC converters in industrial and consumer applications has been slow and many manufacturers still use analog controllers for their simplicity, reliable performance and reduced implementation cost.

In digital based controllers, an analog-to-digital converter (ADC) is required to read the output voltage of a DC/DC converter and compare it with a reference voltage to generate an error signal. Obtaining a high performance digital controller requires a precision high sampling rate ADC and a processor or logic circuitry clocked at tens to hundreds of megahertz. For applications and loads that don't demand a high performance controller, using an ADC may not be the best design solution. In [46] and [47], a comparator is used in a digital controller for an ultra-low power buck converter instead of an ADC to provide the error signal. This drives an up/down digital counter representing the duty cycle of the pulse width modulated (PWM) signal that controls the switches of the buck converter. The output voltage of the converter will not settle at a steady voltage but instead enters a limit cycle about the desired level. Roh [48] further improved the controller by using a hysteresis or deadzone comparator to reduce the limit cycle in the output voltage. However, the controller was based on an ideal model of a buck converter and did not include the parasitic resistances of the converter's elements. The parasitic resistances should be considered and included in the DC/DC converter's model especially in high power converters as their influence on the converter's output and response is significant and cannot be ignored.

This paper investigates the performance and the suitability of the one-comparator counter-based controller applied to synchronous buck DC/DC converters used in voltage ripple insensitive applications such as motor drives and battery chargers. A large-signal low-frequency model of a synchronous buck DC/DC converter is derived including the parasitics of its elements. The effect of resolution limitations of PWM generators and clock frequencies of digital counters, the values of passive components and the effect of the deadtime of MOSFET drivers on the limit cycles in the output voltage and the response time of the controller are discussed.

This paper is organised as follows. In Section II the controller's principle of operation is described, the hardware components that form the controller are modelled. Mathematical analysis based on the describing function method is performed and the equations that describe the amplitude and the frequency of the limit cycles as well as the transient response are derived for several cases depending on the resolution of the counter, the PWM generator and the clock frequency. In Section III, simulation results are presented and the proposed controller's performance is assessed by comparing its performance with a linear analog controller. Section IV describes the experimental setup of the controller and presents experimental results that show the performance and response of the prototype converter using the proposed controller under different loading conditions. Conclusions and future work are discussed in Sec. V.